UNIVERSITA' DEGLI STUDI DI VERONA

DEPARTMENT OF

BIOTECHNOLOGY

DOCTORAL PROGRAM IN

BIOTECHNOLOGY

WITH THE FINANCIAL CONTRIBUTION OF

MUR Dottorati di Ricerca PNRR D.M. 351

XXXVIII / 2022

TITLE OF THE DOCTORAL THESIS

Tailored Molecularly Imprinted Polymers Nanoparticles as Recognition Elements for High-Performance Sensing Platforms

S.S.D. CHIM/01

Coordinator: Prof.ssa Favia Guzzo

Signature _____

Tutor: Prof.ssa Alessandra Maria Bossi

Signature _____

Co-tutor: Prof. Devid Maniglio

Signature _____

Doctoral Student: Dott.ssa Alice Marinangeli

Signature _____

Table of Contents

Acknowledgements

I would like to express my sincere gratitude to the Italian Ministry of University and Research (MUR) and to the National Recovery and Resilience Plan (PNRR) for funding my doctoral fellowship and supporting the development of this research project.

My deepest thanks go to Professor Alessandra Bossi, my supervisor, for her guidance, scientific insight and constant support throughout these years. I am deeply thankful for the trust she placed in me from the very beginning, for believing in my potential and for teaching me the rigour, precision and curiosity that underpin this profession. Her enthusiasm and her commitment in involving me in so many inspiring research projects have played a central role in my scientific development and in fostering my passion for this field.

I am equally grateful to Prof. Devid Maniglio for his support and guidance throughout these three years. His patience, calm attitude and constant encouragement, especially during moments of difficulty, have been invaluable in helping me progress and achieve my goals.

I would also like to thank Cranfield University and the Biosensor Laboratory within the School of Aerospace, Transport and Manufacturing for hosting me during my six-month research stay. My sincere thanks go to Dr. Iva Chianella, whose support, availability and scientific expertise enabled me to learn new techniques and to develop my work with growing autonomy. This period has been fundamental for my scientific development and has greatly enriched my personal experience.

I am also grateful to Professor Pinar Hatir Cakir for her kindness and the collaborative spirit she brought to our work together. The opportunity to contribute to such an interesting project through our collaboration has been truly valuable for my scientific development.

I am also grateful to the Centro Piattaforme Tecnologiche (CPT) for providing access to the instrumentation and facilities essential for the experimental work presented in this thesis.

List of publications

This thesis is based on the following publications:

- Bossi, A. M., Marinangeli, A., Quaranta, A., Pancheri, L., & Maniglio, D. (2023). Time-resolved fluorescence spectroscopy of molecularly imprinted nanoprobes as an ultralow detection nanosensing tool for protein contaminants. *Biosensors*, *13*(7), 745.
- Marinangeli, A., Chianella, I., Radicchi, E., Maniglio, D., & Bossi, A. M. (2024). Molecularly Imprinted Polymers Electrochemical Sensing: The Effect of Inhomogeneous Binding Sites on the Measurements. A Comparison between Imprinted Polyaniline versus nanoMIP-Doped Polyaniline Electrodes for the EIS Detection of 17β-Estradiol. *ACS sensors*, *9*(9), 4963-4973.
- Hatir, P. C., Marinangeli, A., Bossi, A. M., & Cayli, G. (2025). Castor oil-based molecularly imprinted nanoparticles for the detection of cardiac troponin I: Towards green molecularly imprinted nanoreceptors. *Talanta Open*, *11*, 100439.
- Marinangeli A., Hatir P.C., Yagci M.B. & Bossi A.M. (2026). Highly Sensitive Biosensor for the Detection of Cardiac Troponin I in Serum via Surface Plasmon Resonance on Polymeric Optical Fiber Functionalized with Castor Oil-derived Molecularly Imprinted Nanoparticles. *Biosensors*, *16*, 12.

Publications not included in the thesis:

- Bossi, A. M., Casella, S., Stranieri, C., Marinangeli, A., Bucciarelli, A., Pasini, A. M. F., & Maniglio, D. (2025). Protein-based molecular imprinting: gelatin nanotraps for interleukin-6 sequestration in inflammation cell models. *Trends in Biotechnology*.
- Vurro, F., Dembech, E., Manfredi, R., Debbi, G., Bettelli, M., Marinangeli, A., ... & Coppedè, N. (2025). Glucose selective textile OECT based on molecularly imprinted nanoparticles functionalized channel for in vivo plants monitoring. *Sensors and Actuators B: Chemical*, *436*, 137640.

List of abbreviations

2-VP	2-vinylpyridine
4-VP	4-vinylpyridine
AA	Acrylic acid
Aam	Acrylamide
AFM	Atomic Force Microscopy
AIBN	Azobisisobutyronitrile
AMR	Acrylated Methyl Ricinoleate
APS	Ammonium Persulfate
ATRP	Atom Transfer Radical Polymerization
BPA	Bisphenol A
BSA	Bovine Serum Albumin
CE	Counter Electrode
CRP	Controlled or Living Radical Polymerization
CV	Cyclic Voltammetry
Cyt c	Cytochrome c
DLS	Dynamic Light Scattering
DP	Differential Power
DPV	Differential Pulse Voltammetry
E2	17β-estradiol
EC_{50}	Half-Maximal Effective Concentration
EG-FETs	Electrolyte-Gated Field-Effect Transistors
EGMEA	Ethylene Glycol Methyl Ether Acrylate
EIS	Electrochemical Impedance Spectroscopy
Fluo-nanoMIPs	Fluorescence Molecularly Imprinted Polymer Nanoparticles
FluorMAA	Fluorescein O-Methacrylated
FRET	Förster Resonance Energy Transfer
FRP	Free-Radical Polymerization
FT-IR	Fourier-Transform Infrared Spectroscopy
GreenNanoMIPs	Green Molecularly Imprinted Polymer Nanoparticles
HSA	Human Serum Albumin
HTR	Human Transferrin
ITC	Isothermal Titration Calorimetry
IUPAC	International Union of Pure and Applied Chemistry
K_{aff}	Apparent Affinity Constant
K_D	Apparent Dissociation Constant
k_{on}	Kinetic Rate-on Constant
LAP	Lithium Phenyl-2,4,6-trimethylbenzoylphosphinate
LCST	Lower Critical Solution Temperature

LOD	Limit of Detection
LOQ	Limit of Quantification
MAA	Methacrylic Acid
MBA	N, N′-Methylenebis(Acrylamide)
MBAAm	N, N-Methylenebisacrylamide
MIP	Molecularly Imprinted Polymer
nanoMIPs	MIP nanoparticles
NHMAm	N-Hydroxymethylacrylamide
NIPAAm	N-IsopropylAcrylamide
NMP	Nitroxide-Mediated Polymerization
NR10	C-terminal peptide of cTnI
NR10-FITC	C-terminal peptide of cTnI labelled with Fluorescein
OECTs	Organic Electrochemical Transistors
P	Progesterone
PANI	Polyaniline
PDI	PolyDispersity Index
PET	Photoinduced Electron Transfer
PETOD	Poly(3,4-Ethylenedioxythiophene)
PMBI	Poly(Mercaptobenzimidazole)
POF	Plastic Optical Fiber
PPy	Polypyrrole
PTM	Photomultiplier
QCM	Quartz Crystal Microbalances
RAFT	Reversible Addition-Fragmentation Chain Transfer
Rct	Charge Transfer Resistance
RE	Reference Electrode
SAM	Self-Assemble Monolayer
SAW	Surface Acoustic Wave
SELEX	Systematic Evolution of Ligands by EXponential enrichment
SEM	Scanning Electron Microscopy
S_{low}	Sensitivity at Low Concentration
SPE	Screen Printed Electrode
SPR	Surface Plasmon Resonance
SWV	Square Wave Voltammetry
TBAam	Tert-Butylacrylamide
TCSPC	Time-Correlated Single Photon Counting
TEMED	N,N,N',N'-Tetramethylethylenediamine
Th	Thiophene
WE	Working Electrode
XPS	X-ray Photoelectron Spectroscopy

Abstract

This PhD thesis focuses on the design, fabrication and analytical evaluation of molecularly imprinted polymer (MIP)-based sensing platforms, with the goal of developing highly selective and sensitive sensors for the detection of analytes at ultra-low concentrations.

Molecular imprinting offers a powerful and versatile approach to create synthetic receptors with biomimetic recognition capabilities, combining the selectivity of natural receptors with the chemical and physical robustness of synthetic polymers. Within this framework, the research presented herein explores different strategies aimed at enhancing the overall performance of MIP-based sensors.

The first part of the thesis provides an in-depth theoretical background on sensors and molecular imprinting polymers. The second part assembles the research results, which are illustrated through four scientific publications, each describing a specific strategy developed to improve the sensitivity and the overall performance of MIP-based sensors.

Paper I presents the development of fluorescent MIP nanoparticles for the ultra-low detection of protein contaminants, using human serum albumin as a proof-of-concept. The work introduces a strategy based on the controlled incorporation of fluorophores into the polymer matrix to maximize signal responsiveness. By fine-tuning the fluorophore-to-template ratio during polymerization, the study achieves enhanced sensitivity and demonstrates the successful integration of MIP-based recognition elements with time-resolved fluorescence spectroscopy as an effective optical transduction approach.

Paper II investigates how the structural homogeneity of imprinted binding sites influences the analytical performance of electrochemical MIP-based sensors. Two architectures were compared: an electropolymerized imprinted polyaniline layer, representing an inhomogeneous distribution of recognition sites, and a polyaniline layer doped with pre-synthesized uniform MIP nanoparticles. Using 17β-estradiol as analyte, the study demonstrates that the configuration with homogeneous MIP nanoparticles provides enhanced sensitivity and lower detection limits, confirming

that structural uniformity is a key factor in achieving high-performance electrochemical sensing.

Paper III reports the development of green MIP nanoparticles as biocompatible and sustainable synthetic receptors for the detection of cardiac troponin I, a key biomarker of myocardial infarction. The study introduces a design strategy based on renewable castor oil–derived monomers as eco-friendly functional components in MIP synthesis. The resulting MIP nanoparticles exhibit excellent stability and high recognition performance, demonstrating that environmentally sustainable materials can effectively replace conventional monomers in advanced MIP-based sensors.

Paper IV presents the development of a high-sensitivity optical sensor for cardiac troponin I detection, integrating castor oil-derived green MIP nanoparticles into a miniaturized plastic optical fiber surface plasmon resonance transducer. The study evaluates the feasibility of employing these sustainable nanoreceptors in a plasmonic configuration to achieve ultrasensitive and selective detection suitable for point-of-care diagnostics.

Riassunto

Questa tesi di dottorato è incentrata sulla progettazione, fabbricazione e valutazione analitica di piattaforme sensoriali basate su polimeri a stampo molecolare (Molecularly Imprinted Polymers), con l'obiettivo di sviluppare sensori altamente selettivi e sensibili per la rilevazione di analiti a concentrazioni ultrabasse. La tecnica dell'imprinting molecolare rappresenta un approccio potente e versatile per la realizzazione di recettori sintetici dotati di capacità di riconoscimento biomimetico, combinando la selettività tipica dei recettori naturali con la robustezza chimica e fisica dei polimeri sintetici. In questo contesto, il lavoro di ricerca qui presentato esplora diverse strategie volte a migliorare le prestazioni complessive dei sensori basati su MIPs.

La prima parte della tesi fornisce un approfondito inquadramento teorico sui sensori e sui polimeri a stampo molecolare. La seconda parte raccoglie i risultati sperimentali, illustrati attraverso quattro lavori scientifici, ciascuno dei quali descrive una specifica strategia sviluppata per incrementare la sensibilità e le prestazioni complessive dei sensori basati sui MIPs.

Il **Paper I** descrive lo sviluppo di nanoparticelle MIP fluorescenti per la rivelazione di contaminanti proteici, utilizzando l'albumina sierica umana come proof-of-concept. Il lavoro introduce una strategia basata sull'incorporazione controllata di fluorofori nella matrice polimerica, dimostrando che l'ottimizzazione del rapporto fluoroforo–templato durante la polimerizzazione incrementa la sensibilità del sensore e consente l'efficace integrazione degli MIP come elementi di riconoscimento in un approccio di trasduzione ottica basato sulla spettroscopia di fluorescenza risolta nel tempo.

Il **Paper II** analizza l'influenza dell'omogeneità dei siti di riconoscimento dei MIP sulle prestazioni analitiche di sensori elettrochimici. Sono state confrontate due architetture: uno strato elettropolimerizzato di polianilina imprintato, caratterizzato da una distribuzione non omogenea dei siti di riconoscimento, e uno strato di polianilina in cui sono state incorporate nanoparticelle MIP pre-sintetizzate e omogenee. Utilizzando il 17β-estradiolo come analita modello, lo studio dimostra

che la configurazione contenente nanoparticelle MIP uniformi offre maggiore sensibilità e limiti di rilevazione più bassi.

Il **Paper III** presenta lo sviluppo di nanoparticelle MIP "green" come recettori sintetici biocompatibili e sostenibili per la rilevazione della troponina cardiaca I, un biomarcatore chiave dell'infarto miocardico. Il lavoro propone una strategia di sintesi dei MIP basata sull'utilizzo di un componente derivato da olio di ricino, impiegato come monomero funzionale che consente di ottenere nanoparticelle stabili e dotate di elevate prestazioni di riconoscimento.

Il **Paper IV** descrive lo sviluppo di un sensore ottico ad alta sensibilità per la rilevazione della troponina cardiaca I, ottenuto integrando le nanoparticelle MIP "green" derivate da olio di ricino con un trasduttore plasmonico miniaturizzato basato su fibra ottica in plastica. Lo studio valuta la possibilità di impiegare questi nanorecettori sostenibili in configurazioni plasmoniche, ottenendo rilevazioni ultra-sensibili e selettive adatte ad applicazioni diagnostiche point-of-care.

Chapter I – Sensor

Sensors have become an integral part of modern life, often operating silently and unnoticed. They are everywhere: temperature sensors regulate refrigeration systems; pressure sensors monitor oil levels in vehicles; and photosensors control street lighting based on ambient light conditions. This widespread presence highlights the crucial role of sensors as intelligent interfaces between the physical world and digital control systems, enabling automation, safety, efficiency, and comfort across innumerable applications. Beyond physical sensors, which respond directly to changes in physical parameters such as temperature, pressure or light intensity, an important class of analytical devices is represented by chemical sensors and biosensors, which convert specific chemical or biochemical interactions into measurable signals [1]. Today, there is no shared definition of the term sensor, chemical sensor, or biosensor. This lack of standardisation has led to a certain degree of confusion and inconsistency in the terminology used across disciplines. In 1991, it was officially adopted by the International Union of Pure and Applied Chemistry (IUPAC) officially define a chemical sensor as "a device that converts chemical data, ranging from the concentration of a single sample component to complete composition analysis, into an analytically usable signal" [2]. This concise definition captures the core function of chemical sensors, that is the transformation of chemical information into a measurable and processable signal suitable for quantitative or qualitative analysis. An additional, widely cited description found in the literature, often referred to as the Cambridge definition, emphasizes the operational capabilities of chemical sensors: "Chemical sensors are miniaturized devices which can deliver real-time and on-line information on the presence of specific compounds or ions in even complex samples." [3]. This definition highlights two key strengths of chemical sensors, namely their ability to perform continuous real-time monitoring and their applicability even in challenging sample matrices.

Although different definitions of sensors coexist in literature, a general consensus has emerged on their architecture. their functional understanding ultimately relies

on the analysis of their internal organization. Based on this, every sensor can be described in terms of three fundamental components that act in sequence to convert an input stimulus into a measurable output. These are the recognition element (receptor), the transducer and the signal processor (Figure 1.1). The receptor, which can be of biological or synthetic origin, is responsible for the selective interaction with the target analyte. This molecular interaction triggers a physicochemical response, which is then converted into a measurable signal by the transducer. Therefore, this second element translates the recognition event into a readable signal, which may be electrochemical, electric, optical, thermal, or piezoelectric in nature, depending on the type of sensor. The signal is subsequently processed, amplified, and interpreted by the processor, ultimately providing a quantitative or qualitative output.

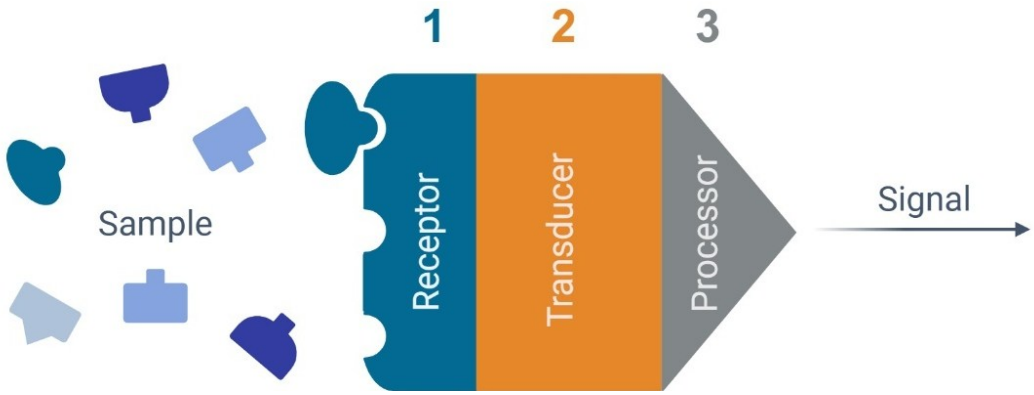

Figure 1.1 Scheme of the architecture of a sensor: receptor, transducer and signal processor.

The recognition element, or receptor, is the core component of a sensor responsible for the selective interaction with the analyte of interest. It can be of biological or synthetic nature, and its principal role is to ensure specificity, ideally allowing only the target molecule to bind, while minimizing non-specific interactions. Biological receptors, widely used in biosensors, include enzymes, antibodies, nucleic acids, and even whole cells.

Enzymes are among the commonly used biological recognition elements in biosensors, as their catalytic activity ensures high specificity toward target substrates while simultaneously providing intrinsic signal amplification, since a

single enzyme molecule can convert numerous substrate molecules without being consumed. Despite these advantages, their use is often limited by sensitivity to environmental changes, such as temperature and pH, as well as by a relatively short shelf life [4, 5]. Antibodies represent another important class of biological recognition elements widely employed in biosensors for applications ranging from clinical diagnostics to environmental monitoring, food safety, and pharmaceutical analysis. Their intrinsic ability to bind specific antigens with high affinity allows selective detection of the analyte even in complex matrices. However, their performance can be affected by factors such as denaturation or degradation during storage, which may affect their binding performance and stability over time [6, 7]. Whole cells can also act as biological recognition elements in biosensors, responding to external stimuli through physiological and metabolic changes and thereby enabling the detection of target analytes while simultaneously providing information on their effects on cellular functions. Such cellular receptors are particularly valuable in pharmacology, toxicology and cell biology where functional responses such as variations in gene expression, metabolism or adhesion are of primary interest [8, 9].

Alongside enzymes, antibodies, and whole cells, nucleic acids have emerged as another important class of biological recognition elements thanks to their well-defined structures and tunable physicochemical properties, they can function as highly specific probes for hybridization with complementary sequences or as selective receptors capable of binding a variety of chemical and biochemical targets. Unlike protein-based receptors, nucleic acid recognition layers can be synthetically produced and regenerated for repeated use, offering significant advantages in terms of stability, reproducibility, and cost-effectiveness. In particular, single-stranded DNA or RNA probes, commonly employed in genosensors, are highly valuable for the detection of mutations, pathogens, and genetic biomarkers, making them useful in clinical diagnostics [10, 11]. A particularly versatile class of nucleic acid receptors is represented by aptamers, short single-stranded DNA or RNA oligonucleotides that can fold into well-defined three-dimensional structures capable of binding selectively to a wide variety of targets, including small molecules, proteins, and even whole cells. Aptamers are generated through an *in*

vitro selection process known as SELEX (Systematic Evolution of Ligands by EXponential enrichment), which allows the isolation of high-affinity binders without the need for immunization or biological production systems. Despite being composed of natural biomolecules, their synthetic origin and programmable nature position them at the interface between biological and synthetic recognition elements [12, 13].

Although biological receptors exhibit high specificity, their application is frequently limited by factors such as reduced stability, susceptibility to denaturation, and high production costs. These challenges have driven growing interest in synthetic recognition elements, which provide enhanced chemical and thermal stability, simpler manufacturing and lower costs.

A prominent example of synthetic recognition elements is represented by molecularly imprinted polymers (MIPs), which are defined as biomimetic materials tailored with molecular imprinted cavities complementary in shape, size and functional groups to a target molecule [14, 15]. These imprinted cavities act as specific recognition sites, analogous to enzyme's active site or antibody's binding domain, and confer the ability to selectively bind the target molecule of interest. In addition to their selectivity, MIPs offer chemical and thermal stability, cost-effectiveness, and the ability to operate under harsh environmental conditions. Their versatility and custom-made nature make them suitable for a wide range of applications. Due to their relevance to this thesis, MIPs will be discussed in depth in Chapters II and III.

Once the target analyte has been selectively recognized by the receptor element, the subsequent step in the sensing process is the conversion of this recognition event into a measurable signal. As introduced earlier, this task is performed by the transducer, which converts the chemical or biological interaction occurring at the molecular level into a measurable physical signal. The nature of the transduction mechanism largely defines the mode of operation of the sensor and the type of signal generated (Figure 1.2).

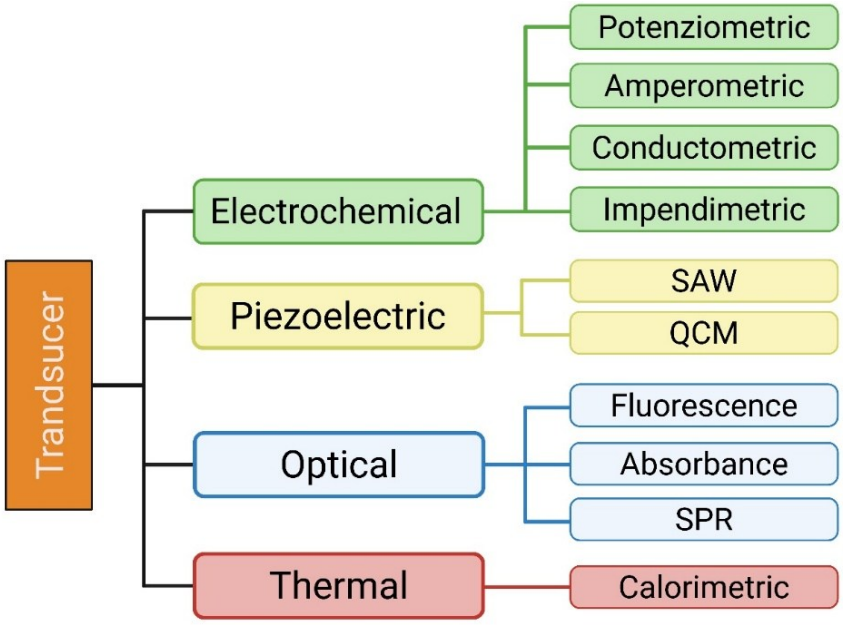

Figure 1.2 Classification of the main transduction methods.

Electrochemical transducers measure electrical signals that arise from redox reactions or changes in charge distribution at the sensor interface. They include amperometric, potentiometric, conductometric and impedimetric devices, which are widely employed due to their high sensitivity, low cost, and compatibility with miniaturized platforms. Optical transducers rely on variations in optical properties such as absorbance, fluorescence or surface plasmon resonance upon analyte binding. Fluorescence-based methods offer high sensitivity, multiplexing capability and suitability for imaging applications, although they generally require the use of external labels. In contrast, surface plasmon resonance (SPR) enables real-time and label-free monitoring of molecular interactions. Piezoelectric transducers, such as quartz crystal microbalances (QCM) or surface acoustic wave (SAW) devices, convert mass changes on a sensing surface into frequency shifts, thus enabling the detection of analytes without labelling. Thermal transducers detect variations in heat resulting from exothermic or endothermic reactions upon analyte binding. Among these classes of transduction, electrochemical and optical are particularly relevant to the present thesis and will be discussed in greater detail in Chapter IV. The selection of a suitable transduction mechanism depends on several factors, including the physicochemical nature of the analyte, the required detection limits,

the sample matrix, and practical aspects such as power consumption, response time, and the feasibility of integration into portable or implantable platforms [*16*]. In practice, this choice is often guided by a balance between analytical performance, level of integration, and application-specific constraints. As illustrated in Figure 1.3, different sensing approaches can be positioned according to their degree of integration and the need for labelling, reflecting the trade-offs between sensitivity, complexity of sample preparation, and potential for miniaturization.

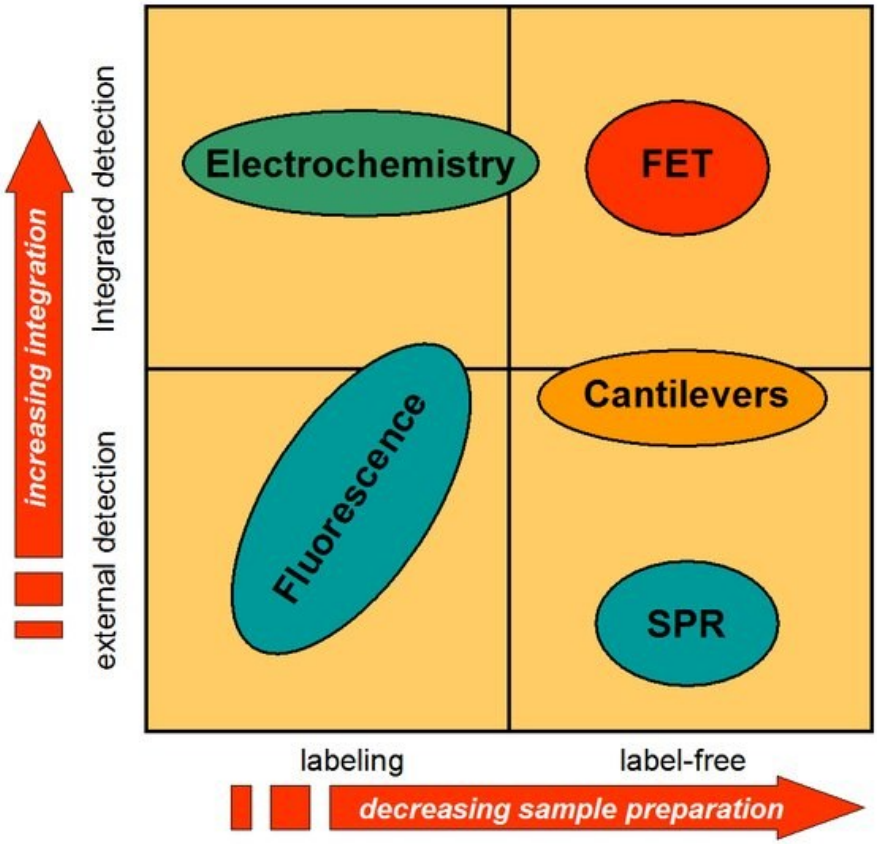

Figure 1.3 Choice of transduction methods according to the type of detection and sample preparation [17].

The signal processor represents the third and final component and its role is to condition and interpret the primary signal generated by the transducer, transforming it into a user-readable output. Signal processing commonly involves amplification, filtering, noise reduction and digitalization, all of which are critical to improving the accuracy, reliability and resolution of the measurement. Modern sensor platforms often incorporate microcontrollers, wireless communication modules and

embedded algorithms for real-time data analysis [18]. While the recognition element, transducer, and signal processor determine how a sensor operates, its analytical performance is assessed through a series of key parameters (Figure 1.4).

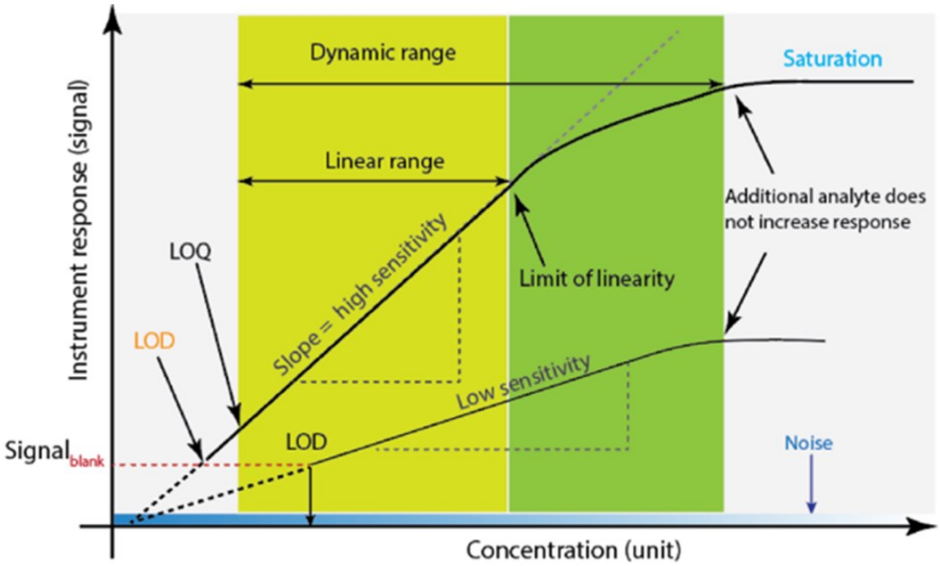

Figure 1.4 Main sensor's operational parameters [19].

The dynamic range defines the overall concentration interval within which a sensor provides a measurable response to the analyte and it extends from the lowest concentration distinguishable from background noise to the point of saturation, where additional analyte no longer produces an increase in signal intensity. Within this broad interval lies the linear range, which is the concentration range over which the sensor response is directly proportional to the analyte concentration, enabling accurate and quantitative analysis [20]. The sensitivity represents the ability of the sensor to generate a measurable signal in response to small changes in analyte concentration and corresponds to the slope of the linear response region. At low analyte concentrations, the sensitivity becomes particularly critical since it determines the ability to resolve small signal variations where the signal-to-noise ratio is minimal. The sensitivity at low concentration (S_{low}) can be expressed as:

$$S_{low} = \frac{|y_{final} - y_{start}|}{K_{app}}$$

Where y_{final} and y_{start} are the sensor responses at the final and initial analyte concentrations [20, 21]. The limit of detection (LOD) is defined as the lowest

analyte concentration that can be distinguished from background noise, typically calculated as three times the standard deviation of the blank divided by the sensitivity at low detection [22]:

$$LOD = \frac{3 \cdot St.Dev._{blank}}{Sensitivity\ at\ low\ concentration}$$

Closely related to the LOD, the limit of quantification (LOQ) represents the lowest analyte concentration that can be quantitatively determined with acceptable precision and accuracy. It is commonly estimated as ten times the standard deviation of the blank divided by the slope of the calibration curve at low concentration levels [22]:

$$LOQ = \frac{10 \cdot St.Dev._{blank}}{Sensitivity\ at\ low\ concentration}$$

An additional descriptor is the half-maximal effective concentration (EC_{50}) which is a parameter obtained directly from the sensor response curve and represents the analyte concentration that produces 50% of the maximum measurable signal. In systems operating under equilibrium conditions and linear conditions, EC_{50} typically approximates the apparent dissociation constant (K_D), which represents the equilibrium concentration of analyte at which half of the available binding sites are occupied, thus providing a thermodynamic descriptor of the binding affinity. The K_D is often used together with its reciprocal, referred to as the apparent affinity constant (K_{aff}):

$$\mathrm{K_{aff}} = \frac{1}{\mathrm{K_D}}$$

Although the terms "affinity and dissociation constant" are commonly employed in the biosensing literature, they should be regarded as a quantitative indicator of binding strength rather than a true thermodynamic constant in the strict sense [23, 24].

Selectivity reflects the sensor's capability to discriminate the target analyte in the presence of potential interferents and can be further quantified in terms of cross-reactivity toward structurally similar compounds. Response Time indicates the duration required for the sensor to reach a stable signal upon analyte exposure. Reproducibility and Repeatability assess the consistency of the sensor's response,

either across multiple devices, operators, or days, or under identical conditions. Finally, stability and lifetime describe the sensor's ability to maintain performance over time and usage. These parameters are often limited by receptor degradation, surface fouling, or drift in the transduction system [20].

References

[1] Nagl, S., & Wolfbeis, O. S. (2008). Classification of chemical sensors and biosensors based on fluorescence and phosphorescence. In *Standardization and Quality Assurance in Fluorescence Measurements I: Techniques* (pp. 325-346). Berlin, Heidelberg: Springer Berlin Heidelberg.

[2] Hulanicki, A., Glab, S., & Ingman, F. O. L. K. E. (1991). Chemical sensors: definitions and classification. *Pure and applied chemistry*, *63*(9), 1247-1250.

[3] Cammann, K., Guibault, E. A., Hall, H., Kellner, R., & Wolfbeis, O. S. (1996). The Cambridge definition of chemical sensors. In *Proceedings of the Cambridge workshop on chemical sensors and biosensors. Cambridge University Press, New York*.

[4] Melo, R. L. F., Neto, F. S., Dari, D. N., Fernandes, B. C. C., Freire, T. M., Fechine, P. B. A., ... & Dos Santos, J. C. S. (2024). A comprehensive review on enzyme-based biosensors: Advanced analysis and emerging applications in nanomaterial-enzyme linkage. *International Journal of Biological Macromolecules*, *264*, 130817.

[5] Kaur, J., Choudhary, S., Chaudhari, R., Jayant, R. D., & Joshi, A. (2019). Enzyme-based biosensors. *Bioelectronics and Medical Devices*, 211-240.

[6] Zeng, X., Shen, Z., & Mernaugh, R. (2012). Recombinant antibodies and their use in biosensors. *Analytical and bioanalytical chemistry*, *402*(10), 3027-3038.

[7] Luppa, P. B., Sokoll, L. J., & Chan, D. W. (2001). Immunosensors—principles and applications to clinical chemistry. *Clinica chimica acta*, *314*(1-2), 1-26.

[8] Bousse, L. (1996). Whole cell biosensors. *Sensors and Actuators B: Chemical*, *34*(1-3), 270-275.

[9] Gui, Q., Lawson, T., Shan, S., Yan, L., & Liu, Y. (2017). The application of whole cell-based biosensors for use in environmental analysis and in medical diagnostics. *Sensors*, *17*(7), 1623.

[10] Kavita, V. J. J. B. B. S. (2017). DNA biosensors-a review. *J. Bioeng. Biomed. Sci*, *7*(2), 222.

[11] Ranallo, S., Porchetta, A., & Ricci, F. (2018). DNA-based scaffolds for sensing applications. *Analytical chemistry*, *91*(1), 44-59.

[12] Tombelli, S., Minunni, M., & Mascini, M. (2007). Aptamers-based assays for diagnostics, environmental and food analysis. *Biomolecular engineering*, *24*(2), 191-200.

[13] Tombelli, S., Minunni, M., & Mascini, M. (2005). Analytical applications of aptamers. *Biosensors and Bioelectronics*, *20*(12), 2424-2434.

[14] Wulff, G., Sarhan, A., & Zabrocki, K. (1973). Enzyme-analogue built polymers and their use for the resolution of racemates. *Tetrahedron Letters*, *14*(44), 4329-4332.

[15] Arshady, R., & Mosbach, K. (1981). Synthesis of substrate-selective polymers by host-guest polymerization. *Die Makromolekulare Chemie: Macromolecular Chemistry and Physics*, *182*(2), 687-692.

[16] Wu, A., & Khan, W. S. (Eds.). (2020). *Nanobiosensors: from design to applications*. John Wiley & Sons.

[17] Moina, C., & Ybarra, G. (2012). Fundamentals and applications of immunosensors. *Advances in immunoassay technology*, *66*.

[18] Devices, A., Staff, T., & Kester, W. (2005). Sensor Signal Conditioning. In *Sensor Technology Handbook* (pp. 31-136). Newnes.

[19] Abdel-Karim, R. (2024). Nanotechnology-enabled biosensors: a review of fundamentals, materials, applications, challenges, and future scope. *Biomedical Materials & Devices*, *2*(2), 759-777.

[20] Skoog, D. A., Holler, F. J., & Crouch, S. R. (2018). Principles of instrumental analysis seventh edition. *Cengage learning*.

[21] Ekins, R., & Edwards, P. (1997). Point on the meaning of "sensitivity". *Clinical chemistry*, *43*(10), 1824-1831.

[22] Shrivastava, A., & Gupta, V. B. (2011). Methods for the determination of limit of detection and limit of quantitation of the analytical methods. *Chron. Young Sci*, *2*(1), 21-25.

[23] Hulme, E. C., & Trevethick, M. A. (2010). Ligand binding assays at equilibrium: validation and interpretation. *British journal of pharmacology*, *161*(6), 1219-1237.

[24] Janata, J. (2009). *Principles of chemical sensors*. Springer Science & Business Media.

Chapter II – Molecularly imprinted polymers

Historical Background

The concept of molecular imprinting can be traced back to the 1930s, when synthetic strategies for polymer production were first explored by the chemist Polyakov [1]. He reported unusual adsorption properties in silica particles prepared using a novel synthesis procedure, resulting in a "memory effect" that enhanced the material's uptake capacity for specific molecules. A decade later, in 1940, Pauling hypothesized that a process similar to molecular imprinting could account for the selectivity of antibodies toward their respective antigens [2]. This idea was supported by experiments conducted by his student Dickey, who demonstrated selective adsorption of dyes in silica matrices. The modern development of MIPs, however, is attributed to Wulff in the 1970s [4, 5]. Wulff introduced the concept of using covalent bonding interactions between functional monomers and a template molecule during polymerization, specifically employing vinyl polymers. This covalent approach is effective only if the bond is reversible, allowing the easy extraction of the template. A decade later, in 1981, Mosbach proposed a non-covalent imprinting approach in which the polymerization process relies on weak interactions between selected monomers and the template [5, 6]. The non-covalent approach proved more versatile than the covalent strategy, as the template-monomer complex can form rapidly and be easily disrupted. The non-covalent approach facilitated practical applications of MIPs, enabling template removal after polymerization and the creation of imprinting cavities for molecules of different sizes and types, including ions [7], macromolecules [8], viruses [9], and even microorganisms and cells [10]. Subsequently, the semi-covalent approach was introduced by Sellergren and Andersson [11], and Whitcombe [12]. In this strategy, the template is covalently bound to a functional monomer during polymerization, as in the covalent approach, but rebinding of the template relies exclusively on non-covalent interactions, combining the advantages of both methods.

Since these pioneering studies, molecular imprinting has rapidly evolved (Figure 2.1), driven by the continuous development of new monomers, cross-linkers, polymerization techniques, and combinatorial strategies that have greatly enhanced the versatility and performance of MIPs, establishing them as a key technology in analytical chemistry and materials science.

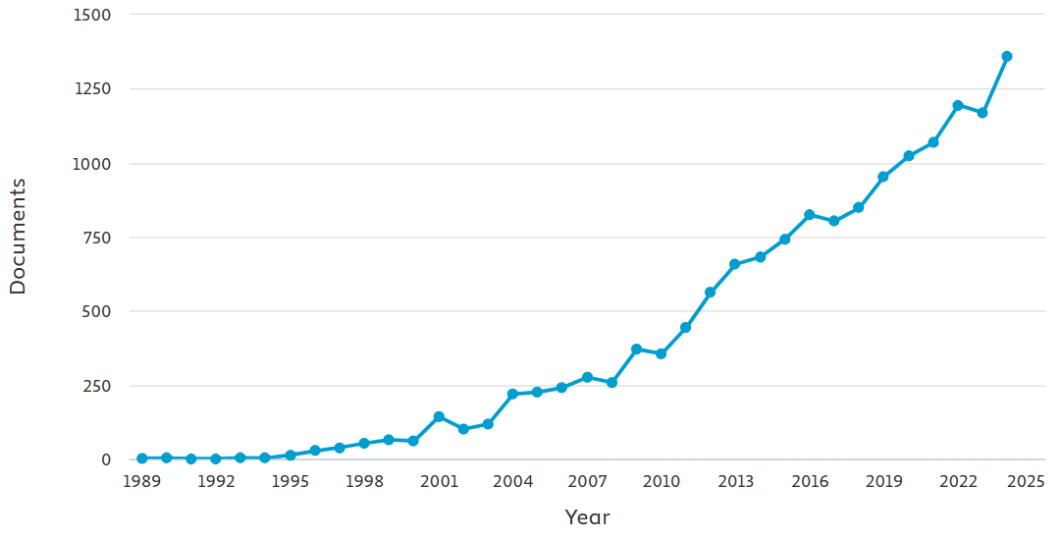

Figure 2.1 Trend of the publication regarding MIPs, between 1989 and 2024. Via Scoups.

Fundamentals of MIPs, mechanisms and building blocks

Molecularly imprinted polymers, usually referred to also as artificial antibodies, are defined as synthetic polymeric materials designed to replicate the molecular recognition capabilities of biological receptors, such as antibodies and enzymes. While biological receptors display remarkable selectivity owing to their specific affinity for target molecules, they often suffer from several drawbacks, including sensitivity to environmental conditions, requirements of precise storage and handling, batch-to-batch variability and expensive and labour-intensive production. In contrast, MIPs offer several advantages as they combine high molecular selectivity, arising from a lock-and-key-like recognition mechanism, with exceptional robustness and versatility. They possess mechanical and thermal stability and are resistant to pH extremes, can be stored for extended periods without

degradation, and can even be tailored to recognize molecules for which no natural receptor exists (Table 2.1) [13].

Table 2.1 Comparison between MIPs and biological receptors.

Feature	MIPs	Biological Receptors
Nature	Synthetic polymeric materials	Molecules of biological origin
Target range	Theoretically prepared for any template molecule	Limited to biologically compatible or immunogenic targets
Selectivity	High, depending on imprinting quality	Intrinsically high
Stability	Highly robust and stable in multiple conditions (high/low pHs, pressure, and temperature)	Limited stability and susceptibility to environmental changes
Production	Simple, fast and inexpensive	Complex, time-consuming and expensive
Storage conditions	Long-term storage	Require controlled conditions

The high specificity and selective recognition ability of MIPs originate from their synthetic process, which involves the co-polymerization of functional monomers and cross-linkers in the presence of the target molecule, known as the template. During this process, a three-dimensional polymeric network is formed around the template, creating binding sites that are complementary in size, shape, and chemical functionality to the target of interest (Figure 2.2). Particularly, in the first step, the template molecule interacts with selected functional monomers to form a pre-polymerization complex in solution. Depending on the chemical functionalities of the monomers, these interactions may rely on covalent or, more commonly, non-covalent forces such as hydrogen bonding, electrostatic attractions, π-π stacking, hydrophobic effects or van der Waals interactions. Then, the pre-assembled complexes are co-polymerized with the addition of a cross-linker, which confers three-dimensional rigidity to the polymer matrix and, as polymerization progresses, the template remains entrapped within the formed material. The final stage consists of template removal which leaves binding cavities stereochemical complementary

to the original template, which constitute the “molecular memory” of the polymer and enable MIPs to selectively rebind the target molecule [14].

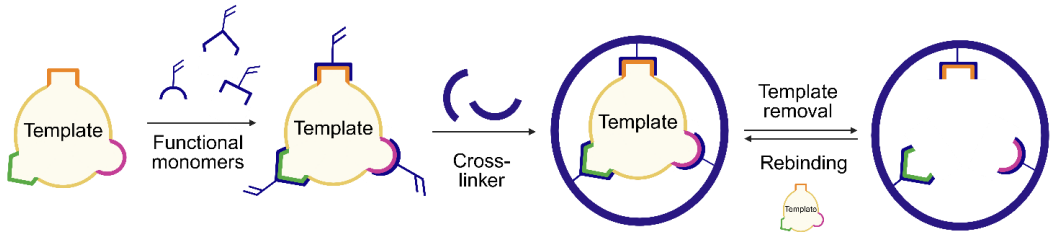

Figure 2.2 Synthetic process of MIPs fabrication.

The choice of ingredients in MIP design is crucial, as each component directly affects the polymer’s performance. Central to MIP synthesis is the choice of the template molecule, which, to be ideal, should meet several criteria: it must be soluble under the imprinting conditions, chemically stable throughout the polymerization process, inert so as not to interfere with the reaction and, most importantly, should possess functional groups capable of forming reversible or irreversible interactions with the chosen functional monomers [15, 16]. The size and structural characteristics of the template also influence the selection of the imprinting strategy. For small organic molecules, such as pharmaceuticals, pesticides, amino acids, peptides, nucleotide bases, steroids, and sugars, imprinting is well established and generally straightforward. In contrast, imprinting larger biomacromolecules poses significant challenges [17]. Proteins, for instance, possess complex tertiary and quaternary structures that make it difficult to form well-defined binding cavities due to their large size and structural heterogeneity. Moreover, they may undergo conformational changes or denaturation during the imprinting process. To overcome these limitations, the epitope imprinting approach can be employed, in which a short and stable peptide fragment of a protein is used as the template instead of the entire biomolecule. This method is particularly valuable not only for proteins themselves but also for complex targets such as viruses, bacteria, and cells, which often expose characteristic proteins on their surfaces [18, 19].

Functional monomers represent another crucial component in MIP synthesis, as they interact with the template molecule to form a pre-polymerization complex that serves as a structural guide for the cavities responsible for target recognition. The selection of appropriate functional monomers requires a thorough assessment of their chemical functionalities to guarantee compatibility with the template. In certain cases, the use of multiple monomers can improve the complementarity with the template molecule, although this strategy introduces additional complexity and necessitates fine optimization of the formulation and polymerization conditions [20, 21]. Moreover, another key factor in MIP synthesis is the template-to-monomer ratio: a low ratio may lead to insufficient binding site formation due to dominant monomer-monomer interactions, whereas a high ratio can produce heterogeneous cavities and increase non-specific binding [15, 22].

Computational modelling can assist in predicting and optimizing the interactions between the template and potential functional monomers, allowing the identification of the most stable complexes prior to synthesis, for example by calculating their Gibbs free energy (ΔG) [23, 24].

The cross-linker is a crucial, yet sometimes underestimated, component in MIP synthesis, as it provides structural rigidity to the polymer matrix even after template removal, thereby preserving the shape and functionality of the imprinted cavities [15, 16]. The type and amount of cross-linker directly influence the polymer's rigidity, porosity, and accessibility of the cavities. A higher cross-linking density generally results in a more rigid and stable polymer capable of retaining well-defined cavities, even under harsh conditions, while excessive rigidity can sometimes limit the accessibility of the binding sites to the target molecule. Conversely, a lower degree of cross-linking increases flexibility and may enhance binding site accessibility but at the cost of reduced mechanical stability and potential loss of functional monomers [25, 26].

The choice of solvent, or porogen, is another critical factor in MIP synthesis, as it not only dissolves the template, functional monomers and cross-linkers but also strongly influences the stability of the pre-polymerization complex. In cases where the template and monomers interact primarily through hydrophobic interactions, water is often preferred as the solvent, whereas polar solvents can assist in the

imprinting of hydrophilic or weakly polar templates [15, 16]. Moreover, the solvent plays a key role in defining the porosity and format of the resulting MIP as it can promote the formation of a porous network, which facilitates rapid mass transfer of the target molecule to and from the binding cavities, thereby enhancing binding kinetics and overall MIP performance [27]. In summary, the design of a MIP requires the careful selection and balance of all components: template, functional monomer(s), crosslinker(s), and solvent, to achieve a polymer network capable of selective, high-affinity recognition of the target molecule.

Polymerisation Methods in Molecular Imprinting and MIP Formats

The polymerization method dictates how these building blocks, template, functional monomer and cross-linker are assembled into a stable three-dimensional network, thereby influencing not only the efficiency of imprinting but also the morphology and final performance of the material. It should be noted that there is no universally accepted classification of polymerization methods, as different authors categorize them according to distinct criteria such as the underlying chemical mechanism, the polymerization medium or the morphology of the final material.

For clarity, in this paragraph polymerization approaches are discussed from two complementary perspectives: the chemical mechanism by which the polymer network is formed and the physical format of the resulting polymer.

From a chemical perspective, MIP synthesis can be achieved through different polymerization mechanisms, each offering specific advantages and limitations in terms of control over network structure, reproducibility and applicability to diverse templates. The most widely employed approaches include free-radical polymerization, controlled/living radical polymerization, sol-gel processes, and electropolymerization.

Free-radical polymerization (FRP) represents the most widely employed approach for the synthesis of MIPs, owing to its operational simplicity, broad applicability and compatibility with a large variety of functional and cross-linking monomers. FRP develops through four fundamental stages: initiation, propagation, chain transfer, and termination (Figure 2.3). In the initiation step, reactive radicals are

generated by the thermal, photochemical or chemical decomposition of an initiator. These radicals react with the monomers, leading to the formation of the first active radical species. During propagation, successive additions of monomer units to the growing radical extend the polymer chain while maintaining the radical character at its reactive end. Finally, termination occurs when two free radicals combine or one is quenched, thus halting the growth of the polymer chain.

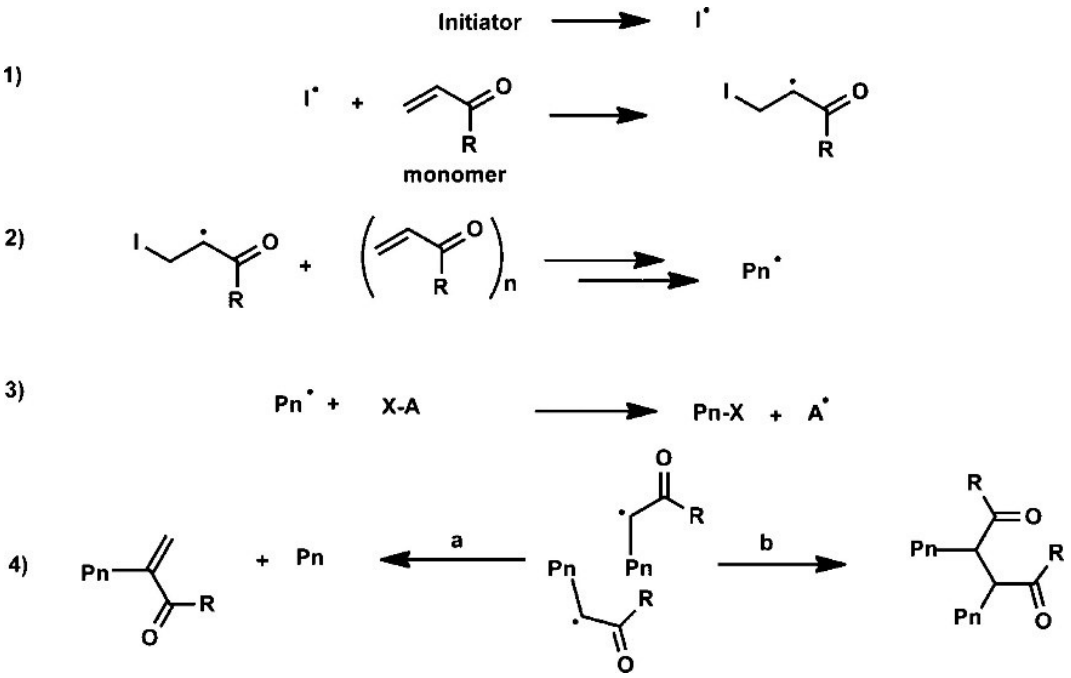

Figure 2.3 Mechanism of free radical polymerization: (1) initiation, (2) propagation, (3) chain transfer, (4) termination via (a) disproportionation and (b) combination. Picture reproduced from [28].

FRP can be carried out using different polymerization formats (Figure 2.4):

- Bulk polymerization is based on the combination of the template, functional monomer, cross-linker, initiator, and porogen in a single reaction mixture, leading to the formation of a highly cross-linked monolithic polymer. Once polymerization is complete, the bulk material must be mechanically ground to obtain particulates of usable size. This post-processing step often produces particles with irregular shapes and broad size distribution (between 20 µm and 50 µm) and can partially damage the imprinted binding sites, leading to heterogeneous recognition properties [29, 30].

- Precipitation polymerization is performed in a large excess of solvent, which serves as a dispersion medium. The polymer chains formed during the early stages of the reaction remain soluble until they reach a critical molecular weight, beyond which they precipitate out of solution, giving rise to spherical polymer particles. This approach produces relatively uniform microspheres or nanospheres without the need for mechanical grinding, resulting in more homogeneous binding sites and improved reproducibility [31].
- Suspension polymerization involves dispersing the polymerizable phase into a non-solvent continuous medium, where polymerization occurs within the suspended droplets. This technique enables control over particle size, typically yielding microsized particles with relatively uniform morphology. However, the presence of a continuous phase often necessitates the use of stabilizers or surfactants to prevent droplet coalescence, which can potentially interfere with the imprinting efficiency [32, 33].
- Emulsion polymerization is based on the use of surfactants, which create stable emulsion of monomer in an aqueous continuous phase. Polymerization occurs within these emulsions, producing highly uniform and monodisperse particles, usually ranging from 50 to 500 nm [34, 35].

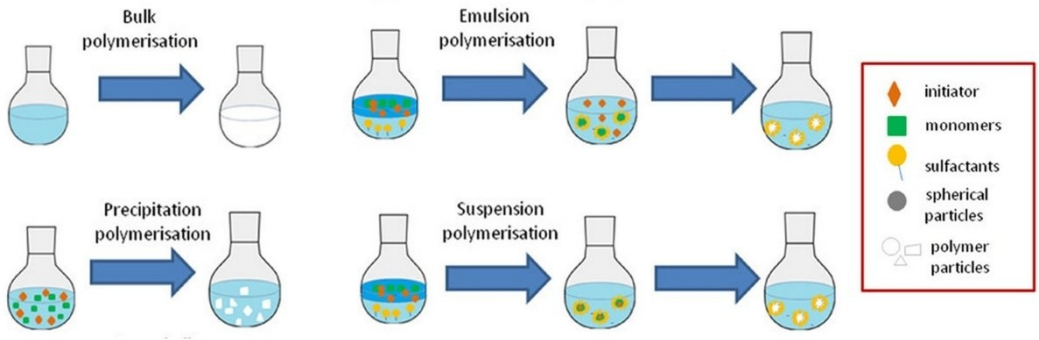

Figure 2.4 Different polymerization techniques used for MIP preparation. Picture reproduced from [36].

While FRP remains the most common approach, alternative strategies have been developed. Among these are controlled or living radical polymerization techniques (CRP), including ATRP (atom transfer radical polymerization), RAFT (reversible addition-fragmentation chain transfer), and NMP (nitroxide-mediated polymerization), which allow precise control over polymer chain growth [37-40].

Although CRP techniques provide enhanced control over chain growth and termination processes, they often require specialized initiators, chain transfer agents, or catalytic systems, which makes the synthetic procedure more complex and sometimes less compatible with certain templates or functional monomers [41, 42].

In addition to organic polymer networks, sol-gel polymerization offers a complementary approach for preparing inorganic MIPs [43-45]. In this approach, metal oxide precursors undergo hydrolysis and condensation in acidic or basic conditions, leading to the formation of a three-dimensional, highly stable inorganic-based polymers. Sol-gel polymerization allows the preparation of materials with high thermal and mechanical stability due to the presence of metal oxides. This method does not typically require initiators or surfactants, which simplifies the procedure and reduces overall costs [46]. Despite these advantages, sol-gel polymerization generally proceeds more slowly than free-radical polymerization, and the resulting materials may exhibit lower sensitivity and slower response times [47].

Another method is electropolymerization, which involves the oxidative or reductive polymerization of monomers directly onto a conductive surface, resulting in a thin MIP film (Figure 2.5). The main advantages of this approach include rapid formation, strong adhesion to the electrode and the possibility of spatially controlled deposition. Furthermore, the polymer thickness and morphology can be finely tuned by adjusting parameters such as the applied potential and deposition time. However, the technique also presents certain limitations, as it requires the use of electroactive monomers and the template must remain electrochemically inert within the applied potential range to prevent degradation or interference during the imprinting process. Moreover, electropolymerization is generally restricted to conductive or semiconductive substrates, limiting its applicability to specific platforms [48-51].

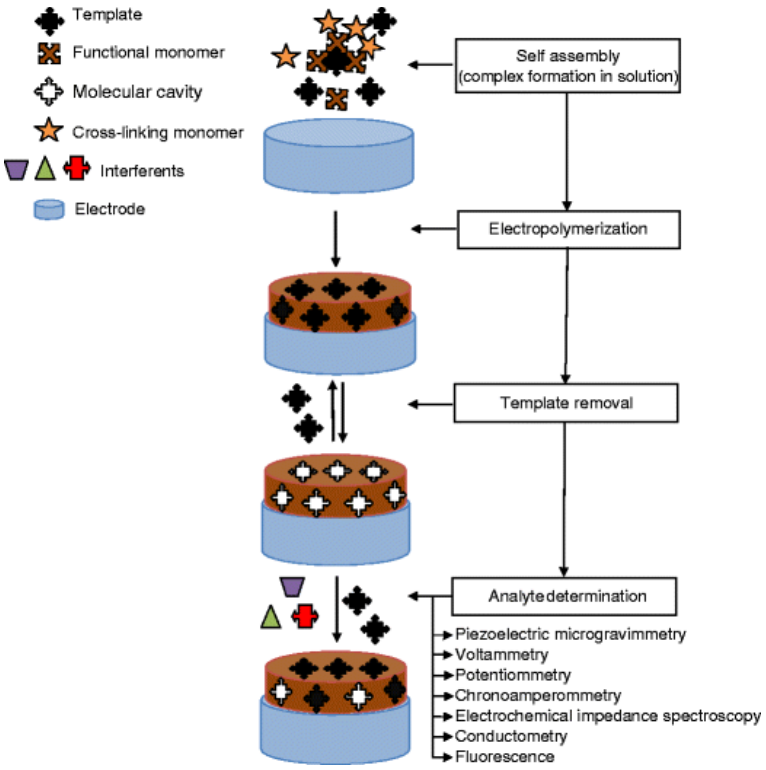

Figure 2.5 General procedure for molecular imprinting with an electroactive functional monomer and typical signal transduction methods employed in detection. Picture reproduced from [51].

In addition to the classical polymerization methods, several operational strategies have been developed to further enhance control over MIP morphology, binding site accessibility and reproducibility. Among these, core-shell imprinting represents an alternative strategy to electropolymerization for producing MIP layers (Figure 2.6), in which the polymer is formed on the surface of preformed core particles such as silica, polymers, or materials with specific properties like conductive metals (e.g., Au, Ag, Pd), magnetic substrates, or semiconductors [52, 53]. The core provides structural support, while the MIP shell contains the molecular recognition sites, which are readily accessible, thereby reducing mass transfer limitations and enhancing binding kinetics [54].

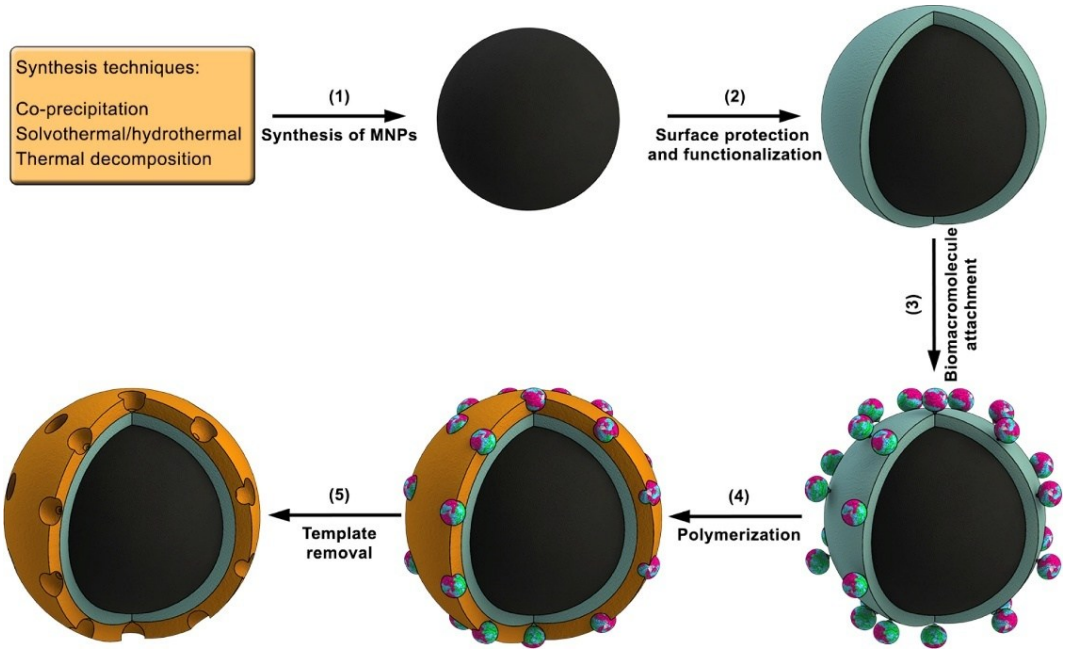

Figure 2.6 General steps for the preparation of core-shell MMIPs for biomacromolecules. Picture reproduced from [55].

High-dilution polymerization represents an effective strategy aimed at minimizing uncontrolled aggregation phenomena during MIP formation. By operating at highly diluted monomer and template concentrations, polymer chain growth is limited, thereby preventing premature precipitation and promoting the formation of material even at the nanometric scale [56, 57].

Finally, solid-phase synthesis (Figure 2.7) represents an advanced approach designed to enhance the homogeneity of MIPs in terms of binding affinity, while simultaneously addressing the problem of leakage of template molecules. The distinguishing feature of this approach lies in the immobilization of the template on a solid support, typically silica, glass or magnetic beads or other functionalized particles [58, 59]. This configuration ensures that the template remains confined to a distinct phase during polymerization, which not only facilitates the imprinting process but also enables affinity-based separation of the resulting polymer particles according to their binding quality. On the other hand, the main limitations of this technique are its relatively low yield and its limited effectiveness for templates with large or complex structures [60].

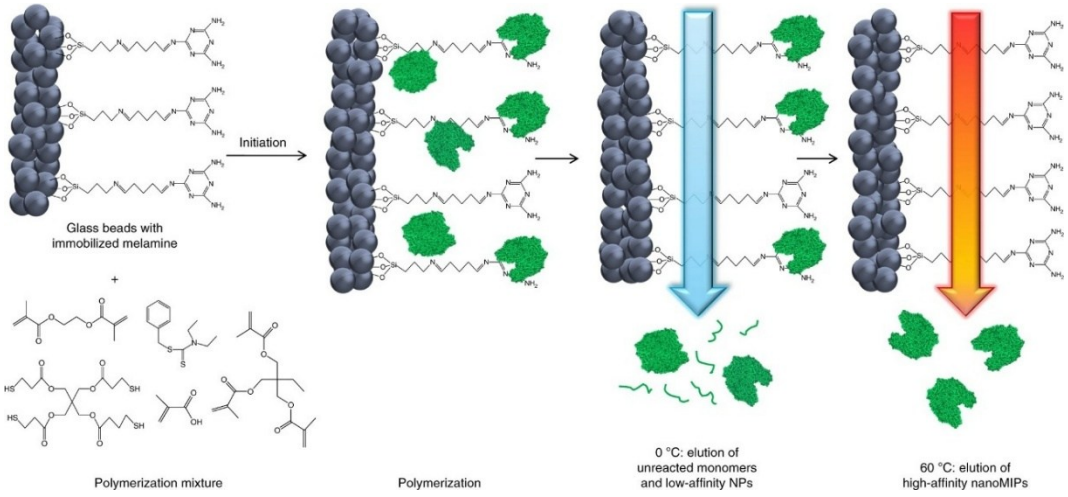

Figure 2.7 Solid-phase synthesis and separation of nanoMIPs by photopolymerization, using melamine as a model template. Picture reproduced from [58].

The type of polymerization mechanism and the experimental conditions employed in MIP synthesis not only determine the chemical nature of the resulting MIP but also strongly influence its physical format and morphology (Table 2.2). Indeed, the polymerization method largely dictates whether the final material will take the form of a bulk monolith, a thin film or discrete micro- or nanoparticles.

These formats can also be viewed in terms of their structural scale, which provides a more functional classification of MIPs as macrostructured, microstructured, or nanostructured materials. The earliest MIPs were typically prepared as macrostructured materials, obtained through bulk polymerization and subsequent mechanical grinding of the monolith to produce usable particles. As described before, although these systems provided the proof-of-concept for molecular recognition in synthetic polymers, their heterogeneous binding site distribution, limited diffusion, and poor reproducibility soon revealed significant practical limitations [29, 61].

In response to these challenges, the field progressively evolved toward smaller-scale formats, leading first to the development of micro- and subsequently to nanostructured MIPs. This transition represented a major advance in molecular imprinting, allowing improved control over polymer architecture and enabling formats better suited to modern analytical and sensing applications [62].

Table 2.2 Relationship between polymerization method and MIP format.

Polymerization method	Typical MIP format	Pros	Cons
Bulk (FRP)	Macroporous monoliths (macrostructured MIPs)	Simple and versatile	Grinding damages binding sites and yields heterogeneous particle sizes
Precipitation / Suspension / Emulsion polymerization (FRP)	Micro or nanoparticles	Uniform particles and high yield	Long time required, need of a high amount of template and solvent; Required purification and use of a stabilizer
Controlled / Living radical polymerization (CRP)	Micro or nanoparticles	Control of molecular weight distribution and stereochemistry	Lack of control of the nanoparticles size; limited range of suitable monomers; requires specific catalysts or initiators and more complex reaction setups
Sol-gel polymerization	Inorganic micro or nanoparticles	High thermal/mechanical stability	slower process, sometimes limited sensitivity and response time
Electropolymerization	Thin films or nanolayers on conductive surfaces	Control on MIPs size; excellent adhesion and fast response	limited to conductive substrates and electropolymerizable monomers
Core-shell imprinting	Surface-imprinted nanostructures	Control on MIPs size; excellent adhesion and fast response	synthesis can be complex; Not effective for big and complex templates
High-dilution polymerization	nanoparticles	Produces uniform nanoparticles with minimal aggregation;	High amount of solvent
Solid-phase synthesis	nanoparticles	Very high affinity; homogeneous distribution of the recognition sites; recycle of the template	low yield and limited to small or medium-sized templates

In particular, at the nanoscale range, the increased surface-to-volume ratio enhances the exposure and accessibility of imprinted cavities, thereby promoting more efficient analyte diffusion throughout the polymer matrix. Consequently, the shorter diffusion paths typical of nanometric architectures enable rapid association and dissociation of target molecules, yielding faster equilibration and reduced response times compared to bulk or microstructured systems. From an application standpoint, nanoMIPs can be easily handled and immobilized onto different substrates, which facilitates their integration into diverse analytical and sensing platforms. Their nanometric dimensions allow direct and efficient coupling with optical, plasmonic, and electrochemical transducers, enabling the development of highly sensitive and compact sensing devices [63]. Within the broad category of nanostructured MIPs, two main morphological formats can be distinguished: nanoparticles and nanolayers or nanofilms.

MIP nanoparticles (nanoMIPs) are defined as discrete, spherical particles generally spanning diameters from 10 to 500 nm, depending on the polymerization conditions and formulation parameters [63, 64]. NanoMIPs can be synthesized through a variety of routes, most commonly using a chemical or photochemical polymerization process. In chemical polymerization, radical initiation is typically triggered by redox pairs such as ammonium persulfate (APS) and N,N,N',N'-tetramethylethylenediamine (TEMED), or by thermal initiators like azobisisobutyronitrile (AIBN), enabling the controlled formation of polymeric networks under mild conditions. Photopolymerization, by contrast, employs photosensitive initiators such as lithium phenyl-2,4,6-trimethylbenzoylphosphinate (LAP), which generate radicals upon light exposure [65, 66]. Commonly employed functional monomers include acrylamide derivatives, such as acrylamide (AAm), tert-Butylacrylamide (TBAAm), N-isopropylacrylamide (NIPAAm), N, N-methylenebisacrylamide (MBAAm) and N-hydroxymethylacrylamide (NHMAm), which provide amide functionalities capable of forming hydrogen bonds with a wide range of templates [67, 68]. Other widely used monomers for nanoMIPs synthesis include methacrylic acid (MAA) and its esters, such as methyl methacrylate, which are used due to their carboxylic and ester functionalities, which enable hydrogen bonding and ionic interactions with basic or polar templates.

Similarly, acrylic acid (AA) and its derivatives, including trans-3-(3-pyridyl)-acrylic acid, introduce carboxylic and aromatic moieties that facilitate both hydrogen-bonding and π–π interactions, thus enhancing affinity toward aromatic or heteroaromatic targets. Styrene and vinylpyridine- or vinylimidazole-based monomers, such as 4-vinylpyridine (4-VP), 2-vinylpyridine (2-VP) and 1-vinylimidazole, provide aromatic and basic functionalities that promote π–π stacking and electrostatic interactions with acidic or polar analytes [16]. In addition to conventional synthetic monomers recent research has focused on the use of biopolymers and other sustainable monomers as building blocks for MIPs. These materials provide several advantages, including biocompatibility, biodegradability, and reduced environmental impact, which are particularly relevant for biomedical applications and green chemistry practices [69]. Representative bio- and green-monomers include sugar-based polymers such as cellulose derivatives, chitosan, and alginates; protein-derived polymers including gelatin, silk fibroin, keratins, and zeins; as well as nucleic acids, polyphenols, and tannic acid. Vegetable oil-derived monomers have also recently attracted attention, contributing to the development of next-generation, biocompatible, and environmentally sustainable MIPs that align with the principles of circular economy and green material design [70, 71].

Nanolayers are surface-confined imprinted coatings, typically ranging from 0.5 to 30 nm in thickness, grown directly onto solid supports such as grown directly onto conductive or optically active substrates such as gold, platinum, or silver electrodes, glassy carbon, gold nanoparticles, and optical fibers. Because the recognition sites are concentrated at the interface, thin films enable rapid diffusion of ions and small molecules across the matrix, resulting in fast and sensitive responses. An additional advantage of this approach is the minimal amount of template required for film preparation, combined with relatively simple washing procedures to remove it. In recent years, several authors have reported the *in situ* polymerization of imprinted thin films by a variety of techniques, including spin-coating, layer-by-layer deposition, surface grafting and, most extensively electropolymerization [50, 72, 73].

Among electropolymerizable monomers, polypyrrole (PPy) is among the most widely employed materials in electrochemical imprinting, due to its excellent

conductivity, stability, and ease of electrosynthesis. o-Phenylenediamine (1,2-benzenediamine) is another well-established monomer, forming thin, compact, and pinhole-free MIP films with good permselectivity.

Phenol and its derivatives, as well as aniline, have also been extensively used for in situ electrooxidative polymerization, yielding conductive matrices. More recently, thiophene (Th) derivatives, in particular poly(3,4-ethylenedioxythiophene) (PEDOT), have been explored as functional monomers for MIP electrosynthesis, combining high conductivity with chemical robustness. Other notable examples include poly(3-aminophenylboronic acid), which provides reversible complexation via electrostatic and covalent interactions of its $B(OH)_2$ groups, and poly(mercaptobenzimidazole) (PMBI), whose sulfur and nitrogen heteroatoms contribute to selective binding and enhanced electron transfer. Scopoletin and dopamine have likewise gained attention as electropolymerizable monomers for the preparation of nanometric MIP films, the latter giving rise to biocompatible layers, highly attractive for biosensing interfaces [50, 74].

MIPs applications

The intrinsic versatility of MIPs, in terms of both the wide variety of target molecules they can recognize and the diversity of synthesis strategies and polymer formats available, translates into their applicability across multiple fields [75]. Besides the sensor applications that will be discussed in Chapter III, other key areas of application for MIPs include analytical separation, sample preparation, catalysis, and drug delivery.

Among the earliest and most consolidated application areas of MIPs is analytical separation. In this context, MIPs have been successfully integrated both as stationary phases in chromatographic techniques (e.g., HPLC, TLC, LEC, SFC, frontal chromatography), where they enable the selective separation of analytes [76], and as selective sorbents in solid-phase extraction [77]. In the latter case, molecularly imprinted solid-phase extraction allows for the enrichment, cleanup, and preconcentration of analytes, including drugs, metabolites, amino acids, peptides, nucleic acids, proteins, hormones and carbohydrates [78-80].

MIPs have proven potential as catalytic materials, acting as enzyme-mimetic catalysts. MIPs can be designed to facilitate a variety of chemical reactions, from stereoselective transformations to acid-base catalysis and metal-complex-mediated processes. In some cases, the imprinted binding sites themselves possess catalytic activity, stabilizing transition states or mimicking enzyme active sites. In other cases, the sites mainly serve to concentrate reactants on the polymer surface or regulate access to an embedded catalytic core. Additionally, certain MIPs can enhance reaction efficiency by selectively binding reaction products, shifting the equilibrium in favour of the desired outcome [81, 82].

Molecularly imprinted polymers are also being explored as carriers for drug delivery, where they offer the possibility of controlled and targeted release of therapeutic agents [83]. This represents an emerging and highly promising application of MIPs in the pharmaceutical field. In particular, MIP nanoparticles have attracted attention due to their ability to release drugs in response to specific environmental stimuli, such as changes in pH or temperature, or to selectively deliver drugs at the desired site of action [84]. Their spherical geometry further improves performance by avoiding the anisotropic swelling typically observed in other polymer formats, thereby ensuring a more uniform and predictable release profile. In parallel, molecular imprinting has also been applied to hydrogel-based systems, such as soft contact lenses [85]. In this case, swelling and shrinking are not a limitation but rather a functional property, which can be deliberately engineered to respond to external triggers, including pressure, temperature, or concentration gradients, thus enabling advanced controlled-release strategies.

References

[1] Polyakov, M. V. (1931). Adsorption properties and structure of silica gel. *Zhur Fiz Khim*, *2*, 799-805.

[2] Pauling, L. (1940). A theory of the structure and process of formation of antibodies. *Journal of the American Chemical Society*, *62*(10), 2643-2657.

[3] Wulff, G., Sarhan, A., & Zabrocki, K. (1973). Enzyme-analogue built polymers and their use for the resolution of racemates. *Tetrahedron Letters*, *14*(44), 4329-4332.

[4] Wulff, G., Grobe-Einsler, R., Vesper, W., & Sarhan, A. (1977). Enzyme-analogue built polymers, 5. On the specificity distribution of chiral cavities prepared in synthetic polymers. *Die Makromolekulare Chemie: Macromolecular Chemistry and Physics*, *178*(10), 2817-2825.

[5] Arshady, R., & Mosbach, K. (1981). Synthesis of substrate-selective polymers by host-guest polymerization. *Die Makromolekulare Chemie: Macromolecular Chemistry and Physics*, *182*(2), 687-692.

[6] Sellergren, B., Ekberg, B., & Mosbach, K. (1985). Molecular imprinting of amino acid derivatives in macroporous polymers: Demonstration of substrate-and enantio-selectivity by chromatographic resolution of racemic mixtures of amino acid derivatives. *Journal of chromatography A*, *347*, 1-10.

[7] Rezanavaz, R., Petcu, M., Le Guen, M. J., & Dubois, A. (2024). Three-dimensional printing of molecularly imprinted polymers by digital light processing for copper ion sequestration. *3D Printing and Additive Manufacturing*, *11*(2), e619-e627.

[8] Akgönüllü, S., Kılıç, S., Esen, C., & Denizli, A. (2023). Molecularly imprinted polymer-based sensors for protein detection. *Polymers*, *15*(3), 629.

[9] Antipchik, M., Reut, J., Ayankojo, A. G., Öpik, A., & Syritski, V. (2022). MIP-based electrochemical sensor for direct detection of hepatitis C virus via E2 envelope protein. *Talanta*, *250*, 123737.

[10] Piletsky, S., Canfarotta, F., Poma, A., Bossi, A. M., & Piletsky, S. (2020). Molecularly imprinted polymers for cell recognition. *Trends in biotechnology*, *38*(4), 368-387.

[11] Sellergren, B., & Andersson, L. I. (2000). Application of imprinted synthetic polymers in binding assay development. *Methods*, *22*(1), 92-106.

[12] Whitcombe, M. J., Rodriguez, M. E., Villar, P., & Vulfson, E. N. (1995). A new method for the introduction of recognition site functionality into polymers prepared by molecular imprinting: synthesis and characterization of polymeric receptors for cholesterol. *Journal of the American Chemical Society*, *117*(27), 7105-7111.

[13] Haupt, K., Linares, A. V., Bompart, M., & Bui, B. T. S. (2011). Molecularly imprinted polymers. *Molecular imprinting*, 1-28.

[14] BelBruno, J. J. (2018). Molecularly imprinted polymers. *Chemical reviews*, *119*(1), 94-119.

[15] Spivak, D. A. (2005). Optimization, evaluation, and characterization of molecularly imprinted polymers. *Advanced drug delivery reviews*, *57*(12), 1779-1794.

[16] Sajini, T., & Mathew, B. (2021). A brief overview of molecularly imprinted polymers: Highlighting computational design, nano and photo-responsive imprinting. *Talanta Open*, *4*, 100072.

[17] Li, S., Cao, S., Whitcombe, M. J., & Piletsky, S. A. (2014). Size matters: Challenges in imprinting macromolecules. *Progress in Polymer Science*, *39*(1), 145-163.

[18] Nishino, H., Huang, C. S., & Shea, K. J. (2006). Selective protein capture by epitope imprinting. *Angewandte Chemie*, *118*(15), 2452-2456.
[19] Pasquardini, L., & Bossi, A. M. (2021). Molecularly imprinted polymers by epitope imprinting: a journey from molecular interactions to the available bioinformatics resources to scout for epitope templates. *Analytical and Bioanalytical Chemistry*, *413*(24), 6101-6115.
[20] Karim, K., Breton, F., Rouillon, R., Piletska, E. V., Guerreiro, A., Chianella, I., & Piletsky, S. A. (2005). How to find effective functional monomers for effective molecularly imprinted polymers?. *Advanced drug delivery reviews*, *57*(12), 1795-1808.
[21] Fu, X., Yang, Q., Zhou, Q., Lin, Q., & Wang, C. (2015). Template-monomer interaction in molecular imprinting: is the strongest the best?. *Open Journal of Organic Polymer Materials*, *5*(02), 58.
[22] Kim, H., & Spivak, D. A. (2003). New insight into modeling non-covalently imprinted polymers. *Journal of the American Chemical Society*, *125*(37), 11269-11275.
[23] Nicholls, I. A., Adbo, K., Andersson, H. S., Andersson, P. O., Ankarloo, J., Hedin-Dahlström, J., ... & Wikman, S. (2001). Can we rationally design molecularly imprinted polymers?. *Analytica chimica acta*, *435*(1), 9-18.
[24] Hasanah, A. N., Safitri, N., Zulfa, A., Neli, N., & Rahayu, D. (2021). Factors affecting preparation of molecularly imprinted polymer and methods on finding template-monomer interaction as the key of selective properties of the materials. *Molecules*, *26*(18), 5612.
[25] Ikeda-Fukazawa, T., Ikeda, N., Tabata, M., Hattori, M., Aizawa, M., Yunoki, S., & Sekine, Y. (2013). Effects of crosslinker density on the polymer network structure in poly-N, N-dimethylacrylamide hydrogels. *Journal of Polymer Science Part B: Polymer Physics*, *51*(13), 1017-1027.
[26] Sellergren, B., & Shea, K. J. (1993). Influence of polymer morphology on the ability of imprinted network polymers to resolve enantiomers. Journal of Chromatography A, 635(1), 31-49.
[27] Booker, K., Holdsworth, C. I., Doherty, C. M., Hill, A. J., Bowyer, M. C., & McCluskey, A. (2014). Ionic liquids as porogens for molecularly imprinted polymers: propranolol, a model study. *Organic & biomolecular chemistry*, *12*(37), 7201-7210.
[28] Beyazit, S., Bui, B. T. S., Haupt, K., & Gonzato, C. (2016). Molecularly imprinted polymer nanomaterials and nanocomposites by controlled/living radical polymerization. *Progress in Polymer Science*, *62*, 1-21.
[29] Ye, L., & Mosbach, K. (2001). Molecularly imprinted microspheres as antibody binding mimics. *Reactive and Functional Polymers*, *48*(1-3), 149-157.
[30] Mohajeri, S. A., Karimi, G., Aghamohammadian, J., & Khansari, M. R. (2011). Clozapine recognition via molecularly imprinted polymers; bulk polymerization versus precipitation method. *Journal of Applied Polymer Science*, *121*(6), 3590-3595.
[31] Li, P., Rong, F., & Yuan, C. (2003). Morphologies and binding characteristics of molecularly imprinted polymers prepared by precipitation polymerization. *Polymer international*, *52*(12), 1799-1806.
[32] Mayes, A. G., & Mosbach, K. (1996). Molecularly imprinted polymer beads: suspension polymerization using a liquid perfluorocarbon as the dispersing phase. *Analytical Chemistry*, *68*(21), 3769-3774.

[33] Geng, L., Kou, X., Lei, J., Su, H., Ma, G., & Su, Z. (2012). Preparation, characterization and adsorption performance of molecularly imprinted microspheres for erythromycin using suspension polymerization. *Journal of Chemical Technology & Biotechnology*, *87*(5), 635-642.
[34] Zhao, G., Liu, J., Liu, M., Han, X., Peng, Y., Tian, X., ... & Zhang, S. (2020). Synthesis of molecularly imprinted polymer via emulsion polymerization for application in solanesol separation. *Applied Sciences*, *10*(8), 2868.
[35] Dvorakova, G., Haschick, R., Chiad, K., Klapper, M., Müllen, K., & Biffis, A. (2010). Molecularly imprinted nanospheres by nonaqueous emulsion polymerization. *Macromolecular rapid communications*, *31*(23), 2035-2040.
[36] Kwaśniewska, K., Gadzała-Kopciuch, R., & Buszewski, B. (2015). Magnetic molecular imprinted polymers as a tool for isolation and purification of biological samples. *Open Chemistry*, *13*(1), 000010151520150137.
[37] Matyjaszewski, K., Patten, T. E., & Xia, J. (1997). Controlled/"living" radical polymerization. Kinetics of the homogeneous atom transfer radical polymerization of styrene. *Journal of the American Chemical Society*, *119*(4), 674-680.
[38] Martínez, I. V., Ek, J. I., Ahn, E. C., & Sustaita, A. O. (2022). Molecularly imprinted polymers via reversible addition–fragmentation chain-transfer synthesis in sensing and environmental applications. *RSC advances*, *12*(15), 9186-9201.
[39] Boonpangrak, S., Whitcombe, M. J., Prachayasittikul, V., Mosbach, K., & Ye, L. (2006). Preparation of molecularly imprinted polymers using nitroxide-mediated living radical polymerization. *Biosensors and Bioelectronics*, *22*(3), 349-354.
[40] Otsu, T. (2000). Iniferter concept and living radical polymerization. *Journal of Polymer Science Part A: Polymer Chemistry*, *38*(12), 2121-2136.
[41] Matyjaszewski, K., & Müller, A. H. (Eds.). (2009). *Controlled and living polymerizations: from mechanisms to applications*. John Wiley & Sons.
[42] Tsarevsky, N. V., & Sumerlin, B. S. (Eds.). (2013). *Fundamentals of controlled/living radical polymerization* (Vol. 4). Royal Society of Chemistry.
[43] Díaz-García, M. E., & Laínño, R. B. (2005). Molecular imprinting in sol-gel materials: Recent developments and applications. *Microchimica Acta*, *149*(1), 19-36.
[44] Ang, Q. Y., & Low, S. C. (2015). Morphology and kinetic modeling of molecularly imprinted organosilanol polymer matrix for specific uptake of creatinine. *Analytical and bioanalytical chemistry*, *407*(22), 6747-6758.
[45] Queirós, R. B., Silva, S. O., Noronha, J. P., Frazão, O., Jorge, P., Aguilar, G., ... & Sales, M. G. F. (2011). Microcystin-LR detection in water by the Fabry–Pérot interferometer using an optical fibre coated with a sol–gel imprinted sensing membrane. *Biosensors and Bioelectronics*, *26*(9), 3932-3937.
[46] Moein, M. M., Abdel-Rehim, A., & Abdel-Rehim, M. (2019). Recent applications of molecularly imprinted sol-gel methodology in sample preparation. *Molecules*, *24*(16), 2889.
[47] Adumitrăchioaie, A., Tertiș, M., Cernat, A., Săndulescu, R., & Cristea, C. (2018). Electrochemical methods based on molecularly imprinted polymers for drug detection. A review. *International Journal of Electrochemical Science*, *13*(3), 2556-2576.

[48] Ramanavičius, S., Morkvėnaitė-Vilkončienė, I., Samukaitė-Bubnienė, U., Ratautaitė, V., Plikusienė, I., Viter, R., & Ramanavičius, A. (2022). Electrochemically deposited molecularly imprinted polymer-based sensors. *Sensors*, *22*(3), 1282.
[49] Malitesta, C., Losito, I., & Zambonin, P. G. (1999). Molecularly imprinted electrosynthesized polymers: new materials for biomimetic sensors. *Analytical Chemistry*, *71*(7), 1366-1370.
[50] Malitesta, C., Mazzotta, E., Picca, R. A., Poma, A., Chianella, I., & Piletsky, S. A. (2012). MIP sensors–the electrochemical approach. *Analytical and bioanalytical chemistry*, *402*(5), 1827-1846.
[51] Sharma, P. S., Pietrzyk-Le, A., D'souza, F., & Kutner, W. (2012). Electrochemically synthesized polymers in molecular imprinting for chemical sensing. *Analytical and bioanalytical chemistry*, *402*(10), 3177-3204.
[52] Tan, C. J., & Tong, Y. W. (2007). Molecularly imprinted beads by surface imprinting. *Analytical and bioanalytical chemistry*, *389*(2), 369-376.
[53] Pérez-Moral, N., & Mayes, A. G. (2004). Noncovalent imprinting in the shell of core–shell nanoparticles. *Langmuir*, *20*(9), 3775-3779.
[54] Wan, L., Chen, Z., Huang, C., & Shen, X. (2017). Core–shell molecularly imprinted particles. *TrAC Trends in Analytical Chemistry*, *95*, 110-121.
[55] Dinc, M., Esen, C., & Mizaikoff, B. (2019). Recent advances on core–shell magnetic molecularly imprinted polymers for biomacromolecules. *TrAC Trends in Analytical Chemistry*, *114*, 202-217.
[56] Çakir, P., Cutivet, A., Resmini, M., Bui, B. T. S., & Haupt, K. (2013). Protein-size molecularly imprinted polymer nanogels as synthetic antibodies, by localized polymerization with multi-initiators. *Advanced Materials*, *25*(7), 1048-1051.
[57] Wang, S., Yin, D., Wang, W., Shen, X., Zhu, J. J., Chen, H. Y., & Liu, Z. (2016). Targeting and imaging of cancer cells via monosaccharide-imprinted fluorescent nanoparticles. *Scientific reports*, *6*(1), 22757.
[58] Canfarotta, F., Poma, A., Guerreiro, A., & Piletsky, S. (2016). Solid-phase synthesis of molecularly imprinted nanoparticles. *Nature protocols*, *11*(3), 443-455.
[59] Xu, J., Medina-Rangel, P. X., Haupt, K., & Bui, B. T. S. (2017). Guide to the preparation of molecularly imprinted polymer nanoparticles for protein recognition by solid-phase synthesis. In *Methods in enzymology* (Vol. 590, pp. 115-141). Academic Press.
[60] Poma, A., Guerreiro, A., Whitcombe, M. J., Piletska, E. V., Turner, A. P., & Piletsky, S. A. (2013). Solid-phase synthesis of molecularly imprinted polymer nanoparticles with a reusable template–"plastic antibodies". *Advanced functional materials*, *23*(22), 2821-2827.
[61] Mohajeri, S. A., Karimi, G., Aghamohammadian, J., & Khansari, M. R. (2011). Clozapine recognition via molecularly imprinted polymers; bulk polymerization versus precipitation method. *Journal of Applied Polymer Science*, *121*(6), 3590-3595.
[62] Tokonami, S., Shiigi, H., & Nagaoka, T. (2009). Micro-and nanosized molecularly imprinted polymers for high-throughput analytical applications. *Analytica chimica acta*, *641*(1-2), 7-13.
[63] Poma, A., Turner, A. P., & Piletsky, S. A. (2010). Advances in the manufacture of MIP nanoparticles. *Trends in biotechnology*, *28*(12), 629-637.

[64] Zhang, H. (2020). Molecularly imprinted nanoparticles for biomedical applications. *Advanced Materials*, *32*(3), 1806328.
[65] Muhammad, T., Nur, Z., Piletska, E. V., Yimit, O., & Piletsky, S. A. (2012). Rational design of molecularly imprinted polymer: the choice of cross-linker. *Analyst*, *137*(11), 2623-2628.
[66] Wackerlig, J., & Lieberzeit, P. A. (2015). Molecularly imprinted polymer nanoparticles in chemical sensing–Synthesis, characterisation and application. *Sensors and Actuators B: Chemical*, *207*, 144-157.
[67] Yu, C., & Mosbach, K. (1998). Insights into the origins of binding and the recognition properties of molecularly imprinted polymers prepared using an amide as the hydrogen-bonding functional group. *Journal of Molecular Recognition: An Interdisciplinary Journal*, *11*(1-6), 69-74.
[68] Sullivan, M. V., Dennison, S. R., Hayes, J. M., & Reddy, S. M. (2021). Evaluation of acrylamide-based molecularly imprinted polymer thin-sheets for specific protein capture—a myoglobin model. *Biomedical Physics & Engineering Express*, *7*(4), 045025.
[69] Cowen, T., Maniglio, D., & Bossi, A. M. (2025). Molecular imprinting using biopolymers as building Blocks: Sustainable and biocompatible metamaterials for smart recognition and selective biointerfaces. *TrAC Trends in Analytical Chemistry*, 118422.
[70] Cakir Hatir, P., & Cayli, G. (2019). Environmentally friendly synthesis and photopolymerization of acrylated methyl ricinoleate for biomedical applications. *Journal of Applied Polymer Science*, *136*(38), 47969.
[71] Le Goff, N., Fomba, I., Prost, E., Merlier, F., Haupt, K., Duma, L., ... & Falcimaigne-Cordin, A. (2020). Renewable plant oil-based molecularly imprinted polymers as biopesticide delivery systems. *ACS Sustainable Chemistry & Engineering*, *8*(42), 15927-15935.
[72] Asif, I. M., Di Giulio, T., Gagliani, F., Malitesta, C., & Mazzotta, E. (2025). Advances in the Direct Nanoscale Integration of Molecularly Imprinted Polymers (MIPs) with Transducers for the Development of High-Performance Nanosensors. *Biosensors*, *15*(8), 509.
[73] Ayankojo, A. G., Reut, J., & Syritski, V. (2024). Electrochemically synthesized MIP sensors: applications in healthcare diagnostics. *Biosensors*, *14*(2), 71.
[74] Mazzotta, E., Di Giulio, T., & Malitesta, C. (2022). Electrochemical sensing of macromolecules based on molecularly imprinted polymers: challenges, successful strategies, and opportunities. *Analytical and bioanalytical chemistry*, *414*(18), 5165-5200.
[75] Shah, N., Ul-Islam, M., Haneef, M., & Park, J. K. (2012). A brief overview of molecularly imprinted polymers: from basics to applications. *J. Pharm. Res*, *5*(3309), e3317.
[76] Song, Z., Li, J., Lu, W., Li, B., Yang, G., Bi, Y., ... & Chen, L. (2022). Molecularly imprinted polymers based materials and their applications in chromatographic and electrophoretic separations. *TrAC Trends in Analytical Chemistry*, *146*, 116504.
[77] Pichon, V., & Haupt, K. (2006). Affinity separations on molecularly imprinted polymers with special emphasis on solid-phase extraction. *Journal of liquid chromatography & related technologies*, *29*(7-8), 989-1023.
[78] Vlatakis, G., Andersson, L. I., Müller, R., & Mosbach, K. (1993). Drug assay using antibody mimics made by molecular imprinting. *Nature*, *361*(6413), 645-647.

[79] Dai, S., Shin, Y. S., Barnes, C. E., & Toth, L. M. (1997). Enhancement of Uranyl Adsorption Capacity and Selectivity on Silica Sol− Gel Glasses via Molecular Imprinting. *Chemistry of materials*, *9*(11), 2521-2525.
[80] Sellergren, B. (1999). Polymer-and template-related factors influencing the efficiency in molecularly imprinted solid-phase extractions. *TrAC Trends in Analytical Chemistry*, *18*(3), 164-174.
[81] Wulff, G. (2002). Enzyme-like catalysis by molecularly imprinted polymers. *Chemical reviews*, *102*(1), 1-28.
[82] Piletsky, S. A., & Piletsky, S. S. (2025). Molecularly Imprinted Polymers as Artificial Catalysts–Recent Trends and Emerging Applications. *TrAC Trends in Analytical Chemistry*, 118435.
[83] Suravajhala, R., Burri, H. R., & Malik, B. (2020). Selective targeted drug delivery mechanism via molecular imprinted polymers in cancer therapeutics. *Current Topics in Medicinal Chemistry*, *20*(22), 1993-1998.
[84] Norell, M. C., Andersson, H. S., & Nicholls, I. A. (1998). Theophylline molecularly imprinted polymer dissociation kinetics: a novel sustained release drug dosage mechanism. *Journal of Molecular Recognition: An Interdisciplinary Journal*, *11*(1-6), 98-102.
[85] Alvarez-Lorenzo, C., Hiratani, H., Gomez-Amoza, J. L., Martínez-Pacheco, R., Souto, C., & Concheiro, A. (2002). Soft contact lenses capable of sustained delivery of timolol. *Journal of pharmaceutical sciences*, *91*(10), 2182-2192.

Chapter III – MIP-based sensors

MIPs have emerged as one of the most versatile and promising classes of synthetic recognition materials for sensor development. The concept of molecular imprinting originated in the early 1970s, but the application of MIP materials to sensing started only two decades later, with the first examples of MIP-based sensors in the early 90s [1]. In 1994, Piletsky et al. reported one of the earliest examples of an electrochemical MIP sensor, proving the demonstration that a highly substrate-selective MIP polymeric membrane could act as a synthetic receptor capable of detecting low-molecular weight organic substrates, including AMP, L-Phenylalanine, atrazine and cholesterol. From that point onward, the use of MIPs as synthetic receptors in sensing has expanded exponentially, driven by their ability to emulate biological recognition processes. Building on their chemical robustness, operational stability, and cost-effective synthesis, MIPs have provided a solid foundation for the design of sensors applied to medical diagnostics, environmental monitoring, food safety and quality control and pharmaceutical analysis, as reported in several comprehensive reviews on the topic [2-5].

As shown in Chapter I, the analytical performance of a sensor heavily depends on the design of the recognition element and on its integration with the transducer. High-performing sensors should ensure fast diffusion of the target analyte to the receptor, so to attain rapid response times, while the presence of homogeneous and oriented binding sites allows efficient and directional interactions with the target, dictated by the kinetic rate-on constant (k_{on}) of the interaction, thus generating sharp and reproducible recognition profiles. Additionally, requirements of selectivity and of low levels of non-specific interactions lead to improved target detection and to minimized non-specific binding. Finally, enhancement of the overall sensor sensitivity can be pursued through the use of responsive recognition materials, capable of amplifying the transduction signal.

MIPs in principle possess all the mentioned characteristics, making them ideal recognition elements for sensing. As follows, each point will be discussed individually.

Concerning the fast response, one of the most significant advances in MIP's design has been the miniaturization into nanostructured architectures, encompassing formats such as nanoparticles and nanolayers. As outlined in Chapter II, reducing the imprinted architecture to the nanoscale fundamentally improved analyte accessibility and binding kinetics. Thin MIP nano-materials with thickness of few nanometers up to nanoparticles of few tens of nm are expected to have the recognition sites located predominantly on or near the surface, ensuring rapid mass transport and efficient interaction with target molecules, with sensor's response times on the timescale of up to few minutes [6-8]. From a technological standpoint, the nanoscale format offers additional advantages for sensor integration. Nanostructured MIPs can be immobilized onto a wide range of transducers, including metallic and semiconductor surfaces, optical fibers, and carbon-based electrodes, through simple physical adsorption, covalent coupling, or electropolymerization, ensuring excellent compatibility with a variety of sensing platforms [9-11].

While nanoscale miniaturization significantly improves analyte diffusion, hence response dynamics, achieving a sharp and reproducible signal also requires precise control over the quality of the recognition sites. In this regard, a number of strategies are available to produce MIPs with homogeneous binding sites, meeting the needs of sensor technology.

Usually, most of the MIP synthesis procedures (Chapter II) have the drawback to form binding cavities with intrinsic heterogeneity. This heterogeneity arises from several factors, including random template orientation within the pre-polymerization mixture, non-uniform distribution or excess of functional groups, and differences in site accessibility within the polymeric network. As a result, not all imprinted sites exhibit identical affinity or spatial arrangement toward the target, leading to variations in binding strength and selectivity, and ultimately negatively affecting the reproducibility of the sensor response [12]. In contrast, controlled and surface-confined polymerization techniques have been introduced to achieve higher homogeneity and accessibility of the imprinted sites. In particular, the electropolymerization of thin MIP films has enabled a precise control over the film thickness (5-20 nm) and the density of the binding sites simply by tuning the

number of polymerization cycles. The resulting films display a more uniform distribution of recognition cavities, improved mass transport, and enhanced reproducibility in sensing measurements [13-17]. Furthermore, within electropolymerized nanolayers, oriented imprinting, where the spatial arrangement of the template is pre-defined before polymerization, has emerged as an effective strategy to further enhance the uniformity of the binding sites.

In practice, oriented imprinting is typically achieved by modifying the surface or support used for polymerization with functional groups capable of selectively interacting with the target analyte. This functionalization allows the template to be anchored in a spatially defined orientation prior to polymerization, and its subsequent removal leaves directionally organized cavities that reproduce the geometry and chemical functionalities of the target molecule.

One of the most established examples is boronate-affinity-oriented imprinting, in which boronic acids form reversible covalent bonds with *cis*-diol-containing compounds such as sugars, glycoproteins, and glycopeptides under alkaline conditions, while the complexes dissociate under acidic environments [18-24].

Other chemistries have been explored to achieve similar control over template orientation, such as borazine (B_3N_3)-assisted oriented imprinting [25], the use of cyclodextrin-based anchoring systems [26] or orientation strategies which exploit specific protein-ligand interactions to guide template immobilization [27].

Although surface functionalization strategies have greatly improved control over template orientation, the degree of spatial organization achievable remains inherently limited, especially in the case of large biomolecules used as templates. This limitation arises because, during polymerization, large and flexible biomolecules can still interact with multiple sites on the surface or with surrounding monomers, resulting in multipoint binding and only partial control of the imprinting geometry.

Alternative approaches employ template engineering as the strategy to achieve improved orientation control. in the case, the orientational control is introduced directly through chemical functionalization of the template, allowing its selective immobilization or interaction with the surrounding monomers during polymerization. This concept significantly reduces the need for pre-functionalized

surfaces, as the template itself carries the anchoring functionalities required for selective immobilization [28-30]. Among the various template engineering strategies, one of the most widely used involves the incorporation of specific amino acid residues, such as cysteine or histidine, into the epitope sequence [31-36].

A representative example of this strategy was reported by Drzazgowska *et al.*, who proposed a refined orientation method based on a doubly cysteine-modified peptide used to form a self-assembled monolayer (SAM) bridge on a gold electrode prior to polymerization. In this configuration, both the N- and C-terminal cysteine residues were covalently anchored to the gold surface, creating a bridge-like template on which the MIP layer was subsequently deposited via electropolymerization. The resulting thin and uniformly oriented polymer film exhibited improved recognition site homogeneity and significantly enhanced analytical performance, enabling detection of analyte concentrations up to twelve times lower than the clinical threshold, with a dissociation constant below to 65 pM and minimal cross-reactivity toward four nonspecific molecules [37].

In summary, strategies such as surface-confined polymerization and oriented imprinting have significantly improved the structural definition and reproducibility of binding sites, leading to more consistent molecular recognition and sensor performance. However, these approaches remain largely confined to electropolymerized thin films, limiting their applicability to other sensing configurations. In this context, it becomes particularly relevant to assess whether pre-synthesized MIP nanoparticles, widely available, easily tailored to specific templates, and characterized by excellent site accessibility, can achieve a comparable level of binding-site homogeneity and, consequently, deliver equivalent or even superior sensing performance compared to conventionally electropolymerized layers [38].

Beyond improving analyte diffusion and optimizing the homogeneity and orientation of binding sites, the third key aspect in sensing is the amplification of the signal, thus enabling the detection of analytes at ultralow concentrations. In advanced sensing technologies such as organic electrochemical transistors (OECTs) and electrolyte-gated field-effect transistors (EG-FETs), the sensing interface itself, by converting ion changes into large current changes due to ionic modulation of the

whole semiconducting bulk, contributes to signal amplification, allowing ultra-sensitive or even single-molecule detection [39, 40]. Similarly, in MIP-based sensors, this goal can be pursued by designing receptors that not only recognize the target but also actively modulate the transduction response.

A particularly effective approach in this direction is represented by the development of hydrogel- and nanogel-based MIPs, characterized by flexible and soft three-dimensional polymer networks that can reversibly change their volume through swelling or shrinking in response to specific stimuli, thereby acting as intrinsic amplification mechanisms [41-44].

Within this class of materials, analyte-responsive MIP nanogels constitute a particularly interesting subgroup, in which the specific binding of the analyte to the imprinted sites induces local conformational rearrangements or volumetric variations in the polymer matrix, effectively translating the molecular recognition event into a measurable physical signal [45-47, 8].

A representative example is the deformable nanoMIP system reported by Cennamo et al., in which soft molecularly imprinted nanogels, selective for human transferrin (HTR), were synthesized and integrated into a surface plasmon resonance (SPR) sensor based on a plastic optical fiber (POF). Upon analyte binding, conformational rearrangements within the nanogel network produced significant optical shifts in the plasmonic spectrum, clearly demonstrating that the structural flexibility of the MIPs directly contributed to the signal transduction process and acted as an intrinsic amplifier of the plasmonic response [8].

Beyond analyte-induced deformation, further amplification and control of the sensing response can be achieved through stimuli-responsive MIPs, whose structural or chemical properties change in response to external triggers such as temperature, pH, or light. These materials enable active modulation of the transduction signal, either by amplifying the measurable response or by facilitating sensor regeneration and reusability [48-51].

Thermo-responsive MIPs constitute a class of materials capable of reversible structural transitions upon temperature variation, typically achieved by incorporating temperature-sensitive monomers such as *N*-isopropylacrylamide (NIPAAm) within the imprinted matrix [52, 53]. These monomers endow the

polymer with a well-defined lower critical solution temperature (LCST), below which hydrophilic interactions dominate, maintaining the polymer in a swollen and hydrated state, whereas above this temperature hydrophobic interactions prevail, causing network collapse and changes in porosity and analyte accessibility [54-62]. In a similar manner, pH-responsive MIPs are obtained by integrating ionizable monomers whose protonation state varies with pH, altering the internal charge distribution and the hydrogen-bonding network of the polymer. These materials can reversibly swell or contract depending on environmental acidity, thereby modulating analyte diffusion and binding affinity [48, 50].

Particularly, in cationic polymers, protonation of basic functionalities at low pH generates electrostatic repulsion along the polymer chains, resulting in network expansion, while at higher pH values, deprotonation decreases charge density and favours polymer-polymer interactions, resulting in contraction. Conversely, in anionic polymers, acidic groups are protonated under acidic conditions, promoting hydrophobic interactions and network shrinkage, whereas at higher pH they dissociate into carboxylate ions, increasing charge repulsion and inducing swelling [63-66].

Photo-responsive MIPs, on the other hand, incorporate photoactive moieties capable of reversibly modulating the structural and chemical properties upon light irradiation [67, 68]. The use of light as a stimulus is particularly advantageous as it provides a clean, non-invasive and precisely tunable control over the system, both spatially and temporally, without perturbing the surrounding environment [48, 50, 69]. Among photoactive monomers, azobenzene derivatives are the most widely employed due to their well-known reversible *trans–cis* photoisomerization.

This light-induced transition can significantly alter the geometry and size of the imprinted cavities, alter their polarity and accessibility, or even trigger analyte release thus allowing optical control over the recognition and release processes [70 -74].

References

[1] Piletsky, S. A., Parhometz, Y. P., Lavryk, N. V., Panasyuk, T. L., & El'Skaya, A. V. (1994). Sensors for low-weight organic molecules based on molecular imprinting technique. *Sensors and Actuators B: Chemical*, *19*(1-3), 629-631.

[2] Wackerlig, J., & Lieberzeit, P. A. (2015). Molecularly imprinted polymer nanoparticles in chemical sensing–Synthesis, characterisation and application. *Sensors and Actuators B: Chemical*, *207*, 144-157.

[3] Ahmad, O. S., Bedwell, T. S., Esen, C., Garcia-Cruz, A., & Piletsky, S. A. (2019). Molecularly imprinted polymers in electrochemical and optical sensors. *Trends in biotechnology*, *37*(3), 294-309.

[4] Saylan, Y., Akgönüllü, S., Yavuz, H., Ünal, S., & Denizli, A. (2019). Molecularly imprinted polymer based sensors for medical applications. *Sensors*, *19*(6), 1279.

[5] Lowdon, J. W., Diliën, H., Singla, P., Peeters, M., Cleij, T. J., van Grinsven, B., & Eersels, K. (2020). MIPs for commercial application in low-cost sensors and assays–An overview of the current status quo. *Sensors and Actuators B: Chemical*, *325*, 128973.

[6] Ton, X. A., Tse Sum Bui, B., Resmini, M., Bonomi, P., Dika, I., Soppera, O., & Haupt, K. (2013). A Versatile Fiber-Optic Fluorescence Sensor Based on Molecularly Imprinted Microstructures Polymerized in Situ. *Angewandte Chemie*, *125*(32), 8475-8479.

[7] Cennamo, N., Pasquardini, L., Arcadio, F., Vanzetti, L. E., Bossi, A. M., & Zeni, L. (2019). D-shaped plastic optical fibre aptasensor for fast thrombin detection in nanomolar range. *Scientific reports*, *9*(1), 18740.

[8] Cennamo, N., Maniglio, D., Tatti, R., Zeni, L., & Bossi, A. M. (2020). Deformable molecularly imprinted nanogels permit sensitivity-gain in plasmonic sensing. *Biosensors and Bioelectronics*, *156*, 112126.

[9] Chiappini, A., Pasquardini, L., & Bossi, A. M. (2020). Molecular imprinted polymers coupled to photonic structures in biosensors: The state of art. *Sensors*, *20*(18), 5069.

[10] Ma, J., Yan, M., Feng, G., Ying, Y., Chen, G., Shao, Y., ... & Abd El-Aty, A. M. (2021). An overview on molecular imprinted polymers combined with surface-enhanced Raman spectroscopy chemical sensors toward analytical applications. *Talanta*, *225*, 122031.

[11] Asif, I. M., Di Giulio, T., Gagliani, F., Malitesta, C., & Mazzotta, E. (2025). Advances in the Direct Nanoscale Integration of Molecularly Imprinted Polymers (MIPs) with Transducers for the Development of High-Performance Nanosensors. *Biosensors*, *15*(8), 509.

[12] Wei, S., & Mizaikoff, B. (2007). Binding site characteristics of 17β-estradiol imprinted polymers. *Biosensors and Bioelectronics*, *23*(2), 201-209.

[13] Malitesta, C., Mazzotta, E., Picca, R. A., Poma, A., Chianella, I., & Piletsky, S. A. (2012). MIP sensors–the electrochemical approach. *Analytical and bioanalytical chemistry*, *402*(5), 1827-1846.

[14] Lahcen, A. A., & Amine, A. (2019). Recent advances in electrochemical sensors based on molecularly imprinted polymers and nanomaterials. *Electroanalysis*, *31*(2), 188-201.

[15] Palladino, P., Bettazzi, F., & Scarano, S. (2019). Polydopamine: surface coating, molecular imprinting, and electrochemistry—successful applications and future perspectives in (bio) analysis. *Analytical and bioanalytical chemistry*, *411*(19), 4327-4338.

[16] Unger, C., & Lieberzeit, P. A. (2021). Molecularly imprinted thin film surfaces in sensing: Chances and challenges. *Reactive and Functional Polymers*, *161*, 104855.

[17] Wang, L., Pagett, M., & Zhang, W. (2023). Molecularly imprinted polymer (MIP) based electrochemical sensors and their recent advances in health applications. *Sensors and Actuators Reports*, *5*, 100153.

[18] Wang, S., Ye, J., Bie, Z., & Liu, Z. (2014). Affinity-tunable specific recognition of glycoproteins via boronate affinity-based controllable oriented surface imprinting. *Chemical Science*, *5*(3), 1135-1140.

[19] Bie, Z., Chen, Y., Ye, J., Wang, S., & Liu, Z. (2015). Boronate-affinity glycan-oriented surface imprinting: a new strategy to mimic lectins for the recognition of an intact glycoprotein and its characteristic fragments. *Angewandte Chemie International Edition*, *54*(35), 10211-10215.

[20] Liu, Y., & Yu, J. (2016). Oriented immobilization of proteins on solid supports for use in biosensors and biochips: a review. *Microchimica Acta*, *183*(1), 1-19.

[21] You, M., Yang, S., Tang, W., Zhang, F., & He, P. G. (2017). Ultrasensitive electrochemical detection of glycoprotein based on boronate affinity sandwich assay and signal amplification with functionalized SiO2@ Au nanocomposites. *ACS applied materials & interfaces*, *9*(16), 13855-13864.

[22] Lang, J. Y., Bai, C. C., Yu, S. S., Chen, M. Y., Dong, L. Y., Zhao, Z. Y., & Wang, X. H. (2022). Fabrication of self-healing magnetic nanoreceptors for glycoprotein via integrating boronate-affinity-oriented and sequential surface imprinting. *Analytica chimica acta*, *1221*, 340108.

[23] Chen, F., Lv, C., Xing, Y., Luo, L., Wang, J., Cheng, Y., & Xie, X. (2023). Electrospinning carbon fibers based molecularly imprinted polymer self-supporting

electrochemical sensor for sensitive detection of glycoprotein. *Sensors and Actuators B: Chemical*, *396*, 134552.

[24] Li, D., Wang, Y., Zhang, F., Zhao, Y., Zong, X., & Wang, S. (2024). Oriented surface imprinted 96-well microplate-based fluorescent biosensor for glycoprotein detection by boronate affinity sandwich assay. *International Journal of Biological Macromolecules*, *279*, 135128.

[25] Cetinkaya, A., Unal, M. A., Nazır, H., Çorman, M. E., Uzun, L., & Ozkan, S. A. (2024). Development of borazine-assisted-oriented molecularly imprinted electrochemical sensor for the detection of umifenovir in serum and urine by EIS and DPV methods. *Sensors and Actuators B: Chemical*, *420*, 136519.

[26] Longsompurana, P., Wolschann, P., Subannajui, K., Lieberzeit, P. A., & Poo-Arporn, R. P. (2025). Cyclodextrin-integrated molecularly imprinted polymer-based QCM sensor for sensitive, label-free detection of Gal3. *Biosensors and Bioelectronics*, 117712.

[27] Kamon, Y., Matsuura, R., Kitayama, Y., Ooya, T., & Takeuchi, T. (2014). Precisely controlled molecular imprinting of glutathione-s-transferase by orientated template immobilization using specific interaction with an anchored ligand on a gold substrate. *Polymer Chemistry*, *5*(16), 4764-4771.

[28] Suda, N., Sunayama, H., Kitayama, Y., Kamon, Y., & Takeuchi, T. (2017). Oriented, molecularly imprinted cavities with dual binding sites for highly sensitive and selective recognition of cortisol. *Royal Society open science*, *4*(8), 170300.

[29] Ma, X. T., He, X. W., Li, W. Y., & Zhang, Y. K. (2019). Oriented surface epitope imprinted polymer-based quartz crystal microbalance sensor for cytochrome c. *Talanta*, *191*, 222-228.

[30] Kalecki, J., Iskierko, Z., Cieplak, M., & Sharma, P. S. (2020). Oriented immobilization of protein templates: a new trend in surface imprinting. *ACS sensors*, *5*(12), 3710-3720.

[31] Senwu, L., Kaiguang, Y., Jianxi, L., Bo, J., Lihua, Z., & Yukui, Z. (2015). Surface-Imprinted Nanoparticles Prepared with a His-Tag-Anchored Epitope as the Template.

[32] Tchinda, R., Tutsch, A., Schmid, B., Süssmuth, R. D., & Altintas, Z. (2019). Recognition of protein biomarkers using epitope-mediated molecularly imprinted films: Histidine or cysteine modified epitopes?. *Biosensors and Bioelectronics*, *123*, 260-268.

[33] Pirzada, M., Sehit, E., & Altintas, Z. (2020). Cancer biomarker detection in human serum samples using nanoparticle decorated epitope-mediated hybrid MIP. *Biosensors and Bioelectronics*, *166*, 112464.

[34] Wei, H., Wang, Z., Wang, Y., Ma, J., Chen, Y., Guo, M., ... & Hu, F. (2023). Detection of depression marker ASS1 in urine by gold nanoparticles based dual epitope-peptides imprinted sensor. *Analytica Chimica Acta*, *1273*, 341479.

[35] Han, W., Chai, Y., Du, Y., Wang, L., Fu, G., & Ou, L. (2024). Oriented surface imprinting of epitopes anchored on silica nanoparticles containing quantum dots by thiol-disulfide exchange reactions for the enhanced fluorescence detection of proteins. *Talanta*, *280*, 126636.

[36] Hasabnis, G. K., & Altintas, Z. (2024). Cardiac troponin i-responsive nanocomposite materials for voltammetric monitoring of acute myocardial infarction. *ACS omega*, *9*(28), 30737-30750.

[37] Drzazgowska, J., Schmid, B., Süssmuth, R. D., & Altintas, Z. (2020). Self-assembled monolayer epitope bridges for molecular imprinting and cancer biomarker sensing. *Analytical chemistry*, *92*(7), 4798-4806.

[38] Marinangeli, A., Chianella, I., Radicchi, E., Maniglio, D., & Bossi, A. M. (2024). Molecularly Imprinted Polymers Electrochemical Sensing: The Effect of Inhomogeneous Binding Sites on the Measurements. A Comparison between Imprinted Polyaniline versus nanoMIP-Doped Polyaniline Electrodes for the EIS Detection of 17β-Estradiol. *ACS sensors*, *9*(9), 4963-4973.

[39] Macchia, E., Manoli, K., Holzer, B., Di Franco, C., Ghittorelli, M., Torricelli, F., ... & Torsi, L. (2018). Single-molecule detection with a millimetre-sized transistor. *Nature communications*, *9*(1), 3223.

[40] Macchia, E., Picca, R. A., Manoli, K., Di Franco, C., Blasi, D., Sarcina, L., ... & Torsi, L. (2020). About the amplification factors in organic bioelectronic sensors. *Materials Horizons*, *7*(4), 999-1013.

[41] Xu, S., Lu, H., Zheng, X., & Chen, L. (2013). Stimuli-responsive molecularly imprinted polymers: versatile functional materials. *Journal of Materials Chemistry C*, *1*(29), 4406-4422.

[42] Pinelli, F., Magagnin, L., & Rossi, F. (2020). Progress in hydrogels for sensing applications: A review. *Materials Today Chemistry*, *17*, 100317.

[43] Herrmann, A., Haag, R., & Schedler, U. (2021). Hydrogels and their role in biosensing applications. *Advanced healthcare materials*, *10*(11), 2100062.

[44] Silva, A. T., Figueiredo, R., Azenha, M., Jorge, P. A., Pereira, C. M., & Ribeiro, J. A. (2023). Imprinted hydrogel nanoparticles for protein biosensing: a review. *ACS sensors*, *8*(8), 2898-2920.

[45] Matsui, J., Akamatsu, K., Nishiguchi, S., Miyoshi, D., Nawafune, H., Tamaki, K., & Sugimoto, N. (2004). Composite of Au nanoparticles and molecularly imprinted polymer as a sensing material. *Analytical chemistry*, *76*(5), 1310-1315.

[46] Culver, H. R., Clegg, J. R., & Peppas, N. A. (2017). Analyte-responsive hydrogels: intelligent materials for biosensing and drug delivery. *Accounts of chemical research*, *50*(2), 170-178.

[47] Cennamo, N., Bossi, A. M., Arcadio, F., Maniglio, D., & Zeni, L. (2021). On the effect of soft molecularly imprinted nanoparticles receptors combined to nanoplasmonic probes for biomedical applications. *Frontiers in Bioengineering and Biotechnology*, *9*, 801489.

[48] Xu, S., Lu, H., Zheng, X., & Chen, L. (2013). Stimuli-responsive molecularly imprinted polymers: versatile functional materials. *Journal of Materials Chemistry C*, *1*(29), 4406-4422.

[49] Chen, L., Wang, X., Lu, W., Wu, X., & Li, J. (2016). Molecular imprinting: perspectives and applications. *Chemical society reviews*, *45*(8), 2137-2211.

[50] Li, Z., Deng, J., Ma, P., Bai, H., Jin, Y., Zhang, Y., ... & Burenjargal, M. (2024). Stimuli-Responsive Molecularly Imprinted Polymers: Mechanism and Applications. *Journal of Separation Science*, *47*(19), e202400441.

[51] Li, Z., Deng, J., Ma, P., Bai, H., Jin, Y., Zhang, Y., ... & Burenjargal, M. (2024). Stimuli-Responsive Molecularly Imprinted Polymers: Mechanism and Applications. *Journal of Separation Science*, *47*(19), e202400441.

[52] Heskins, M., & Guillet, J. E. (1968). Solution properties of poly (N-isopropylacrylamide). *Journal of Macromolecular Science—Chemistry*, *2*(8), 1441-1455.

[53] Li, J., He, W. D., He, N., Han, S. C., Sun, X. L., Li, L. Y., & Zhang, B. Y. (2009). Synthesis of PEG-PNIPAM-PLys hetero-arm star polymer and its variation of thermo-responsibility after the formation of polyelectrolyte complex micelles with PAA. *Journal of Polymer Science Part A: Polymer Chemistry*, *47*(5), 1450-1462.

[54] Li, S., Pilla, S., & Gong, S. (2009). Modulated molecular recognition by a temperature-sensitive molecularly-imprinted polymer. *Journal of Polymer Science Part A: Polymer Chemistry*, *47*(9), 2352-2360.

[55] Qin, L., He, X. W., Yuan, X., Li, W. Y., & Zhang, Y. K. (2011). Molecularly imprinted beads with double thermosensitive gates for selective recognition of proteins. *Analytical and bioanalytical chemistry*, *399*(10), 3375-3385.

[56] Zhang, W., He, X. W., Li, W. Y., & Zhang, Y. K. (2012). Thermo-sensitive imprinted polymer coating CdTe quantum dots for target protein specific recognition. *Chemical Communications*, *48*(12), 1757-1759.

[57] Li, S., Yang, K., Deng, N., Min, Y., Liu, L., Zhang, L., & Zhang, Y. (2016). Thermoresponsive epitope surface-imprinted nanoparticles for specific capture and release of target protein from human plasma. *ACS applied materials & interfaces*, *8*(9), 5747-5751.

[58] Li, H., Wang, X., Wang, Z., Jiang, J., Wei, M., Zheng, J., ... & Li, C. (2017). Thermo-responsive molecularly imprinted sensor based on the surface-enhanced Raman scattering for selective detection of R6G in the water. *Dalton Transactions*, *46*(34), 11282-11290.

[59] Wu, Y., Yan, M., Lu, J., Wang, C., Zhao, J., Cui, J., ... & Yan, Y. (2017). Facile bio-functionalized design of thermally responsive molecularly imprinted composite membrane for temperature-dependent recognition and separation applications. *Chemical Engineering Journal*, *309*, 98-107.

[60] Wei, Y., Zeng, Q., Hu, Q., Wang, M., Tao, J., & Wang, L. (2018). Self-cleaned electrochemical protein imprinting biosensor basing on a thermo-responsive memory hydrogel. *Biosensors and Bioelectronics*, *99*, 136-141.

[61] Hong, L., Pan, M., Yang, X., Xie, X., Liu, K., Yang, J., ... & Wang, S. (2022). A UCMPs@ MIL-100 based thermo-sensitive molecularly imprinted fluorescence sensor for effective detection of β-lactoglobulin allergen in milk products. *Journal of Nanobiotechnology*, *20*(1), 51.

[62] Yang, X., Huo, C., Ji, Y., Xu, S., Zhang, C., Xia, C., ... & Miao, Z. (2023). A molecularly imprinted sensor based on thermo-responsive calcium alginate nanohydrogels for lysozyme detection. *Colloid and Polymer Science*, *301*(3), 229-237.

[63] Gao, F. X., Zhao, X. L., He, X. W., Li, W. Y., & Zhang, Y. K. (2013). A pH and temperature dual-responsive macroporous molecularly imprinted cryogel for enhanced recognition capability towards ovalbumin. *Analytical Methods*, *5*(23), 6700-6708.

[64] Matsumoto, K., Kawamura, A., & Miyata, T. (2017). Conformationally regulated molecular binding and release of molecularly imprinted polypeptide hydrogels that undergo helix–coil transition. *Macromolecules*, *50*(5), 2136-2144.

[65] Li, Q., Wang, M., Jin, Y., Lu, Y., Xiong, S., Wang, M., ... & Li, J. (2023). Microfluidic synthesis of pH-responsive molecularly imprinted silica nanospheres for fluorescence sensing target glycoprotein. *Food Chemistry*, *426*, 136570.

[66] Wang, C., Javadi, A., Ghaffari, M., & Gong, S. (2010). A pH-sensitive molecularly imprinted nanospheres/hydrogel composite as a coating for implantable biosensors. *Biomaterials*, *31*(18), 4944-4951.

[67] Rad, J. K., Balzade, Z., & Mahdavian, A. R. (2022). Spiropyran-based advanced photoswitchable materials: A fascinating pathway to the future stimuli-responsive

devices. *Journal of Photochemistry and Photobiology C: Photochemistry Reviews*, *51*, 100487.

[68] Zhang, Y., Zhao, X., Yuan, J., An, X., Sun, X., Yi, J., & Song, X. M. (2021). Fast and self-recoverable photoinduced deformation behavior of azobenzene-containing poly (arylene ether) s with binaphthalene groups. *Journal of Materials Chemistry C*, *9*(40), 14139-14145.

[69] Tomatsu, I., Peng, K., & Kros, A. (2011). Photoresponsive hydrogels for biomedical applications. *Advanced drug delivery reviews*, *63*(14-15), 1257-1266.

[70] Gong, C., Wong, K. L., & Lam, M. H. (2008). Photoresponsive molecularly imprinted hydrogels for the photoregulated release and uptake of pharmaceuticals in the aqueous media. *Chemistry of Materials*, *20*(4), 1353-1358.

[71] Takeuchi, T., Akeda, K., Murakami, S., Shinmori, H., Inoue, S., Lee, W. S., & Hishiya, T. (2007). Photoresponsive porphyrin-imprinted polymers prepared using a novel functional monomer having diaminopyridine and azobenzene moieties. *Organic & Biomolecular Chemistry*, *5*(15), 2368-2374.

[72] Yang, W., Shen, J., Zhu, S., Si, H., Song, F., Zhang, W., ... & Huang, W. (2022). Preparation and characterisation of photoresponsive molecularly imprinted polymer based on 5-[(4-(methacryloyloxy) phenyl) diazenyl] isophthalic acid for the determination of sulfamethazine. *Microchemical Journal*, *182*, 107823.

[73] Chen, M. J., Yang, H. L., Si, Y. M., Tang, Q., Chow, C. F., & Gong, C. B. (2021). A hollow visible-light-responsive surface molecularly imprinted polymer for the detection of chlorpyrifos in vegetables and fruits. *Food chemistry*, *355*, 129656.

[74] Sun, Y., Yin, X., Zhang, L., & Cao, M. (2021). Preparation and evaluation of photo-responsive hollow SnO 2 molecularly imprinted polymers for the selective recognition of kaempferol. *Analytical Methods*, *13*(7), 925-932.

Chapter IV – Methods and Instrumentations

This chapter presents the main experimental methods and instrumental techniques employed throughout the research described in this thesis. The selected methodologies allowed for a detailed physical and functional characterisation of MIP materials and to evaluate the performance of MIP-based sensors.

Dynamic Light Scattering

Dynamic light scattering (DLS) is a widely used technique to determine size distribution in terms of hydrodynamic diameter for macromolecules or particles dispersed in solution [1]. In particular, DLS measures the Brownian motion of the particles suspended in a liquid by illuminating them with a monochromatic light source, such as a laser, and relates motion to the size by analysing the time-dependent fluctuations in the scattered light intensity [2]. The principle of Brownian motion is that particles in a suspension are constantly colliding with solvent molecules and this cause a certain amount of energy to be transferred, which induces particle movement. As the particles are constantly in motion, the light intensity scattered by the particles is not constant but will fluctuate over time [3]. As a result, smaller particles exhibit faster diffusion and thus more rapid intensity fluctuations, whereas larger particles diffuse more slowly and generate slower variations in the scattered light signal [4]. The scattered light intensity is collected at defined angles (commonly 90°, or a backscatter detection system at 173° or at 158°, depending on instrument configuration), and the resulting intensity data are processed by a correlator to obtain the autocorrelation function (Figure 4.1 A).
The autocorrelation function describes the temporal correlation of the scattered light intensity and reflects how long a particle is located at the same spot. Initially, the autocorrelation function is linear and almost constant, indicating minimal particle displacement. As time progress, the function starts to decay exponentially due to particle movement, and the decay rate is directly related to the translational diffusion coefficient (D) of the particles (Figure 4.1 B) [5].

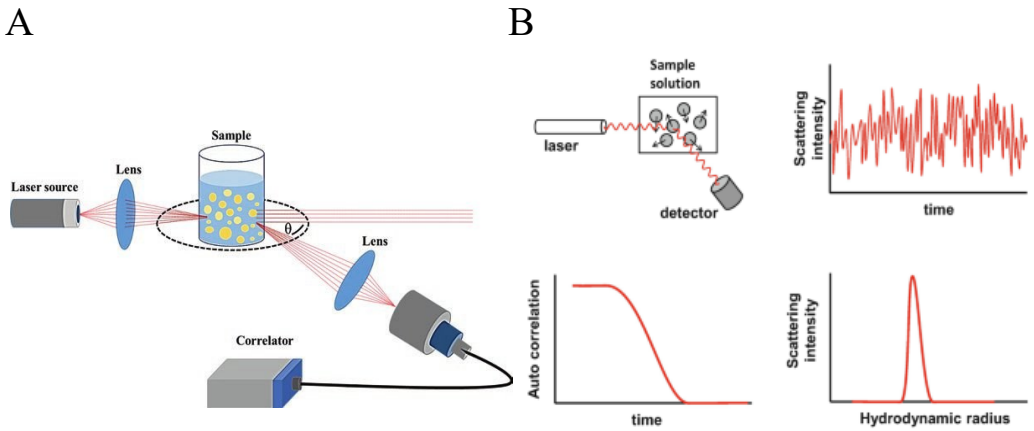

Figure 4.1 (A) Representation of dynamic light scattering principle. Picture reproduced from [6]. (B) Process from dynamic light scattering measurement to obtaining particle size distribution. Picture reproduced from [7].

This value is then used to calculate the hydrodynamic diameter using the Stokes-Einstein equation:

$$d_H = \frac{k_b T}{3\pi\eta D} \qquad \text{Eq. 1}$$

In which d_H describes the hydrodynamic diameter of the suspended particles, k_b is the Boltzmann constant, T is the temperature, η is the viscosity of the medium, and D is the translational diffusion coefficient.

The output of a DLS measurement typically includes two main parameters: the Z-average diameter and the PolyDispersity Index (PDI). The Z-average is an intensity-weighted harmonic mean derived from cumulant analysis, providing a robust and reproducible measurement that is relatively insensitive to noise. The PDI quantifies the breadth of the size distribution and values below 0.2 are indicative of homogeneity, while higher values suggest polydispersity or the presence of aggregates or no uniform material [8]. Furthermore, the measured hydrodynamic diameter is influenced not only by the core size of the particles but also by the electrical double layer that surrounds them. In high ionic strength media, this double layer is compressed, leading to a smaller measured size, while low ionic strength results in a more extended layer and a larger apparent size [9].

Although the primary size distribution provided by DLS is based on intensity, it can be converted to volume- or number-weighted distributions. The volume-weighted distribution reflects the relative proportion of particles based on their size or volume, while the number-weighted distribution represents the actual count of particles in each size class [10].

Isothermal Titration Calorimetry

Isothermal titration calorimetry (ITC) is a label-free, in-solution technique based on the direct measurement of heat released or absorbed during a binding event, allowing the determination of the complete thermodynamic profile of molecular interactions at constant temperature. A schematic representation of an ITC instrument is shown in Figure 4.2.

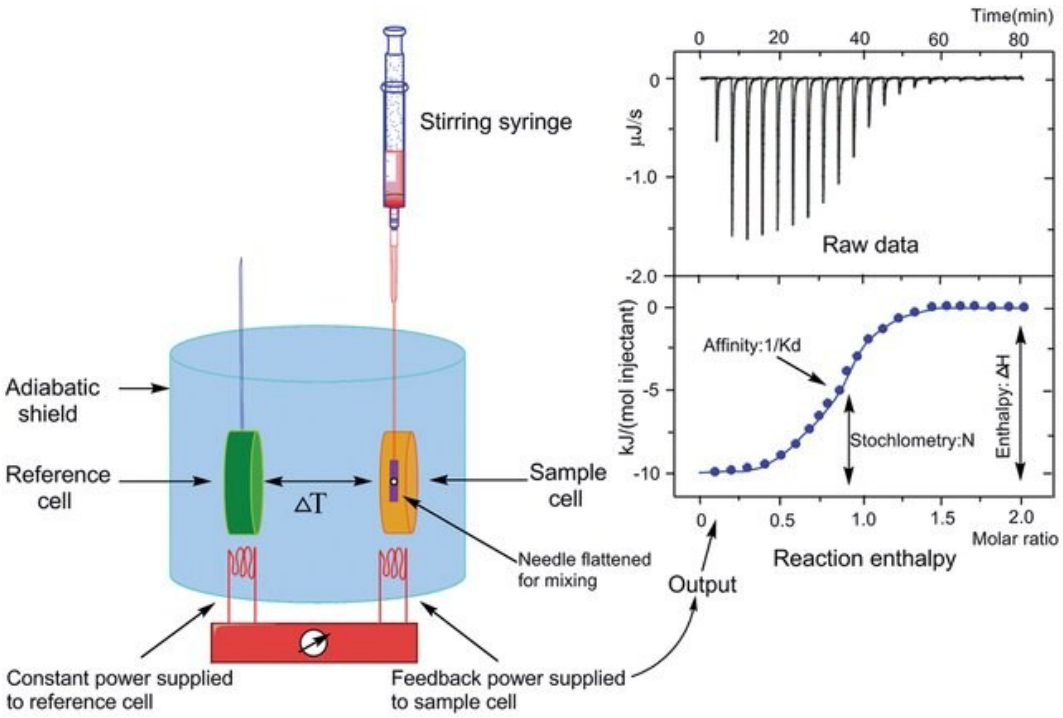

Figure 4.2 Basic principle of isothermal titration calorimetry. Schematic representation of the isothermal titration calorimeter (left) and a characteristic titration experiment (upper right) with its evaluation (lower right). Picture reproduced from [11].

The calorimeter is composed of two cells inside an adiabatic chamber, a reference cell and a sample cell, and an injection syringe. Both cells are equipped with a feedback heater that maintains a constant temperature, and the two cells are joined by a thermocouple device in the middle, which monitors any temperature differences between them. The injection syringe has a long needle that is inserted into the sample cell, and the syringe is attached to a rotation assembly, which

ensures the complete mixing of the solution inside the sample cell by stirring the syringe at a constant speed [12].

During an ITC experiment, the titrant is injected into the sample cell in small, precisely controlled aliquots. If a binding interaction occurs, the temperature of the sample cell changes depending on the type of reaction occurring inside. The thermocouple device detects the changes in temperature and activates the feedback heater to apply a different amount of power to adjust and bring the temperature of the sample cell back to the temperature of the reference cell. The power required to restore thermal equilibrium, called differential power (DP), is directly proportional to the heat associated with the binding event [13]. As a result, when the reaction inside the sample cell is endothermic, the feedback heater supplies more current, resulting in an increase in DP output. When the reaction inside the sample cell is exothermic, the feedback heat supplies less current, resulting in a decrease in DP output. When the reaction inside the sample cell reaches equilibrium (or when the reaction is complete), then the DP returns to the baseline with the same amount of heat applied to the sample cell and the reference cell.

Each injection produces a thermal pulse, which is recorded and plotted in real-time as power *versus* time, resulting in a series of peaks. The area under each peak is integrated to obtain the heat released or absorbed per injection, which is then plotted against the molar ratio of titrant to analyte, generating the binding isotherm. From this curve, non-linear fitting is performed by a software to extract key parameters: the binding stoichiometry (n), the affinity constant (K_{aff}), from which the more commonly used equilibrium dissociation constant (K_D) can be derived and the thermodynamic parameters of the binding reaction such as the enthalpy change ΔH°, the entropy change ΔS° and Gibbs free energy ΔG°, calculated as [14]:

$$\Delta G^{\circ} = -RTlnK = \Delta H^{\circ} - T\Delta S^{\circ} \qquad \text{Eq. 2}$$

Where R is the gas constant and T is the absolute temperature in Kelvin.

A crucial factor in determining the quality of ITC data is the Wiseman c-parameter, defined as:

$$c = n[M]_t K \qquad \text{Eq. 3}$$

where n is the stoichiometry, $[M]_t$ is the concentration of the molecule in the sample cell, and K is the binding constant. The shape and sharpness of the binding isotherm depend strongly on the c-value: between 10 and 500 is considered optimal for reliable curve fitting, while outside this range, the data may be less precise or difficult to interpret due to flattening or steepening of the isotherm [15, 16].

Optical transduction methods

Optical transduction encompasses a range of techniques that convert molecular interactions or chemical changes into measurable optical signals by exploiting the fundamental interactions between light and matter. These interactions are modulated by the presence and concentration of specific molecules and are typically monitored through changes in light properties [17]. A wide variety of optical transduction approaches have been developed, including absorptiometry, reflectometry, fluorescence-based techniques (i.e. fluorescence intensity, polarization or lifetime decay time), interferometry, surface plasmon resonance, infrared and Raman spectroscopy and its enhanced variant, surface-enhanced Raman scattering [18].

The core physical principles of all these different approaches include absorption, luminescence or reflection. [19].

Absorption is a physical process in which the energy of incident photons is taken up by molecules, resulting in the promotion of these species to higher energy states. This occurs only when the photon energy exactly matches the energy difference between two quantised states of the system. Depending on the energy of the radiation, different types of transitions can be induced: electronic transitions with ultraviolet or visible light, vibrational transitions with infrared light and rotational transitions with microwave radiation [19]. Absorption is directly linked to the properties of the material through which the light beam passes and is quantitatively described by the Beer-Lambert law. This law states that the absorbance (A) of collimated monochromatic light passing through a homogeneous and isotropic medium is proportional to the optical path length (l) and to the concentration (c) of the absorbing species, according to the equation:

$$A = log_{10}\left(\frac{I_0}{I}\right) = \varepsilon cl \qquad \text{Eq. 4}$$

Where I_0 is the intensity of the incident light, I is the intensity of the transmitted light, and ε is the molar absorption coefficient [20].

Luminescence refers to the emission of light by a substance following the absorption of photons. Depending on the electronic spin state of the excited species, luminescence can be classified as either fluorescence or phosphorescence.

Fluorescence occurs when the excited electron returns to the ground state without a change in spin orientation. This process is rapid, typically occurring within 1-100 ns. In contrast, in phosphorescence, the excited electron undergoes spin inversion, resulting in an unpaired spin relative to the ground state. Because of this spin mismatch, the return to the ground state is slower, with emission lifetimes ranging from 1-1000 µs, and it often continues even after the excitation source has been removed. In both cases, the intensity of luminescence I_L for weakly absorbing species (A< 0.05) can be calculated as:

$$I_L = k' I_0 \varepsilon l \theta c \qquad \text{Eq. 5}$$

Where I_0 is the luminescence intensity in the absence of the analyte, k' is the instrumental constant, ε is the molar absorptivity, l is the length of the light path in the sample, θ is the quantum efficiency of the luminescence, and c is the analyte concentration. However, the luminescence intensity may deviate from linearity due to the presence of quenching species. This effect is commonly described by the Stern-Volmer equation:

$$\frac{I_0}{I_L} = 1 + K_{SV} c_q \qquad \text{Eq. 6}$$

Where K_{SV} is the Stern-Volmer constant and c_q is the concentration of the quencher [19, 21].

Reflection is the redirection of light at the interface between two different media and occurs when incident light encounters a surface and part of its energy is returned into the original medium rather than being transmitted or absorbed. There are two main types of reflection: specular reflection, which occurs on smooth, mirror-like surfaces where light reflects at a predictable angle, and diffuse reflection, which arises from rough or complex surfaces where the incident light is scattered in multiple directions due to surface irregularities or internal inhomogeneities. In this context, the Kubelka–Munk function relates the reflectance R to analyte concentration c via:

$$F(R) = \frac{(1-R)^2}{2R} = \frac{\varepsilon c}{S} \qquad \text{Eq. 7}$$

Where S is the scattering coefficient [19, 22].

In the following sections, we focus on two approaches: fluorescence-based sensing, which includes fluorescence intensity and lifetime, and SPR.

Fluorescence Spectroscopy

Fluorescence is a photophysical phenomenon belonging to the broader class of luminescence and more specifically to photoluminescence. It describes the property of certain substances to absorb electromagnetic radiation, typically in the ultraviolet or visible range, and subsequently emit part of that energy as light at a longer wavelength and lower energy [23].

This process involves a series of well-defined electronic and vibrational transitions typically illustrated using a Jablonski diagram, which provides a simplified representation of the energy levels involved in photon absorption, excited-state relaxation and subsequent light emission (Figure 4.3) [24]. In this diagram, thick horizontal lines represent electronic states, typically the singlet ground state (S_0), the first and second excited singlet states (S_1 and S_2), and the first excited triplet state (T_1), while thinner lines indicate the vibrational sublevels associated with each electronic state. Upon absorption of a photon, a molecule is promoted from the ground state S_0 to an electronically excited singlet state, usually S_1 or S_2, typically reaching a higher vibrational sublevel of that state. Almost immediately, the molecule undergoes vibrational relaxation, dissipating excess vibrational energy non-radiatively as it relaxes to the lowest vibrational level of S_1. If the initial excitation occurs to a higher singlet state, such as S_2, an additional internal conversion takes place, transferring the molecule to S_1 through non-radiative transitions (10^{-12} s or less). Once in the lowest vibrational level of the S_1 state, the molecule may return to the ground state S_0 by emitting a photon in a fluorescence process. The radiative decay from S_1 to S_0 typically occurs in a timescale ranging from 10^{-9} to 10^{-7} seconds and involves transitions between singlet states, where the electron spins are paired. Alternatively, the molecule in the S_1 state may undergo intersystem crossing to the triplet state T_1, a spin-forbidden process that involves a change in electron spin configuration. From T_1, the molecule may return to the S_0 either non-radiatively or through phosphorescence, a slower radiative process that

occurs in a timescale ranging from 10^{-3} to 100 seconds, due to the spin-forbidden nature of the transition [21, 23].

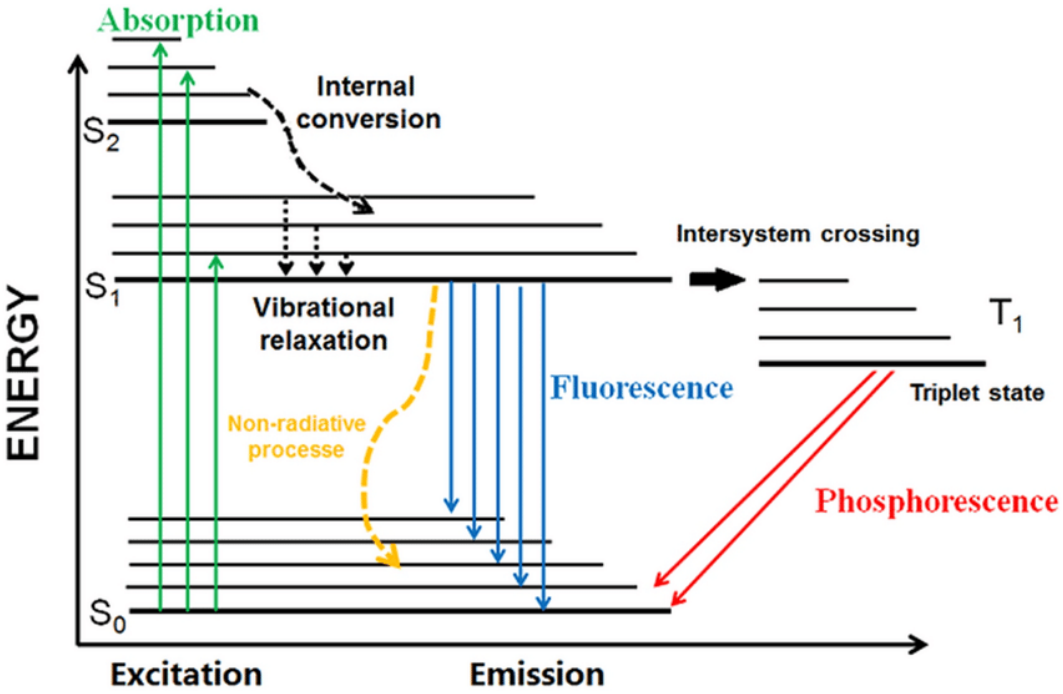

Figure 4.3 Perrin Jablonski diagram of fluorescence and phosphorescence. Picture reproduced from [25].

The photophysical basis of fluorescence, as previously described, can be effectively exploited for analytical purposes using dedicated instrumentation called fluorescence spectrometer, also known as a spectrofluorometer (Figure 4.4). The system consists of a light source for sample excitation, monochromators to select specific wavelengths of both excitation and emission light, a sample holder and a detector, usually a photomultiplier tube (PMT), that captures and amplifies the emitted fluorescence signal. Optical components such as filters are commonly used to select specific emission wavelengths and reduce background signal [23, 26, 27]. The light source is typically a xenon lamp, which provides a continuous emission spectrum spanning over a broad range (approximately 175 to 800 nm), although modern systems increasingly employ light sources with temporally stable intensity or pulsed light sources, such as light-emitting diodes (LEDs) or laser diodes, which not only improve stability and precision of the measurement, but also offer advantages such as lower power consumption, reduction in heat generation, and

minimised photodamage to the sample due to the absence of continuous illumination [23, 26].

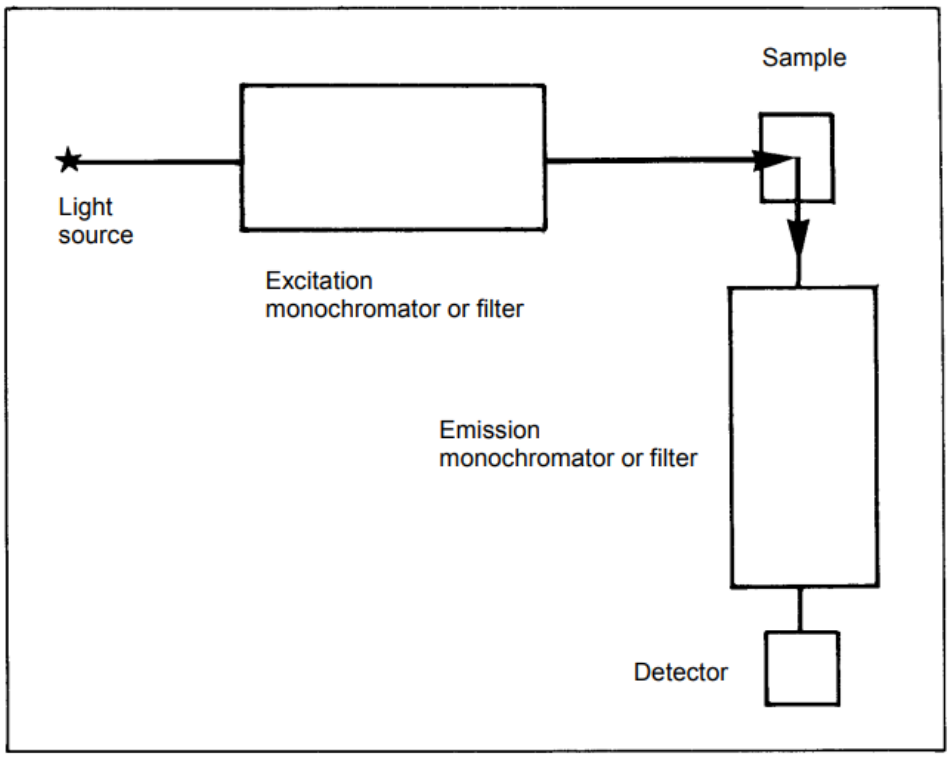

Figure 4.4 Schematic representation of a typical spectrofluorometer. Picture reproduced from [26].

In standard fluorescence spectroscopy setups, the emission signal is typically collected at a 90° angle relative to the incident excitation beam in order to minimize the amount of excitation light that reaches the detector. However, complete elimination of the excitation light is not possible as scattering phenomena, originating from solvent and solute molecules, suspended particles, or refractive index mismatches at interfaces, which contribute to a residual background signal that must be considered during analysis [26, 27].

Depending on the type of detection system and temporal resolution, fluorescence spectroscopy can be conducted in steady-state or time-resolved modes. In steady-state fluorescence spectroscopy, the sample is excited with a continuous beam of light, and the main measurable parameter is the fluorescence intensity, which is recorded as an emission spectrum at a fixed excitation wavelength. Alternatively,

excitation spectra can be obtained by monitoring the emission intensity at a fixed wavelength while scanning the excitation [21, 23]. In particular, the excitation spectrum represents the efficiency with which the fluorophore absorbs light across different wavelengths, while the emission spectrum describes the distribution of emitted light intensities as a function of wavelength following excitation. An example of excitation and emission spectra is shown in Figure 4.5.

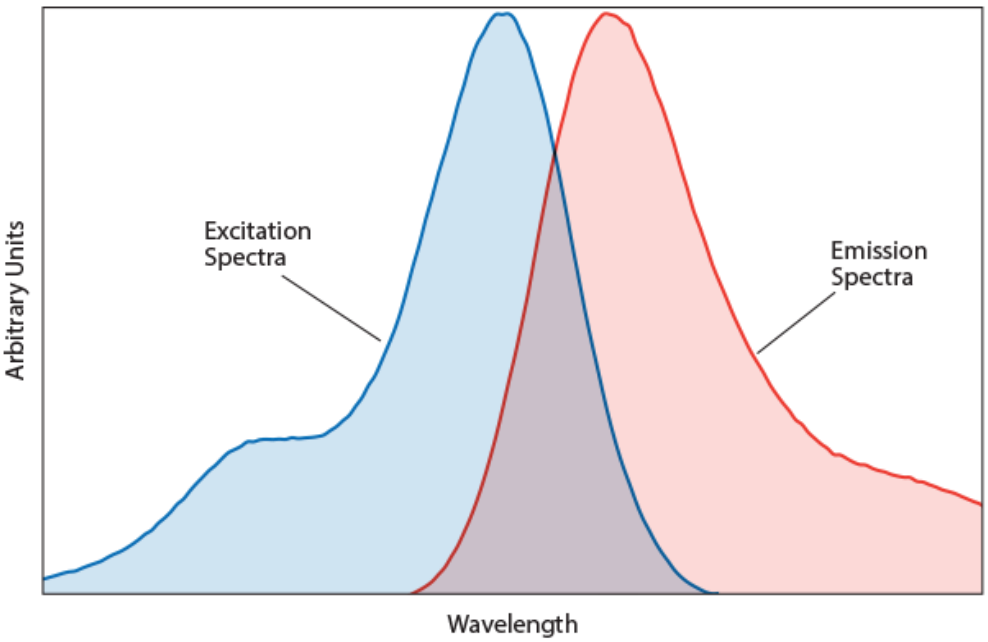

Figure 4.5 Example of steady-state fluorescence excitation and emission spectra. Picture reproduced from [28].

The fluorescence intensity is directly related to the intrinsic properties of the fluorophore such as molecular structure, concentration, absorption and quantum yield, but also on a variety of external factors [21, 23, 29] that include environmental conditions such as temperature [30], pH [31] and ionic strength [32], solvent polarity [33] and the presence of quenchers or energy transfer processes, such as photoinduced electron transfer (PET) and Förster resonance energy transfer (FRET) [21, 23, 34, 35]. In particular, the presence of fluorescence quenchers can lead to a reduction in emission intensity through dynamic (collisional) processes or static mechanisms. In dynamic quenching, the quencher interacts with the fluorophore during its excited-state lifetime, leading to a non-radiative deactivation

of the excited state, while static quenching involves the formation of a non-fluorescent ground-state complex between the fluorophore and the quencher [23]. On the other hand, time-resolved fluorescence spectroscopy measures the fluorescence decay over time following excitation by a short light pulse, where the pulse width is typically shorter than the decay time of the sample. The resulting time-dependent signal reflects the fluorescence lifetime (τ), which is defined as the average time a fluorophore remains in the excited state before returning to the ground state [23, 36]. The fluorescence decay of a population of fluorophores typically follows an exponential behaviour and the fluorescence intensity at a given time *t* can be described by the equation:

$$I(t) = I_0 e^{-t/\tau} \quad \text{Eq. 8}$$

where I_0 is the initial fluorescence intensity. By this definition, the fluorescence lifetime corresponds to the time required for the excited-state population to decay to $1/e$ (approximately 36.8%) of its initial value due to all deactivation processes and the lifetime can be expressed as:

$$\tau = \frac{1}{\Sigma k} \quad \text{Eq. 9}$$

where Σk represents the sum of all the rate constants of radiative and non-radiative deactivation processes [26, 37].

A typical time-resolved fluorescence measurement produces a decay curve in which the emission intensity decreases exponentially after excitation by a short pulse. The fluorescence lifetime τ can be extracted by fitting the decay profile, as illustrated in Figure 4.6.

Fluorescence lifetime is an intrinsic property of the fluorophore and, as such, is largely independent of external factors such as fluorophore concentration, photobleaching or light scattering. It is also more robust to experimental variations, including fluctuations in the excitation source, duration of light exposure, one- or multiphoton excitation, detector sensitivity and sample turbidity [23, 37].

Compared to steady-state measurements, time-resolved fluorescence provides access to additional molecular-level information by capturing the dynamic behaviour of fluorophores in the excited state. One of the principal advantages is the ability to resolve multiple fluorescence lifetimes, thereby revealing the presence

of heterogeneity within the system under study, such as the coexistence of multiple conformational states or binding modes, that would be otherwise obscured by time-average measurements [23].

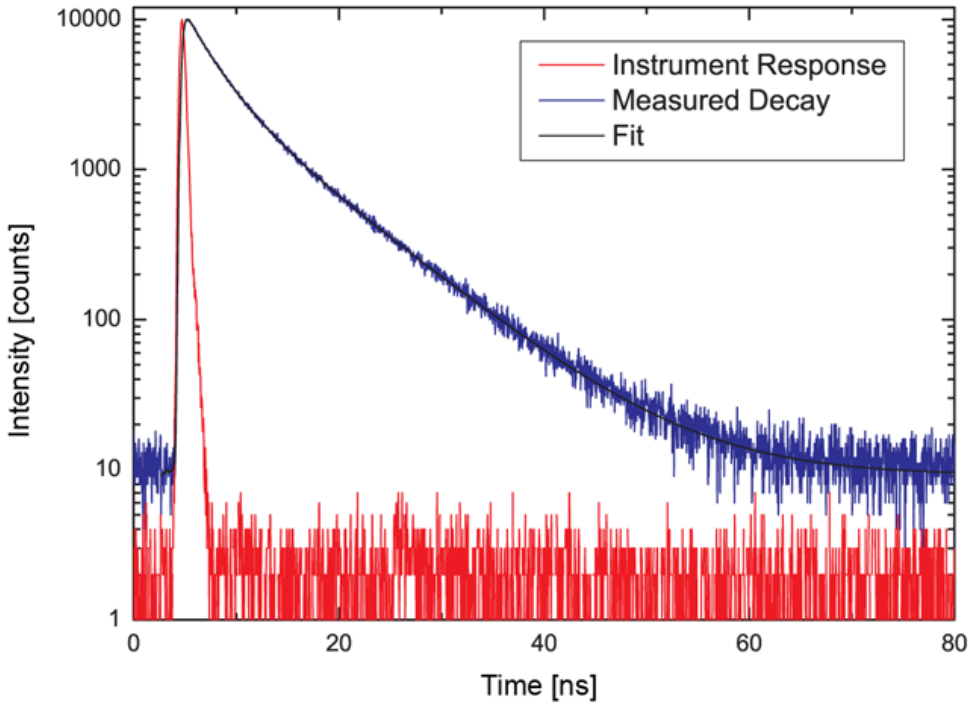

Figure 4.6 Example of a fluorescence decay curve. The plot shows the instrument response function (red line), the measured decay (blue line) and the exponential fit used to extract the fluorescence lifetime (black line). Picture reproduced from [38].

Two methods of measuring time-resolved fluorescence are in widespread use: the time-domain and frequency-domain methods [39].

In the time-domain method, also known as pulsed method, the sample is excited by a short light pulse and the subsequent decay in fluorescence intensity is recorded as a function of time [23, 37]. A widely adopted approach for time-domain lifetime measurements is Time-Correlated Single Photon Counting (TCSPC) which is based on the statistical analysis of time intervals between excitation events and the arrival of individual fluorescence photons. TCSPC relies on the repetitive excitation of the sample using a pulsed light source emitting light pulses with well-defined timing and short durations. Each excitation pulse triggers a timing sequence (*start* signal),

which is subsequently stopped upon detection of a single emitted photon (*stop* signal). The operating principle of TCSPC is illustrated in Figure 4.7. For each excitation pulse, the system records the time delay between the excitation event and the detection of a single emitted photon and assigned to a discrete time bin of fixed width (Δt), incrementing the corresponding bin counter. Repeating this excitation-detection process many times, typically until a total of 10000 counts is accumulated in the peak channel, allows the construction of a histogram where the number of counts per bin reflects the frequency of photon arrivals at specific time delays after excitation. The resulting histogram is a high-resolution representation of the fluorescence decay curve, showing the probability distribution of photon arrival times and thus the excited-state dynamics of the fluorophore [23, 40].

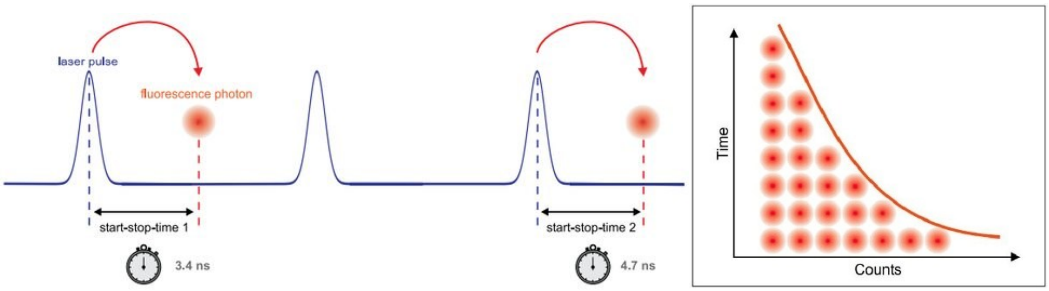

Figure 4.7 Schematic representation of the Time-Correlated Single Photon Counting (TCSPC) method. For each excitation pulse, the system measures the time delay between excitation (start) and detection of a single fluorescence photon (stop), progressively building the decay histogram. Picture reproduced from [38].

The final decay curve obtained from the histogram follows an exponential (or multi-exponential) function depending on the complexity of the system. When the decay is single exponential and the fluorescence lifetime is significantly longer than the excitation pulse width, the lifetime can be estimated directly from the slope of the decay curve on a semi-logarithmic plot [41].

Alternative approach is provided by the frequency-domain method, in which the excitation light is sinusoidally modulated in intensity at high frequencies, and the emitted fluorescence is analyzed in terms of phase shift (φ) and demodulation relative to the excitation signal [23, 37].

These two parameters are mathematically related to the fluorescence lifetime respect the following equations:

$$\tan(\varphi) = \omega\tau \qquad \text{Eq. 10}$$

$$M = (1 + \omega^2\tau^2)^{-1/2} \qquad \text{Eq. 11}$$

where ω is the angular modulation frequency and M is the modulation ratio. The degree of modulation and the phase shift provide independent and complementary information about the decay kinetics, and lifetime values can be extracted with high precision.

Surface Plasmon Resonance

Surface plasmon resonance is an optical phenomenon that arises at the interface between a thin metal film, typical gold, and a dielectric medium when the surface is illuminated by polarized light under total internal reflection conditions. At a specific angle of incidence, known as the resonance angle, the momentum of the incident photons matches that of the surface plasmons, which are collective oscillations of free electrons at the metal-dielectric interface. Under this resonance condition, part of the light energy is transferred to the surface plasmons, resulting in a sharp decrease in the intensity of the reflected light [42].

In particular, at resonance, the momentum of the incident photons matches that of the surface plasmon wave propagating along the metal-dielectric interface. The propagation constant β of this wave depends on the dielectric properties of the two media and is given by:

$$\beta = \frac{\omega}{c}\sqrt{\frac{\varepsilon_M \varepsilon_D}{\varepsilon_M + \varepsilon_D}} \qquad \text{Eq. 12}$$

where ω is the angular frequency, c is the speed of light in vacuum, and ε_D and ε_M are dielectric functions of the dielectric and metal, respectively [42, 44]. Since for dielectrics $\varepsilon_D = n_D^2$, the propagation constant β, and thus the resonance condition, depends directly on the refractive index n_D of the medium in contact with the metal. Consequently, any change in n_D, such as that caused by molecular adsorption or binding near the metal surface, shifts the resonance angle or wavelength. This sensitivity to refractive index variations forms the basis of SPR-based sensing in which any local variation in the refractive index, induced, for instance, by molecular binding, modifies the resonance conditions, thereby modulating the SPR signal (Figure 4.8) [44, 45].

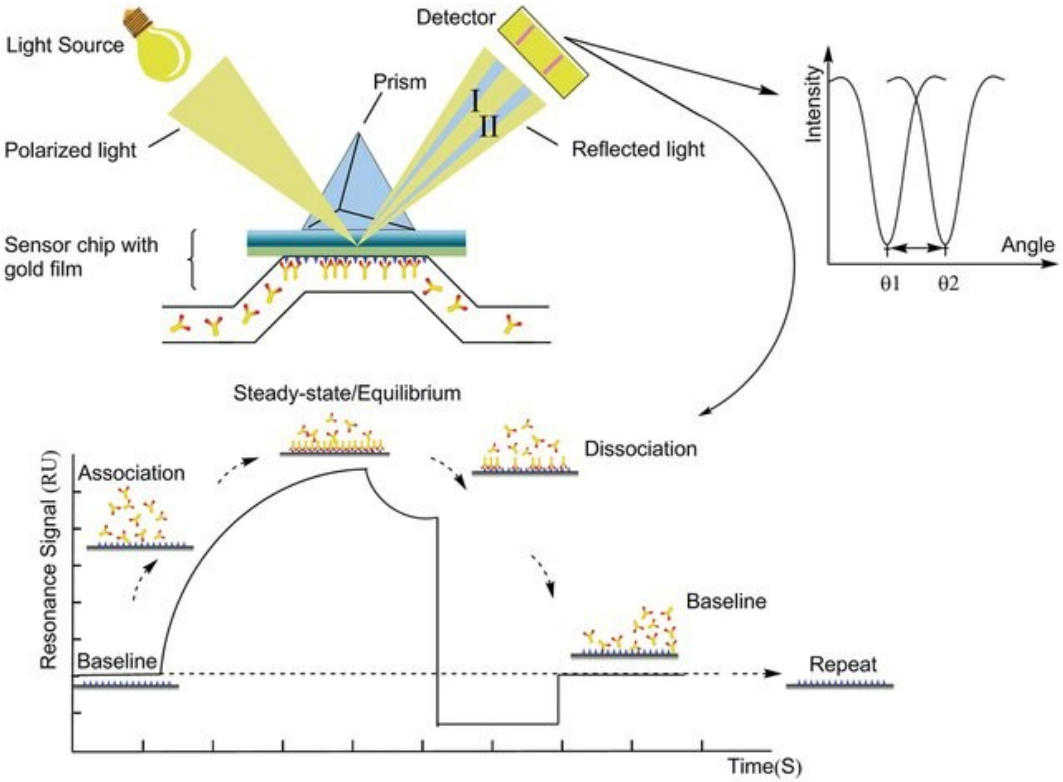

Figure 4.8 The schematic illustration of SPR-sensor system. SPR detects changes in the refractive index in the immediate vicinity of the surface layer of a sensor chip. Picture reproduced from [46].

The most common configuration employed in commercial SPR instruments is the Kretschmann configuration (Figure 4.9a). It consists of a prism, a thin metal film (typically 40-50 nm of gold) deposited on a glass substrate, and a dielectric medium (usually the sample solution) in contact with the metal surface. A polarized monochromatic light beam, often from a laser or LED source, is directed through the prism and reflected at the metal-dielectric interface under total internal reflection conditions. When the incidence angle satisfies the resonance condition, part of the incident light energy is absorbed to excite the surface plasmons, leading to a sharp dip in the reflected intensity, which is recorded by a photodetector [44, 45]. An alternative approach is represented by waveguide-based systems (Figure 4.9b), in which the light is guided through an optical waveguide coated with a thin metallic layer. When the guided light propagates in the region adjacent to the metal film, its evanescent field penetrates through the metal and excites a surface plasmon at the outer interface. This configuration is particularly

attractive for integrated optics and lab-on-chip platforms, as it allows for compact, planar architectures compatible with miniaturized devices [45, 47]. A further variation is the grating-coupled SPR configuration (Figure 4.9c), where the metal surface is periodically patterned to form a diffraction grating. The grating provides an additional momentum required to match the wavevector of the incident photons with that of the surface plasmons, thereby enabling their excitation even without total internal reflection. This method also offers spectral tunability, as the resonance condition can be controlled by adjusting the grating period or angle of incidence [45].

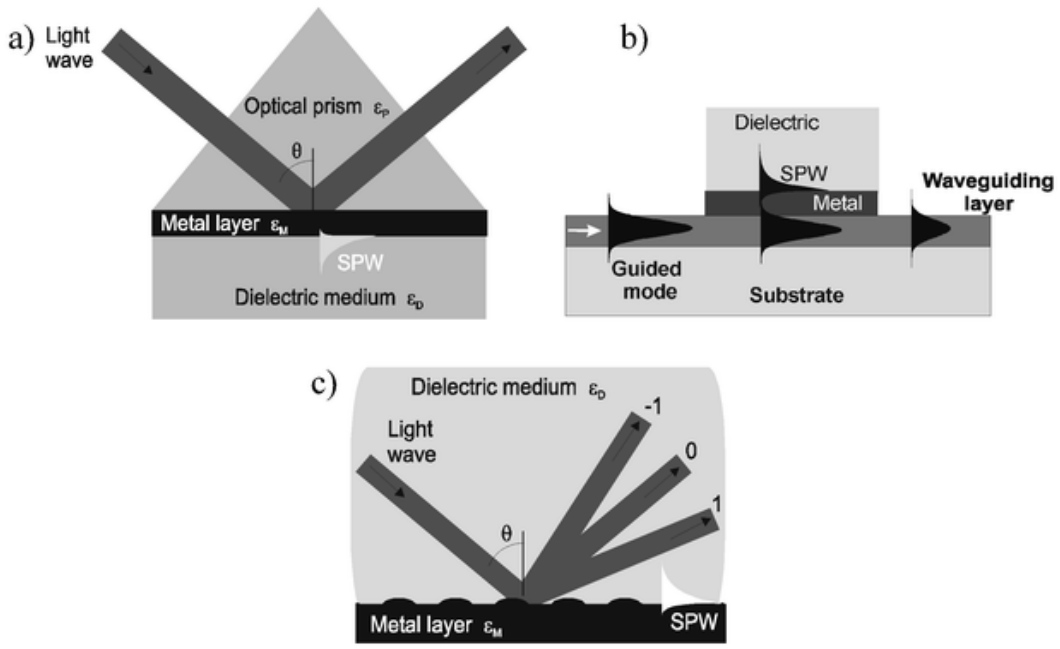

Figure 4.9 Excitation of surface plasmon-polaritons: (a) by a light beam via prism coupling, (b) by a guided mode of optical waveguide, and (c) by light diffraction on a diffraction grating. Picture reproduced from [45].

A further class of SPR architectures is represented by optical fiber-based coupling systems, which exploit optical fibers as light-guiding elements (Figure 4.10). In this approach, light propagates through the fiber by total internal reflection and appropriate modifications of the fiber allow interaction between the guided light and the plasmonic structure [48].

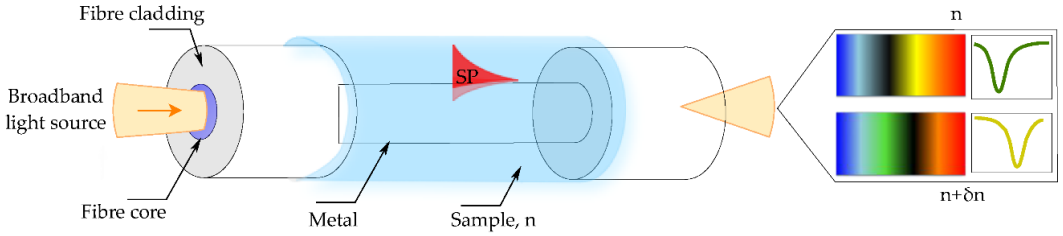

Figure 4.10 Fiber-based SPR sensor. Picture reproduced from [48].

The fiber can be modified according to different geometries to enable efficient coupling between the guided light and the surface plasmon mode (Figure 4.11). Among the most investigated geometries are tapered fiber [49], in which the fiber is stretched reducing the core diameter, D-shaped fiber [50], in which a portion of the cladding and core is removed to expose a flat surface for metal deposition, and U-shaped fiber, where the cladding is stripped in the curved region of the fiber, in which the cladding is removed in the curved region to enable plasmonic interactions [51].

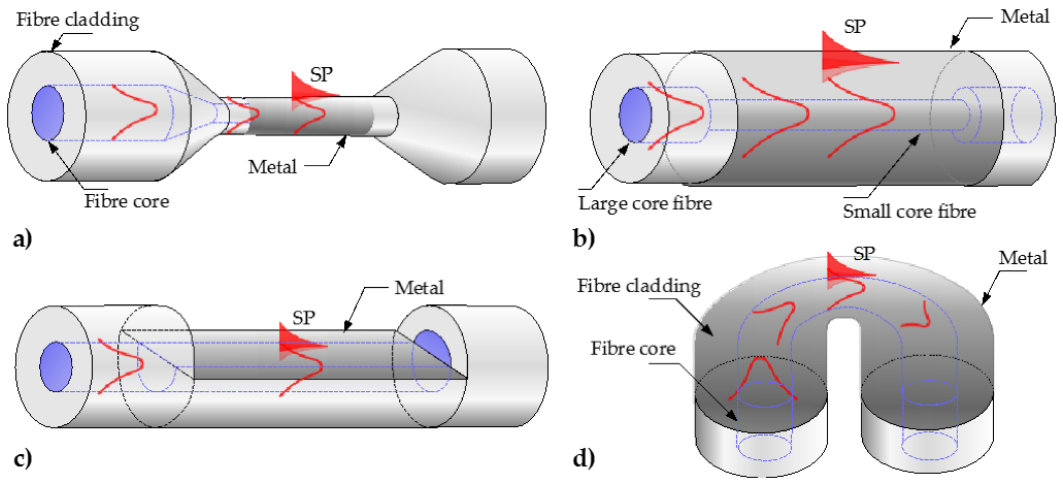

Figure 4.11 Schematics of geometry-modified optical fiber SPR sensors: (a) Tapered fiber SPR probe; (b) Hetero-core structure; (c) D-shaped SPR probe; (d) U-shaped SPR probe. Picture reproduced from [48].

Electrochemical transduction methods

Electrochemical transduction techniques rely on the detection of electrical signals (such as current, potential, conductance or impedance) generated by redox reactions or ionic transport phenomena. Typically, an electrochemical system consists of three electrodes, a working, a reference and a counter electrode (Figure 4.12), immersed in an electrolyte solution [52].

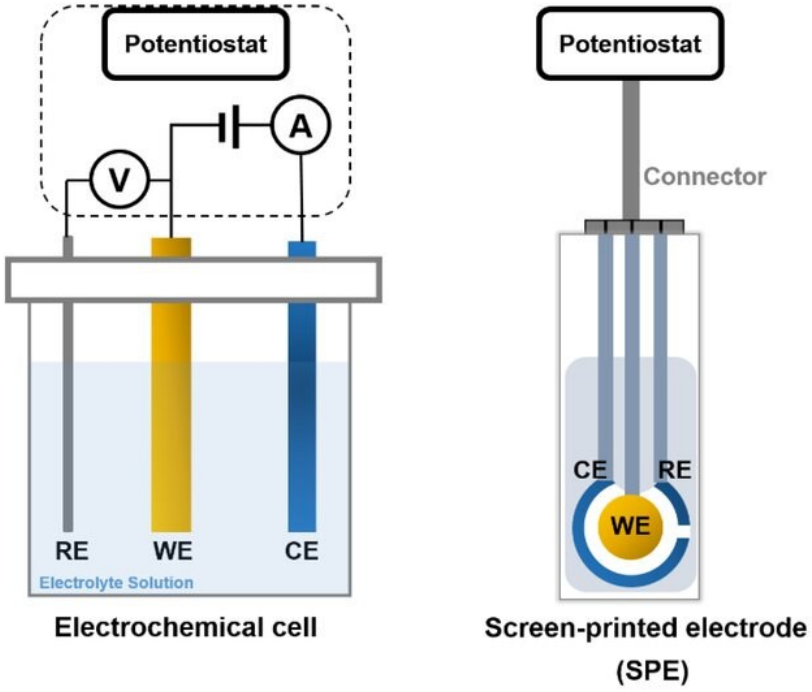

Figure 4.12 Electrochemical sensors with three electrodes: reference (RE), working (WE), and counter (CE) connected to a potentiostat. Picture reproduced from [53].

The working electrode (WE) is the core component of the system and serves as the site where the redox processes occur. Typical WE materials include noble metals (e.g., platinum or gold), carbon-based materials (e.g., graphite, glassy carbon) and semiconductors (e.g., silicon). The reference electrode (RE) provides a stable and well-defined potential against which the potential of the working electrode is measured. Among the most commonly used are those made from silver/silver chloride (Ag/AgCl) electrodes. The counter electrode (CE), usually fabricated from platinum, gold or carbon, completes the electrical circuit by allowing the flow of

electrons necessary to balance the current generated at the working electrode. Although it does not directly participate in the redox reaction, it ensures electrical neutrality and supports current flow during the electrochemical process [54, 55].

The proper functioning of an electrochemical system depends not only on the electrode configuration but also on the electrolyte solution, which provides the ionic environment necessary for charge transport. Normally, to ensure ion conduction between electrodes, the electrolyte contains redox-active species, commonly referred to as mediators, that act as artificial electron shuttles and enhance electron-transfer efficiency [55]. An ideal mediator should display fast and reversible redox kinetics at the electrode surface, allowing multiple oxidation-reduction cycles without degradation. It should also be electrochemically regenerated at low overpotentials, ensuring low energy consumption and stable operation under mild conditions. Furthermore, both its oxidized and reduced forms must remain chemically and electrochemically stable throughout the experiment. Among inorganic mediators, the ferri/ferrocyanide redox couple ($[Fe(CN)_6]^{3-}$ / $[Fe(CN)_6]^{4-}$) is widely used due to its reversible redox behaviour, low toxicity and commercial availability. Other common mediators include organic compounds such as quinones, viologens, and phenazines, as well as metal complexes based on ruthenium or osmium bipyridine derivatives [56].

Electrochemical transduction methods can be classified according to the nature of the electrical process being monitored. Broadly, they can be divided into two main categories [57]:

A) Conductometric techniques, which measure the transport properties of ions in the bulk solution. These methods rely on the variation of the electrical conductivity or resistance of the electrolyte and are mainly used to monitor changes in ionic concentration, mobility or total ionic strength.

B) Interfacial charge-transfer techniques, which monitor redox or capacitive processes occurring at the electrode-electrolyte interface.

These can be further subdivided into:

1. Static methods are carried out under conditions where no net current flows in the system and the measurable signal is the potential difference between electrodes (i.e. potentiometry).

2. Dynamic methods involve the application of an external potential or current to the working electrode, which perturbs the system from equilibrium, inducing electron transfer processes at the electrode surface which generate measurable responses such as current variations or changes in impedance (i.e. voltammetry, amperometry and impedimetric).

In the following sections, particular attention will be dedicated to cyclic voltammetry and electrochemical impedance spectroscopy.

Cyclic Voltammetry

Cyclic voltammetry (CV) is a voltammetric technique used for investigating redox processes and interfacial charge-transfer phenomena. In this method, the potential applied to the working electrode is varied linearly from an initial value (V_i) to a final value (V_f) and subsequently reversed back to the V_i, generating a characteristic symmetrical triangular waveform (Figure 4.13) [58].

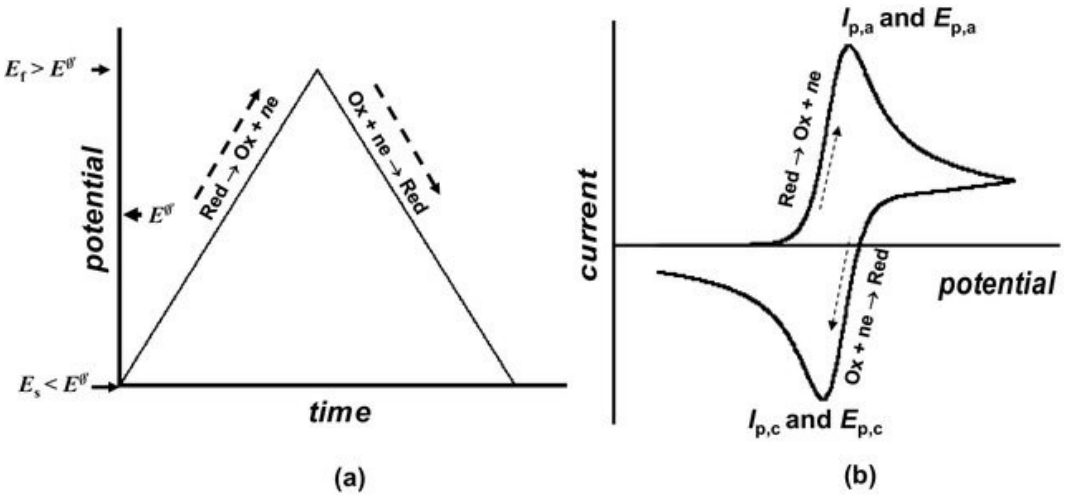

Figure 4.13 Typical potential variation and the shape of the I-E curve. Picture reproduced from [59].

As the potential is modulated, redox-active species located near the electrode surface undergo electron transfer reactions, leading to the appearance of typical anodic or cathodic current peaks. The resulting plot, known as a voltammogram, typically displays the current (i) as a function of applied potential (E). The shape, position, and intensity of these peaks provide critical insights into the redox

behaviour of the molecules, including their formal potential, the reversibility of the redox process, electron transfer kinetics and diffusion coefficients [52].

In a reversible system, the potential at which oxidation or reduction occurs follows the Nernst equation:

$$E = E_0 + \frac{RT}{nF} ln\left(\frac{[Ox]}{[Red]}\right) \quad \text{Eq. 13}$$

where E_0 is the formal potential, n is the number of electrons transferred, and $[Ox]/[Red]$ is the concentration ratio of oxidized and reduced species at the electrode interface. While this equation governs the thermodynamic position of redox transitions, the magnitude of the peak current in CV is primarily governed by the mass transport of electroactive species, and is quantitatively described by the Randles-Ševčík equation:

$$i_p = (2.69 \cdot 10^5) n^{3/2} A C D^{1/2} v^{1/2} \quad \text{Eq. 14}$$

where, i_p is the peak current (in A), A is the electrode area (cm^2), C the bulk concentration of the analyte (mol/cm^3), D the diffusion coefficient (cm^2/s), and v the scan rate (V/s). This relationship highlights that, under diffusion-controlled conditions, the peak current increases linearly with the square root of the scan rate. Conversely, a linear dependence of i_p on v indicates an adsorption-controlled process [59]. The scan rate is a critical factor, since the duration of a scan must provide sufficient time to allow for a meaningful chemical reaction to occur. Modulating the scan rate alters the temporal resolution of the measurement: slower scan rates favour the observation of slow chemical transformations that follow the redox event, while faster scan rates can kinetically isolate the electron transfer step, suppressing chemical reactions [55, 60]. Despite its versatility and ease of implementation, CV presents both strengths and limitations that should be carefully considered in analytical applications. In fact, CV is generally considered less sensitive compared to more advanced voltammetric techniques such as differential pulse voltammetry (DPV) or square wave voltammetry (SWV). As such, CV is primarily employed for qualitative assessments rather than quantitative determinations, especially during early-stage studies and in the characterization of electrode surfaces [55].

Electrochemical Impedance Spectroscopy

Electrochemical Impedance Spectroscopy (EIS) is a powerful and non-destructive electrochemical technique that provides detailed information on the kinetic and transport processes occurring at the electrode–electrolyte interface. EIS is based on the perturbation of a system at equilibrium through the application of a small-amplitude sinusoidal excitation signal, either a *ac* voltage or a *ac* current, over a broad range of frequencies. The resulting current (or voltage) response of the system is measured, and from this, the impedance Z is determined as a function of the angular frequency ω [61]. Mathematically, impedance $Z(\omega)$ is defined according to the generalized Ohm's law as:

$$Z(\omega) = \frac{U(\omega)}{I(\omega)} = |Z(\omega)|e^{j\theta} \qquad \text{Eq. 15}$$

Where $U(\omega)$ and $I(\omega)$ are the frequency-dependent complex voltage and current, respectively, $U|(\omega)|$ is the magnitude of the impedance, θ is the phase shift between the voltage and current, and j is the imaginary unit ($j^2 = -1$) [62]. The impedance, which consists of both a real component (resistance) and an imaginary component (reactance), provides critical insight into the electrochemical and physicochemical processes occurring at the electrode-electrolyte interface. This complex quantity captures not only the magnitude of the impedance but also the phase shift θ between the applied sinusoidal signal and the resulting current response, offering a comprehensive description of the system's dynamic behaviour across a wide frequency range [63].

The impedance spectrum is commonly represented using a Nyquist plot (Figure 4.14), which displays the imaginary component (Z'') versus the real component (Z'). In this two-dimensional complex plane, each point corresponds to the impedance measured at a specific frequency. The vector length from the origin to any given point represents the modulus $|Z|$ while the angle between the vector and the real axis corresponds to the phase shift θ, providing information about the capacitive or inductive nature of the system's response. In many electrochemical systems, the Nyquist plot typically exhibits a semicircular shape in the high-to-mid-frequency range, often followed by a linear tail at lower frequencies. The diameter

of the semicircle is associated with the charge transfer resistance (Rct), which is sensitive to interfacial processes such as molecular recognition or binding events [61].

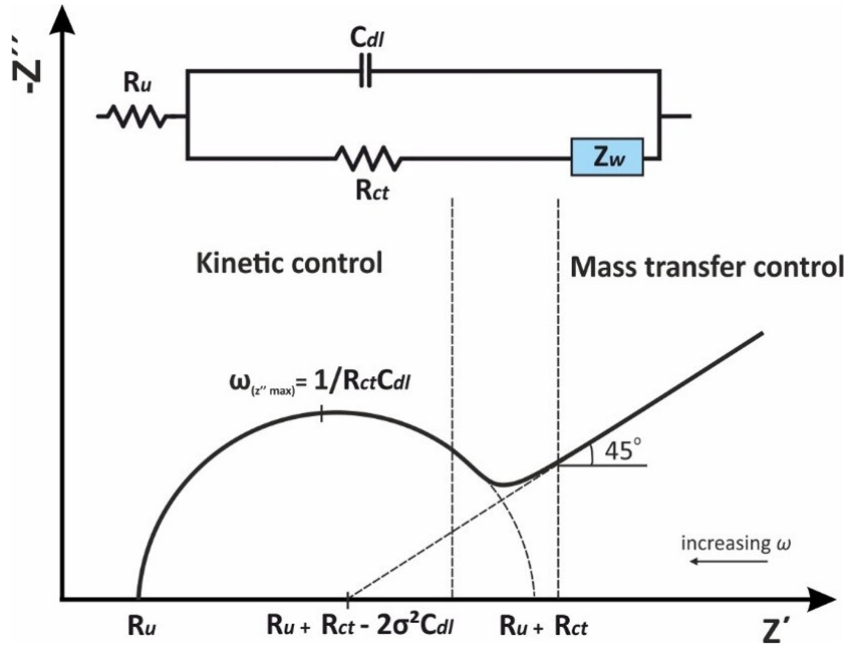

Figure 4.14 Nyquist plot and Randles equivalent electrical circuit over a wide frequency range. Picture reproduced from [61].

The impedance response can also be visualized through a Bode plot, in which both the magnitude $Z|(\omega)|$ and the phase angle θ are plotted as functions of the logarithm of frequency. The Bode representation offers a complementary perspective, particularly useful for identifying characteristic time constants and evaluating the frequency-dependent behaviour of the system [61].

The experimental data are typically interpreted using an equivalent electrical circuit model, in which each element represents a specific electrical component, such as resistors, capacitors and inductors [62]. A commonly used equivalent electrical circuit is the Randles circuit (Figure 4.11), which consists of the solution resistance (Rs) in series with a parallel combination of a double-layer capacitance (Cdl) and a Rct. In cases where mass transport limitations are significant, a Warburg element (Zw) accounting for diffusion processes is also included [64]. In the context of electrochemical sensors, EIS offers several advantages, foremost among them being its ability to provide label-free and highly sensitive detection of interfacial events.

The technique is non-destructive and operates under mild perturbation conditions, allowing real-time in situ monitoring of electrochemical systems without significantly disturbing their native state. All these characteristics make EIS an indispensable transduction technique for the qualitative and quantitative characterization of sensor interfaces and electrochemical systems [65, 66].

References

[1] Berne, B. J., & Pecora, R. (2000). *Dynamic light scattering: with applications to chemistry, biology, and physics*. Courier Corporation.

[2] Hassan, P. A., Rana, S., & Verma, G. (2015). Making sense of Brownian motion: colloid characterization by dynamic light scattering. *Langmuir*, *31*(1), 3-12.

[3] Technical Committee ISO/TC 24, Particle characterization including sieving. Subcommittee SC 4, Particle characterization. (2017). *Particle Size Analysis: Dynamic Light Scattering (DLS)*. ISO.

[4] Lavalette, D., Hink, M. A., Tourbez, M., Tétreau, C., & Visser, A. J. (2006). Proteins as micro viscosimeters: Brownian motion revisited. *European Biophysics Journal*, *35*(6), 517-522.

[5] Pusey, P. N. (1974). Macromolecular diffusion. In *Photon correlation and light beating spectroscopy* (pp. 387-428). Boston, MA: Springer US.

[6] Choudhary, R. C., Kumaraswamy, R. V., Kumari, S., Pal, A., Raliya, R., Biswas, P., & Saharan, V. (2017). Synthesis, characterization, and application of chitosan nanomaterials loaded with zinc and copper for plant growth and protection. In *Nanotechnology: an agricultural paradigm* (pp. 227-247). Singapore: Springer Singapore.

[7] Misono, T. (2019). Dynamic light scattering (DLS). In *Measurement techniques and practices of colloid and interface phenomena* (pp. 65-69). Singapore: Springer Singapore.

[8] Malvern Instruments Ltd (2004). *Zetasizer Nano Series: User manual*, England.

[9] Maguire, C. M., Rösslein, M., Wick, P., & Prina-Mello, A. (2018). Characterisation of particles in solution–a perspective on light scattering and comparative technologies. *Science and technology of advanced materials*, *19*(1), 732-745.

[10] Stetefeld, J., McKenna, S. A., & Patel, T. R. (2016). Dynamic light scattering: a practical guide and applications in biomedical sciences. *Biophysical reviews*, *8*(4), 409-427.

[11] Song, C., Zhang, S., & Huang, H. (2015). Choosing a suitable method for the identification of replication origins in microbial genomes. *Frontiers in microbiology*, *6*, 1049.

[12] Wiseman, T., Williston, S., Brandts, J. F., & Lin, L. N. (1989). Rapid measurement of binding constants and heats of binding using a new titration calorimeter. *Analytical biochemistry*, *179*(1), 131-137.

[13] Freire, E., Mayorga, O. L., & Straume, M. (1990). Isothermal titration calorimetry. *Analytical chemistry*, *62*(18), 950A-959A.

[14] Saponaro, A. (2018). Isothermal titration calorimetry: a biophysical method to characterize the interaction between label-free biomolecules in solution. *Bio-protocol*, *8*(15), e2957-e2957.

[15] Pierce, M. M., Raman, C. S., & Nall, B. T. (1999). Isothermal titration calorimetry of protein–protein interactions. *Methods*, *19*(2), 213-221.

[16] Turnbull, W. B., & Daranas, A. H. (2003). On the value of c: can low affinity systems be studied by isothermal titration calorimetry?. *Journal of the American Chemical Society*, *125*(48), 14859-14866.

[17] Sevilla III, F., & Narayanaswamy, R. (2003). Optical chemical sensors and biosensors. In *Comprehensive Analytical Chemistry* (Vol. 39, pp. 413-435). Elsevier.

[18] Wolfbeis, O. S. (2005). Materials for fluorescence-based optical chemical sensors. *Journal of Materials Chemistry*, *15*(27-28), 2657-2669.

[19] Narayanaswamy, R. (1993). Tutorial review—Optical chemical sensors: transduction and signal processing. *Analyst*, *118*(4), 317-322.

[20] Nilapwar, S. M., Nardelli, M., Westerhoff, H. V., & Verma, M. (2011). Absorption spectroscopy. In *Methods in enzymology* (Vol. 500, pp. 59-75). Academic Press.

[21] Valeur, B., & Berberan-Santos, M. N. (2013). *Molecular fluorescence: principles and applications*. John Wiley & Sons.

[22] Lekner, J. (2013). *Theory of reflection of electromagnetic and particle waves* (Vol. 3). Springer Science & Business Media.

[23] Lakowicz, J. R. (Ed.). (2006). *Principles of fluorescence spectroscopy*. Boston, MA: springer US.

[24] Jabłoński, A. (1935). Über den mechanismus der photolumineszenz von farbstoffphosphoren. *Zeitschrift für Physik*, *94*(1), 38-46.

[25] Schweizer, T., Kubach, H., & Koch, T. (2021). Investigations to characterize the interactions of light radiation, engine operating media and fluorescence tracers for the use of qualitative light-induced fluorescence in engine systems. *Automotive and engine technology*, *6*(3), 275-287.

[26] Moggi, L., Juris, A., & Gandolfi, M. T. (2006). Manuale del Fotochimico-Tecniche e Medodologie.

[27] Schulman, S. G. (2017). *Fluorescence and phosphorescence spectroscopy: physicochemical principles and practice*. Elsevier.

[28] Chroma Technology Corp. (2025). *Fluorochrome spectra*. US.

[29] Zacharioudaki, D. E., Fitilis, I., & Kotti, M. (2022). Review of fluorescence spectroscopy in environmental quality applications. *Molecules*, *27*(15), 4801.

[30] Baker, A. (2005). Thermal fluorescence quenching properties of dissolved organic matter. *Water research*, *39*(18), 4405-4412.

[31] Ghosh, K., & Schnitzer, M. (1980). Macromolecular structures of humic substances. *Soil science*, *129*(5), 266-276.

[32] Mikalauskaite, K., Ziaunys, M., Sneideris, T., & Smirnovas, V. (2020). Effect of ionic strength on thioflavin-T affinity to amyloid fibrils and its fluorescence intensity. *International Journal of Molecular Sciences*, *21*(23), 8916.

[33] Gemeda, F. T. (2017). A review on effect of solvents on fluorescent spectra. *Chem. Sci. Int. J*, *18*, 1-12.

[34] Medintz, I. L., & Hildebrandt, N. (Eds.). (2013). *FRET-Förster resonance energy transfer: from theory to applications*. John Wiley & Sons.

[35] De Silva, A. P., Gunaratne, H. N., Gunnlaugsson, T., Huxley, A. J., McCoy, C. P., Rademacher, J. T., & Rice, T. E. (1997). Signaling recognition events with fluorescent sensors and switches. *Chemical reviews*, *97*(5), 1515-1566.

[36] Hercules, D. M. (1966). Fluorescence and phosphorescence analysis: principles and applications. *Fluorescence and Phosphorescence Analysis: Principles and Applications/Ed. David M. Hercules. New York*.

[37] Berezin, M. Y., & Achilefu, S. (2010). Fluorescence lifetime measurements and biological imaging. *Chemical reviews*, *110*(5), 2641-2684.

[38] PicoQuant GmbH. (n.d.). *Time-resolved fluorescence: Life science applications*. Germany.

[39] Jones, C., Mulloy, B., & Thomas, A. H. (2008). *Microscopy, optical spectroscopy, and macroscopic techniques* (Vol. 22). Springer Science & Business Media.

[40] O'Connor, D. (2012). *Time-correlated single photon counting*. Academic press.

[41] O'Connor, D. V., Ware, W. R., & Andre, J. C. (1979). Deconvolution of fluorescence decay curves. A critical comparison of techniques. *Journal of Physical Chemistry*, *83*(10), 1333-1343.

[42] Otto, A. (1968). Excitation of nonradiative surface plasma waves in silver by the method of frustrated total reflection. *Zeitschrift für Physik A Hadrons and nuclei*, *216*(4), 398-410.

[43] Raether, H. (2006). Surface plasmons on gratings. In *Surface plasmons on smooth and rough surfaces and on gratings* (pp. 91-116). Berlin, Heidelberg: Springer Berlin Heidelberg.

[44] Kumari, A., Yadav, A., Singh, O. P., & Sharan, P. (2024). A review of surface plasmon resonance (SPR) technology in biosensing: innovations, applications and future trends. *Journal of Optics*, 1-9.

[45] Homola, J. (2003). Present and future of surface plasmon resonance biosensors. *Analytical and bioanalytical chemistry*, *377*(3), 528-539.

[46] Song, C., Zhang, S., & Huang, H. (2015). Choosing a suitable method for the identification of replication origins in microbial genomes. *Frontiers in microbiology*, *6*, 1049.

[47] Homola, J., Čtyroký, J., Skalský, M., Hradilova, J., & Kolářová, P. (1997). A surface plasmon resonance based integrated optical sensor. *Sensors and Actuators B: Chemical*, *39*(1-3), 286-290.

[48] Klantsataya, E., Jia, P., Ebendorff-Heidepriem, H., Monro, T. M., & François, A. (2016). Plasmonic fiber optic refractometric sensors: From conventional architectures to recent design trends. *Sensors*, *17*(1), 12.

[49] Caucheteur, C., Guo, T., & Albert, J. (2015). Review of plasmonic fiber optic biochemical sensors: improving the limit of detection. *Analytical and bioanalytical chemistry*, *407*(14), 3883-3897.

[50] Yu, H., Chong, Y., Zhang, P., Ma, J., & Li, D. (2020). A D-shaped fiber SPR sensor with a composite nanostructure of MoS2-graphene for glucose detection. *Talanta*, *219*, 121324.

[51] Shukla, G. M., Punjabi, N., Kundu, T., & Mukherji, S. (2019). Optimization of plasmonic U-shaped optical fiber sensor for mercury ions detection using glucose capped silver nanoparticles. *IEEE sensors journal*, *19*(9), 3224-3231.

[52] Grieshaber, D., MacKenzie, R., Vörös, J., & Reimhult, E. (2008). Electrochemical biosensors-sensor principles and architectures. *Sensors*, *8*(3), 1400-1458.

[53] Damiati, S., & Schuster, B. (2020). Electrochemical biosensors based on S-layer proteins. *Sensors*, *20*(6), 1721.

[54] Baranwal, J., Barse, B., Gatto, G., Broncova, G., & Kumar, A. (2022). Electrochemical sensors and their applications: A review. *Chemosensors*, *10*(9), 363.

[55] Bard, A. J., Faulkner, L. R., & White, H. S. (2022). *Electrochemical methods: fundamentals and applications*. John Wiley & Sons.

[56] Chaubey, A., & Malhotra, B. (2002). Mediated biosensors. *Biosensors and bioelectronics*, *17*(6-7), 441-456.

[57] Shanbhag, M. M., Manasa, G., Mascarenhas, R. J., Mondal, K., & Shetti, N. P. (2023). Fundamentals of bio-electrochemical sensing. *Chemical Engineering Journal Advances*, *16*, 100516.

[58] Kissinger, P. T., & Heineman, W. R. (1983). Cyclic voltammetry. *Journal of chemical education*, *60*(9), 702.

[59] Mirceski, V., Skrzypek, S., & Stojanov, L. (2018). Square-wave voltammetry. *ChemTexts*, *4*(4), 17.

[60] Savéant, J. M. (2006). Coupling of electrode electron transfers with homogeneous chemical reactions. *Elements of Molecular and Biomolecular Electrochemistry*, 78-181.

[61] Lazanas, A. C., & Prodromidis, M. I. (2023). Electrochemical impedance spectroscopy─ a tutorial. *ACS measurement science au*, *3*(3), 162-193.

[62] Lasia, A. (2002). Electrochemical impedance spectroscopy and its applications. In *Modern aspects of electrochemistry* (pp. 143-248). Boston, MA: Springer US.

[63] Orazem, M. E., & Tribollet, B. (2008). Electrochemical impedance spectroscopy. *New Jersey*, *1*(906), 383-389.

[64] Randles, J. E. B. (1947). Kinetics of rapid electrode reactions. *Discussions of the faraday society*, *1*, 11-19.

[65] Park, S. M., & Yoo, J. S. (2003). Peer reviewed: electrochemical impedance spectroscopy for better electrochemical measurements.

[66] Magar, H. S., Hassan, R. Y., & Mulchandani, A. (2021). Electrochemical impedance spectroscopy (EIS): Principles, construction, and biosensing applications. *Sensors*, *21*(19), 6578.

Scope of the thesis

The aim of this PhD thesis was to exploit the potential of MIPs for the development of highly sensitive and selective sensors. MIPs, due to their intrinsic molecular recognition capability, chemical stability and cost-effectiveness, represent promising alternatives to biological receptors. The primary objective of this work was to design and synthesize MIP-based sensors with enhanced sensitivity, capable of detecting extremely low analyte concentrations across various application fields, including food safety and control, environmental monitoring and medical diagnostics.

To reach this goal, several strategies were implemented and experimentally validated through the research studies and publications included in this thesis. Each study represents a specific approach aimed at improving the sensor performance, mainly by optimizing the synthesis of the MIP materials and by tailoring their integration with suitable optical or electrochemical transduction methods.

One of the strategies pursued in this thesis focused on controlling the morphology and dimensions of the MIPs to obtain nanostructured spherical materials with high surface area and improved diffusion kinetics, thereby increasing the accessibility of the recognition sites. In addition to tuning MIP size and morphology, further work was carried out to introduce additional functionalities into the MIP nanostructures, in particular, fluorescent features aimed at enabling optical detection. Within this framework, the strategy focused on modulating the fluorescence properties of the MIPs by optimizing the ratio between the fluorescent probe and the template molecule, in order to achieve an efficient and stable signal response.

Building on this optical design, the work further explored the potential of time-resolved fluorescence spectroscopy, introducing fluorescence lifetime measurements as a transduction method for nanoMIP-based sensors. Although rarely applied to MIP technology, this approach proved particularly suitable for developing ultra-sensitive detection.

Another key aspect of this PhD thesis was the evaluation how the quality and homogeneity of the binding sites influence the sensing response. The study aimed to verify whether improving the uniformity of the recognition sites within the MIP structure could effectively enhance the sensor's sensitivity. To this end, different MIP architectures were compared, from conventional imprinted polymer layers to conductive matrices incorporating nanoMIPs, confirming that the development of more homogeneous binding sites leads to a more efficient and reproducible signal, ultimately improving the overall sensor performance.

The work also explored the design of stimuli-responsive hydrogel and nanogel MIPs, capable of undergoing shrinking or swelling upon analyte binding. This deformable behaviour was exploited as a mean to amplify the transduction signal, particularly in plasmonic configurations.

Finally, special emphasis was placed on the use of green and sustainable monomers for the synthesis of nanoMIPs. An innovative green monomer was used with the aim to prepare homogeneous and stable “green” nanoMIPs, combining environmental sustainability with selective recognition. The resulting nanoMIPs were tested using different transduction approaches to assess their versatility across sensing platforms.

Chapter V – Scientific Contributions

Paper I

Time-Resolved Fluorescence Spectroscopy of Molecularly Imprinted Nanoprobes as an Ultralow Detection Nanosensing Tool for Protein Contaminants

Summary

This work focuses on the development of fluorescent molecularly imprinted polymer nanoparticles (Fluo-nanoMIPs) designed to act as synthetic recognition elements in optical sensing systems for ultralow detection of protein contaminants, using human serum albumin (HSA) as a proof-of-concept, through time-resolved fluorescence spectroscopy.

The Fluo-nanoMIPs were synthesized using fluorescein O-methacrylate (FluorMAA) as a fluorescent reporter co-monomer and HSA as the template protein. To investigate how the amount of incorporated fluorophore influences the optical properties and sensing performance, the synthesis was optimized by varying the molar ratio between the FluorMAA and the template molecule. Specifically, three different formulations were prepared by incorporating 1.3, 13, or 130 nmol of FluorMAA per 15 nmol of HSA, corresponding to approximate molar ratios of 1:0.1, 1:1, and 1:10 (template:fluorescent monomer). The resulting Fluo-nanoMIPs, called 0.1×, 1× and 10×, were spherical and monodisperse, with an average hydrodynamic diameter of about 120 nm and a low PDI, indicating a homogeneous size distribution, as confirmed by DLS, Scanning Electron Microscopy (SEM) and Atomic Force Microscopy (AFM) analyses.

The functional characterization of the Fluo-nanoMIPs was carried out using steady-state fluorescence spectroscopy by titrating the nanoparticle suspension with increasing concentrations of the HSA. The fluorescence intensity was monitored to evaluate how the incorporated amount of fluorophore influences the optical response upon protein binding. For the 0.1× and 1× formulations, a clear decrease in fluorescence intensity was observed upon analyte addition, indicating a quenching effect associated with the interaction between the Fluo-nanoMIPs and

the target protein. In contrast, the fluorescence signal of the 10× formulation displayed a lower initial fluorescence intensity compared to the other samples, and its signal remained essentially unchanged upon binding to HSA. These findings supported the hypothesis that when the FluorMAA is added in molar excess with respect to the template, multiple fluorescent units are randomly distributed within the polymeric matrix. This configuration likely leads to the inclusion of fluorophores outside the specific binding sites, promoting self-quenching phenomena and resulting in an overall fluorescence response that is insensitive to analyte binding events.

To further investigate the optical transduction behaviour of the optimized Fluo-nanoMIPs, time-resolved fluorescence spectroscopy measurements were performed. This technique allows monitoring of changes in the fluorescence lifetime of the embedded fluorophore upon analyte binding, providing information that is independent of probe concentration or light scattering effects. The fluorescence decay profiles were analyzed using a bi-exponential fitting model, which offered an acceptable approximation to discriminate between the contributions of fluorophores randomly distributed along the polymer backbone and those effectively located within or near the imprinted binding cavities. In this model, the shorter lifetime component (τ_1) was considered a global descriptor of non-specific decays occurring outside the recognition sites, whereas the longer component (τ_2) reflected fluorophores involved in binding-related interactions within the cavities. The fluorescence lifetime of the Fluo-nanoMIPs was recorded before and after exposure to increasing concentrations of HSA. For the 0.1× and 1× nanoparticles, a clear decrease in fluorescence lifetime was observed as a function of HSA concentration, demonstrating a direct correlation between the binding event and the excited-state deactivation of the fluorophore. In contrast, the 10× Fluo-nanoMIPs, containing a higher amount of fluorophore, exhibited shorter fluorescence lifetimes compared to the other formulations. This effect can be attributed to the excess of fluorescent units randomly distributed within the polymer matrix, where a significant fraction of the fluorophores is located outside the specific binding cavities and others are exposed to the solvent environment. As a result, these reporters experience a microenvironment similar to that of free

FluorMAA in solution, resulting in a lower lifetime value. Importantly, the fluorescence lifetime of the 10× formulation remained unchanged upon addition of HSA, confirming that the exposed fluorophores do not participate in specific recognition events and that the material is non-responsive to target binding.

Among the tested formulations, the 1× Fluo-nanoMIPs was identified as the most suitable for sensing applications based on the fitting parameters obtained from the calibration data. In particular, the empirical parameter *n*, which in this system correlates with the number of optically active binding sites, increased from 0.86 for the 0.1× to 1.89 for the 1× Fluo-nanoMIPs, indicating a higher proportion of binding sites effectively contributing to the optical response. The optimized 1× formulation exhibited an K_{app} of 18 pM, a LOD of 1.26 pM, a sensitivity at low concentration of 7.14×10^{9}, and a linear dynamic range extending from 3 to 83.5 pM.

The selectivity of the 1× Fluo-nanoMIPs was assessed by exposing the sensor to non-target proteins, including bovine serum albumin (BSA), human transferrin (HTR), ovalbumin and lysozyme under identical experimental conditions and no variations in fluorescence lifetime were observed in the presence of these interferents, confirming the specificity of the imprinted sites for HSA and the absence of significant cross-reactivity.

To evaluate the applicability in real matrices, the 1× Fluo-nanoMIPs sensor was tested using wine samples spiked with known concentrations of both HSA (1.5 nM) or HTR (1.3 nM). A clear decrease in fluorescence lifetime was observed only in the presence of HSA, confirming that the nanosensor remains responsive even in complex matrices and that its signal is exclusively associated with the specific recognition of the target protein.

Overall, this study contributes to the general aim of the thesis by demonstrating an effective strategy to enhance the performance of MIP-based sensors through the optimization of fluorophore incorporation. The results highlight the critical importance of adjusting the fluorophore-to-template ratio during the polymerization stage to achieve an optimal spatial positioning of the fluorescent reporter within or near the imprinted cavities, which in turn enhances the responsiveness of the nanoMIPs upon analyte binding. Furthermore, this work confirms the feasibility of

coupling MIP-based recognition systems with time-resolved fluorescence spectroscopy as a transduction method, a combination that is still rarely explored in the literature, thereby expanding the range of strategies available for developing highly sensitive and selective MIP-based optical sensors.

Published article

biosensors

MDPI

Article

Time-Resolved Fluorescence Spectroscopy of Molecularly Imprinted Nanoprobes as an Ultralow Detection Nanosensing Tool for Protein Contaminants

Alessandra Maria Bossi [1,*], Alice Marinangeli [1,2], Alberto Quaranta [2,3], Lucio Pancheri [2] and Devid Maniglio [2]

[1] Department of Biotechnology, University of Verona, Strada Le Grazie 15, 37134 Verona, Italy; alice.marinangeli@univr.it
[2] Department of Industrial Engineering, University of Trento, Via Sommarive 9, Povo, 38123 Trento, Italy; alberto.quaranta@unitn.it (A.Q.); lucio.pancheri@unitn.it (L.P.); devid.maniglio@unitn.it (D.M.)
[3] INFN—TIFPA, Via Sommarive 14, Povo, 38123 Trento, Italy
* Correspondence: alessandramaria.bossi@univr.it; Tel.: +39-045-8027-946

Abstract: Currently, optical sensors based on molecularly imprinted polymers (MIPs) have been attracting significant interest. MIP sensing relies on the combination of the MIP's selective capability, which is conveyed to the polymeric material by a template-assisted synthesis, with optical techniques that offer exquisite sensitivity. In this work, we devised an MIP nanoparticle optical sensor for the ultralow detection of serum albumin through time-resolved fluorescence spectroscopy. The Fluo-nanoMIPs (∅~120 nm) were synthetized using fluorescein-O-methacrylate (0.1×, 1×, 10× mol:mol versus template) as an organic fluorescent reporter. The ability of 0.1× and 1×Fluo-nanoMIPs to bind albumin (15 fM–150 nM) was confirmed by fluorescence intensity analyses and isothermal titration calorimetry. The apparent dissociation constant (K_{app}) was 30 pM. Conversely, the 10× fluorophore content did not enable monitoring binding. Then, the time-resolved fluorescence spectroscopy of the nanosensors was studied. The 1×Fluo-nanoMIPs showed a decrease in fluorescence lifetime upon binding to albumin (100 fM–150 nM), K_{app} = 28 pM, linear dynamic range 3.0–83.5 pM, limit of detection (LOD) 1.26 pM. Selectivity was confirmed testing 1×Fluo-nanoMIPs against competitor proteins. Finally, as a proof of concept, the nanosensors demonstrated detection of the albumin (1.5 nM) spiked in wine samples, suggesting a possible scaling up of the method in monitoring allergens in wines.

Keywords: lifetime decay; molecularly imprinted polymers; time resolved fluorescence spectroscopy; nanosensor; wine; optical sensor

Citation: Bossi, A.M.; Marinangeli, A.; Quaranta, A.; Pancheri, L.; Maniglio, D. Time-Resolved Fluorescence Spectroscopy of Molecularly Imprinted Nanoprobes as an Ultralow Detection Nanosensing Tool for Protein Contaminants. *Biosensors* **2023**, *13*, 745. https://doi.org/10.3390/bios13070745

Received: 1 June 2023
Revised: 29 June 2023
Accepted: 11 July 2023
Published: 19 July 2023

1. Introduction

Optical sensing based on synthetic artificial chemosensors has led to promising results and developments are foreseen [1–4]. Emphasis is on molecular probes that rely on a variety of chemical structures, such as host–guest macrocycles, cavitands or nucleic acids, which are exploited as chemosensors and share high affinity as a common signature. When provided with optical-responsive reporters, a quantifiable optical signal change, such as the emergence or disappearance of a spectroscopic feature, is measured upon their binding to the targeted analyte [1]. Molecular probes are exploited as standalone, or combined with nanoparticles, singly or in multiple copies, homo- or hetero-, leading to different photophysical features, and falling under the broad definition of optical nanosensors. Some polymeric biomimetics, which belong to the class of synthetic receptors, ought to be also included among the alternative and emerging category of nanosensors. In particular, molecularly imprinted polymers (MIPs) [5] are a class of synthetic receptors that provide tailor-made recognition toward a target analyte, that is conveyed by means of a

template-assisted synthesis [6,7]. For the synthesis, functional monomers and crosslinkers are solvated together with the targeted analyte, this latter acting as a molecular template. Throughout the polymerization, molecular cavities stereo-chemically complementary to the template are imprinted in the nascent polymeric network. The formed MIP is able to selectively and specifically re-bind the analyte [8]. MIPs offer several advantages: they are cheap and easy to produce, possess mechanical and thermal stability and are resistant to pH extremes [9]. Recent advances in polymer synthesis permitted preparing nanometric sized MIPs (nanoMIPs) [10,11], leading to recognition materials with a higher surface-to-volume ratio. These materials were characterized by faster binding kinetics, which is a characteristic that suits sensing. MIPs have been included in a variety of optical sensor designs, ranging from optical fibers [12–14] to photonic structures [15] and spectroscopic readouts [16,17]. The combination of molecular imprinting, as a method for generating chemically selective binding sites, to fluorescence, as a means of signaling the presence and the concentration of a target analyte, is particularly attractive [18]. In fact, on one side, fluorescence is a widespread technique in sensing due to the high sensitivity, the low detection limits, the real-time response, and the simple format [19]. On the other side, MIP materials can easily embed fluorescent functionalities through a variety of synthetic routes [20]. Both organic fluorescent monomers, such as N-allyl-4-ethylenediamine-1,8-natphalimide, anthracene-based monomers, or 3′-Methacryloxyspirobenzo[c]-furan [1,9′]xanthen-3-one, as well as inorganics fluorescent materials, such as quantum dots (QDs), lanthanides, metal nanoclusters and upconverting nanoparticles, have been combined to the MIPs, as widely described in [17,18]. Indeed, when a fluorophore is integrated in the MIP polymer network, it effectively reports upon the binding of the analyte by changing the overall optical response. In one of the first examples, a polymerizable trans-4-[p-(N,N-dimethylamino)styryl]-N-vinylbenzylpyridinium chloride was used as an organic fluorescent monomer in the synthesis of an MIP targeting adenosine 3′,5′ cyclic monophosphate (cAMP); the presence of cAMP was detected in aqueous solutions in the range between 10 nM and 100 µM as a quenching of the fluorescent emission [21]. Later, hybrid MIP/QDs materials were introduced [18,22–24]. In an example, composite nanospheres made of Mn^{2+}-doped ZnS QD/MIP were prepared, showing an ability to recognize the pesticide diazinon with a linear response in the range 50–600 ng/mL [22]. Another strategy proceeded through the polymerization of MIPs thin-layer membranes, in which the fluorescence was entailed embedding L-cysteine-capped Mn^{2+}-doped ZnS QDs, as reported in the case of a lysozyme-templated MIP [23]. Upon the binding of the lysozyme (100–1000 nM) to the MIP, the electron transfer between the QDs and the protein resulted in a fluorescence quenching proportional to the concentration of the analyte, addressing a limit of detection (LOD) of 10.2 nM [23].

In addition to the possibility of determining the target analyte via fluorescence amplitude changes, fluorescence decay times, or fluorescence lifetime, is an additional tool for optical sensing that is worth exploring. Lifetime measurements provide unique information about the system under consideration and have the advantage, unlike amplitude, of being considered as absolutes. In fact, for low concentration values, lifetime is a phenomenon largely independent from fluorescence intensity and/or the fluorophore concentration [25]. Moreover, fluorescence lifetime can be considered as a state function, since it does not depend on the initial perturbation conditions, such as excitation wavelength, duration of light exposure, single- or multi-photon excitation, measurement method, nor it is affected by photobleaching [26]. Despite the foreseen advantages, to date, sensing based on MIPs and fluorescence lifetime seems seriously under-explored.

Wandelt and colleagues prepared a fluorescent MIP, integrating the polymerizable trans-4-[p-(N,N-dimethylamino)-styril]-N-vinylbenzylpyridinium chloride moiety as a fluorescent reporter and using cAMP as the template [27]. The bulk MIP was ground into microparticles and used as suspension; when challenged with cAMP (10^{-5} to 10^{-3} M), the MIP microparticles showed a decrease in the fluorescence lifetime from 2.79 to 2.70 ns [27]. Using a similar recipe, fluorescent MIPs were also prepared in the form of sensing surfaces for the recognition of cAMP by the photopolymerization of an MIP thin

film on a quartz support. Results showed a change in the fluorescence lifetime from 2.11 to 1.99 ns upon the binding of cAMP (10^{-3} M) [28]. Later, inorganic fluorophores based on rare earths and QDs, characterized by the advantage of extended lifetimes, were integrated into MIPs [25]. QDs were embedded into MIP silica-based microparticles of 25–30 µm in diameter and imprinted for the recognition of malachite green. Challenging these micro-MIPs with malachite green (10 µM) resulted in a decrease in the lifetime from 79 to 60 ns [29]. Quílez-Alburquerque and colleagues developed a sensor for tenuazonic acid mycotoxin (TeA) using a tailored multifunctional Ru(II) complex as a fluorescent probe [30]. An MIP nanolayer was polymerized onto 200 nm silica beads, using the trifunctional luminescent acrylate-Ru(II)-biimidazole monomer. The MIP core–shell nanoparticles had a lifetime of 72 ns, while in the presence of TeA (0.5–400 µM), a 30% decrease in the average emission lifetime was observed [30].

In the present work, we studied the effect of entailing an organic fluorescent moiety, i.e., fluorescein methacrylate, to water-soluble MIP nanoparticles (Fluo-nanoMIPs) of about 120 nm in hydrodynamic diameter that were selective for the protein human serum albumin (HSA), with the aim of devising a lifetime-based nanosensor for the assessment of protein traces. It is anticipated that Fluo-nanoMIPs nanosensors' time-resolved fluorescent spectroscopy enabled attaining an ultralow detection of proteins, suggesting the potential for future applications in clinical, food and environmental areas.

2. Materials and Methods

2.1. Chemicals

Acrylamide (Aam), N-*tert*-butylacrylamide (tBAm), methacrylic acid (MAA), N,N′-methylene bisacrylamide (BIS), N,N,N′,N′-tetramethyl ethylenediamine (TEMED), ammonium persulfate (APS), fluorescein O-methacrylate (FluorMAA), human serum albumin (HSA, Cat. No. A9731), human transferrin (HTR, Cat. No. T3705), bovine serum albumin (BSA, Cat. No. A7906), lysozyme (Lyz, Cat. No. 10837059001), ovalbumin (Cat. No. 05440), trypsin, phosphate buffer (PB), saline phosphate buffer (PBS), tris(hydroxymethyl)-aminomethane (TRIS), 1-Ethyl-3-(3-dimethylaminopropyl) (EDC), N-hydroxysuccinimide (NHS), 2-(N-morpholino)ethane-sulfonic acid (MES), ethanol, acetonitrile and N-Cyclohexyl-2-aminoethanesulfonic acid (CHES) were from Sigma-Aldrich (Darmstadt, Germany).

2.2. Synthesis of Fluo-nanoMIPs

The synthesis of the fluorescent nanoMIPs (Fluo-nanoMIPs) was carried out using a total monomer concentration of 0.2% (w/v). The monomers Aam, MAA and tBAm were used in a ratio 8, 8 and 4% moles, respectively, and admixed to 80% (moles) of BIS in 20 mM PB at pH 7.4, as described in [16]. Fluorescence was entailed adding fluorescein methacrylate in a quantity of 1.3, or 13, or 130 nmol with respect to the total monomers. The template, HSA, was 15 nmol. Vials were closed with rubber caps and bubbled with N_2 for 10 min. The catalysts, APS (0.04% w/v) and TEMED (0.03% w/v), were added and the polymerization was carried out overnight at room temperature under mild stirring. At the completion of the polymerization, the removal of the template was carried out by enzymatic digestion with trypsin (100 µg) for 2 h at 37 °C, which was followed by dialysis (M.W.C.O. 14.000 Da, Sigma-Aldrich, Darmstadt, Germany) with 3 × 3 L of MilliQ water. Next, the Fluo-nanoMIPs were freeze-dried and stored. The yield of polymerization was 85%, as estimated from the weight of the lyophilized nanoparticles with respect to the total weight of the monomers used in the synthesis.

2.3. Calibration Curve for FluorMAA

The fluorescence intensity of increasing concentrations of FluorMAA (81.25, 162.5, 325, 650 and 1300 nM) was measured using a spectrofluorometer (FP-8200, Jasco Ltd., Heckmondwike, UK) with an excitation wavelength at 488 nm and reading the emission intensity at 514 nm, corresponding to the emission peak. The calibration curve for FluorMAA

and the associated equation are reported in Supplementary Section S1. The fluorescence intensities at the emission wavelength λ_{em_max} = 514 nm of the Fluo-nanoMIPs samples (1 mg/mL) were measured, and the calibration was used to estimate the amount of fluorophore incorporated within the polymeric network during the synthesis. Measurements were in triplicate.

2.4. Dynamic Light Scattering (DLS)

Size distribution and the polydispersity index (PDI) were determined using a Zetasizer Nano ZEN3600 (Malvern Instruments Ltd., Malvern, UK) equipped with a 633 nm He-Ne laser at a detection angle of 173°. Fluor-nanoMIPs were suspended in water to the final concentration of 1 mg/mL. The material refractive index (RI) was 1.490 and the absorption value was 0.01; the dispersant RI was 1.332 for water, while the viscosity was 0.89 cP as reported by the Zetasizer V.6.32 software (Malvern instruments Ltd., Malvern, UK). The temperature was set at 298° K. Measurements were in triplicate.

2.5. Scanning Electron Microscopy (SEM)

Images were collected with a secondary electron detector at 15 keV beam energies on a Supra 40 Field Emission SEM (Zeiss, Oberkochen, Germany). Prior to SEM analysis, samples were suspended in ultrapure water at 150 µg/mL final concentration and briefly ultrasonicated. Then, 5 µL of the suspension were deposited on a silicon wafer substrate mounted with carbon double tape on an aluminum stub, after which it was dried at 60 °C for 24 h or 30 °C for 72 h. A platinum/palladium ultrathin coating (2 nm) was deposited by means of plasma sputtering to ensure electrical conductivity.

2.6. Fluorescence Intensity of Fluo-nanoMIP

Fluo-nanoMIPs, respectively, synthetized with 1.3, 13 and 130 nmol of FluorMAA, were dissolved at 0.2 mg/mL and incubated with increasing concentrations (from 15 fM to 150 nM) of human serum albumin, or with the same concentrations of human serum transferrin, i.e., a non-template protein chosen for selectivity tests. The equilibrium time, previously tested over 60 min, was reached in 20 min. After 30 min of incubation, samples were plated in triplicate on a 96-well plate hydroGrade (BRANDplates, Germany) with a volume of 60 µL per well. Steady-state measurements of Fluo-nanoMIPs were carried out using the microplate reader Infinite 200 PRO (Tecan Group Ltd., Männedorf, Switzerland) at the emission wavelength of 522 nm. Emission intensities were measured as relative fluorescent units (rfu). Isotherm was fitted with OriginPro 9.0 using the Langmuir model equation: y = START + (END − START) × x/(k + x), where START and END were the initial and final y values; x was the concentration of HSA; and k was the half-saturation or apparent dissociation constant (EC_{50} or apparent dissociation constant K_{app}).

2.7. Fluorescence Lifetime of Fluo-nanoMIP

The fluorescence lifetime of a population, measured in the time-domain, also called fluorescence intensity decay, follows the equation:

$$I(t) = I_0 e^{-t/\tau} \quad (1)$$

where $I(t)$ is the intensity at time t; I_0 is the intensity at $t = 0$; t is the time after the absorption; and τ is the fluorescence lifetime. Time-resolved fluorescence intensities were collected using a single photon counting spectrometer Nanolog/Fluorolog-3-2iHR320 (Horiba-Jobin Yvon, Kyoto, Japan) equipped with a NanoLED source with a wavelength of 453 nm. The emission was monitored at the angle of 90° with respect to the excitation. Data were collected in 1023 channels to 10,000 counts in the peak, while the calibration time was 109.73 ps per channel. The voltage at the photomultiplier (PTM) was set to 950 V. Measurements were performed in a 1 mL quartz cuvette, using a fixed concentration of 0.2 mg/mL of nanoMIPs in PBS (10 mM pH 7.4), adding increasing concentrations of HSA

(100 fM–150 nM). To allow binding kinetics' stabilization, a 20 min incubation was awaited before performing each measurement.

A 0.2 mg/mL Fluo-nanoMIP suspension was excited at λ_{exc} = 453 nm to obtain the instrumental response (prompt) for the deconvolution. The sample decays were recorded at λ_{em} = 522 nm.

Data were elaborated with the Decay Analysis Software V. 6.8 (Horiba Scientific, Yvon, Kyoto, Japan), choosing a biexponential fitting equation model:

$$I(t) = A + B_1 e^{-t/\tau 1} + B_2 e^{-t/\tau 2} \quad (2)$$

The biexponential fitting was used to take into account the heterogeneity of the system due to the random incorporation of the fluorophore in the Fluo-nanoMIPs polymeric network during the synthesis. The two components, τ_1 and τ_2, are used to describe the presence of two different populations of fluorophores: one integrated inside the stamped molecular cavities and the other outside the binding cavities, randomly distributed in the nanoMIP, according to [30,31].

2.8. Sensor Parameters

The lifetime values (τ_2), plotted as a function of HSA concentration, described the binding isotherm for the sensing system. Data were fitted with the Hill equation model (OriginPro 9.0):

$$\tau_2 = \tau_{2\_max} \frac{x^n}{(K + x^n)} \quad (3)$$

where τ_2 is the lifetime at concentration x of the ligand (i.e., HSA); τ_{2_max} is the τ value at binding saturation; n is the Hill parameter, which correlates with the number of binding sites, and K is the apparent dissociation constant derived from the law of mass action, which is represented by the following equation:

$$K = \frac{[A] \cdot [B]}{[AB]} \quad (4)$$

where $[A]$ is the molar concentration of the receptor which in our case consists of the 1×Fluo-nanoMIPs; $[B]$ is the molar concentration of the analyte and $[AB]$ is the concentration of the complex between the 1×Fluo-nanoMIPs and the analyte.

2.9. Selectivity of 1×Fluo-nanoMIPs

Different competitor proteins were chosen for the selectivity of fluorescent nanoMIPs. A solution of 1×Fluo-nanoMIPs at 0.2 mg/mL was incubated for 20 min in the presence of 18 pM of BSA, or 20 pM of HTR, or 11 pM of ovalbumin, or 17 pM of lysozyme. Fluorescence lifetime was measured as explained above. Measurements were performed in triplicate.

2.10. Fluorescence Lifetime of 1×Fluo-nanoMIPs in Wine

Measurements were performed in a 1 mL quartz cuvette, using chardonnay white wine, spiked with 1.5 nM of serum albumin, diluted 1:5 in PBS 10 mM pH 7.4 into which 1×Fluo-nanoMIPs were dispersed at a concentration of 0.2 mg/mL. In this case, the prompt was prepared with the same wine dilution and nanoparticles but without the spike and recorded according to Section 2.8. Selectivity was tested using the same concentration of human transferrin. Measurements in triplicate were performed as described above.

2.11. Isothermal Titration Calorimetry (ITC)

Isothermal titration calorimetry (ITC) was performed on a MicroCal PEAQ-ITC (Malvern Panalytical Ltd., Worcestershire, UK) instrument. All solutions were filtered and degassed prior to use. The 1×Fluo-nanoMIPs, human serum albumin and human serum transferrin (HTR) were solubilized in 10 mM PBS pH 7.4. Then, 1 µM of 1×Fluo-nanoMIPs (200 µL) was titrated with 30 nM to 10 µM of serum albumin at 25 °C, and the

heats of the interactions were recorded. Dilution heats were estimated from the titration of the proteins in buffer. Raw heats were subtracted from the dilution heat and integrated. Integrated heats were plotted as a function of the molar ratio between the titrand and the titrant and fitted with one set of sites modeled with the MicroCal PEAQ-ITC Analysis Software 1.22.1293 to estimate values for the binding constant (K_D) and the enthalpy variation associated with binding (ΔH).

2.12. Atomic Force Microscopy (AFM)

For the AFM, nanoMIPs were covalently coupled to support surfaces with the protocol reported in [14]. The surface topography of the of Fluo-nanoMIPs was studied using a NT-MDT Solver Pro system equipped with a Nova scanner. Samples were imaged in semi-contact mode using super sharp diamond-like carbon tips (NSG01_DLC, NT-MDT, 1 nm nominal tip radius, 150 kHz, force constant 5.5 N/m), collecting 1 × 1 μm, 512 points resolution topography images. AFM data were analyzed with the support of Gwyddion analysis software [32].

3. Results and Discussion

3.1. Effects on the Lifetime Due to Interaction between the Fluorophore and Albumin

Initially, the effects on the fluorophore lifetime due to the interaction between the chosen organic fluorescent monomer (FluorMAA) and the target analyte was studied by time-resolved fluorescent spectroscopy (SI Section S2). FluorMAA (155 pmol) was incubated with increasing concentrations of albumin (15 fM–15 nM), and the lifetimes (τ) were measured (Figure 1).

A

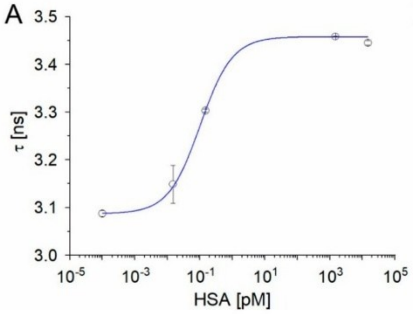

B

Parameters	FluorMAA
τ_0 (ns)	3.086 ± 0.018
τ_{max} (ns)	3.457 ± 0.002
EC_{50} (pM)	0.10 ± 0.05
n	0.885 ± 0.998
R^2_{adj}	0.9952

Figure 1. (**A**) Fluorescence lifetime of FluorMAA as a function of albumin concentration (n = 3) fitted with Hill model equation. (**B**) Fitting parameters of the fluorescent decays of FluorMAA in the presence of albumin (monoexponential model, SI Section S2).

The lifetime increased with the albumin concentration following a sigmoidal profile, with values shifting from 3.086 ± 0.018 to 3.457 ± 0.002 ns and plateauing for protein concentrations around 10 pM (Figure 1; fitting parameters in the inset table). Such a behavior was indicative of an interaction taking place between the fluorophore and the protein. In line with previous observations, increments of τ values of the protein's endogenous reporters (tryptophans) were observed in the case of non-specific interactions with the environment, such as bovine serum albumin adsorbing to ZnO core–shell nanoparticles [33].

3.2. Synthesis and Characterization of Fluorescent NanoMIPs

A library of fluorescent nanoMIPs, herein called Fluo-nanoMIPs, was synthesized using a total monomer concentration of 0.2% *w*/*v*. In particular, acrylamide (Aam), *tert*-butylacrylamide (tBAm), and methacrylic acid (MAA) were admixed to N,N′-methylene bis-acrylamide (BIS), used as a reticulating agent, as reported in [14]. Human serum

albumin (15 nmol) was chosen as a model template and added to the pre-polymerization mixture (V_{final} = 10 mL) [34]. According to the scheme reported in Figure 2, fluorescence was entailed by using the fluorescein–methacrylate (FluorMAA) monomer, which was added to the syntheses at 1.3, or 13, or 130 nmol to the final synthetic volume, in order to study the effect of the molar ratio between the fluorescent-reporter (0.1×, 1×, 10×) and the template on the fluorescent readouts (Table 1). At the completion of the syntheses, the degree of incorporation of the fluorophore into the MIP nanoparticles was estimated by means of the calibration curve: y (λ_{em}@522 nm) = 0.82 × ([FluorMAA], nM) − 0.12 (details in SI Section S1 Calibration Curve). Results indicated the FluorMAA incorporation for the 0.1×, 1× and 10×FluorMAA was, respectively, 28, 23 and 52% (Table 1).

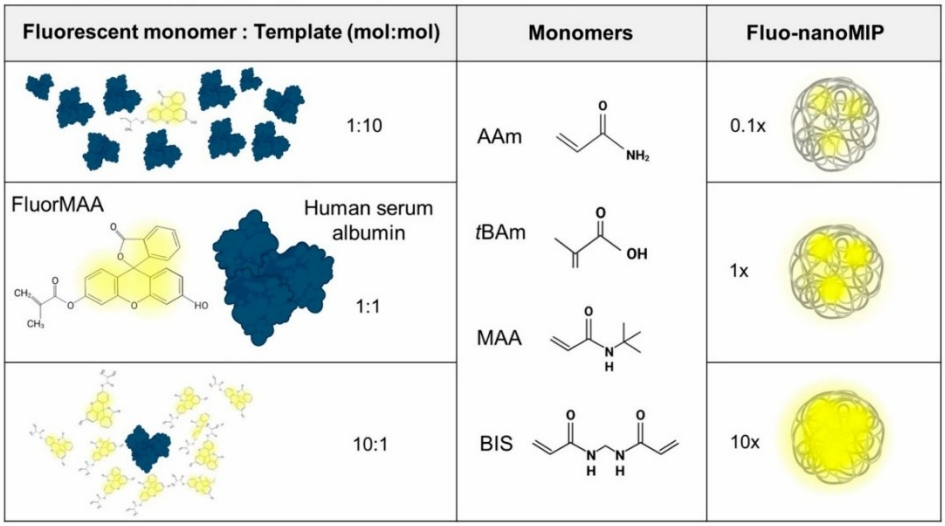

Figure 2. Scheme of the polymerization conditions used to prepare the library of Fluo-nanoMIPs.

Table 1. Fluorescence and physical characteristics of the nanoMIPs.

Sample Name	FluorMAA Added to Polymerization (pmol/mg)	FluorMAA Incorporated (pmol/mg)	$Z_{average}$ (nm)	PDI
0.1×Fluo-nanoMIP	65	20 ± 5	115.6 ± 0.8	0.20
1×Fluo-nanoMIP	650	155 ± 20	123.9 ± 0.1	0.22
10×Fluo-nanoMIP	6500	3380 ± 300	176.6 ± 0.4	0.34

The Fluo-nanoMIPs dimensions were characterized by means of dynamic light scattering (DLS), and the estimated sizes are reported in Table 1. The hydrodynamic sizes of the nanoparticles were about a hundred nanometers, while the polydispersity index (PDI) indicated a homogeneous distribution. As a confirmation, Figure 3 reports the scanning electron microscopy (SEM) and atomic force microscopy (AFM) images of the Fluo-nanoMIPs, showing spherical nanoparticles with dimensions in agreement with DLS data.

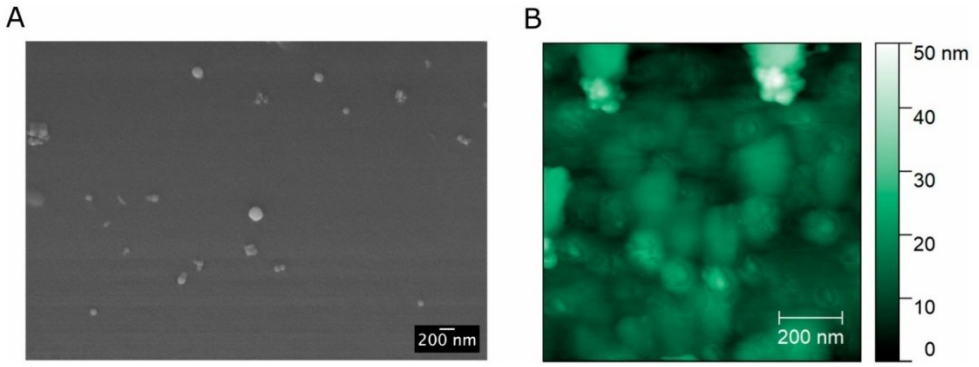

Figure 3. (**A**) Exemplificative SEM image of Fluo-nanoMIPs; (**B**) AFM image of Fluo-nanoMIP covalently coupled to silica supports.

3.3. Functional Characterization of the Fluo-nanoMIPs

Study of the Fluorescence Intensity of the Library of Fluo-nanoMIPs upon Binding

The functional characterization of the library of Fluo-nanoMIPs was assessed by means of fluorescent intensity binding studies. Each batch of Fluo-nanoMIPs, i.e., 0.1×, 1× and 10×, was incubated for 20 min with increasing concentrations of HSA (15 fM–150 nM), and the fluorescence emission at 522 nm was monitored. Quenching of the emission intensities was observed both for the 0.1× and the 1×Fluo-nanoMIPs challenged with increasing concentrations of albumin (Figure 4A,B). Binding data were fit with a Langmuir equation model, and the resulting parameters are reported in Table 2. Worth of note is the value of the half saturation, EC_{50}, which corresponds to the apparent dissociation constant (K_{app}), which was estimated in the pM range, indicating a remarkably high affinity of the imprinted nanomaterial for its targeted protein. Both the tested quantities of fluorescent reporter, i.e., 0.1× or 1× moles with respect to the moles of the template, yielded to Fluo-nanoMIPs sensitive to binding events in the range between the fM and the pM, indicating these nanosensors' compositions were apt to detect traces of the protein template. In contrast, in the case of the 10×Fluo-nanoMIPs, no variation in the emission intensity was observed upon albumin addition (Figure 4C). This supported the hypothesis that a synthetic condition, in which the fluorophore reporter is added in molar excess with respect to the template protein, does result in several fluorescent labels per nanoparticle being randomly distributed in the polymeric network. Such a condition likely includes the placement of fluorophores outside of the formed binding sites, together with self-quenching effects, making the overall fluorescence response non-sensitive to the binding events.

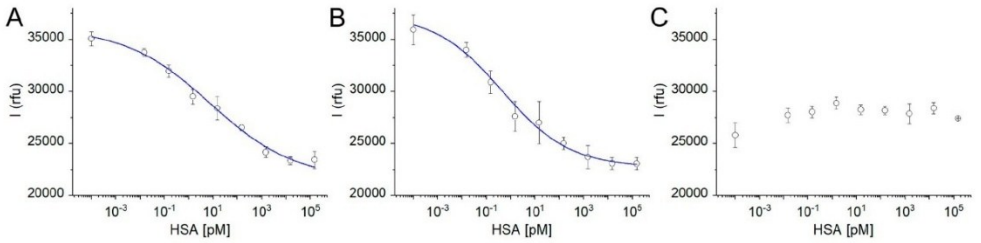

Figure 4. Emission intensity at 522 nm of: (**A**) 0.1×Fluo-nanoMIP; (**B**) 1×Fluo-nanoMIP; (**C**) 10×Fluo-nanoMIP challenged with albumin.

Table 2. Fitting parameters of emission intensity measurements of Fluo-nanoMIPs 0.1×, 1× and 10× incubated with increased concentrations of albumin.

Parameters	0.1×Fluo-nanoMIP	1×Fluo-nanoMIP	10×Fluo-nanoMIP
I_0 (rfu)	33,578 ± 535	34,399 ± 476	25,805 ± 1175
I_{min} (rfu)	23,452 ± 547	23,103 ± 282	28,890 ± 573
EC_{50} (pM)	65 ± 20	30 ± 9.5	n.a. *
R^2_{adj}	0.9690	0.9883	n.a.

* Fitting did not converge.

Therefore, 0.1× and 1×Fluo-nanoMIPs demonstrated the crucial effect of a careful adjustment of the quantity of fluorescent reporter (in moles) with respect to the moles of the template (i.e., 1:10 and 1:1). Both compositions relied on a restricted number of fluorescent tags per molecule of albumin in the pre-polymerization mix, which was a condition hypothesized to favor the fluorophore to albumin pairing during the pre-synthetic stage, and ultimately leading to a superior control of the placement of the few fluorescent reporters in, or close by, the binding cavity, in the formed nanomaterials. Yet, the best fluorescent performance at binding was observed for the composition based on a one-to-one fluorophore to albumin molar ratio, as shown by the steeper slope of the fitting curve reported in Figure 4B when compared to 4A. It appears that the strategy to modulate the number of fluorescent tags on the nanoMIPs as a function of the quantity of template used in the synthesis is very straightforward and easy to perform yet lacking the fidelity that can be achieved by the post-synthetic chemical tagging of MIPs with fluorescent probes, as reported for the post-imprinting approach proposed by [35,36].

As an independent proof, the specific binding between albumin and the synthesized 1×Fluo-nanoMIPs was assessed by isothermal titration nanocalorimetry (ITC) [37]. The interaction between the nanomaterial and its targeted analyte is reported in Figure 5. As shown in Figure 5B, the integrated heats described a sigmoidal profile, which is typically associated with interacting molecules. The steep transition is typical of a binding event characterized by extremely high affinity; in fact, the dissociation constant was in the pM range. The ITC confirmed the effective stamping of binding sites on the 1×Fluo-nanoMIPs [37,38]. In contrast, when 1×Fluo-nanoMIPs were titrated with a non-template protein, no interaction was observed (SI Section S4 Isothermal Titration Calorimetry).

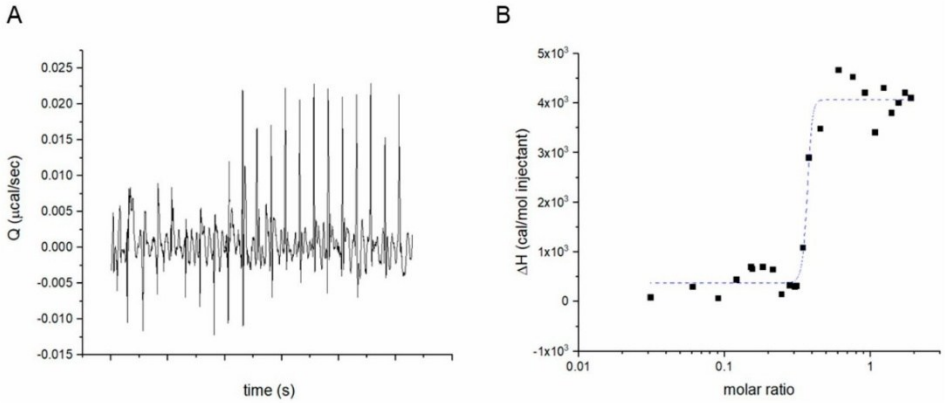

Figure 5. Isothermal titration nanocalorimetry data of 1×Fluo-nanoMIP titrated with human serum albumin: (**A**) raw heats over time; (**B**) solid squares, integrated heats fitted with a one-site equation model for the titration with serum albumin with 1×Fluo-nanoMIPs.

3.4. Fluorescence Lifetime of the Fluo-nanoMIPs

The feasibility of devising soluble nanosensors, based on Fluo-nanoMIPs, to monitor the presence of serum albumin, as the target analyte, by fluorescence lifetime decay was next investigated. The intensity decay curve of Fluo-nanoMIPs (0.2 mg/mL) was recorded at λ_{em} = 522 nm, allowing the samples to equilibrate for 20 min. Data were fitted with a biexponential fitting (τ_1 and τ_2). Indeed, this was an approximate, though acceptable [33], model to represent and discriminate between the decay's contributions given by the fluorescent reporters randomly placed on the polymer backbone and the ones related to effectively placed fluorescent reporters, i.e., located within, or nearby, the imprinted binding site in the Fluo-nanoMIPs. In detail, a fixed τ_1 was used as a global descriptor of all the non-specific decays occurring outside the molecularly imprinted cavities, whereas the binding-related interactions were observed as τ_2. It appeared that both solvated 0.1× and 1×Fluo-nanoMIPs in the absence of the analyte displayed very similar τ_2 values, i.e., 4.154 ± 0.015 and 4.183 ± 0.009 ns, respectively, which is in agreement with the theory of lifetime decay that postulates the independence of the τ value from the concentration of fluorophore at low concentrations. Additionally, we observed a significative difference in the τ values of free FluorMAA (Figure 1) with respect to τ of the fluorophore incorporated in the nanoMIP (Table 3) due to the different environment surrounding the molecule and accounting for its shielded integration within the nanoMIP. In contrast, the 10×Fluo-nanoMIPs, characterized by evenly distributed reporters and/or self-quenching effects, showed significantly lower values of τ. It can be expected that the more the fluorophores on the nanoMIPs are freely exposed to the solvent, the more the τ value should approach that of the free Fluor-MAA. Overall, the differences in fluorophore decays observed by comparing the 0.1× and 1×, versus 10×Fluo-nanoMIPs, were evidence of the strong correlation between the decay's properties and the fluorescent reporter's placement in the nanoMIP's backbone [26]. Next, Fluo-nanoMIPs (0.1×, 1×, and 10×) were solvated in PBS at the concentration of 0.2 mg/mL and challenged with increasing concentrations of albumin, from 100 fM to 150 nM. The results are reported in Figure 6. Characteristics saturation binding isotherms were observed for 0.1× and 1×Fluo-nanoMIPs (Figure 6B,C), whereas 10×Fluo-nanoMIPs did not report any response to binding events (Figure 6D). Table 3 reports the data of the binding fitted with the Hill equation model.

Concerning 0.1× and 1×Fluo-nanoMIPs, the nanosensor's half saturation was in the pM range, which was a value that remained consistent with the observations reported for the fluorescent intensity experiments (Table 2). Fitting parameters showed how an n value, which in this case correlates with the number of optically active binding sites, increased from 0.86 to 1.89 when nanoMIPs were prepared with 10 times more of the fluorescent reporter. This suggested that the 1×Fluo-nanoMIPs should be preferred for sensing.

The sensor's operational parameters in PBS, associated to the 1×Fluo-nanoMIP nanosensors, were then extrapolated and are reported in Table 4, indicating that the nanomaterial herein prepared can be exploited to determine serum albumin in the picomolar range.

Table 3. Fitting parameters of fluorescence lifetime measurements of Fluo-nanoMIPs 0.1×, 1× and 10× incubated with increased concentrations of albumin.

Parameters	0.1×Fluo-nanoMIP	1×Fluo-nanoMIP	10×Fluo-nanoMIP
τ_{2_0} (ns)	4.154 ± 0.015	4.183 ± 0.009	4.008 ± 0.018
τ_{2_max} (ns)	3.944 ± 0.009	3.983 ± 0.006	4.000 ± 0.018
EC_{50} (pM)	28 ± 13	18 ± 4.2	n.a. *
n	0.86	1.89	n.a.
R^2_{adj}	0.9678	0.9803	n.a.

* Fitting did not converge.

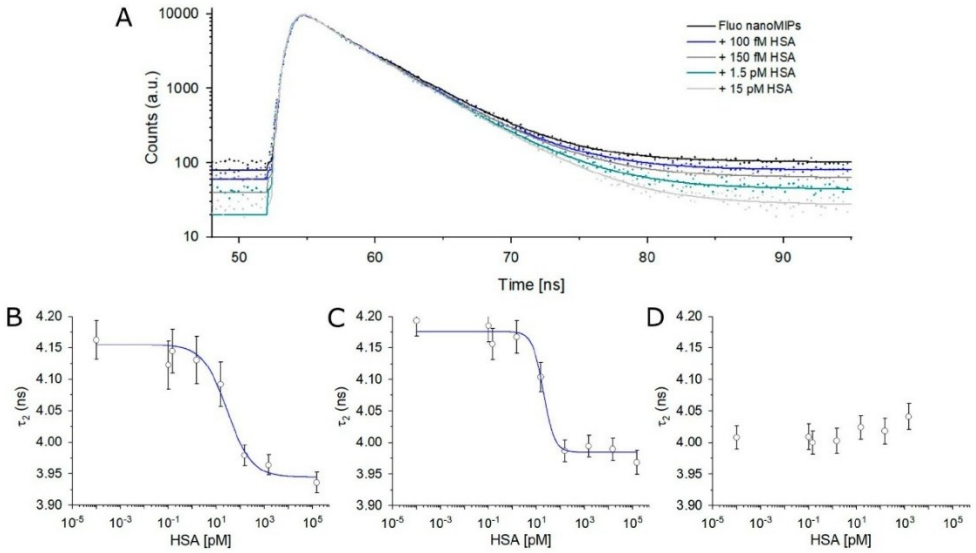

Figure 6. (**A**) Lifetime fluorescence spectra of Fluo-nanoMIPs in the presence of increasing concentrations of albumin. Fluorescence lifetime (τ_2) of (**B**) 0.1×Fluo-nanoMIP, (**C**) 1×Fluo-nanoMIP and (**D**) 10×Fluo-nanoMIP as a function of albumin concentration. Binding curves were fitted with Hill model equation.

Table 4. Parameters for the 1×Fluo-nanoMIP lifetime nanosensor.

τ_{2_0} (ns)	4.183 ± 0.009	
τ_{2_max} (ns)	3.983 ± 0.006	
K_{app} (pM)	18 ± 4.2	
K_{aff} (M^{-1})	1.4×10^{10}	Kaff = 1/K (M^{-1})
LOD (pM)	1.26	$3 \times \text{std.dev}_{blank}/\text{Sensitivity}_{low\ conc}$
Sensitivity at low concentration	7.14×10^{9}	$\lvert\Delta\tau_{2\_max} - \Delta\tau_{2\_0}\rvert/K$
χ^2_{red}	0.941	
Linear dynamic range (pM)	3.0–83.5	10–90%

3.5. Selectivity of the 1×Fluo-nanoMIP Nanosensor

Finally, a selectivity test was carried out to confirm that the variations in lifetime decays reported in Figure 6 were due to specific binding events. The selectivity test was per-formed by choosing different proteins as interferents. Bovine serum albumin (BSA), which is characterized by molecular weight (MW 66,000 g/mol) and isoelectric point (pI 6.8) similar to HSA, was selected to epitomize the ability of Fluo-nanoMIPs to bind with other mammalian albumins. Hen egg ovalbumin (MW 42,700 g/mol, pI 5.1) was chosen for testing the selectivity toward an albumin from a different species (*Gallus gallus*), whereas the hen egg lysozyme that is characterized by a higher pI and a significantly smaller size (MW 14,400 g/mol, pI 9.36) was chosen for devising the effect of charge on the Fluo-nanoMIP binding. Finally, another highly abundant serum protein, namely human serum transferrin (HTR, MW 77,000 g/mol, pI 6.8), was also tested. As shown from the histogram chart reported in Figure 7A, the incubation of the nanosensors with HSA (18 pM) produced a 40% drop in the τ_2 value. In contrast, the nanosensors in the presence of any of the non-template proteins did not produce significant changes in the lifetime decays.

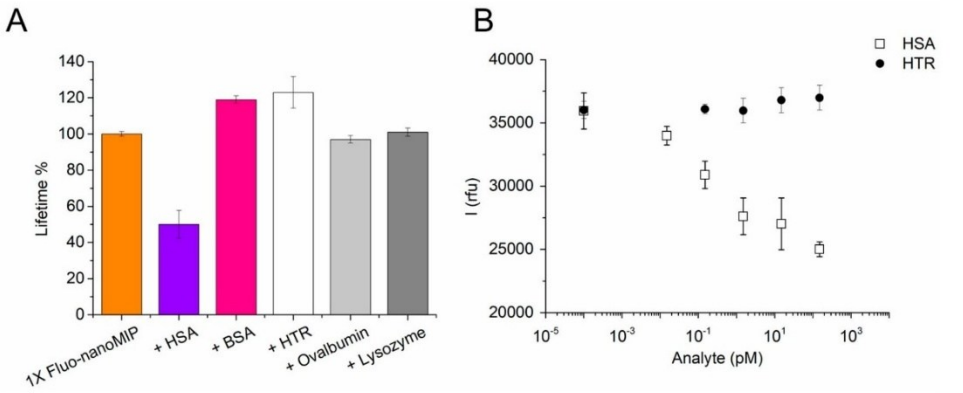

Figure 7. (**A**) Selectivity of 1×Fluo-nanoMIPs studied by time-resolved fluorescence spectroscopy. Orange bar reports τ_2 of a sample with just 1×Fluo-nanoMIPs, in purple τ_2 for 1×Fluo-nanoMIPs incubated with HSA (18 pM) and compared with pink for τ_2 of the same Fluo-nanoMIPs incubated with bovine serum albumin (18 pM); white for τ_2 of HTR (20 pM); light gray for τ_2 of ovalbumin (11 pM); or dark gray for τ_2 of lysozyme (17 pM). (**B**) For a better comparison, the selectivity of 1×Fluo-nanoMIPs was studied in terms of emission intensity at λ_{max}= 522 nm. Open squares represent 1×Fluo-nanoMIP incubated with the targeted HSA; solid circles represent 1×Fluo-nanoMIP incubated with the competitor HTR.

In the case of BSA and of HTR, a slight increment in lifetime was observed, which was possibly ascribed to non-specific interactions between the interferent protein and the biomimetic nanomaterial [33]. As an independent proof, the specificity of the 1×Fluo-nanoMIP nanosensors was also tested by comparative binding, in fluorescence emission, indicating the effect of increasing concentrations of HSA (Figure 7B, open squares) or of the HTR (Figure 7B, solid circles). Results confirmed quenching of the emission solely associated to the binding of, or occurring nearby, the optical-responsive reporters of the nanosensor, whereas no emission changes were observed when the HTR interferent was tested. This confirmed the selectivity of the 1×Fluo-nanoMIPs and supported their use as soluble nanosensors for albumin detection.

3.6. Fluo-nanoMIP Nanosensors for the Determination of Albumin Allergen in Wine Samples

The sensitivity of the herein synthesized 1×Fluo-nanoMIP nanosensors supported their use in real scenarios in order to determine the albumin contamination at ultralow concentrations, such as in the case of protein allergen traces in wines [39]. In a preliminary experiment, we tested the use of the nanosensors in real wine samples (n = 2) that were spiked with albumin (1.5 nM), whereas control samples were both not spiked and spiked with the non-related protein HTR. All samples (final volume of 1 mL) were supplied with a fixed quantity of nanosensors (0.2 mg/mL), incubated for 20 min and measured. Figure 8 reports the measured lifetime decays. It was observed that the percentage of the τ_2 value dropped exclusively when in the presence of albumin, confirming the selectivity of the nanosensors.

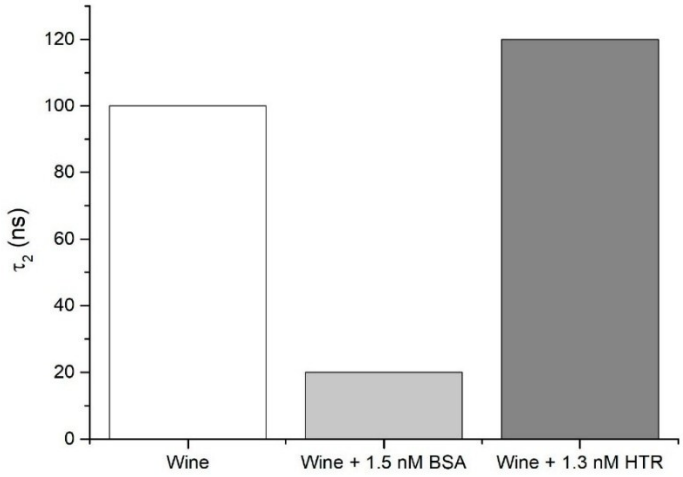

Figure 8. Real sample testing by means of 1×Fluo-nanoMIP nanosensors. White bars: wine sample; Gray bar: wine sample spiked with a known concentration of albumin; Dark-gray bar: wine sample spiked with a known concentration of HTR as an example of unrelated protein.

4. Conclusions

The fluorescence lifetime is an intrinsic property of fluorescent probes that is highly sensitive to the microenvironment [40], while it is largely independent from both the fluorescence intensity and the fluorophore concentration; therefore, it can be effectively used as a reporter of molecular interactions. In the present work, we exploited an organic fluorophore monomer (Fluor-MAA) to synthesize analyte-selective fluorescent polymeric nanosensors by means of the MIP technology. A known nanoMIP composition, suitable to recognize HSA [14], was entailed of the fluorescent reporter Fluor-MAA, and the binding was studied through fluorescence decay, which was a yet not-investigated response for the system. Valuable information about the binding event was reported as a decrease in the lifetime decays. It was observed that sub- to stoichiometric quantities of Fluor-MAA with respect to the albumin template, i.e., 0.1× and 1×Fluo-nanoMIPs, appear to statistically guide the placement of the fluorescence probe within the imprinted binding cavity, allowing to determine the presence of the target protein at picomolar levels, which is a limit significantly improved over the current literature [30]. These achievements contribute to the advancement of nanosensing by means of the MIP technology and to the in-solution real-time determination of protein markers [4].

Currently, the interest in the use of nanoMIPs is mainly in clinical diagnostics, but expected areas of application concern the detection of traces of proteins that are causative agents of allergies in foods. Along the way to develop nanosensors for allergies, we started by studying the Fluo-nanoMIP's ability to monitor ultralow quantities of the model protein HSA in the wine matrix. The results were positive, opening to the further synthesis and to further lifetime interrogations of Fluo-nanoMIPs tailored to the specific allergenic proteins found in wines (i.e., lysozyme, ovalbumin) [41]. From the present results, it appeared that Fluo-nanoMIPs can constitute a general answer to the growing need for ultralow sensitive analytical devices for the determination of protein contaminations in beverages [42]. Additionally, we foresee the possibility to devise multiple Fluo-nanoMIPs, each templated toward the recognition of a specific allergenic target, expanding the current MIP sensing portfolio. In view of a multi-targeting nanosensing and to their translation to

the market, it would be beneficial to explore the solid-phase synthesis approach, which is compatible to mass production of the Fluo-nanoMIPs [11,43].

Supplementary Materials: The following supporting information can be downloaded at: https://www.mdpi.com/article/10.3390/bios13070745/s1, Figure S1: Calibration curve of FluorMAA; Table S1: Equation parameters of the FluorMAA calibration curve; Figure S2: Examples of DLS measurements of (A) 0.1× and (B) 1×Fluo-nanoMIPs; Figure S3: Isothermal titration nanocalorimetry data of 1×Fluo-nanoMIP titrated with the non-template protein human serum transferrin and expressed as raw heats over time.

Author Contributions: Conceptualization, A.M.B., L.P., A.Q. and D.M.; methodology, L.P., A.Q., A.M.B. and D.M.; validation, A.M.; investigation, A.M., A.M.B., L.P. and D.M.; resources, A.M.B., D.M. and L.P.; data curation, A.M., A.M.B. and D.M.; writing—original draft preparation, A.M., A.M.B. and D.M.; writing—review and editing, A.M.B., L.P., A.Q. and D.M.; supervision, A.M.B., A.Q. and D.M. All authors have read and agreed to the published version of the manuscript.

Funding: This research was funded by Bando COVID-19 of the University of Trento; Italian Ministry of Research and University doctoral program PON PNRR DM351.

Institutional Review Board Statement: Not applicable.

Informed Consent Statement: Not applicable.

Data Availability Statement: The data are available on reasonable request from the corresponding author.

Acknowledgments: D.M and L.P. acknowledge the Bando COVID-19 of the University of Trento for the OPTOVIR project; A.M.B. and A.M. acknowledge the MUR DM 351 PON PNRR doctoral program. A.M.B. acknowledges the Centro Piattaforme Tecnologiche (CPT) of the University of Verona for the facilities Nanolog/Fluorolog-3-2iHR320, DLS and ITC.

Conflicts of Interest: The authors declare no conflict of interest.

References

1. Krämer, J.; Kang, R.; Grimm, L.M.; De Cola, L.; Picchetti, P.; Biedermann, F. Molecular Probes, Chemosensors, and Nanosensors for Optical Detection of Biorelevant Molecules and Ions in Aqueous Media and Biofluids. *Chem. Rev.* **2022**, *122*, 3459–3636. [CrossRef]
2. Wu, D.; Sedgwick, A.C.; Gunnlaugsson, T.; Akkaya, E.U.; Yoon, J.; James, T.D. Fluorescent Chemosensors: The Past, Present and Future. *Chem. Soc. Rev.* **2017**, *46*, 7097–7472. [CrossRef]
3. Dabrowski, M.; Lach, P.; Cieplak, M.; Kutner, W. Nanostructured Molecularly Imprinted Polymers for Protein Chemosensing. *Biosens. Bioelectron.* **2018**, *102*, 17–26. [CrossRef]
4. Leibl, N.; Haupt, K.; Gonzato, C.; Duma, L. Molecularly Imprinted Polymers for Chemical Sensing: A Tutorial Review. *Chemosensors* **2021**, *9*, 123. [CrossRef]
5. Bräuer, B.; Unger, C.; Werner, M.; Lieberzeit, P.A. Biomimetic Sensors to Detect Bioanalytes in Real-Life Samples Using Molecularly Imprinted Polymers: A Review. *Sensors* **2021**, *21*, 5550. [CrossRef]
6. Wulff, G.; Sarhan, A.; Zabrocki, K. Enzyme-Analogue Built Polymers and Their Use for the Resolution of Racemates. *Tetrahedron. Lett.* **1973**, *14*, 4329–4332. [CrossRef]
7. Arshady, R.; Mosbach, K. Synthesis of Substrate-Selective Polymers by Host-Guest Polymerization. *Makromol. Chem.* **1981**, *182*, 687–692. [CrossRef]
8. Vlatakis, G.; Andersson, L.I.; Müller, R.; Mosbach, K. Drug Assay Using Antibody Mimics Made by Molecular Imprinting. *Nature* **1993**, *361*, 645–647. [CrossRef]
9. Ahmad, O.S.; Bedwell, T.S.; Esen, C.; Garcia-Cruz, A.; Piletsky, S.A. Molecularly Imprinted Polymers in Electrochemical and Optical Sensors. *Trends Biotechnol.* **2019**, *37*, 294–309. [CrossRef]
10. Cenci, L.; Tatti, R.; Tognato, R.; Ambrosi, E.; Piotto, C.; Bossi, A.M. Synthesis and Characterization of Peptide-Imprinted Nanogels of Controllable Size and Affinity. *Eur. Polym. J.* **2018**, *109*, 453–459. [CrossRef]
11. Poma, A.; Turner, A.P.F.; Piletsky, S.A. Advances in the Manufacture of MIP Nanoparticles. *Trends Biotechnol.* **2010**, *28*, 629–637. [CrossRef] [PubMed]
12. Çimen, D.; Bereli, N.; Günaydın, S.; Denizli, A. Molecular Imprinted Nanoparticle Assisted Surface Plasmon Resonance Biosensors for Detection of Thrombin. *Talanta* **2022**, *246*, 123484. [CrossRef] [PubMed]
13. Wang, X.D.; Wolfbeis, O.S. Fiber-Optic Chemical Sensors and Biosensors (2015–2019). *Anal. Chem.* **2020**, *92*, 397–430. [CrossRef] [PubMed]

14. Cennamo, N.; Arcadio, F.; Seggio, M.; Maniglio, D.; Zeni, L.; Bossi, A.M. Spoon-Shaped Polymer Waveguides to Excite Multiple Plasmonic Phenomena: A Multisensor Based on Antibody and Molecularly Imprinted Nanoparticles to Detect Albumin Concentrations over Eight Orders of Magnitude. *Biosens. Bioelectron.* **2022**, *217*, 114707. [CrossRef] [PubMed]
15. Chiappini, A.; Pasquardini, L.; Bossi, A.M. Molecular Imprinted Polymers Coupled to Photonic Structures in Biosensors: The State of Art. *Sensors* **2020**, *20*, 5069. [CrossRef]
16. Ma, J.; Yan, M.; Feng, G.; Ying, Y.; Chen, G.; Shao, Y.; She, Y.; Wang, M.; Sun, J.; Zheng, L.; et al. An Overview on Molecular Imprinted Polymers Combined with Surface-Enhanced Raman Spectroscopy Chemical Sensors toward Analytical Applications. *Talanta* **2021**, *225*, 122031. [CrossRef] [PubMed]
17. Lowdon, J.W.; Diliën, H.; Singla, P.; Peeters, M.; Cleij, T.J.; van Grinsven, B.; Eersels, K. MIPs for Commercial Application in Low-Cost Sensors and Assays—An Overview of the Current Status Quo. *Sens. Actuators B Chem.* **2020**, *325*, 128973. [CrossRef]
18. Yang, Q.; Li, J.; Wang, X.; Peng, H.; Xiong, H.; Chen, L. Strategies of Molecular Imprinting-Based Fluorescence Sensors for Chemical and Biological Analysis. *Biosens. Bioelectron.* **2018**, *112*, 54–71. [CrossRef]
19. Kolanowski, J.L.; Liu, F.; New, E.J. Fluorescent probes for the simultaneous detection of multiple analytes in biology. *Chem. Soc. Rev.* **2018**, *47*, 195–2083. [CrossRef]
20. Kriz, D.; Ramström, O.; Mosbach, K. Peer Reviewed: Molecular Imprinting: New Possibilities for Sensor Technology. *Anal. Chem.* **1997**, *69*, 345A–349A. [CrossRef]
21. Turkewitsch, P.; Wandelt, B.; Darling, G.D.; Powell, W.S. Fluorescent Functional Recognition Sites through Molecular Imprinting. A Polymer-Based Fluorescent Chemosensor for Aqueous CAMP. *Anal. Chem.* **1998**, *70*, 2025–2030. [CrossRef]
22. Zhao, Y.; Ma, Y.; Li, H.; Wang, L. Composite QDs@MIP Nanospheres for Specific Recognition and Direct Fluorescent Quantification of Pesticides in Aqueous Media. *Anal. Chem.* **2012**, *84*, 386–395. [CrossRef] [PubMed]
23. Zhang, X.; Yang, S.; Jiang, R.; Sun, L.; Pang, S.; Luo, A. Fluorescent Molecularly Imprinted Membranes as Biosensor for the Detection of Target Protein. *Sens. Actuators B Chem.* **2018**, *254*, 1078–1086. [CrossRef]
24. Liu, H.; Fang, G.; Wang, S. Molecularly Imprinted Optosensing Material Based on Hydrophobic CdSe Quantum Dots via a Reverse Microemulsion for Specific Recognition of Ractopamine. *Biosens. Bioelectron.* **2014**, *55*, 127–132. [CrossRef]
25. Meyer-Almes, F.-J. Fluorescence Lifetime Based Bioassays. *Methods Appl. Fluoresc.* **2017**, *5*, 042002. [CrossRef] [PubMed]
26. Berezin, M.Y.; Achilefu, S. Fluorescence Lifetime Measurements and Biological Imaging. *Chem. Rev.* **2010**, *110*, 2641. [CrossRef]
27. Wandelt, B.; Turkewitsch, P.; Wysocki, S.; Darling, G.D. Fluorescent Molecularly Imprinted Polymer Studied by Time-Resolved Fluorescence Spectroscopy. *Polymer* **2002**, *43*, 2777–2785. [CrossRef]
28. Wandelt, B.; Mielniczak, A.; Cywinski, P. Monitoring of CAMP-Imprinted Polymer by Fluorescence Spectroscopy. *Biosens. Bioelectron.* **2004**, *20*, 1031–1039. [CrossRef]
29. Lin, Z.; Li, W.-J.; Chen, Q.-C.; Peng, A.; Huang, Z. Rapid Detection of Malachite Green in Fish with a Fluorescence Probe of Molecularly Imprinted Polymer. *Int. J. Polym. Anal. Charact.* **2019**, *24*, 121–131. [CrossRef]
30. Quílez-Alburquerque, J.; Descalzo, A.B.; Moreno-Bondi, M.C.; Orellana, G. Luminescent Molecularly Imprinted Polymer Nanocomposites for Emission Intensity and Lifetime Rapid Sensing of Tenuazonic Acid Mycotoxin. *Polymer* **2021**, *230*, 124041. [CrossRef]
31. Birch, D.J.S.; Imhof, R.E. Time-Domain Fluorescence Spectroscopy Using Time-Correlated Single-Photon Counting. *Top. Fluoresc. Spectrosc.* **2002**, *1*, 1–95. [CrossRef]
32. Nečas, D.; Klapetek, P. Gwyddion: An Open-Source Software for SPM Data Analysis. *Cent. Eur. J. Phys.* **2012**, *10*, 181–188. [CrossRef]
33. Chakraborti, S.; Joshi, P.; Chakravarty, D.; Shanker, V.; Ansari, Z.A.; Singh, S.P.; Chakrabarti, P. Interaction of Polyethyleneimine-Functionalized ZnO Nanoparticles with Bovine Serum Albumin. *Langmuir* **2012**, *28*, 11142–11152. [CrossRef]
34. Cennamo, N.; Bossi, A.M.; Arcadio, F.; Maniglio, D.; Zeni, L. On the Effect of Soft Molecularly Imprinted Nanoparticles Receptors Combined to Nanoplasmonic Probes for Biomedical Applications. *Front. Bioeng. Biotechnol.* **2021**, *9*, 801489. [CrossRef] [PubMed]
35. Takeuchi, T.; Sunayama, H.; Takano, E.; Kitayama, Y. Post-Imprinting and In-Cavity Functionalization. *Adv. Biochem. Eng. Biotechnol.* **2015**, *150*, 95–106. [CrossRef]
36. Matsumoto, H.; Sunayama, H.; Kitayama, Y.; Takano, E.; Takeuchi, T. Site-Specific Post-Imprinting Modification of Molecularly Imprinted Polymer Nanocavities with a Modifiable Functional Monomer for Prostate Cancer Biomarker Recognition. *Sci. Technol. Adv. Mater.* **2019**, *20*, 305–312. [CrossRef]
37. Prozeller, D.; Morsbach, S.; Landfester, K. Isothermal Titration Calorimetry as a Complementary Method for Investigating Nanoparticle-Protein Interactions. *Nanoscale* **2019**, *11*, 19265–19273. [CrossRef]
38. Pierce, M.M.; Raman, C.S.; Nall, B.T. Isothermal Titration Calorimetry of Protein–Protein Interactions. *Methods* **1999**, *19*, 213–221. [CrossRef]
39. Kirschner, S.; Belloni, B.; Kugler, C.; Ring, J.; Brockow, K. Allergenicity of Wine Containing Processing Aids: A Double-Blind, Placebo-Controlled Food Challenge. *J. Investig. Allergol. Clin. Immunol.* **2009**, *19*, 210–217.
40. Jain, A.; Blum, C.; Subramaniam, V. Fluorescence Lifetime Spectroscopy and Imaging of Visible Fluorescent Proteins. In *Advances in Biomedical Engineering*; Elsevier: Amsterdam, The Netherlands, 2009; pp. 147–176.
41. Scientific Opinion on Risk Based Control of Biogenic Amine Formation in Fermented Foods. *EFSA J.* **2011**, *9*, 2393. [CrossRef]

42. Khumsap, T.; Bamrungsap, S.; Thu, V.T.; Nguyen, L.T. Development of Epitope-Imprinted Polydopamine Magnetic Nanoparticles for Selective Recognition of Allergenic Egg Ovalbumin. *Chem. Pap.* **2022**, *76*, 6129–6139. [CrossRef]
43. Ambrosini, S.; Beyazit, S.; Haupt, K.; Tse Sum Bui, B. Solid-phase Synthesis of Molecularly Imprinted Nanoparticles for Protein Recognition. *Chem. Commun.* **2013**, *49*, 6746–6748. [CrossRef] [PubMed]

Supplementary information

Time resolved fluorescence spectroscopy of molecularly imprinted nanoprobes as an ultralow detection nanosensing tool for protein contaminants.

1. **Calibration curve FluorMAA**

Figure S1. Calibration curve of FluorMAA

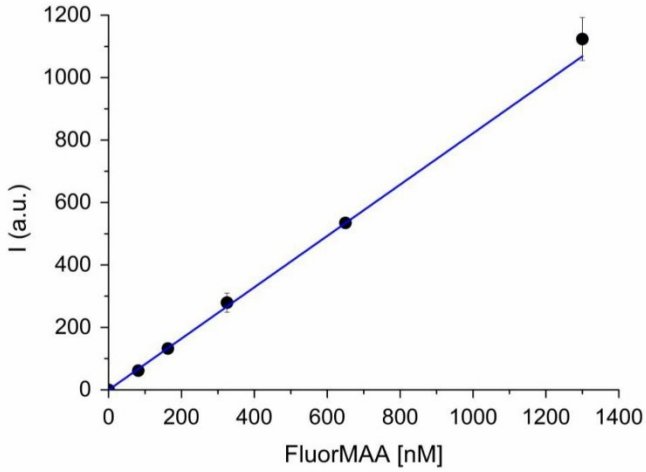

Table S1. Equation parameters of the FluorMAA calibration curve.

Equation	y = a + bx
Intercept (a)	-0.1273
Slope (b)	0.8219
R square	0.9999

2. Fluorescence lifetime of FluorMAA

The time-resolved fluorescence decays were collected as described in Section 2.7. Measurements were performed in a 1 mL quartz cuvette, using a fixed concentration of 155 pmol of FluorMAA in PBS (10 mM pH 7.4), adding increasing concentrations of HSA (15 fM – 15 nM). To allow binding kinetics' stabilization, a 20 min incubation was awaited before performing each measurement.
Because the fluorophore was freely solvated in solution, data were elaborated with the Decay Analysis Software v. 6.8 (Horiba Scientific), choosing the monoexponential fitting equation model:

$$I(t) = A + B_1 e^{-t/\tau 1}$$

3. Dynamic light scattering (DLS) of Fluo-nanoMIPs

Figure S2. Examples of DLS measurements of (A) 0.1× and (B) 1×Fluo-nanoMIPs.

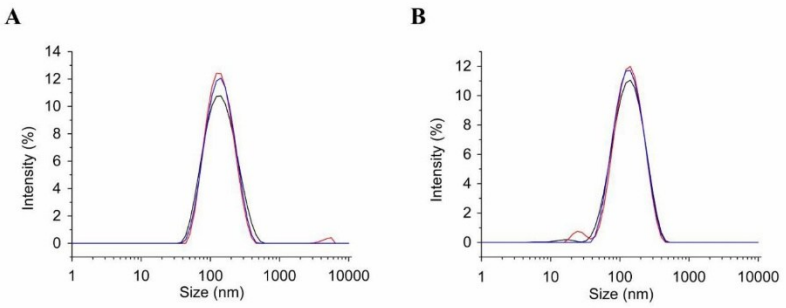

4. Isothermal titration calorimetry

Figure S3. Isothermal titration nanocalorimetry data of 1×Fluo-nanoMIP titrated with the non template protein human serum transferrin and expressed as raw heats over time.

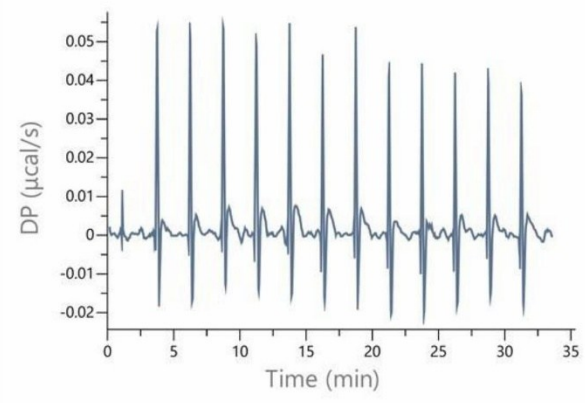

Paper II

Molecularly Imprinted Polymers Electrochemical Sensing: The Effect of Inhomogeneous Binding Sites on the Measurements and Comparison between Imprinted Polyaniline versus nanoMIP-Doped Polyaniline Electrodes for the EIS Detection of 17β-Estradiol

Summary

This work aims to evaluate the effects of inhomogeneous versus homogeneous imprinted binding sites on electrochemical sensing measurements and to determine whether binding site heterogeneity influences the sensor's sensitivity and overall performance. To simulate these two different structural scenarios, two types of electrochemical MIP-based sensors were designed and compared. The first configuration, referred to as the Imprinted PANI layer, consisted of an electropolymerized molecularly imprinted thin layer of polyaniline (PANI) and was considered representative of an inhomogeneous binding site distribution. The second configuration, the NanoMIP-doped PANI, comprised an electropolymerized thin film of PANI doped with pre-synthesized nanoMIPs, which act as discrete and uniform three-dimensional recognition sites, representing a homogeneous binding site distribution. The 17β-estradiol (E2), a hormone that is classified as an endocrine disruptor at certain concentration levels, was selected as the target analyte to compare the electrochemical behaviour of the two sensing architectures through EIS, thereby explaining how the organization of the recognition sites affects the analytical response.

Both sensing architectures were fabricated on gold screen-printed electrodes (SPEs) using PANI as the conductive polymer matrix. The Imprinted PANI layer was prepared by surface electropolymerization of aniline in the presence of E2 as the template molecule, leading to the formation of a thin imprinted film directly onto the electrode surface. In contrast, the NanoMIP-doped PANI electrode was

fabricated by dispersing pre-synthesized nanoMIPs, previously optimized for E2 recognition, into the aniline monomer solution prior to the electropolymerization step. This approach allowed the incorporation of discrete and uniform imprinted nanostructures within the conductive PANI network, combining the high electrical conductivity of the polymer with the molecular selectivity and structural homogeneity of the nanoMIPs. The electrochemical deposition process was monitored by CV to ensure the successful growth of the PANI layer, whose morphology and structural features were further examined by SEM and Fourier-transform infrared spectroscopy (FT-IR) analyses. These complementary characterizations confirmed the uniform coverage of the electrode surface by the PANI layer and the successful incorporation of nanoMIPs within the PANI matrix. The sensing behaviour of the two architectures was evaluated using EIS by recording the variation in Rct upon incubation with increasing concentrations of E2, ranging from 0.01 to 100 ng/mL. For both sensing configurations, a gradual increase in Rct was observed as the E2 concentration increased, indicating a reduction in electron transfer efficiency due to the formation of the analyte-polymer complex. In contrast, the corresponding control electrodes, prepared either as a non-imprinted PANI layer or as a PANI layer doped with non-imprinted polymer nanoparticles, showed no significant change in impedance, confirming that the observed response originated from specific molecular recognition rather than nonspecific adsorption phenomena. To further compare the binding performance and site distribution homogeneity of the two systems, the calibration data were fitted using both the Langmuir model, which is intended to describe monomodal binding sites (n=1), and the Hill equation model, which extends the binding site degree of freedom to n. For the Imprinted PANI layer, the Langmuir model provided a poor fit (R^2=0.8863), suggesting that the electropolymerization of PANI in the presence of the soluble E2 template generated a heterogeneous distribution of binding sites. In contrast, the Hill model yielded a significantly better correlation (R^2=0.9934), but with an n value of 0.34. Considering n as an indicator related to the degree of surface heterogeneity, where n=1 represents full homogeneity, these results confirmed the inhomogeneous nature of the binding cavities in the Imprinted PANI layer. Conversely, the NanoMIP-doped PANI electrode exhibited excellent

fitting to both models (Langmuir R^2=0.9690 and Hill R^2=0.9955), with a Hill model n value of 0.79, much closer to unity than that of the Imprinted PANI layer (n = 0.34). This finding demonstrates that the NanoMIP-doped PANI system possesses a more homogeneous population of binding sites, consistent with the discrete and uniform nature of the nanoMIPs. Furthermore, the linearization parameters derived from the binding curves indicated that the slope of the NanoMIP-doped PANI sensor was almost twice that of the Imprinted PANI layer, revealing a markedly higher sensitivity and confirming that the incorporation of nanoMIPs significantly enhances the recognition efficiency and electrochemical response of the sensor. The superior sensing performance of the NanoMIP-doped PANI electrode was further confirmed by comparing the analytical parameters of the two sensors. In particular, the LOD achieved with the NanoMIP-doped PANI sensor was 2.86 pg/mL, which is lower than that obtained with the Imprinted PANI layer (65 pg/mL), confirming its enhanced capability for trace-level detection of E2.

The selectivity of both sensing architectures was evaluated by exposing the electrodes to structurally related compounds, namely progesterone (P) and bisphenol A (BPA), under the same experimental conditions used for E2 detection. Both the Imprinted PANI and the NanoMIP-doped PANI sensors exhibited negligible variations in charge transfer resistance in the presence of these potential interferents, confirming the high molecular specificity of the imprinted sites toward the target analyte.

Finally, to evaluate the applicability in complex matrices, the optimized NanoMIP-doped PANI sensor was tested in spiked wastewater samples containing known concentrations of E2 (0.1, 1, and 10 ng/mL). The measured recovery values were 98.7%, 96.9%, and 68.7%, respectively, demonstrating that the sensor maintained its selectivity and sensitivity even in complex environmental matrices.

Overall, this study directly contributes to the general aim of the thesis by demonstrating how the homogeneity of imprinted binding sites critically affects the analytical performance of MIP-based sensors. The comparison between the electropolymerized Imprinted PANI layer and the nanoMIP-doped PANI configuration highlights that the incorporation of pre-synthesized, structurally

uniform nanoMIPs provides a more controlled recognition environment, resulting in enhanced sensitivity and lower detection limits. These findings confirm the effectiveness of using homogeneous and nanostructured MIP systems as a key strategy to develop high-performance sensing platforms.

Published article

ACS SENSORS

pubs.acs.org/acssensors Article

Molecularly Imprinted Polymers Electrochemical Sensing: The Effect of Inhomogeneous Binding Sites on the Measurements. A Comparison between Imprinted Polyaniline versus nanoMIP-Doped Polyaniline Electrodes for the EIS Detection of 17β-Estradiol

Alice Marinangeli, Iva Chianella, Eros Radicchi, Devid Maniglio, and Alessandra Maria Bossi*

Cite This: *ACS Sens.* 2024, 9, 4963−4973 Read Online

ACCESS | Metrics & More | Article Recommendations | Supporting Information

ABSTRACT: Molecularly imprinted polymers (MIPs) are synthetic receptors made by template-assisted synthesis. MIPs might be ideal receptors for sensing devices, given the possibility to custom-design selectivity and affinity toward a targeted analyte and their robustness and ability to withstand harsh conditions. However, the synthesis of MIP is an inherently random process that produces a statistical distribution of binding sites, characterized by a variety of affinities. This is verified both for bulk MIP materials and for MIP's thin layers. In the present work, we aimed at assessing the effects of inhomogeneous versus homogeneous imprinted binding sites on electrochemical sensing measurements, and the possible implications on the sensor's performance. In the example of an Electrochemical Impedance Spectroscopy (EIS) sensor for the 17β-estradiol (E2) hormone, the scenario of inhomogeneous binding sites was studied by modifying electrodes with an E2-MIP polyaniline (PANI) thin layer, called the "Imprinted PANI layer". In contrast, the condition of discrete and uniform binding sites was epitomized by electrodes modified with a thin PANI layer purposedly doped with E2-MIP nanoparticles (nanoMIPs), which were referred to as "nanoMIP-doped PANI". The behaviors of the two EIS sensors were compared. Interestingly, the sensitivity of the nanoMIP-doped PANI was almost twice with respect to that of the imprinted PANI layer, strongly suggesting that the homogeneity of the binding sites has a fundamental role in the sensor's development. The nanoMIP-doped PANI sensor, which showed a response for E2 in the range 36.7 pM−36.7 nM and had a limit of detection of 2.86 pg/mL, was used to determine E2 in wastewater.

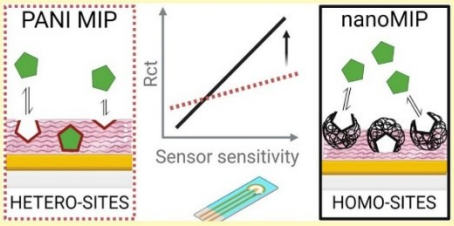

KEYWORDS: *molecularly imprinted polymers, molecularly imprinted nanoparticles, polyaniline, homogeneous binding sites, heterogeneous binding sites, electrochemical impedance spectroscopy, 17β-estradiol, water pollution*

Molecularly imprinted polymers (MIPs) are synthetic polymers engineered to have selective binding sites for specific target analytes.[1,2] MIPs are prepared through template-assisted polymerization in which the target analyte acts as a template. Briefly, solvated functional monomers form a complex with the template, which is fixed next through polymerization. At the completion of the synthesis, the removal of the template frees molecular cavities that are complementary in size, shape, and functional group stereo-arrangements to the target analyte. As a result, MIPs display the ability to specifically and selectively rebind the targeted analyte, qualifying as ideal receptors for sensing applications.

A challenge in molecular imprinting is posed by the heterogeneity of the binding sites formed through the imprinting process. Not all the sites stamped in the MIP material possess identical affinity and specificity for the target analyte, leading to variability in binding efficiency and selectivity.[3] Such heterogeneity is due to variations in the polymerization process,[4] such as the template orientation in the nascent material, an excess of functional groups in the polymer, the distribution of functional groups in the polymeric network, and ultimately the accessibility of the formed binding sites (Figure 1A), with possible detrimental effects on the performance and the reproducibility of the MIP-based sensing measurements.

The issue of heterogeneous binding sites is particularly severe for MIPs prepared in bulk formats, where no control could be attained over the synthesis of the macro-polymer, nor, later, over the accessibility of the imprinted sites.[3] Electro-

Received: July 16, 2024
Revised: August 20, 2024
Accepted: August 23, 2024
Published: August 29, 2024

https://doi.org/10.1021/acssensors.4c01787
ACS Sens. 2024, 9, 4963−4973

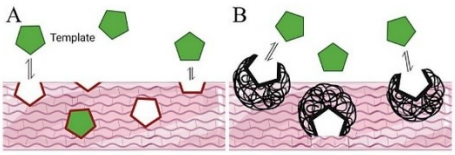

Figure 1. Scheme depicting the heterogeneity of binding sites formed by means of the molecular imprinting process, in the case of electropolymerization of PANI (A); homogeneous binding sites obtained by doping with nanoMIPs PANI (B).

polymerization of MIP's thin films, starting from semiconducting monomers, has gained momentum, offering superior control over the thickness of the nascent MIP layers, being easily attained by varying the number of electropolymerization cycles, with the ultimate effect of gaining higher control over the imprinted sites. As a result, MIP thin films, prepared by electropolymerization, are widely employed in sensing.[5−10] Despite favorable binding kinetics and reproducibility of the synthetic processes, the expectations over the homogeneity of the binding sites produced by electropolymerization of MIP thin films seem somehow contradicted by binding data reported in the literature, which are often best-fitted with isotherm equations that contain a heterogeneity parameter.[11,12]

Several authors have critically discussed the equation models to fit experimental data of an analyte that binds to the MIP.[4,13,14] Briefly, the Langmuir equation is specific to describe binding processes where an analyte binds to a homogeneous surface with a finite number of identical binding sites. Langmuir model is expressed by the formula $q_e = q_m K_L [L]/1 + K_L [L]$, where q_e is the amount of adsorbate per unit mass of adsorbent; q_m is the maximum amount of adsorbate per unit mass of adsorbent; $[L]$ is the concentration of adsorbate; and K_L is the Langmuir constant.

Instead, equations meant to describe heterogeneous binding sites are the Freundlich and Sips models. The Freundlich isotherm is used for describing adsorption on heterogeneous surfaces and is expressed by the equation: $q_e = K_F [L]^{1/n}$, where q_e is the amount of adsorbate per unit mass of adsorbent; $[L]$ is the concentration of adsorbate; K_F is the Freundlich constant; $1/n$ is a heterogeneity factor. Freundlich's model assumes a nonuniform distribution of binding sites and does not assume a fixed number of identical binding sites. Overall, the Freundlich isotherm gives a general description of adsorption capacity across a range of concentrations. As an alternative, the Langmuir−Freundlich isotherm, also called the Sips isotherm, can be used. Sips equation has the following expression: $q_e = K_S [L]^n (1+ K_S [L]^n)^{-1/n}$, where q_e is the amount of adsorbate per unit mass of adsorbent; $[L]$ is the concentration of adsorbate; K_S is the Sips constant and n is the heterogeneity factor, indicating the degree of nonlinearity between solution concentration and adsorption. Sips is a model that combines features of both the Langmuir and Freundlich isotherms, making it suitable for heterogeneous surfaces with a finite number of binding sites. Frequently, the binding of an analyte to its MIP is fitted with the Hill equation, whose expression is $\theta = [L]^n/K_d + [L]^n$, where θ is the fraction of binding sites occupied; $[L]$ is the ligand concentration; K_d is the dissociation constant and n is the Hill coefficient, which is a coefficient intended to indicate cooperativity ($n > 1$ indicates positive cooperativity; $n = 1$ indicates noncooperative (independent) binding; $n < 1$ indicates negative cooperativity). The Hill equation model is meant to describe cooperative binding rather than the heterogeneity of binding sites. However, it can provide insights into apparent heterogeneity, through its description of cooperative effects. In fact, the Hill model can reflect apparent heterogeneity if $n \neq 1$, with the *caveat* that it does not explicitly account for different binding affinities among various sites on the surface.

Very often, the most accurate descriptor of the interaction between an analyte and the MIP-sensor's surface is a model equation that include heterogeneity, such as Hill, Freundlich, Sips equation models, with $n \neq 1$, suggesting the presence of nonuniform binding sites.[11,15]

The present work is intended to assess which effects inhomogeneous *versus* homogeneous imprinted binding sites have on the electrochemical sensing measurements and whether heterogeneity has possible implications on the efficiency of the sensor's performance.

To simulate the different scenarios, we compared the sensing measurements from electrodes modified with a polyaniline (PANI) MIP thin layer, called the "imprinted PANI layer" and epitomizing the inhomogeneous imprinted binding site condition (Figure 1A), with electrodes prepared with an electrochemically deposited PANI thin layer purposedly doped with MIP nanoparticles (nanoMIPs), that acted as discrete and uniform three-dimensional selective binding sites and were called "nanoMIP-doped PANI" (Figure 1B). The model of uniform binding sites, as shown in Figure 1B, assumes a simplified two-state condition system, in which the binding sites are either accessible or nonaccessible to the analyte, depending on the orientation of the nanoMIPs dispersed in the PANI layer.

The target analyte selected for the comparison was 17β-estradiol (E2), an estrogen hormone, vital for human biology and physiology, playing crucial roles in regulating reproduction, cardiovascular health, gastrointestinal processes, bone strength, cognitive behavior, and pregnancy. Released in the environment, for its industrial, agricultural, and feed production uses, E2 has anabolic effects disruptive both for aquatic ecosystems and humans.[16] In fact, E2 is classified as an endocrine-disrupting chemical, interfering with normal endocrine function. Consequently, it is crucial to ensure that E2 levels in the environment remain below accepted No-Observed Effect Levels (NOELs).[17,18]

Electrochemical sensors to determine E2 have long been developed, in view of offering fast and accurate information in a cost-effective manner.[19] Several E2 selective MIPs have been reported as receptor elements with the aim of improving the selectivity of the sensors.[20] Among these, an E2MIP sensor was prepared from a versatile monomer *N*-phenylethylene diamine methacrylamide (NPEDMA),[21] by the electropolymerization of aniline moiety of NPEDMA onto the surface of the electrode, followed by an orthogonally polymerized MIP layer. As a result, the MIP sensor displayed a limit of detection (LOD) of 6.86×10^{-7} M with a linearity range between 1×10^{-7} M and 8×10^{-7} M. Higher sensitivities and lower LODs were reported for electrically conducting materials, such as carbon nanotubes, graphene, and noble metal nanoparticles, deposited at the interface between the electrode and the MIP.[7] Yuan et al. deposited platinum nanoparticles (PtNPs) onto the electrode, so to increase the surface area, hence the conductivity, followed by 6-mercaptonicotinic acid (MNA)

https://doi.org/10.1021/acssensors.4c01787
ACS Sens. 2024, 9, 4963−4973

self-assembling at the PtNPs/GCE surface in the presence of the template E2 and electropolymerization.[22] Differential pulse voltammetry (DPV) detected E2 in the linear range 30 nM−50 μM with a LOD of 16 nM. Additionally, a sandwich-type molecular imprinting electrochemical sensor (MIES) for the determination of E2 in makeups was prepared onto doubly layered reduced graphene oxide (rGO) combined with PtNPs and a MIP film made by the electropolymerization of MNA in the presence of E2.[23] DPV measurements showed a LOD of 2 nM and two linear regions, namely 4−60 nM and 60 nM−50 μM, supporting the heterogeneity of the MIP binding sites.

Electrochemical Impedance Spectroscopy (EIS)[24,25] with gold nanoparticles (AuNPs), instead of PtNPs,[26] and a *p*-aminothiophenol (ATP) electropolymerized E2-MIP, permitted the determination of E2 in milk with a LOD of 1.28 fg/mL and a linear detection range from 1.0 fg/mL to 100 pg/mL. Instead, E2 detection in river waters was reported by Florea et al.[27] with linear sweep voltammetry, LOD of 1.09 fM (0.297 fg/mL), and a linear detection range from 3.6 fM to 3.6 nM (corresponding to 0.981 fg/mL to 0.981 ng/mL).

In the present work, we attempted to study the specific contribution given by the templated binding sites to the sensor's signal. For this, we compared screen-printed gold electrodes (gold SPE) modified with an "imprinted PANI layer", that would presumably bear nonuniform binding sites, to gold SPE modified with a nanoMIP-doped PANI, to simulate discrete and uniform binding sites. The two EIS electrochemical sensors were compared in terms of the sensitivity and performance for the detection of E2. Binding behaviors anticipated that uniform binding sites indeed improved the sensor's performance.

■ EXPERIMENTAL SESSION

Chemicals. Acrylamide (Aam), *N-tert*-butylacrylamide (tBAm), methacrylic acid (MAA), *N*,*N*′-methylene bis(acrylamide) (BIS), *N*,*N*,*N*′,*N*′-tetramethyl ethylenediamine (TEMED), ammonium persulfate (APS), β-estradiol, progesterone, bisphenol A (BPA), *N*-Cyclohexyl-2-aminoethanesulfonic acid (CHES), saline phosphate buffer (PBS), ethanol, sulfuric acid, sodium hydroxide, salt potassium ferrocyanide, and Triton X-100 and were from Sigma-Aldrich (Merck KGaA, Darmstadt, Germany). Aniline was from Thermo Scientific (Thermo Fisher Scientific, Massachusetts, USA).

Synthesis of nanoMIPs and Control NPs. The synthesis of the nanoMIPs was carried out by using a total monomer concentration of 0.2% (w/v). The monomers used were 9.5 μmol of Aam, 10.2 μmol of MAA, 5.3 μmol of *t*BAm, and 103.7 μmol of BIS, admixed in a volume of 10 mL of 20 mM PB at pH 7.4, supplemented with a submicellar concentration of SDS (0.01% w/v). The template, estradiol, was added to the polymerization solution at the final concentration of 1.28 mM. Vials were closed with rubber caps and bubbled with N_2 for 10 min. The catalysts, APS (0.04% w/v) and TEMED (0.03% w/v) were added and the polymerization was carried out overnight at room temperature under mild stirring. Nonimprinted polymers (control NPs) were synthesized with the same protocol without the addition of the template. At the completion of the polymerization of nanoMIPs, the removal of the template was carried out by adding 2 mL of CHES-free base 50 mM to obtain a solution with pH > 9. Both nanoMIPs and control NPs were dialyzed against 1 L of Milli-Q water for 1 h using a dialysis tubing with 14.000 MWCO (Sigma-Aldrich, Milan, Italy). Then nanoparticles were dialyzed with 2 × 3 L of Milli-Q water. Next, the nanoMIPs and control NPs were freeze-dried and stored. The yield of polymerization was 98% for the nanoMIPs and 96% for control NPs, as estimated from the weight of the lyophilized nanoparticles with respect to the total weight of the monomers used in the synthesis.

Dynamic Light Scattering (DLS). Size distribution and polydispersity index (PDI) were determined using a Zetasizer Nano ZEN3600 (Malvern Instruments Ltd., Worcestershire, UK) equipped with a 633 nm He−Ne laser at a detection angle of 173°. NanoMIPs were suspended in water to the final concentration of 1 mg/mL. The material refractive index (RI) was 1.490 and the absorption value was 0.01; the dispersant RI was 1.332 for water, and the viscosity was 0.89 cP as reported by the Zetasizer v.6.32 software (Malvern Instruments Ltd., Worcestershire, UK). The temperature was set at 25 °C. Measurements were in triplicate.

Electrochemical Polymerization of PANI on Gold Electrodes. Electrochemical polymerizations were performed using a Palmsens4 potentiostat (Palmsens BV, Houten, Netherlands) using a screen-printed gold electrode 220BT (Metrohm DropSense S.L., Llanera, Spain) with Au as working and auxiliary electrodes and Ag as the reference electrode. Before the electrochemical polymerization, to clean the sensor surface, electrodes were rinsed with deionized water and then a volume of 200 μL of H_2SO_4 0.25 M was placed on the electrodes and 3 scans of cyclic voltammetry (CV) was performed between −0.6 and +0.5 V at a scan rate of 0.05 V/s. Prior to the preparation of electrodes, the electrochemical behavior of E2 was investigated to confirm no contribution (Figure S1). For the electrochemical polymerization CV was performed between −0.5 and +0.8 V for 15 cycles (Figure S2) at a scan rate of 0.05 V/s in a solution of aniline 0.025 M, previously diluted in H_2SO_4 0.25 M, in the presence of E2 at the final concentration of 660 μM to prepare the imprinted PANI layer and without E2 to prepare the PANI control layer. Both the imprinted PANI and PANI control were then subjected to a sequence of washing steps, carried out in the oven at a temperature of 40 °C. Such steps consisted in dipping the electrodes in a solution of 75% NaOH 0.1 M and 25% EtOH for 15 min, followed by an absolute EtOH solution for 5 min, with the whole process repeated twice. Then, the surface was blocked by placing a volume of 200 μL of PBS pH 5 supplemented with 0.05% Triton X-100 on the electrode for 1 h. The electrodes were washed with deionized water and dried.

Electrochemical Impedance Spectroscopy (EIS). EIS, performed using the Palmsens4, was used to monitor changes at the electrode surface both during the preparation of the sensor (e.g., polymerization, washing, and blocking steps) and to assess rebinding in the presence of increasing concentrations of E2. For the EIS measurements, a volume of 200 μL of 0.01 M $Fe(CN)_6^{3-/4-}$ in PBS pH 5 was first placed on the electrode and incubated for 15 min to equilibrate. Then, the signal was recorded by setting a further equilibration time of 120 s, a 0.01 a.c. s and 0.01 ac and 0.12 d.c. voltages. The frequency varied from 0.1 to 50000 Hz with 6.5 points impedance reading per decade. The impedance data were then represented in the form of Nyquist plots, which were fitted to an equivalent circuit (Figure S3) by the analysis function in PSTrace software (Palmsens BV, Houten, The Netherlands) to extrapolate the charge-transfer resistance (R_{ct}) values.

Electrochemical Polymerization of PANI Doped with nanoMIPs on Gold Electrodes. Electrodes were prepared as reported in Electrochemical polymerization of PANI on gold electrodes section but using a solution of aniline 0.025 M, diluted in H_2SO_4 0.25 M and supplemented with nanoMIPs (or control NPs) at the final concentration of 1 mg/mL.

After electrochemical polymerization, electrodes were washed with deionized water and dried. To block the surface, a volume of 200 μL of PBS pH 5 supplemented with 0.1% Triton X-100 was placed on the electrodes for 1 h. Then the electrodes were washed with deionized water and dried. The same protocol was used for the electrochemical polymerization of PANI doped with the control NPs.

Scanning Electron Microscope (SEM). SEM analysis was conducted using a Supra 40 field emission microscope (Carl Zeiss AG, Oberkochen, Germany), collecting secondary electron emissions with a primary beam acceleration voltage of 2.5 kV.

FT-IR. FTIR spectra were obtained using a Spectrum Two FT-IR spectrometer (PerkinElmer, Massachusetts, USA), covering the spectral range from 400 to 4000 cm^{-1} with a resolution of 1 cm^{-1}.

https://doi.org/10.1021/acssensors.4c01787
ACS Sens. 2024, 9, 4963−4973

Isothermal Titration Calorimetry (ITC). Isothermal titration calorimetry (ITC) was performed on a Nano Isothermal Titration Calorimeter TA (TA Instruments, New Castle, USA) instrument. All solutions were filtered and degassed prior to use. The nanoMIPs were solubilized in 10 mM PBS pH 7.4 at the final concentration of 2 mg/mL. Then, nanoMIP solution (230 μL) was titrated with E2 (3.6 μM, V = 50 μL; 3 μL per injection) at 25 °C, and the heats of the interactions were recorded in triplicate. Dilution heats were estimated from the titration of the E2 in the buffer (n = 3). Raw heats were subtracted from the dilution heats and integrated. Integrated heats were plotted as a function of the molar ratio between the titrand and the titrant and fitted with one set of sites modeled with the NanoAnalyze Software v. 3.4.0 (TA Instruments, New Castle, DE); according to manufacturer: Bound = $(-b - \mathrm{Sqrt}(b \times b - 4a \times c))/(2a)$; $K_{a\_value} = 1/K_d$; the quadratic constants a, b, and c were defined as follows: $a = K_{a\_value}$; $b = -K_{a\_value}$ * (Mol_Syringe (iteration) + Mol_Cell (iteration) * n)−CellVolume (iteration/1e6); $c = K_{a\_value}$ * Mol_Syringe (iteration) * Mol_Cell (iteration) * n. The enthalpy ($\Delta H°$) was calculated from Heat = 1e9 * (Bound − Old bound) * dh; and free energy variation ($\Delta G°$) were calculated from K_D and $\Delta H°$.

Estradiol Rebinding. For the E2 rebinding experiments, a volume of 200 μL of PBS was supplemented with H_2SO_4 to pH 5, without E2 (0) first and then with increasing concentrations of E2 (from 0.01 to 500 ng/mL). Each solution was placed on the electrode for 30 min followed by washing with deionized water. EIS measurements and data fitting were then carried out after each analyte concentration as explained in the Electrochemical Impedance Spectroscopy (EIS) section. The R_{ct} values recorded for each concentration were then normalized using the following formula:

$$\text{Norm. } R_{ct} = \frac{R_{ct\,x} - R_{ct0}}{R_{ct0}} \quad (1)$$

Sensor's Parameters. Normalized R_{ct} values, plotted as a function of E2 concentration, were fitted with Langmuir (eq 2) and Hill (eq 3) equation models (OriginPro 9.0):

$$R_{ct} = R_{ct\_max}\frac{x}{(K + x)} \quad (2)$$

$$R_{ct} = R_{ct\_max}\frac{x^n}{(K + x^n)} \quad (3)$$

where R_{ct} is the impedance at concentration x of the ligand (i.e., [E2]); R_{ct_max} is the R_{ct} value at binding saturation; n is the Hill parameter that correlates with the number of binding sites and K is the apparent dissociation constant derived from the mass law action.

Cross-Reactivity Studies. The selectivity of both imprinted PANI and PANI doped-nanoMIPs electrodes was tested in EIS using two analogues, bisphenol A and progesterone, at three different concentrations (0.1, 1, and 50 ng/mL). Rebiding of analogues was done in the same way as rebiding of E2 and the EIS measurements were performed as reported in the "Electrochemical Impedance Spectroscopy (EIS)" section.

Wastewater Sample Collection. The wastewater sample (1 L) was collected from the outlet of the wastewater treatment tank of the UKCRIC National Research Facilities for Water and Wastewater Treatment situated at Cranfield University. Immediately after collection, the sample was transferred to the laboratory and aliquoted in 50 mL falcon tubes, and these were stored at −20 °C until use.

Real Sample Analysis. Both imprinted PANI and PANI doped-nanoMIPs electrodes were tested with the wastewater sample, spiked with increasing concentrations of estradiol (0.1, 1, and 50 ng/mL). Specifically, the wastewater sample was spiked with estradiol either before or after filtration with a 0.45 μm PTFE filter (Corning Incorporated, New York, USA) and diluted 1:1 with phosphate buffer supplemented with a solution of H_2SO_4 (pH 5). A volume of 200 μL of the spiked sample was then placed on the electrodes, and after 30 min of incubation, EIS measurements were performed as described in the section Electrochemical Impedance Spectroscopy (EIS).

Statistical Analysis. Data significance was evaluated by performing a one-way ANOVA test with posthoc Tukey HSD using the online tool provided at https://astatsa.com.

Computational Details. Density Functional Theory (DFT) simulations were carried out with the ORCA Software, Version 5.0.3.[28−30] Geometry optimization of the monomer-estradiol adducts were performed with the RIJCOSX approximation[31] and employing the B3LYP exchange-correlation functional,[32] a def2-SVP together with the auxiliary def2/J basis sets, and D3BJ to take into account dispersion interactions.

RESULTS AND DISCUSSION

Rational Selection of the Monomers. Molecular modeling by means of DFT was used to estimate the theoretical strength of the interaction between monomers and templates as a method to rationally select the best monomer composition for the imprinting processes.[33] The monomer composition is pivotal for generating stable pre-polymerization complexes in solution, thus fixing the binding cavity's stereochemistry, ultimately favoring highly selective MIPs. Here, we compared the interaction energy between E2 and its imprinted PANI layer, which epitomized the condition of the continuum of binding sites, against the interaction energy between E2 and polyacrylamide's nanoMIPs, prepared by means of a standard monomers mixture composition,[34] which epitomized discrete homogeneous binding sites. The molecular interactions between E2 and aniline or E2 and each functional monomer used for the synthesis of the nanoMIPs are reported in Figure 2. The interaction energies (ΔE) for the

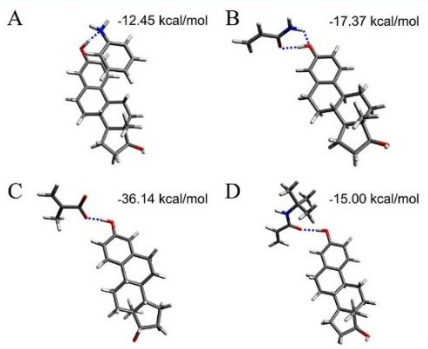

Figure 2. Molecular modeling. Sketches of the interaction between E2 and the monomers: Aniline (A), that is, the monomer used to prepare the imprinted-PANI layer, and the functional monomers used for the synthesis of the nanoMIPs, that are Acrylamide (B), methacrylic acid (C), and *tert*-butylacrylamide (D).

pairs E2/aniline and for E2/acrylamides were calculated from the energy difference between the pair and the isolated E2 and template molecules, resulting in a ΔE of −12,45 kcal/mol for aniline, while this further lowered to −36.14, −17.37, and −15.00 kcal/mol for the deprotonated MAA, Aam, and *t*BAm, respectively, suggesting more stabilizing interactions in the case of the acrylamide derivatives.

Imprinted PANI EIS Sensor. An E2 imprinted PANI EIS sensor was prepared, and its behavior was studied. For the preparation of the electrode, aniline was electrochemically polymerized in the presence of the template (660 nmol of E2).

https://doi.org/10.1021/acssensors.4c01787
ACS Sens. 2024, 9, 4963−4973

The polymerization was carried out in an aqueous solution in strong oxidizing protonic acid H_2SO_4, using potentiodynamic electrochemical polymerization by cycling the potential between −0.5 and +0.8 V at a potential scan rate of 0.02 V/s for 15 cycles and with Ag pseudo reference. Figure 3A, B shows the current−potential curves of potentiodynamic electropolymerization of aniline respectively in the presence of the E2 template, which is referred to as the imprinted PANI layer, and in the absence of E2, defined as PANI control. The anodic peaks at 0.1 V, present in the imprinted PANI layer and in the PANI control, were assigned to the irreversible electro-oxidation of aniline. The peaks were observed growing up to n = 15 CV scans (details in SI), confirming a successful polymerization of aniline and indicating the formation of a conducting thin film.[35] It was observed that the maximum current peak at 0.1 V in the case of the PANI control was higher with respect to that of the imprinted PANI layer, indicating that a thicker PANI layer was deposited in the absence of the template.

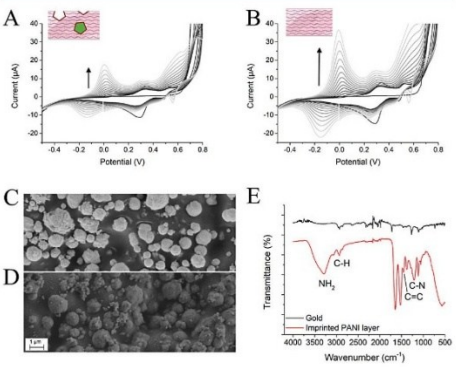

Figure 3. CV of the Imprinted PANI layer (A) and of the PANI control (B). SEM image of the bare electrode (C) and Imprinted PANI layer (D) FT-IR spectra (E).

Subsequently, the template was extracted using 75% NaOH (0.1 M) and 25% EtOH followed by a step in absolute ethanol to disrupt both the electrostatic and hydrophobic interactions. To avoid nonspecific interactions, both control and imprinted PANI-modified electrodes were blocked with a solution of PBS pH 5 supplemented with 0.1% Triton X-100. After equilibrating the pH of the electrodes by incubating them with a drop of 200 μL of PBS pH 5 for 1 h, the template extraction and the blocking steps were monitored with EIS measurements (details in SI). The Nyquist plots of the imprinted PANI layer (Figure S4A) showed a reduction of the charge transfer resistance R_{ct} (bare electrode: 150 Ω; PANI electrode: 34 Ω) associated with the electropolymerization of aniline, while the R_{ct} increased after template removal and blocking (after blocking: 300 Ω). The increase of R_{ct} after washing (and equilibration at pH 5.0) can be attributed to the decrease in conductivity of polyaniline as the pH rises from the highly acidic environment in which the film was formed (0.25 M H_2SO_4). The further increase after blocking is due to the successful deposition of an additional layer of the non-conductive surfactant (Triton-X) that reduces further the overall conductivity of the electrode, increasing the charge-transfer resistance.

PANI control electrodes were prepared and treated in the same manner as the imprinted PANI and showed a similar electrochemical behavior (Figure S4B).

PANI-modified electrodes, both imprinted and controls, were physically characterized. SEM images evidenced the polymer layer (Figure 3D) at the surface of the bare gold electrode (Figure 3C), as a finer structure deposited over the globular gold surface. FT-IR spectra of the PANI film (Figure 3E, red line) compared with that of the bare gold electrode (Figure 3E, black line), showed specific IR bands corresponding to N−H bond vibrations (3200 cm^{-1}), C−H vibrations

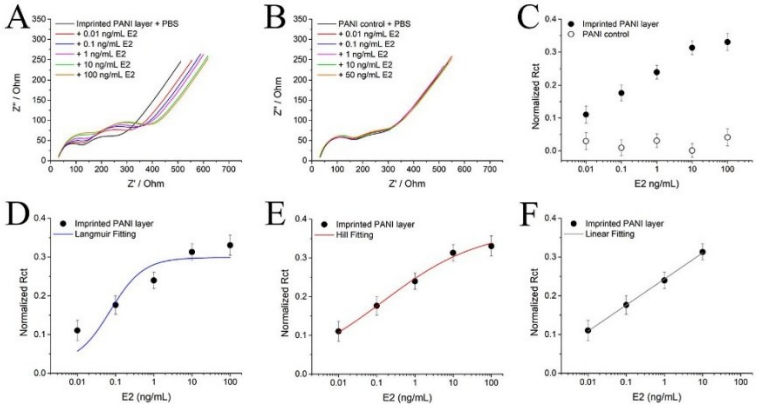

Figure 4. Nyquist plot of the Imprinted PANI layer (A) and of the PANI control (B) incubated with increasing concentrations of E2. Normalized R_{ct} as a function of E2 concentrations of Imprinted PANI layer and PANI control (C). Imprinted PANI layer fitted with Langmuir (D), Hill (E), and Linear (F) equation models.

https://doi.org/10.1021/acssensors.4c01787
ACS Sens. 2024, 9, 4963−4973

Table 1. Fitting Parameters Imprinted PANI Layer

							statistics	
fitting	R_{ct_min}	R_{ct_max}	EC_{50} (ng/mL)	n	intercept	slope	R^2	χ^2
Langmuir	0.0233 ± 0.0790	0.2988 ± 0.0282	0.0722 ± 0.0761	1			0.8863	3.8406
Hill	0.0003 ± 0.1620	0.3740 ± 0.0565	0.1434 ± 0.3003	0.3402 ± 0.2203			0.9934	0.2229
linear					0.2433 ± 0.0018	0.0673 ± 0.0016	0.9982	

(2921, 1373 cm^{-1}), C═N (1650 cm^{-1}), C═C (1515, 1450 cm^{-1}) and C−N (1255 cm^{-1}), thus confirming the deposition of the PANI layer onto the gold SPE.[36]

The ability of the imprinted PANI layer electrode to rebind E2 was tested and compared to the PANI control electrode. Rebinding studies were performed using concentrations of E2 ranging from 0.01 to 100 ng/mL, as shown in Figure 4. It can be observed that the imprinted PANI layer sensor (Figure 4A) showed EIS signals with R_{ct} values increasing proportionally to the concentration of E2 (from 342−455 Ω), indicating the successful binding of a nonconductive molecule on the polyanaline. In contrast, when the PANI control sensor was tested, it did not show changes in the EIS signal upon E2 addition (Figure 4B). The normalized data of R_{ct} obtained from the EIS measurements of the imprinted PANI layer and control and calculated as explained in the "Estradiol rebinding" section were plotted as a function of E2 concentrations (Figure 4C). It can be observed, that normalized R_{ct} for control PANI did not report any binding event, whereas characteristic saturation binding isotherms were observed for the imprinted PANI layer.

Data of the imprinted PANI layer were fitted with the Langmuir isotherm eq (Figure 4D), which is meant to describe monomodal binding sites (n = 1). The sensor's half saturation was estimated with an EC_{50} = 0.0722 ng/mL, but the fitting was quite poor, considering the R^2 = 0.8863 value (Table 1). This suggested that the process of imprinting the E2 soluble template through PANI electropolymerization yielded heterogeneous stamping of the binding sites, as also theorized by Umpleby II.[13] Then, the same set of data was fitted with a Hill model eq (Figure 4E), which extends the liberty degree for the binding sites to n. The value of EC_{50} resulted in 0.1434 ng/mL, n = 0.34, and R^2 = 0.9934 (Table 1). Taking n as an approximation of the heterogeneity of the surface binding sites, the results suggested that the imprinted PANI layer possessed inhomogeneous binding cavities.

The overall operational parameters of the imprinted PANI layer-sensor indicated that the electrode could be exploited to determine the E2 level in the picomolar range. Figure 3F shows the linear correlation plot between normalized R_{ct} and the concentrations of E2. The linear regression equation was: $y(R_{ct}) = 0.2432 + x(\frac{ng}{mL})0.0673$ (R^2= 0.9982) (Table 1) with a LOD of 65.04 pg/mL and a sensitivity at low concentration of 2.60 ng/mL (Table 3).

NanoMIP-Doped PANI EIS Sensor. In the second part of this work, an EIS sensor based on discrete and homogeneous binding sites was studied. Electrodes were modified with a PANI layer, to which the selective recognition was entailed by doping it with E2-selective nanoMIPs and supposedly playing the role of homo-binding cavities (Figure 1B). The performances of the two sensors were ultimately compared.

NanoMIPs were synthesized using a total monomer concentration of 0.2% w/v.[34] Acrylamide (Aam), *tert*-butylacrylamide (*t*BAm), and methacrylic acid (MAA) were admixed to *N*,*N*′-methylene bis-acrylamide (BIS), which was used as a reticulating agent. E2 (1.28 mM) was chosen as a template and added to the pre-polymerization mixture (V_{final} = 10 mL). The nanoMIPs dimensions were characterized by means of dynamic light scattering (DLS; Figure S5). The hydrodynamic sizes of the nanoparticles were about a few hundred nanometers, while the polydispersity index (PDI) indicated a homogeneous distribution (Table S1). The functional characterization of nanoMIPs was assessed by isothermal titration calorimetry (ITC). Figure S6 reports the interaction between the nanoparticles and E2, subtracted from the nonspecific heats, measured by the interaction of E2 with control nonimprinted nanoparticles (control NPs). The integrated heats described a sigmoidal profile typically associated with interacting molecules. Binding data were fit with an independent equation model, showing a dissociation constant of 11 nM and a single binding site per nanoMIP (details in Figure S6 and Table S2). Thus, the ITC confirmed the effective stamping of binding sites on the nanoMIPs.

For the preparation of the electrodes, aniline was electrochemically polymerized in the presence of nanoMIPs or control NPs. The polymerization was carried out under the same conditions reported for the imprinted PANI layer. Figure 5A, B shows the current−potential curves of potentiodynamic

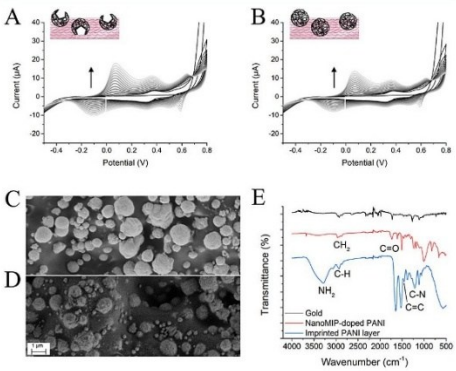

Figure 5. CV of nanoMIP-doped PANI (A) and control NPs-doped PANI (B). SEM image of the bare electrode (C) and of nanoMIP-doped PANI (D) FT-IR spectra (E).

electropolymerization of aniline in the presence of nanoMIPs (nanoMIP-doped PANI) and in the presence of control NPs (control NPs-doped PANI), respectively. The anodic peak at 0.1 V, present in both nanoMIPs-doped PANI and control NPs-doped PANI, was assigned to the irreversible electrooxidation of the aniline. The peak was observed growing up to n = 15 CV scans (details in the SI), confirming the polymerization of aniline and indicating the formation of a

https://doi.org/10.1021/acssensors.4c01787
ACS Sens. 2024, 9, 4963−4973

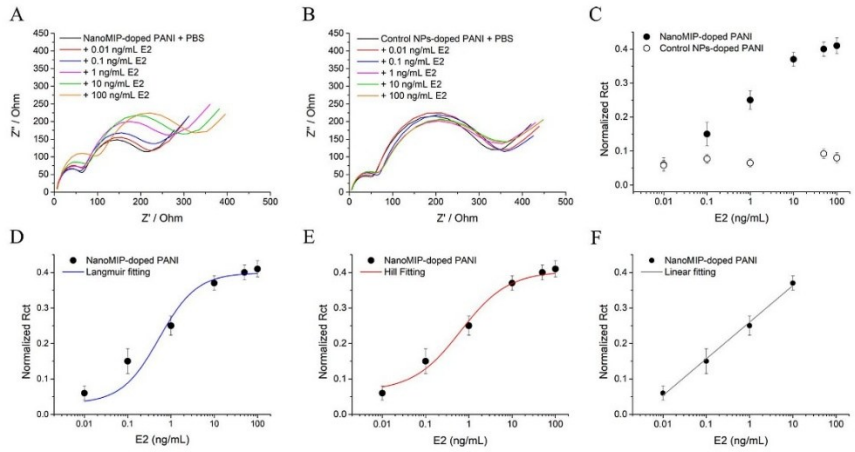

Figure 6. Nyquist plot of nanoMIP-doped PANI (A) and of control NP-doped PANI (B) incubated with increasing concentrations of E2. Normalized R_{ct} as a function of the E2 concentration of nanoMIP-doped PANI and control NP-doped PANI (C). NanoMIP-doped PANI fitted with Langmuir (D), Hill (E), and linear (F) equation model.

conducting thin film, in analogy to what was reported earlier. Subsequently, electrodes were blocked with a solution of PBS pH 5 supplemented with 0.1% Triton X-100 to avoid nonspecific interactions.

The surface of the electrode was imaged by SEM as reported in Figure 5C, confirming the presence of a polymeric layer after modification of the gold SPE with nanoMIP embedded in PANI, similar to what was reported in Figure 3. Moreover, FT-IR spectra of nanoMIP-doped PANI (Figure 3E, red line) showed the typical bands associated with polyacrylamide, thus confirming the incorporation of nanoMIPs at the electrode surface. In particular, the peaks at 2923 cm^{-1}, at 1659 $cm^{-1,}$ and at 1119 cm^{-1} are associated with the $-CH_2$ stretching vibrations, C═O stretching vibrations, and C−N bond, respectively.[37] Moreover, in the nanoMIP-doped PANI FT-IR spectrum, there were bands typical of PANI, suggesting that electropolymerization had occurred. Typically, we reported the peak associated with the N−H bond vibrations (3200 cm^{-1}), C−H vibrations (2921, 1373 cm^{-1}), C═C (1515, 1450 cm^{-1}), and C−N (1255 cm^{-1}).

Figure 6 shows the EIS measurements of nanoMIPs-doped PANI and the control NPs-doped PANI after incubation with concentrations of E2 ranging from 0.01 to 500 ng/mL. The obtained Nyquist plots in Figure 6A demonstrated that increasing E2 concentrations led to an increase in the impedimetric responses of the nanoMIPs-doped PANI sensor, suggesting the formation of bonds between the selective binding cavities on the nanoMIPs and the nonconductive E2 analyte. The E2 to nanoMIP interaction served as a kinetic barrier, inhibiting the transfer of electrons between the sensor surface and the sensing probe in solution, resulting in enhancement of R_{ct} (from 105 to 305 Ω). In contrast, the control NPs-doped PANI sensor, used as a negative control, did not show changes in the EIS signal upon E2 addition.

The normalized R_{ct} data obtained from the EIS measurements of nanoMIPs-doped PANI and control NPs-doped PANI were plotted as a function of the E2 concentration (Figure 6C). Characteristics saturation binding isotherms were observed for nanoMIPs-doped PANI, whereas control NPs doped PANI did not report any response to binding events. Langmuir model eq (Figure 6D) was employed to fit the data of the binding isotherm, showing an EC_{50} of 0.5354 ng/mL and an R^2 = 0.9690 when the binding site density n was equal to 1. Whereas Figure 6E reports the fitting made with the Hill equation model, which estimated an EC_{50} of 0.6440 ng/mL, n = 0.79, and R^2 = 0.9955.

The n parameter, which inversely correlates to the degree of heterogeneity of the binding sites (i.e., homogeneous for n = 1), was much closer to the unit for nanoMIP-doped PANI (n = 0.79) as compared with the imprinted PANI layer (n = 0.34). This observation reinforces the hypothesis that nanoMIPs can act as discrete and homogeneous binding sites. Moreover, the n value for the nanoMIP-doped PANI was not exactly 1, possibly due to influences from nonspecific interactions and from the orientations of nanoMIPs dispersed in the PANI layer, which were assumed to yield on/off binding sites only (Figure 1B), while being more multifaceted. However, despite possible inaccuracies of the model, the n values and the related statistics for nanoMIP-doped PANI compared with the imprinted PANI layer, fully support the effect of nanoMIPs as homogeneous sites (Table 1). This can be taken as a general descriptor of sensors in which nanoMIPs play the role of discrete homogeneous receptors. In fact, in the literature there are examples that report the sensing of cardiac troponin I, a marker for myocardial infarction, with a nanoMIP-receptive layer that yielded binding isotherms best fitted with a Langmuir model (n = 1) and R^2= 0.99, in contrast to the fit values obtained for a Langmuir−Freundlich model, that was n = 0.26 and R^2= 0.89.[38] Another study reports the determination of cilostazol and its pharmacologically active primary metabolite in human plasma performed by means of a nanoMIP chemosensor.[39] The nanoMIP chemosensor was prepared by embedding cilostazol-selective nanoMIPs in a polytyramine layer. Isotherm parameters for the nanoMIP

https://doi.org/10.1021/acssensors.4c01787
ACS Sens. 2024, 9, 4963−4973

Table 2. Fitting Parameters of NanoMIP-Doped PANI

							statistics	
fitting	R_{ct_min}	R_{ct_max}	EC_{50} (ng/mL)	n	intercept	slope	R^2	χ^2
Langmuir	0.0307 ± 0.0304	0.3991 ± 0.0188	0.5354 ± 0.2695	1			0.9690	1.9236
Hill	0.0655 ± 0.0006	0.4038 ± 0.0005	0.6443 ± 0.0078	0.79 ± 0.09			0.9955	0.00006
linear					0.2598 ± 0.0057	0.1031 ± 0.0046	0.9940	

chemosensor curves of normalized DPV peak current *versus* cilostazol concentrations showed that Langmuir model ($n = 1$) had an $R^2 = 0.959$, Freundlich showed an $n = 4.04$ but a poorer $R^2 = 0.86$, and the Langmuir−Freundlich model showed $n = 1.02$ and $R^2 = 0.949$, suggesting that the nanoMIPs indeed behave as homogeneous binding sites.

Here, the operational parameters of the E2 nanoMIPs-doped PANI sensor were estimated from Figure 6. It can be observed how the sensor could be exploited to determine E2 in the nanomolar range.

Figure 6F shows the linear correlation plot between normalized R_{ct} and the logarithm of E2 concentrations. As reported in Table 2, the regression equation normalized was $y = 0.2598 + x\ 0.103$ ($R^2 = 0.9940$) with a LOD of 2.86 pg/mL and a sensitivity at a low concentration of 0.525 ng/mL (Table 3). Table 3 reports the comparison between the performance

Table 3. Operational Parameters Associated to Imprinted PANI Layer and NanoMIP-Doped PANI Sensors

	imprinted PANI layer	nanoMIP-doped PANI
R_{ct_min}	0.0003 ± 0.162	0.0655 ± 0.0006
R_{ct_max}	0.3740 ± 0.0565	0.4038 ± 0.0005
K_{app} (M)	5.14×10^{-10}	2.37×10^{-9}
K_{aff} (M^{-1})[a]	1.95×10^{9}	4.23×10^{8}
LOD (pg/mL)[b]	65.04	2.86
sensitivity at low concentrations[c]	2.606	0.525

[a] $\frac{1}{K_{app}}$. [b] $\frac{(3 \times St.Dev_{Blank})}{Sensitivity\ at\ low\ conc.}$. [c] $\frac{\Delta R_{ct}}{K_{app}}$.

parameters of the imprinted PANI layer and the nanoMIP-doped PANI. It can be observed that both sensors exhibited a response for E2 in the range of 36.7 pM−36.7 nM, indicating superior sensitivity with respect to other MIP electrodes in the literature.[21] Particularly interesting are the linearization parameters (i.e., compare Figures 4F and 6F), where the slope for the imprinted PANI layer was 0.058 Ω/ng mL^{-1}, whereas the slope for the nanoMIP-doped PANI was 0.103 Ω/ng mL^{-1}. A gain of almost twice the sensitivity was therefore achieved for a sensing surface provided with discrete homogeneous binding sites, with respect to when the binding sites were inhomogeneously stamped in the PANI layer.

Selectivity. To test the selectivity of both the imprinted PANI layer and nanoMIPs-doped PANI sensor, the electrode responses were assessed by choosing as interferents two other common water contaminants with structural similarity to E2: bisphenol A (BPA) and progesterone (P) (Figure S7). The interferents were added independently at the concentrations of 0.1, 1, and 50 ng/mL in PBS and the EIS measurements were taken after 30 min of incubation and a quick washing with water. The EIS quantifications were executed in three replicates, and the outcomes are depicted in the histograms reported in Figure 7. The responses for each interferent were compared to those of E2. As shown in Figure 7A, it was clear

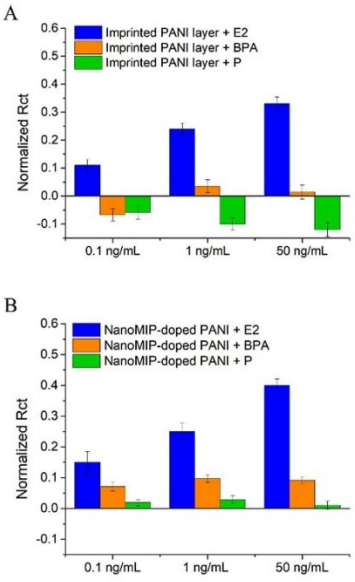

Figure 7. Normalized R_{ct} of Imprinted PANI layer (A) and nanoMIP-doped PANI (B) incubated with E2 (blue bar), BPA (orange bar), and P (green bar) at different concentrations.

that the R_{ct} value of the imprinted PANI layer sensor toward E2 was higher than that of the potential interferents, demonstrating selectivity for E2. Similar behavior can be observed for nanoMIPs-doped PANI electrodes (Figure 7B). NanoMIPs on the electrode presented high selectivity and unique recognition ability toward E2.

Reproducibility. The reproducibility of the Imprinted PANI layer and nanoMIP-doped PANI electrodes was investigated by detecting the concentration of E2 (0.1 and 1 ng/mL), respectively, on three and five electrodes prepared under the same conditions. Figure 8 reports the normalized R_{ct} value of the five nanoMIP-doped PANI electrodes (Figure 8A) and three imprinted PANI layer electrodes (Figure 8B). The relative standard deviations (RSD) reported in Table 4 were calculated for both nanoMIP-doped PANI and Imprinted PANI layer electrodes. The RDS of nanoMIP-doped PANI was significantly lower with respect to that of the Imprinted PANI layer, indicating high sensor-to-sensor reproducibility when the PANI layer is doped with nanoMIPs.

NanoMIPs-Doped PANI Electrode for the Detection of E2 in the Wastewater Sample. At last, the nanoMIPs-doped PANI sensor was tested for its response in real scenario samples for the determination of E2 contamination in

https://doi.org/10.1021/acssensors.4c01787
ACS Sens. 2024, 9, 4963−4973

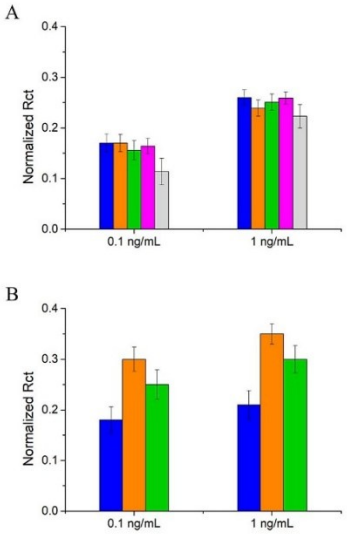

Figure 8. Reproducibility of nanoMIPs-doped PANI (A) and of the Imprinted PANI layer (B).

Table 4. Relative Standard Deviation (RSD)

E2 (ng/mL)	nanoMIP-doped PANI	imprinted PANI layer
0.1	15.194	24.771
1	6.311	24.749

wastewater. Real wastewater samples were spiked with known concentrations of E2, namely, 0.1, 1, and 10 ng/mL, and measured with the nanoMIP-doped PANI sensor. Additionally, to assess the effect on the measurement of sample treatment, wastewater samples were either spiked with E2 before or after filtration (i.e., to remove particulates) with 0.45 μm filters. All spiked wastewater samples were incubated for 30 min on the electrodes and next measured by EIS. Figure 9 reports the normalized R_{ct} as a function of E2 spiked in the wastewater samples. The R_{ct} values increased for increasing E2 concentrations, similar to the results obtained with E2 in PBS (Table S3).

Normalized R_{ct} of E2 in buffer (Figure 9 blue squares) was used as the reference curve. Measurements of E2 in filtered wastewater (Figure 9 red circles) well overlapped with PBS data, with no statistical differences calculated at 0.1 and 1 ng/mL (p-values equal to 0.058 and 0.06, respectively) and moderate statistical difference at 10 ng/mL (p = 0.03). Wastewater samples spiked with E2 prior to filtration (Figure 9 black triangles) instead showed a significative variation of the normalized R_{ct} values with respect to buffer, suggesting that the filtration step might yield partial nonspecific sorption of E2 on the filter.

When the recoveries of E2 in spiked wastewater samples were calculated, these resulted to be 98.7, 96.9, and 68.7%, respectively, for the addition of E2 at the concentrations of 0.1, 1, and 10 ng/mL.

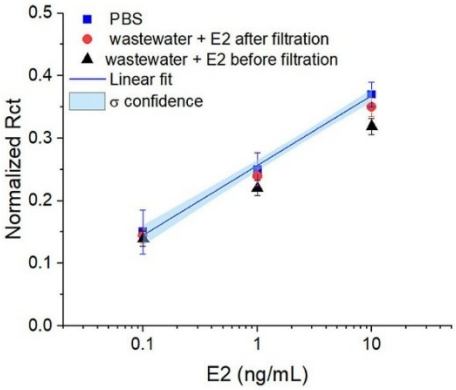

Figure 9. Normalized R_{ct} as a function of E2 concentration of the EIS-nanoMIP-doped PANI sensor incubated with wastewater spiked with different concentrations of E2 before filtration (black triangles), or after filtration (red dots) compared to the E2 measurements in PBS (blue squares); linear fit of E2 in PBS $y = 0.111x + 0.256$ (blue line); light blue halo represents the 1σ confidence level for the fitting.

CONCLUSIONS

MIPs are considered ideal receptor elements for sensing devices, given the possibility to custom-design their selectivity, their affinity toward a targeted analyte, and their robustness, which enable them to withstand harsh conditions. However, MIP synthesis, even in the case of the electropolymerization of MIP thin films, is a random process that produces a statistical distribution of binding sites with a variety of affinities, which might affect the sensor performance. With the aim to investigate the possible implications on the efficiency of the electrochemical sensor's performance of inhomogeneous imprinted binding sites formed at the surface of the working electrode, we simulated two different scenarios. On one side, we prepared an electrode onto which an E2 imprinted PANI layer was electrodeposited, and we compared it with the performance of a PANI layer doped with E2-selective nanoMIPs, these latter intended as a model of homogeneous and discrete binding sites.

Studying the binding behavior of the two sensors toward their analyte, the hormone E2, through the EIS technique, confirmed that the direct imprinting of E2 in the PANI layer allowed the formation of heterogeneous binding sites. In contrast, E2-selective nanoMIPs embedded in an electropolymerized PANI layer provided homogeneity of the binding sites with the key advantage of improving almost twice the sensitivity of the sensor. These results indicate that the quality of the binding sites should play a fundamental role in sensor development.

ASSOCIATED CONTENT

Supporting Information

The Supporting Information is available free of charge at https://pubs.acs.org/doi/10.1021/acssensors.4c01787.

Investigation of the electrochemical behavior of E2; CVs of electrodeposition of aniline for imprinted PANI electrode and nanoMIPsdoped PANI electrode; fitting

https://doi.org/10.1021/acssensors.4c01787
ACS Sens. 2024, 9, 4963−4973

PSTrace software; preparation of the imprinted PANI layer and PANI control; DLS of nanoMIPs; ITC of nanoMIPs; structure of interferents; and real sample measurements (PDF)

AUTHOR INFORMATION

Corresponding Author

Alessandra Maria Bossi − *Department of Biotechnology, University of Verona, 37134 Verona, Italy;* orcid.org/0000-0002-2542-8412; Email: alessandramaria.bossi@univr.it

Authors

Alice Marinangeli − *Department of Biotechnology, University of Verona, 37134 Verona, Italy*

Iva Chianella − *Surface Engineering and Precision Centre, School of Aerospace, Transport and Manufacturing, Cranfield University, Bedford MK43 0AL, U.K.*

Eros Radicchi − *Department of Biotechnology, University of Verona, 37134 Verona, Italy;* orcid.org/0000-0003-0749-3824

Devid Maniglio − *Department of Industrial Engineering, University of Trento, 38123 Trento, Italy;* orcid.org/0000-0002-1653-861X

Complete contact information is available at: https://pubs.acs.org/10.1021/acssensors.4c01787

Author Contributions

Conceptualization, A.M., I.C. and A.M.B.; methodology, A.M., I.C., E.R. and D.M.; validation, A.M.; investigation, A.M., D.M. and E.R.; resources, A.M.B.; data curation, A.M., A.M.B.; writing—original draft preparation, A.M., A.M.B.; writing—review and editing, A.M., I.C., D.M. and A.M.B.; supervision, A.M.B. and I.C. The manuscript was written through contributions of all authors. All authors have given approval to the final version of the manuscript. A.M. and I.C. contributed equally to this work.

Funding

Italian Ministry of Research and University doctoral program PON PNRR D.M.351.

Notes

The authors declare no competing financial interest.

ACKNOWLEDGMENTS

A.M.B. and A.M. acknowledge Ministry of University and Research for MUR D.M. 351 PON PNRR doctoral program. A.M.B. acknowledges the Centro Piattaforme Tecnologiche (CPT) of the University of Verona for the facilities DLS and ITC.

ABBREVIATIONS

MIP, molecularly imprinted polymer; PANI, polyaniline; SPE, screen-printed electrode; EIS, electrochemical impedance spectroscopy; DPV, differential pulse voltammetry; CV, cyclic voltammetry; DLS, dynamic light scattering; SEM, scanning electron microscopy; ITC, isothermal titration nanocalorimetry; LOD, limit of detection; PDI, polydispersity index; RI, refractive index; RSD, relative standard deviation

REFERENCES

(1) Wulff, G.; Sarhan, A.; Zabrocki, K. Enzyme-Analogue Built Polymers and Their Use for the Resolution of Racemates. *Tetrahedron Lett.* **1973**, *14*, 4329−4332.

(2) Arshady, R.; Mosbach, K. Synthesis of Substrate-Selective Polymers by Host-Guest Polymerization. *Makromol. Chem.* **1981**, *182*, 687−692.

(3) Wei, S.; Mizaikoff, B. Binding Site Characteristics of 17β-Estradiol Imprinted Polymers. *Biosens. Bioelectron.* **2007**, *23*, 201−209.

(4) Rushton, G. T.; Karns, C. L.; Shimizu, K. D. A Critical Examination of the Use of the Freundlich Isotherm in Characterizing Molecularly Imprinted Polymers (MIPs). *Anal. Chim. Acta* **2005**, *528*, 107−113.

(5) Malitesta, C.; Mazzotta, E.; Picca, R. A.; Poma, A.; Chianella, I.; Piletsky, S. A. MIP Sensors - The Electrochemical Approach. *Anal. Bioanal. Chem.* **2012**, *402*, 1827−1846.

(6) Wang, L.; Pagett, M.; Zhang, W. Molecularly Imprinted Polymer (MIP) Based Electrochemical Sensors and Their Recent Advances in Health Applications. *Sens. Actuators Rep.* **2023**, *5*, No. 100153.

(7) Lahcen, A. A.; Amine, A. Recent Advances in Electrochemical Sensors Based on Molecularly Imprinted Polymers and Nanomaterials. *Electroanalysis* **2019**, *31*, 188−201.

(8) Ayerdurai, V.; Cieplak, M.; Kutner, W. Molecularly Imprinted Polymer-Based Electrochemical Sensors for Food Contaminants Determination. *Trends Anal. Chem.* **2023**, *158*, No. 116830.

(9) Stojanovic, Z.; Erdőssy, J.; Keltai, K.; Scheller, F. W.; Gyurcsányi, R. E. Electrosynthesized Molecularly Imprinted Polyscopoletin Nanofilms for Human Serum Albumin Detection. *Anal. Chim. Acta* **2017**, *977*, 1−9.

(10) Palladino, P.; Bettazzi, F.; Scarano, S. Polydopamine: Surface Coating, Molecular Imprinting, and Electrochemistry-Successful Applications and Future Perspectives in (Bio)Analysis. *Anal. Bioanal. Chem.* **2019**, *411*, 4327−4338.

(11) Pirzada, M.; Sehit, E.; Altintas, Z. Cancer Biomarker Detection in Human Serum Samples Using Nanoparticle Decorated Epitope-Mediated Hybrid MIP. *Biosens. Bioelectron.* **2020**, *166*, No. 112464.

(12) Kushwaha, A.; Srivastava, J.; Singh, A. K.; Anand, R.; Raghuwanshi, R.; Rai, T.; Singh, M. Epitope Imprinting of Mycobacterium Leprae Bacteria via Molecularly Imprinted Nanoparticles Using Multiple Monomers Approach. *Biosens. Bioelectron.* **2019**, *145*, No. 111698.

(13) Umpleby, R. J.; Baxter, S. C.; Chen, Y.; Shah, R. N.; Shimizu, K. D. Characterization of Molecularly Imprinted Polymers with the Langmuir-Freundlich Isotherm. *Anal. Chem.* **2001**, *73*, 4584−4591.

(14) Pap, T.; Horvai, G. Binding Assays with Molecularly Imprinted Polymers—Why Do They Work? *J. of Chromatogr. B* **2004**, *804*, 167−172.

(15) Drzazgowska, J.; Schmid, B.; Sussmuth, R. D.; Altintas, Z. Self-Assembled Monolayer Epitope Bridges for Molecular Imprinting and Cancer Biomarker Sensing. *Anal. Chem.* **2020**, *92*, 4798−4806.

(16) deCatanzaro, D. Sex Steroids as Pheromones in Mammals: The Exceptional Role of Estradiol. *Horm. Behav.* **2015**, *68*, 103−116.

(17) Shore, L. S.; Shemesh, M. Estrogen as an Environmental Pollutant. *Bull. Environ. Contam. Toxicol.* **2016**, *97*, 447−448.

(18) Nazari, E.; Suja, F. Effects of 17β-Estradiol (E2) on Aqueous Organisms and Its Treatment Problem: A Review. *Rev. Environ. Health* **2016**, *31*, 465−491.

(19) Wang, J. Portable Electrochemical Systems. *Trends Anal. Chem.* **2002**, *21*, 226−232.

(20) Luo, X.; Morrin, A.; Killard, A. J.; Smyth, M. R. Application of Nanoparticles in Electrochemical Sensors and Biosensors. *Electroanalysis* **2006**, *18*, 319−326.

(21) Des Azevedo, S.; Lakshmi, D.; Chianella, I.; Whitcombe, M. J.; Karim, K.; Ivanova-Mitseva, P. K.; Subrahmanyam, S.; Piletsky, S. A. Molecularly Imprinted Polymer-Hybrid Electrochemical Sensor for the Detection of β-Estradiol. *Ind. Eng. Chem. Res.* **2013**, *52*, 13917−13923.

(22) Yuan, L.; Zhang, J.; Zhou, P.; Chen, J.; Wang, R.; Wen, T.; Li, Y.; Zhou, X.; Jiang, H. Electrochemical Sensor Based on Molecularly Imprinted Membranes at Platinum Nanoparticles-Modified Electrode for Determination of 17β-Estradiol. *Biosens. Bioelectron.* **2011**, *29*, 29−33.
(23) Wen, T.; Xue, C.; Li, Y.; Wang, Y.; Wang, R.; Hong, J.; Zhou, X.; Jiang, H. Reduced Graphene Oxide-Platinum Nanoparticles Composites Based Imprinting Sensor for Sensitively Electrochemical Analysis of 17β-Estradiol. *J. Electroanal. Chem.* **2012**, *682*, 121−127.
(24) Magar, H. S.; Hassan, R. Y. A.; Mulchandani, A. Electrochemical Impedance Spectroscopy (EIS): Principles, Construction, and Biosensing Applications. *Sensors* **2021**, *21*, 6578.
(25) Cesiulis, H.; Tsyntsaru, N.; Ramanavicius, A.; Ragoisha, G. The Study of Thin Films by Electrochemical Impedance Spectroscopy. *NanoSci. Technol.* **2016**, 3−42.
(26) Zhang, X.; Peng, Y.; Bai, J.; Ning, B.; Sun, S.; Hong, X.; Liu, Y.; Liu, Y.; Gao, Z. A Novel Electrochemical Sensor Based on Electropolymerized Molecularly Imprinted Polymer and Gold Nanomaterials Amplification for Estradiol Detection. *Sens. Actuators B Chem.* **2014**, *200*, 69−75.
(27) Florea, A.; Cristea, C.; Vocanson, F.; Săndulescu, R.; Jaffrezic-Renault, N. Electrochemical Sensor for the Detection of Estradiol Based on Electropolymerized Molecularly Imprinted Polythioaniline Film with Signal Amplification Using Gold Nanoparticles. *Electrochem. Commun.* **2015**, *59*, 36−39.
(28) Neese, F. The ORCA program system. *Wiley Interdiscip. Rev.: Comput. Mol. Sci.* **2012**, *2*, 73−78.
(29) Neese, F. Software update: The ORCA program system—Version 5.0. *Wiley Interdiscip. Rev.: Comput. Mol. Sci.* **2022**, *12*, 1606.
(30) Neese, F.; Wennmohs, F.; Becker, U.; Riplinger, C. The ORCA quantum chemistry program package. *J. Chem. Phys.* **2020**, *152*, No. 224108.
(31) Helmich-Paris, B.; de Souza, B.; Neese, F.; Izsàk, R. An improved chain of sphere for exchange algorithm. *J. Chem. Phys.* **2021**, *155*, No. 104109.
(32) Becke, A. D. Density-functional thermochemistry. III. The role of exact exchange. *J. Chem. Phys.* **1993**, *98*, 5648−5652.
(33) Nicholls, I. A.; Andersson, H. S.; Charlton, C.; Henschel, H.; Karlsson, B. C. G.; Karlsson, J. G.; O'Mahony, J.; Rosengren, A. M.; Rosengren, K. J.; Wikman, S. Theoretical and Computational Strategies for Rational Molecularly Imprinted Polymer Design. *Biosens. Bioelectron.* **2009**, *25*, 543−552.
(34) Cenci, L.; Tatti, R.; Tognato, R.; Ambrosi, E.; Piotto, C.; Bossi, A. M. Synthesis and Characterization of Peptide-Imprinted Nanogels of Controllable Size and Affinity. *Eur. Polym. J.* **2018**, *109*, 453−459.
(35) Beygisangchin, M.; Rashid, S. A.; Shafie, S.; Sadrolhosseini, A. R.; Lim, H. N. Preparations, Properties, and Applications of Polyaniline and Polyaniline Thin Films—A Review. *Polymers* **2021**, *13*, 2003.
(36) Gvozdenović, M. M.; Jugović, B. Z.; Stevanović, J. S.; Trišović, T. L.; Grgur, B. N. Electrochemical Polymerization of Aniline. In *Electropolymerization*; IntechOpen, 2011.
(37) Curteanu, S.; Dumitrescu, A.; Mihăilescu, C.; Simionescu, B. Neural Network Modeling Applied to Polyacrylamide Based Hydrogels Synthetized By Single Step Process. *Polym. Plast. Technol. Eng.* **2008**, *47*, 1061−1071.
(38) Choudhary, S.; Altintas, Z. Development of a Point-of-Care SPR Sensor for the Diagnosis of Acute Myocardial Infarction. *Biosensors* **2023**, *13*, 229.
(39) Jyoti; Gonzato, C.; Żołek, T.; Maciejewska, D.; Kutner, A.; Merlier, F.; Haupt, K.; Sharma, P. S.; Noworyta, K. R.; Kutner, W. Molecularly Imprinted Polymer Nanoparticles-Based Electrochemical Chemosensors for Selective Determination of Cilostazol and Its Pharmacologically Active Primary Metabolite in Human Plasma. *Biosens. Bioelectron.* **2021**, *193*, No. 113542.

https://doi.org/10.1021/acssensors.4c01787
ACS Sens. 2024, 9, 4963−4973

Supporting Information

Molecularly imprinted polymers electrochemical sensing: the effect of inhomogeneous binding sites on the measurements. Comparison between imprinted polyaniline versus nanoMIP-doped polyaniline electrodes for the EIS detection of 17β-estradiol.

Authors: Alice Marinangeli[1], Iva Chianella[2], Eros Radicchi[1], Devid Maniglio[3], Alessandra Maria Bossi[1*]

Authors address

[1] University of Verona, Department of Biotechnology, Strada Le Grazie 15, 37134, Verona, Italy;
[2] Cranfield University, Surface Engineering and Precision Centre, School of Aerospace, Transport and Manufacturing, Bedford, MK43 0AL, United Kingdom;
[3] University of Trento, Department of Industrial Engineering, Via Sommarive 9, 38123, Povo, Trento, Italy.

*** Corresponding Author**: Alessandra Maria Bossi, Department of Biotechnology, University of Verona, Strada Le Grazie 15, 37134 Verona, Italy. E-mail: alessandramaria.bossi@univr.it

1. **Investigation of electrochemical behaviour of E2**
2. **CVs of electrodeposition of aniline for imprinted PANI electrode and nanoMIPs-doped PANI electrode**
3. **Fitting with PSTrace software**
4. **Preparation of imprinted PANI layer and PANI control**
5. **Dynamic Light Scattering (DLS) of nanoMIPs**
6. **Isothermal Titration Nano Calorimetry (ITC) of nanoMIPs**
7. **Structure of interferents**
8. **Real sample measurements**

1. Investigation of electrochemical behaviour of E2

Preliminary investigation of the electrochemical behaviour of the target analyte 17β-estradiol (E2) at the bare scree-printed gold electrode was assessed by CV. Ideally the target analyte/template used to prepare electropolymerized MIPs should be inert and it should not actively participate in the MIP layer formation. Figure S1 shows a flat voltammogram without any peaks indicating that in the range of -0.5 V and +0.8 V the analyte is not a redox compound. This is crucial as it indicates that any resulting polyaniline layers are void of any interferences from the template.

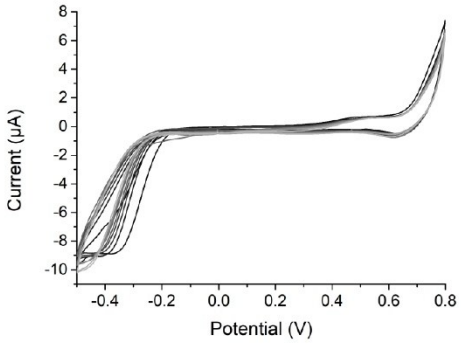

Figure S1. CV of E2.

2. CVs of electrodeposition of aniline for imprinted PANI electrode and nanoMIPs-doped PANI electrode

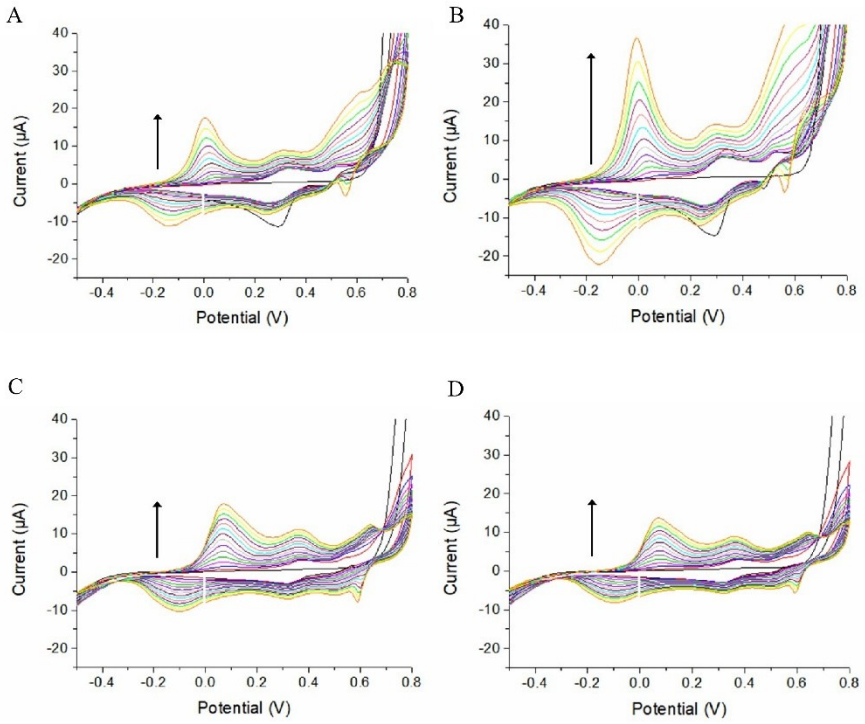

Figure S2. CV of (A) imprinted PANI layer, (B) PANI control, (C) nanoMIPs-doped PANI and (D) NPs control.

3. Fitting with PSTrace software

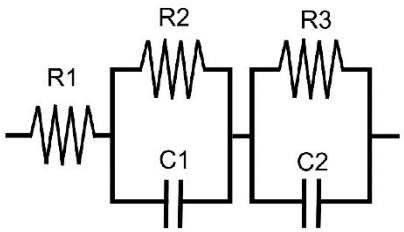

Figure S3. Equivalent circuit used for the fitting of Nyquist plot in PSTrace Software.

4. Preparation of imprinted PANI layer and PANI control

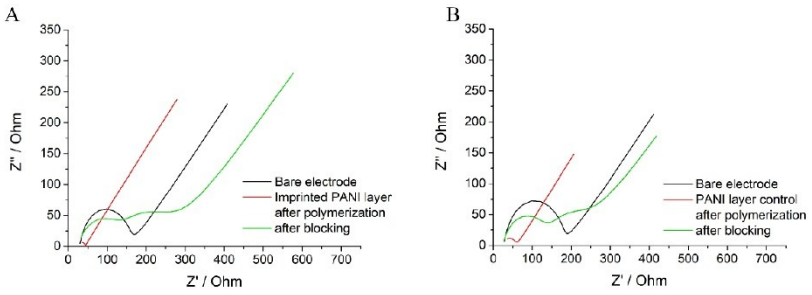

Figure S4. Nyquist plot of Imprinted PANI layer (A) and PANI control (B) after the electropolymerization and after the blocking step.

5. Dynamic Light Scattering (DLS) of nanoMIPs

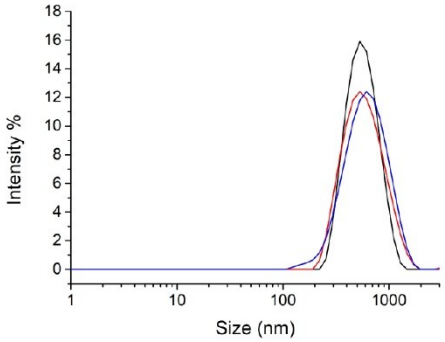

Figure S5. Example of DLS measurements of nanoMIP.

Table S1. Parameters obtained from DLS measurements of nanoMIP.

	Value
Z-average (d.nm)	553.3
PdI	0.275
Intercept	0.937

6. Isothermal Titration Nano Calorimetry (ITC) of nanoMIP

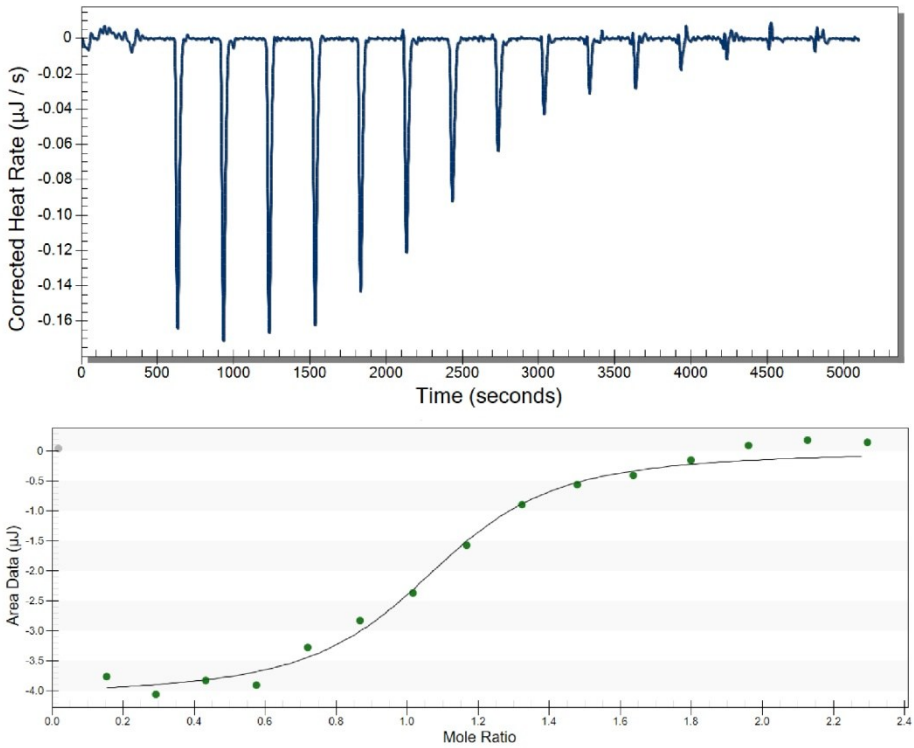

Figure S6. Upper panel: Raw ITC profile of nanoMIPs titrated with the template E2. Lower panel: integrated heats plotted as a function of the molar ratio nanoMIPs/E2 (green circles) and fitting of the data with an independent sites model.

Table S2. ITC fitting parameters.

Parameters	Value
K_d (M)	1.172×10^{-8}
n	1.029
ΔH (kJ/mol)	-380.8
ΔS (J/mol·K)	-1125

7. Structure of interferents

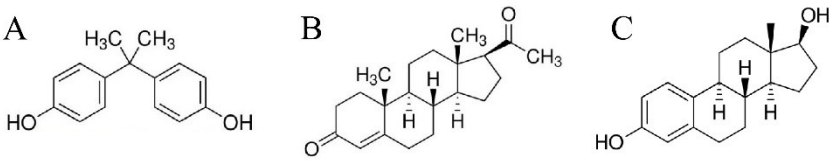

Figure S7. Molecular structure of Bisphenol A (A), Progesterone (B) and 17β-Estradiol (C).

8. Real sample measurements

Table S3. Normalized Rct of NanoMIP-doped PANI electrode tested in real sample

	E2 (ng/mL)	Normalized Rct
PBS	0.1	0.151 ± 0.0032
	1	0.249 ± 0.0037
	10	0.370 ± 0.0032
Wastewater	0.1	0.144 ± 0.0024
	1	0.240 ± 0.0049
	10	0.350 ± 0.0042

Paper III

Castor oil-based molecularly imprinted nanoparticles for the detection of cardiac troponin I: Towards green molecularly imprinted nanoreceptors

Summary

This study investigates the development of green molecularly imprinted polymer nanoparticles (GreenNanoMIPs) as biocompatible and sustainable synthetic receptors for detecting cardiac troponin I (cTnI), a clinically relevant biomarker for myocardial infarction. The work aims to demonstrate that renewable castor oil-derived materials can be successfully employed as functional monomers in MIP synthesis, providing an environmentally friendly alternative to conventional monomers.

The synthesis of the green nanoMIPs was carried out using an epitope-imprinting approach, employing a C-terminal peptide fragment of cTnI, specifically NR10, as the template molecule. The polymerization was performed by combining acrylated methyl ricinoleate (AMR), a hydrophobic sustainable monomer derived from castor oil, with ethylene glycol methyl ether acrylate (EGMEA), a hydrophilic monomer, together with N, N′-Methylenebis(acrylamide) (MBA) as the crosslinker. To identify the most suitable formulation for GreenNanoMIP synthesis, several polymerization formulations were initially performed by varying the monomers and cross-linker composition and also the concentration of the photoinitiator LAP (Table 4.1). Among all the formulations investigated, two compositions emerged as the most promising based on their hydrodynamic size and PDI, as assessed by DLS analysis. These two formulations were designated as GreenNanoMIP I, when AMR accounted for 45% of the total monomer content, and GreenNanoMIP II, when the AMR content was reduced to 25%. In both cases, non-imprinted nanoparticles were also synthesized under identical conditions to serve as a control (Control NPs). Both GreenNanoMIP formulations and their corresponding Control NPs exhibited average hydrodynamic sizes below 100 nm,

confirming the successful formation of nanosized materials. However, a clear difference in PDI was observed between the two formulations: GreenNanoMIP I showed a PDI of approximately 0.06, while GreenNanoMIP II displayed a higher value of around 0.20. This difference can be attributed to the distinct hydrophobic-hydrophilic balance of the monomer mixtures, as the higher hydrophobic content in GreenNanoMIP I promoted more uniform particle growth, whereas the equal proportion of hydrophobic and hydrophilic monomers in GreenNanoMIP II likely resulted in less controlled growth and greater polydispersity. The nanoparticles were also analyzed by FT-IR spectroscopy, which confirmed a uniform chemical composition across the GreenNanoMIPs, and by SEM, which revealed well-defined, nanosized spherical particles. Moreover, the GreenNanoMIPs also exhibited remarkable long-term stability as they show no significant changes in particle size distribution and PDI even after one year of storage.

The binding properties of the GreenNanoMIPs were investigated through fluorescence lifetime measurements using the NR10 peptide labelled with fluorescein (NR10-FITC) as the fluorescent probe. The NR10-FITC solution (10 nM) was incubated with increasing concentrations of nanoparticles, ranging from 0.5 ng/mL to 5000 ng/mL, including GreenNanoMIP I, GreenNanoMIP II and their respective Control NPs. The fluorescence decay profiles were analyzed using a bi-exponential fitting model, in which the shorter lifetime component (τ_1) was fixed as a global descriptor of non-specific decays occurring outside the imprinted cavities, while the longer component (τ_2) reflected fluorophores engaged in binding-related interactions within or near the specific recognition sites. A decrease in fluorescence lifetime of NR10-FITC was observed upon addition of both imprinted GreenNanoMIP formulations, confirming that the nanoparticles effectively interact with the target peptide through specific recognition mechanisms. In contrast, no significant variation in fluorescence lifetime was detected for the non-imprinted Control NPs, indicating the absence of specific binding. The binding data obtained for GreenNanoMIP I were fitted using the Hill equation model, yielding a measurable lifetime variation ($\Delta\tau$) of about 200 ps and an EC_{50} value of 3.31 ng/mL, confirming a strong affinity for the NR10 target sequence. In contrast, GreenNanoMIP II exhibited a higher degree of uncertainty

and variability in the lifetime measurements, likely due to its greater tendency to form aggregates, as supported by its higher PDI values and standard errors. Based on these observations, GreenNanoMIP I emerged as the most reliable and promising formulation for nanosensing applications.

The selectivity of GreenNanoMIP I was evaluated through a competitive binding assay using the fluorescently labeled peptide NR10-FITC as the reporter. In this experiment, GreenNanoMIP I (25 ng/mL) was incubated with a fixed concentration of NR10-FITC (10 nM), corresponding to a condition that saturates the available binding sites. Subsequently, increasing concentrations of potential competitors were added, including the non-fluorescent target peptide NR10 and two unrelated peptides, NR11 and FN11, at molar ratios of 1:1, 10:1, 100:1, and 1000:1 with respect to NR10-FITC. Only the addition of the non-fluorescent NR10 induced a decrease in fluorescence lifetime, consistent with the displacement of the bound NR10-FITC from the imprinted sites. In contrast, incubation with the non-template peptides (NR11 and FN11) produced no significant changes in lifetime, demonstrating the high molecular selectivity of GreenNanoMIP I toward its target peptide sequence. To further assess the applicability of the GreenNanoMIPs for the recognition of the full target protein, additional competitive binding experiments were performed using cTnI and HSA as analytes. Upon incubation with increasing concentrations of cTnI, a clear decrease in fluorescence lifetime was observed, confirming the displacement of the bound NR10-FITC and thus the ability of the GreenNanoMIPs to recognize the native protein containing the imprinted epitope. In contrast, HSA did not produce a dose-dependent displacement, showing only a negligible and non-specific adsorption effect.

Finally, the applicability of GreenNanoMIP I for detection in complex biological matrices was evaluated using human serum samples diluted 50 times. The fluorescence lifetime of the serum containing only the NR10-FITC probe represented the 100% reference signal, while the addition of GreenNanoMIP I (25 ng/mL) led to an almost complete quenching of the fluorescence response, as a consequence of the probe binding to the imprinted sites on the nanoparticles. When cTnI was subsequently introduced at a 1:1 molar ratio with NR10-FITC, a slight increase in the fluorescence lifetime was observed, indicating the partial

displacement of the bound probe from the nanoparticle surface due to the specific interaction between the imprinted cavities and the target protein. Although further optimization would be required to achieve lower detection limits, these results clearly confirm the feasibility of using GreenNanoMIPs for sensing applications. Overall, this study contributes to the general aim of the thesis by introducing a green and sustainable design strategy for MIP-based sensors. The use of castor oil-derived monomers enabled the synthesis of structurally homogeneous, stable and biocompatible nanoMIPs, demonstrating that environmentally friendly materials can achieve high recognition performance.

Table 4.1 GreenNanoMIP formulations for synthesis optimization.

Code of the polymer	AMR (%)	EGMEA (%)	MBA (%)	LAP (%)	Appearance and size (nm)
Pol1	45	5	50	1	Polydisperse, not reliable results
Pol2	25	25	50	1	Polydisperse, not reliable results
Pol3	90	10	/	1	Polydisperse, not reliable results
Pol4	50	50	/	1	Polydisperse, not reliable results
Pol5	45	5	50	10	80.9 nm
Pol6	25	25	50	10	76.3 nm
Pol7	90	10	/	10	Polydisperse, not reliable results
Pol8	50	50	/	10	Polydisperse, not reliable results

Published article

Talanta Open 11 (2025) 100439

Contents lists available at ScienceDirect

Talanta Open

journal homepage: www.sciencedirect.com/journal/talanta-open

Castor oil-based molecularly imprinted nanoparticles for the detection of cardiac troponin I: Towards green molecularly imprinted nanoreceptors

Pinar Cakir Hatir [a,*], Alice Marinangeli [b], Alessandra Maria Bossi [b], Gokhan Cayli [c]

[a] Department of Biomedical Engineering, Faculty of Engineering and Natural Sciences, İstinye University, Ayazağa Mah. Azerbaycan Cad. (Vadistanbul 4A Blok) 34396 Sariyer, İstanbul, Türkiye
[b] Department of Biotechnology, University of Verona, Strada Le Grazie 15, 37134 Verona, Italy
[c] Department of Engineering Sciences, Istanbul Cerrahpasa University, Avcilar Campus, 34320, Istanbul, Türkiye

ARTICLE INFO

Keywords:
Protein recognition
Plant-oil based functional monomer
Castor oil
Acrylated methyl ricinoleate
Molecular imprinting
Cardiac troponin I
Myocardial infarction

ABSTRACT

Molecularly imprinted polymers (MIPs) are synthetic materials that selectively recognize target molecules, offering cost-effective and stable alternatives to antibodies. While MIP nanoparticles are ideal for biomedical applications for their high surface area and their biomolecule-compatible size, traditional monomers used in their synthesis can pose issues in biocompatibility. This study presents a sustainable approach to MIP nanoparticle production using acrylated methyl ricinoleate (AMR), a functional monomer derived from castor oil. These "GreenNanoMIPs" were designed to recognize cardiac troponin I (cTnI), a key biomarker for cardiovascular events. The nanoparticles, with an average size of 81 nm, exhibited exceptional homogeneity in suspension, with a low PDI value of 0.064, and outstanding stability, as no changes in particle size distribution or PDI were observed even after one year. GreenNanoMIPs did recognize the entire cTnI protein thorough the epitope approach. Furthermore, GreenNanoMIPs were successfully used for the detection of the cTnI biomarker directly in serum. The study highlights the potential of eco-friendly, biocompatible MIPs for applications in diagnostics, drug delivery, and environmental sensing.

Introduction

Molecularly imprinted polymers (MIPs) are custom-designed synthetic materials created by means of a template-based synthesis [1,2]. Characteristic of the imprinting process is that the targeted molecule takes the role of a template and establishes specific molecular interactions with functional monomers, when co-solvated. Then, the polymerization is started by the addition of a crosslinker and of the initiator. At the completion, the template is removed, leaving on the formed material molecular cavities complementary, specific and selective for the targeted molecule. MIPs demonstrate superior availability, stability, and resistance to acidic and basic media, as well as to organic solvents, when compared to biomolecules. Additionally, they offer a cost-effective alternative for various applications.

MIPs when prepared of nanometric sizes, i.e. nanoMIPs, gain the typical features of nanomaterials, which have high area-to-volume ratio and bear a low number of binding sites per nanoMIP particle, due to the restricted dimensions, making them resemble to antibodies. The nanoMIPs have dimensions closer to that of biomolecules, enhancing their effectiveness in the biological interactions. As a result, when it comes to biomedical applications nanoMIPs have demonstrated significant potential as biosensors, diagnostics tools, therapeutics and theranostics [3–5], letting suppose widespread applications of nanoMIPs in the biomedical fields in the forthcoming future [6].

In the development of MIPs materials, prioritizing sustainable and less toxic chemical processes and materials supports a transition toward safer, eco-friendly technologies that align with green chemistry principles, ensuring minimal environmental impact while enhancing material safety for biomedical and environmental applications [7]. Along this line, tools to evaluate the overall sustainability of the MIP have been proposed [8]. Traditional monomers used for MIP syntheses can raise concerns due to their potential toxicity and persistence in the environment and eventually in individuals. By shifting to renewable, non-toxic monomers, MIP production can align with green chemistry principles, promoting safer materials for applications such as drug delivery, diagnostics, and environmental sensing. This approach supports both environmental sustainability and human health, paving the way for eco-friendly innovations in MIP technology. In particular, circular

* Corresponding author.
E-mail address: pinar.hatir@istinye.edu.tr (P. Cakir Hatir).

https://doi.org/10.1016/j.talo.2025.100439
Received 19 December 2024; Received in revised form 14 March 2025; Accepted 19 March 2025
Available online 22 March 2025

economy approaches based on the use of raw materials as sources of building blocks for polymer production has increased [9] and can open to whole new libraries of monomers for the synthesis of MIPs, where, depending on the intended applications, functional monomers and crosslinkers can be derived from various renewable materials. Even though, using green approaches in MIP synthesis and applications offer promising new opportunities, studies performed on the synthesis of MIPs using renewable resources and environmentally friendly synthesis methods are still limited.

Natural polymers like chitosan and cellulose have been explored for MIP synthesis as renewable resources in the last years [10,11]. Beyond natural polymers, plant oils also represent a promising option as renewable resources. Le Goff and coworkers developed novel bio-based MIPs using epoxidized soybean oil acrylate, as a plant oil-based cross-linker, for the controlled delivery of antifungal compounds [12]. Fatty acids, a key component of plant oils, are particularly promising for synthesizing various monomers and tailored polymers due to their potential functionality. Furthermore, compared to petroleum-based raw materials, renewable raw materials may offer natural polymer networks, resulting in improved biocompatibility and fewer immunological reactions. Consequently, plant-oil based renewable resources are often considered more suitable for biomedical applications [13,14]. To date, no fatty acid has been employed in the synthesis of molecularly imprinted polymers. In this study, we present the use of a fatty acid-derived functional monomer for the first time. Acrylated methyl ricinoleate (AMR), a functional monomer derived from castor oil, was employed in the synthesis of green molecularly imprinted polymer nanoparticles (GreenNanoMIPs).

Proteins serve as crucial analytical markers for diagnosing diseases, offering insights into the onset, progression, severity and therapeutic responses of various medical conditions. In the present work, we targeted the cardiac troponin I protein (cTnI), whose presence in blood is

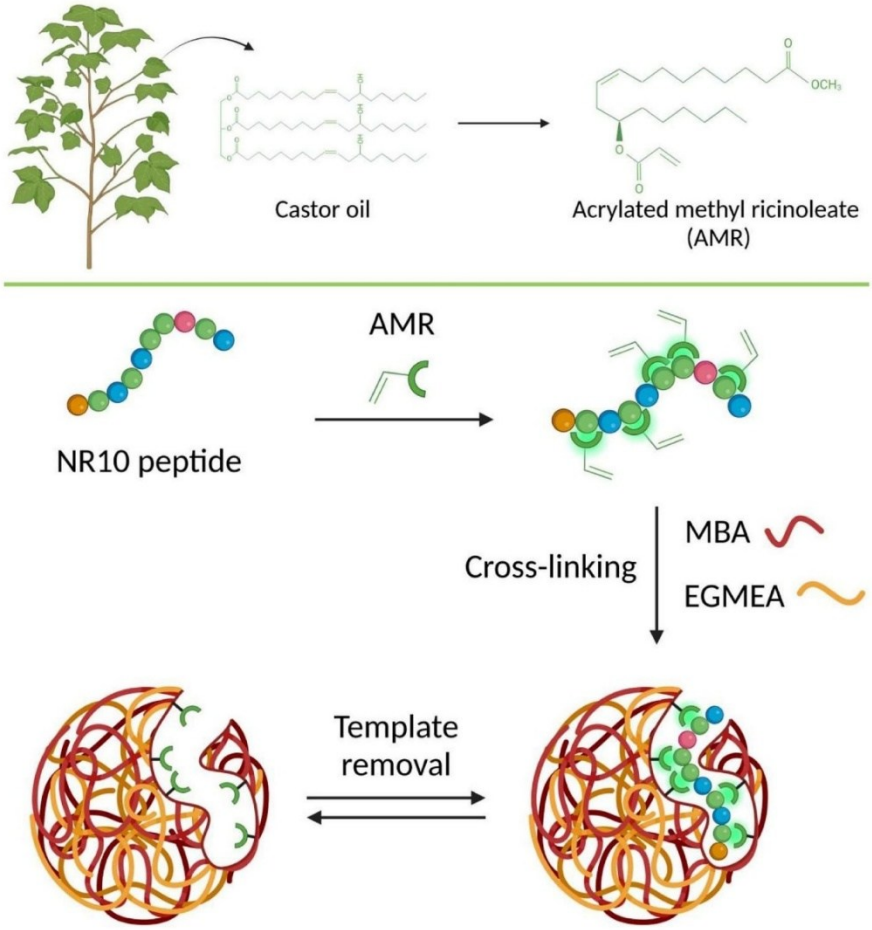

Fig. 1. Scheme of the synthesis of GreenNanoMIP selective for the cardiac troponin I protein recognition, starting from sustainable monomers derived from plant oil.

associated with cardiovascular events and in particular with myocardical infarction (MI) [15]. The cTnI enables to detect the onset of a MI event, because of its cardiac specificity, thus elevated circulating levels of cTnI strongly correlate to heart muscle damage. Additionally, cTnI allows for an early detection of MI, as its levels start to rise within a few hours after the onset of myocardial injury (typically 3–6 h). Moreover, cTnI can remain elevated for up to 10–14 days after the MI, allowing for the detection of recent myocardial damages even if in the case of delays from the patient in seeking medical care, thus being considered a marker both sensitive and of long duration. Finally, cTnI is an accurate marker, characterized by high sensitivity and specificity, thus suitable to reduce false positives and give a clearer indication of MI compared to other markers, such as creatine kinase and myoglobin. In order to prepare MIPs for the selective binding of cTnI, protein imprinting strategies were herein exploited [16]. In particular, the chosen approach was to select as template a unique peptide of cTnI, relying on the so-called epitope imprinting [17,18]. Epitopes are stretches of sequential aminoacids, mostly located in turns, loops, or at the termini of the protein structure. Ideal epitope-templates are oligopeptides, with a typical length of 8–20 aminoacids. The epitope, being a peptide with no precoined fold, withstands a broad range of polymerization conditions without alteration. Additionally, epitopes are cost-effectively produced by artificial synthesis, making the protein-recognizing MIPs significantly cheaper than antibodies [19]. The present study aims to synthesize nanoMIPs using a plant oil-derived functional monomer for the targeted recognition of cTnI. Acrylated methyl ricinoleate, obtained from castor oil, was employed as the functional monomer and used for the synthesis of cTnI nanoMIP, as schematized in Fig. 1. The resulting MIP nanoparticles were called GreenNanoMIPs. It is anticipated that GreenNanoMIPs demonstrated successful recognition of the cTnI protein through the epitope approach even in serum.

Experimental section

Materials and methods

Acrylated methyl ricinoleate (AMR) was synthesized from castor oil as described in our previous work [13]. All solvents, Ethylene glycol methyl ether acrylate (EGMEA), Lithium phenyl-2,4,6-trimethylbenzoylphosphinate (LAP), N, N′-Methylenebis(acrylamide) (MBA) and Human serum albumin (HSA) were purchased from Sigma-Aldrich (Darmstadt, Germany). Cardiac troponin I (cTnI) was purchased from GenScript. The peptides NR10 of sequence NIDALSGMGR, the NR10 labelled with fluorescein (FITC-NIDALSGMGR), NR11 of sequence NIDALSGMEGR and FN11 of sequence FGSNVTDCSGN were custom synthesized from TAG-Copenhagen. DMSO, ultra-pure water and PBS 10 mM pH 7.4 (filtered) were used. The chemical structures of polymer nanoparticles were evaluated using Jasco 4600 Fourier Transform Infrared Spectroscopy (FTIR) with a wavenumber range of 400–4000 cm^{-1}. Morphology of nanoparticles was investigated using JCM-5000 NeoScope QUATTRO S scanning electron microscope (SEM). Particle size distribution was investigated by Dynamic Light Scattering (Malvern Zetasizer Nano ZS). Time-resolved fluorescence intensities were collected using a single photon counting spectrometer Nanolog/Fluorolog-3-2iHR320 (Horiba-Jobin Yvon, Kyoto, Japan).

Synthesis of GreenNanoMIPs

AMR, EGMEA and the template-peptide solution (as shown in Table SI1) were mixed and left for 15 min to form an intermolecular complex via noncovalent interactions. Then, the required amount of solvent composition (90:10, DMSO:H_2O) was transferred into each reaction medium inside a glass vial. The monomer concentration was kept at 0.5 % (wt/wt). MBA and the initiator (10 % wt/wt, of the final weight of the monomers) were subsequently added. The vials were placed under an LED UV lamp (365 nm). After 2 min of UV irradiation, the reaction was terminated. Each solution then received 2 mL of Tris free base (50 mM) and was left in the dark for 30 min. The polymerization solutions were then transferred into dialysis membranes (12000 Da MWCO) and dialyzed against 5 L of water, repeated three times. Finally, the solutions were transferred into falcon tubes and freeze-dried. Non-imprinted polymer nanoparticles were synthesized using the same method in the absence of the peptide.

Fluorescence lifetime measurements

The fluorescence lifetime of a population, measured in the time-domain, follows the equation:

$$I(t) = I_0 e^{-t/\tau}$$

where $I(t)$ is the intensity at time t; I_0 is the intensity at t = 0; t is the time after the absorption; and τ is the fluorescence lifetime. Time-resolved fluorescence intensities were collected using a single photon counting spectrometer Nanolog/Fluorolog-3-2iHR320 (Horiba-Jobin Yvon, Kyoto, Japan) equipped with a NanoLED source with a wavelength of 453 nm. The emission was monitored at the angle of 90° with respect to the excitation. Data were collected in 1023 channels to 10,000 counts in the peak, while the calibration time was 109.73 ps per channel. The voltage at the photomultiplier (PTM) was set to 950 V. Measurements were performed in a 1 mL quartz cuvette, using a fixed concentration of NR10-FITC (10 nM) diluted in PBS (10 mM pH 7.4), adding increasing concentrations of NPs (0.5 ng/mL–5000 ng/mL). A 10 nM of NR10-FITC was excited at λ_{exc}= 453 nm to obtain the instrumental response (prompt) for the deconvolution. The sample decays were recorded at λ_{em}= 522 nm.

Data were elaborated with the Decay Analysis Software V. 6.8 (Horiba Scientific, Yvon, Kyoto, Japan), choosing a biexponential fitting equation model:

$$I(t) = A + B_1 e^{-t/\tau 1} + B_2 e^{-t/\tau 2}$$

The lifetime values (τ_2), plotted as a function of NPs concentration, described the binding isotherm for the interaction. Data were fitted with the Hill equation model (OriginPro 9.0):

$$\tau_2 = \tau_{2\_max} \frac{x^n}{(K + x^n)}$$

where τ_2 is the lifetime at concentration x of the ligand; τ_2_max is the τ value at binding saturation; n is the Hill parameter, which correlates with the number of binding sites, and K is the apparent dissociation constant.

Selectivity test

Different competitors were chosen to test the selectivity of NPs: NR10 (NIDALSGMGR), NR11 (NIDALSGMEGR) and FN11 (FGSNVTDCSGN). A solution of NPs at the final concentration of 25 ng/mL was incubated with a fixed concentration of NR10-FITC (10 nM). Competitors were added to this solution at different concentrations (10 nM, 100 nM, 1μM and 10 μM) to study the displacement of the analyte NR10-FITC. Additionally, the ability of NPs to bind the target protein (cTnI) and with a non-target protein (HSA) was tested using the concentrations of 100 nM and 1 μM. Fluorescence lifetime was measured as explained above. Measurements were performed in triplicate.

Lifetime measurements in human serum

Human serum from a pool of healthy donors was diluted 1:50. Measurements were performed by recording the τ_2 of NR10-FITC at the final concentration of 10 nM. The NPs were dispersed in serum at the concentration of 25 ng/mL, added of NR10-FITC (10 nM), and lifetime

was measured. Finally, serum with NPs (25 ng/mL) and NR10-FITC (10 nM) was spiked with 1 μM of cTnI and τ_2 was recorded.

Results and discussion

Synthesis and characterization of MIP nanoparticles

Castor oil-based monomers, acrylated methyl ricinoleate (AMR), synthesized as reported in our previous work [13] were employed to the synthesis of GreenNanoMIPs. The peptide epitope used as a template has a combination of hydrophilic and hydrophobic groups, therefore in designing the synthetic mixture for the MIP synthesis, a combination of a hydrophobic sustainable monomer AMR and of a hydrophilic monomer EGMEA was used. Initially, the synthetic space was explored by testing a range of conditions (Table S1), which included to vary the molar ratios of the sustainable monomer, AMR, and of the hydrophilic monomer EGMEA (either 9:1 or 1:1 molar ratio) and to inspect whether the presence or the absence of the crosslinker MBA had an effect, finally nanoparticles were synthesized both in the presence or absence of the template. GreenNanoMIPs were respectively called I, when the AMR monomer used was at a 45 % molar ratio, and as II when AMR was used at a 25 % molar ratio. All the nanoparticles were synthesized in an aqueous solution (10 % DMSO) using a high-dilution method under UV irradiation [20,21]. Specifically, the prepolymerization solution contained a total monomer concentration of 0.5 % (wt/wt) to ensure a highly diluted medium, that is known as one of the most used and straightforward methods for producing monodisperse nanoparticles. At the end of the reaction, GreenNanoMIPs I and II and its controls were observed to yield to monodisperse and stable nanomaterials, as indicated by the sizes below 100 nm and the PDI values below 0.2, and in some cases below 0.1, measured at DLS (Fig. 2). Considering that GreenNanoMIP II and Control NP II have an equal molar ratio of hydrophobic and hydrophilic moieties, whereas GreenNanoMIP I and Control NP I contain a higher proportion of hydrophobic moieties, the difference in the PDIs observed between the nanoparticles I and II may be related to the respective monomer compositions. Higher proportion of hydrophobic groups can promote more uniform growth. However, nanoparticles with an equal hydrophilic-hydrophobic balance may grow at different rates in distinct solubility regions, leading to increased polydispersity (Table SI1). Finally, in the absence of the crosslinker, large, polydisperse polymer particles exhibiting sedimentation were produced. In the presence of the crosslinker, monodisperse nanoparticles with low PDI were obtained.

The polymerization yields of GreenNanoMIPs and Control NPs were determined by the ratio of the weight of the NPs after lyophilization respect to the total weight of the monomers used in the reaction, multiplied by 100. Fig. 2B reports the yield % of GreeenNanoMIPs and of the control NPs. For both samples, GreenNanoMIP I and GreenNanoMIP II, the imprinted polymer nanoparticles exhibited higher polymerization yields of 92.8 % and 86.4 %, respectively, compared to their corresponding non-imprinted controls, Control NP I and Control NP II. The presence of the template molecule likely facilitates the formation of a stable complex, maintaining the proximity of the functional monomers and consequently resulting in an increased polymerization yield. Additionally, it was also observed that the polymerization yield appeared to increase with increasing AMR molar ratio.

FTIR spectra of the polymer nanoparticles are shown in Fig. 2A. All the spectra fully overlap, indicating the polymer nanoparticles have the same composition. In the spectra of the polymer nanoparticles, a strong peak at 1725 cm^{-1} is observed, corresponding to saturated ester moieties arising from the ricinoleate ester carbonyl and the polymerization of acrylate groups in AMR and EGMEA. The presence of a single ester peak, rather than two distinct ester carbonyl peaks, confirms the absence of unreacted acrylate ester carbonyl groups in the polymer nanoparticles [13]. Amide I and amide II bands are visible at 1649 and 1527 cm^{-1}. The intensity of the broad band observed at around 3300 cm^{-1}, caused by NH stretching of secondary amide. Scanning electron microscopy (SEM) was utilized to perform the morphological analysis of GreenNanoMIPs. Fig. 2C and D present SEM images of GreenNanoMIPs at low and high magnifications, respectively. The SEM analysis reveals well-defined, monodisperse spherical nanoparticles.

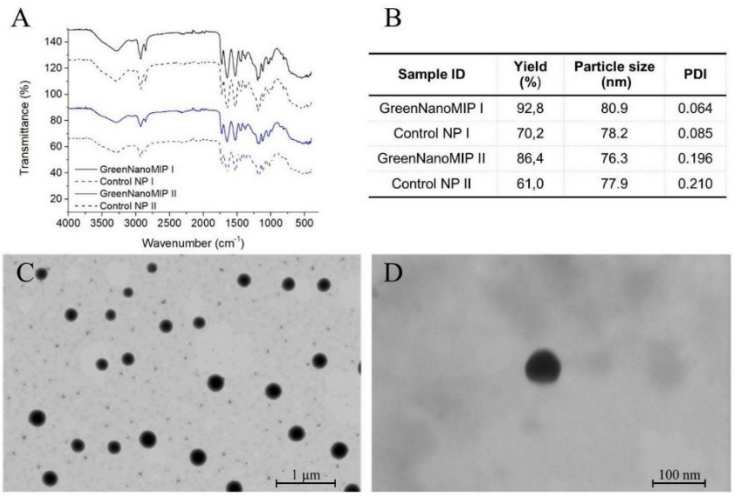

Sample ID	Yield (%)	Particle size (nm)	PDI
GreenNanoMIP I	92,8	80.9	0.064
Control NP I	70,2	78.2	0.085
GreenNanoMIP II	86,4	76.3	0.196
Control NP II	61,0	77.9	0.210

Fig. 2. A: FTIR spectra of GreenNanoMIPs and Control NPs; B: the yield (%), the particle size and the PDI of GreenNanoMIPs and Control NPs; C and D: SEM images of GreenNanoMIP I.

Particle size distribution

The size distribution of the synthesized GreenNanoMIPs and control NPs was determined by dynamic light scattering (DLS) technique. Polymer nanoparticles were tested after dialysis. The average particle sizes and polydispersity index values (PDI) are exhibited in Fig. 2B. GreenNanoMIP I, Control NP I, GreenNanoMIP II and Control NP II have average particle sizes of 80.9 nm, 78.2 nm, 76.3 nm and 77.9 nm, respectively. GreenNanoMIP I exhibited a remarkable homogeneity, having a PDI value as low as 0.064, which is significantly unusual for polymeric NPs. It should be noted that, even though all the NP solutions have monodispersed character with only one population, GreenNanoMIP II and Control NP II have higher PDI with larger particle population. In general, it was observed that PDI of the NPs decreased with increasing AMR molar ratio.

Stability of GreenNanoMIP in aqueous dispersion

GreenNanoMIP I and II and their controls were solvated in distilled water at 1 mg/mL concentrations. The solutions were kept at 4 °C and measured over time, up to after 1 year. Fig. 3 demonstrates the outstanding stability of the formed NPs, as there was no change in particle size distribution or PDI after one year. Notably, the solutions remained free from sedimentation or agglomeration. Additionally, particle size distribution analyses were performed under various conditions to assess the stability of nanoparticles for potential applications. The size distributions were measured at pH 4.0, pH 8.5, and 40 °C (Fig. SI2). With increasing temperature, the nanoparticles exhibited a slight reduction in size, confirming their thermoresponsive nature. At pH 8.5, they became larger while maintaining a monodisperse character, whereas at low pH, agglomeration was observed.

Binding studies of GreenNanoMIPs by means of Fluorescence Lifetime Measurements

The ability of GreenNanoMIPs I and II to bind the target analyte was investigated by means of fluorescence lifetime decay [22]. Chosen analyte was a unique peptide of cTnI labelled with the organic fluorophore fluorescein and indicated as NR10-FITC. NR10-FITC was used at the concentration of 10 nM and was incubated with increasing concentrations, from 0.5 ng/mL to 5000 ng/mL of NPs (GreenNanoMIP I, Control NP I, GreenNanoMIP II and Control NP II). The intensity decay curve of NR10-FITC was recorded at λ_{em} = 522 nm. Data were fitted with a biexponential fitting (τ_1 and τ_2) with fixed τ_1, in similarity to experimental conditions previously optimized [22]. Data were fitted with a biexponential fitting (τ_1 and τ_2) with fixed τ_1, in similarity to experimental conditions previously optimized [22]. Indeed, this was an approximate, though acceptable, model to represent and discriminate between the decay's contributions given by the fluorescent peptides randomly placed in solution and the decay's related to fluorescent peptides effectively bound to the imprinted binding sites of the GreenNanoMIPs. In detail, a fixed τ_1 was used as a global descriptor of all the non-specific decays occurring outside the molecularly imprinted cavities, whereas the binding-related interactions were observed as τ_2. Fig. 4 shows the binding curves related to NR10-FITC incubated with increasing concentrations of NPs GreenNanoMIP I with the relative non-imprinted Control NP I (Fig. 4A) and NPs GreenNanoMIP II with the relative non-imprinted Control NP II (Fig. 4B). The fluorescence lifetime of NR10-FITC decreases upon the addition of imprinted NPs (GreenNanoMIP I and GreenNanoMIP II) whereas no variation was observed for non-imprinted NPs (Control NP I and Control NP II). This suggested that the imprinting process effectively stamped binding sites on the nanoparticles. GreenNanoMIP II showed high uncertainty in the lifetime decays, possibly given by the tendency of these NPs to form aggregates, as supported by the larger PDIs values and the standard errors. Table 1 reports the data of the GreenNanoMIP I binding curve fitted with the Hill equation model. The GreenNanoMIP I measurement's space was of ~200 ps, with a half saturation which correlates with the dissociation constant at 3.31 ng/mL. The statistical number of binding sites per particle, n, had a value of 0.45 indicating that not all the formed binding sites were accessible. Out of this evidence, GreenNanoMIP I resulted promising for nanosensing applications. Fig. 4C and D report, respectively, the nonlinear fitting and the fitting with a linear equation model of just the linear portion of the binding isotherm of GreenNanoMIP I, with the parameters reported in Table 1.

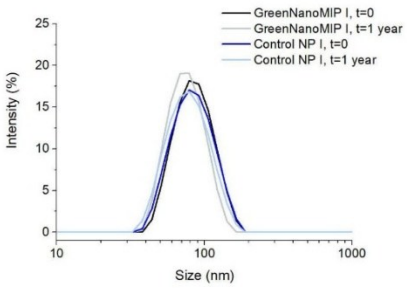

Fig. 3. Particle size distributions at the initial measurement and subsequently after one year.

Selectivity test

In order to test the binding selectivity of GreenNanoMIP I, a fluorescence lifetime experiment was carried out, so to confirm that the binding to the imprinted NPs, GreenNanoMIP I, was specific and selective for the targeted analyte (i.e. the cTnI peptide NR10). The peptides chosen as competitors were compared for their physicochemical characteristics, as reported in Table SI2. The target peptide NR10 is characterized by an isoelectric point (pI 7.00) alike its labelled form NR10-FITC, that was used as a probe for the lifetime measurements. In contrast, NR11 and FN11 peptides which are characterized by lower pIs, 4.07 and 3.12 respectively, were chosen to devise the effect of charge on NPs binding.

For the competition experiment, a solution of GreenNanoMIP I (25 ng/mL) was incubated with a fixed concentration of NR10-FITC (10 nM), in a condition that saturates the available binding sites. Then, each competitor, i.e. the non-fluorescent target NR10 and the non-related peptides NR11 and FN11, was added at the molar ratios of 1:1, 10:1, 100:1 and 1000:1 with respect to NR10-FITC. As shown in Fig. 5A, the incubation of the mix NPs GreenNanoMIP I and NR10-FITC with NR10 produced a drop of the fluorescence lifetime, indicating a displacement of the NR10-FITC as expected. In contrast, the incubation with non-template peptides did not produce significant changes in the τ_2, demonstrating the selectivity of the NPs GreenNanoMIP I *versus* the targeted peptide.

Overall, these tests allowed to get insights into the key mechanisms of the molecular recognition between NR10 and the GreenNanoMIPs I. In fact, the peptides NR11 and FN11 had molecular weight's values close to that of the template NR10, but different sequences, showing the binding is mainly driven by the sequence recognition than by the peptide's length. The sequence effect was investigated more in details using the peptide NR11, which share the same sequence of NR10, with the addition of a single aminocid (a glutamic acid within the sequence). As a result, the presence of a single aminoacid can be disruptive for the binding, especially if this produces a change in the pI of the peptide. Concerning the pI, NR10 was close to neutrality, whereas the competitor peptides were mild acidic, this showed that the effect of charge on the binding is crucial. The effect of hydrophobicity with its correlating GRAVY parameter, supported a favorable binding to GreenNanoMIP I for NR10, slightly more hydrophobic than NR11 and FN11.

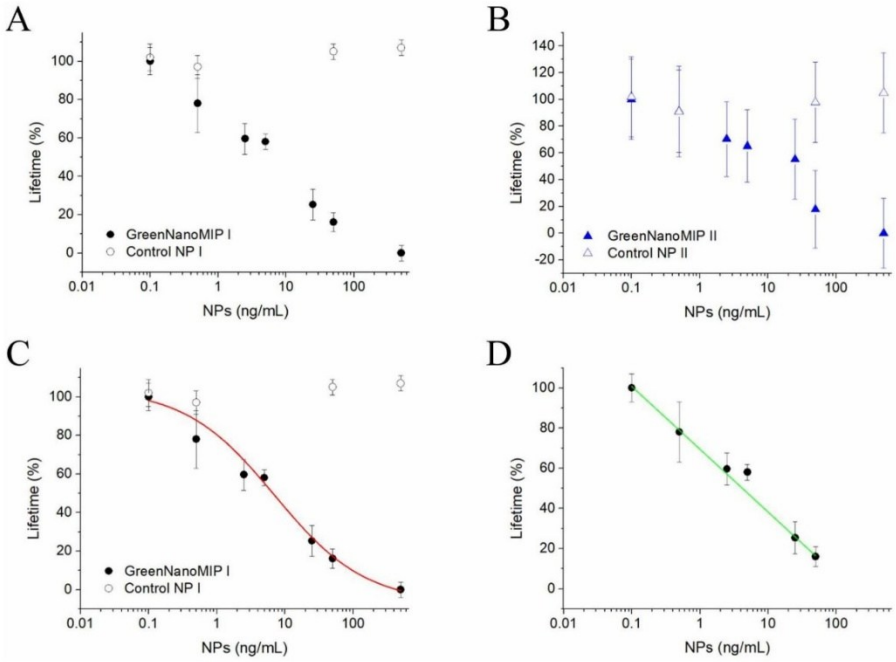

Fig. 4. A: Imprinted and control NPs incubated with increased concentrations of NR10-FITC (GreenNanoMIP I and Control NP I); B: Imprinted and control NPs incubated with increased concentrations of NR10-FITC (GreenNanoMIP II and Control NP II). C Imprinted NPs binding curve fitted with Hill equation model (red line) and (D) linear (green line) equation model.

Table 1
Binding values from the Hill and linear equation model.

Parameters	GreenNanoMIP I
$\tau_{2,0}$ (ns)	3.7633 ± 0.0396
$\tau_{2,max}$ (ns)	3.5259 ± 0.0252
EC_{50} (ng/mL)	3.3162 ± 0.0444
n	0.4527 ± 0.0164
R^2_{adj}	0.98531
Parameters	GreenNanoMIP I
Intercept	3.6656 ± 0.0009
Slope	−0.0528 ± 0.0005
R^2_{adj}	0.99959

In order to prove the effectiveness of the epitope-imprinting strategy hence the formation of imprinted binding sites in GreenNanoMIP I suitable to recognize the whole cTnI protein, the binding of cTnI to GreenNanoMIP I was tested in a competitive experiment in fluorescence lifetime, using NR10-FITC as a fluorescent probe and results were compared to the ability of GreenNanoMIP I in rebinding a MI non-related protein, that was human serum albumin (HSA) and was chosen for its abundance in serum, that might be the specimen next used for testing patients for suspected MI. Fig. 5B shows that the whole protein biomarker, cTnI, produced a clear displacement of the NR10-FITC probe. In contrast, HSA did not show a dose-related displacement, but possibly a minor and non-specific adsorption effect. Overall, these results clearly indicate the epitope approach proved effective, as the NR10 imprinted GreenNanoMIPs demonstrated to bind selectively the whole cardiac Troponin I protein (Fig. 5B). As a further control of the specific and selective binding, control non-imprinted NPs (Control NP I) were tested in a competition experiment in fluorescent lifetime and using NR10-FITC as a probe. The results, reported in in Fig. 6 showed that NPs Control NP I do not bind the fluorescent probe, as indicated by the non-significative change in the τ_2 upon NPs addition. Moreover, proteins, both the target cTnI and serum albumin, produced the same and concentration independent effect on the measurement. These results strongly support the non-specific character of the Control NPs, respect to the imprinted GreenNanoMIPs.

Measurements in human serum

Finally, the ability of GreenNanoMIPs to rebind the targeted biomarker in serum was also tested. A sample of pooled sera from healthy volunteers (Sigma-Merck) was diluted and spiked with a known concentration of cTnI (1 μM). Sera, control and the cTnI spiked one, were then incubated with a known concentration of GreenNanoMIP I (25 ng/mL) and a known quantity of NR10-FITC probe. Lifetime measurements results are reported in Fig. 7. It can be appreciated that the GreenNanoMIP I and NR10-FITC fluorescent probe provide a determination method that can be used in serum, opening to the development of GreenNanoMIP I nanosensors assays, Additionally, these preliminary results show that the GreenNanoMIP I competitive strategy indeed provided the detection of the biomarker cTnI directly in serum (Fig. 7).

GreenNanoMIP I enabled to determine cTnI directly in serum without pre-treatments, despite optimization is needed to achieve lower detection limits. In the literature, there are examples of MIP-based

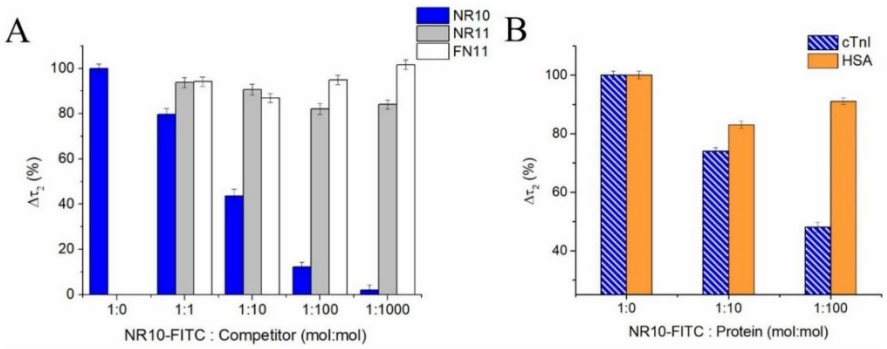

Fig. 5. A: selectivity of GreenNanoMIP I NPs using different peptide; B: Selectivity test of GreenNanoMIP I using different protein.

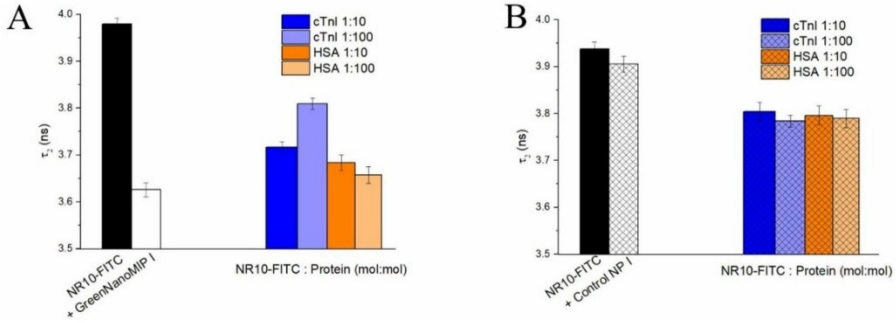

Fig. 6. Competitive lifetime experiments to evaluate the selectivity of GreenNanoMIP I NPs and of Control NP I. A: lifetime decay of NR-10-FITC only (solid black bar); upon the addition of GreenNanoMIP I NPs (white bar); upon the addition of competitors to the NR-10-FITC + GreenNanoMIP I NPs, namely cTnI 10x blue or 100x light blue; HSA 10x orange or 100x light orange; B: lifetime decay of NR-10-FITC only (solid black bar); upon the addition of Control I NPs (white striped bar); and upon the addition of competitors to the NR-10-FITC + Control I NPs, namely cTnI 10x striped blue or 100x striped light blue; HSA 10x striped orange or 100x striped light orange.

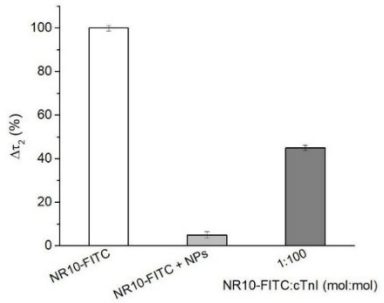

Fig. 7. Lifetime competitive measurements of spiked cTnI in human serum. White bar: NR10-FITC in cTnI depleted serum; light grey bar: NR10-FITC in cTnI depleted serum upon the addition GreenNanoMIP I; dark grey bar: GreenNanoMIP I particles added to NR10-FITC in serum spiked with cTnI.

sensing of cTnI, as reported in Table 2, mostly with electrochemical transduction. However, to attain the LODs required in clinical assessments often samples are pretreated, either centrifugated or enriched by preconcentration steps on columns.

At last, a comparison was made between GreenNanoMIP I and others, more traditional, MIP materials, equally prepared for the recognition of cTnI. It was observed that castor-oil based MIP nanoparticles displayed an affinity for cTnI of about 3×10^{11} M^{-1}, which was alike, or superior to that reported for traditional MIPs. In particular, the group of Altintas prepared p-NIPAM-co-APM in the form of nanoMIPs, with a reported affinity for cTnI of 3×10^{10} M^{-1} [23] and later electropolymerized a MIP in the form of a thin layer, made staring from 2-Aminophenol, that exhibited an affinity of 5×10^{11} M^{-1} [25]. These results support the competitivity of the GreenNano MIPs, made starting from more sustainable building blocks, in terms of affinity of the interaction.

Conclusions

In this study, we introduce a fatty acid-derived functional monomer for the first time in the synthesis of MIP nanomaterials. Acrylated methyl ricinoleate (AMR), derived from castor oil, was utilized in the synthesis

Table 2
Literature examples of MIP-based sensing of cTnI.

MIP NPs type	MIP composition	Detection	Range concentration	LOD	Reference
MIP immobilized on Au surface	NIPAm[a] APM[b]	SPR	0.78–50 ng/mL	0.52 ng/mL	[23]
MIP/QDs/GCE	Pyrrole	DPV	0.01–5 ng/mL	0.0005 ng/mL	[24]
MIP electropolymerized layer	2-AP[c]	SWV	0.005–10 ng/mL	0.5 pg/mL	[25]
MIP electropolymerized layer on GCE	DA[d]	ECL	0.005–10^4 ng/mL	0.0184 ng/mL	[26]
GCE/MIP	O-AP[e]	EIS	0.05–5 nM	0.027 nM	[27]
MIPs layer/MWCNTs/GS on GCE	MAA[f]	DPV	0.005 to 60 ng/mL	0.0008 ng/mL	[28]
Magnetic MIP	MAA[f] DMAm[g]	Raman spectroscopy	0.001–100 ng/mL	0.063 pg/mL	[29]
GreenNanoMIP	AMR, EGMEA	Fluorescence LT	0.1–50 ng/mL	1.6 ng/mL	This work

[a] N-Isopropylacrylamide
[b] N-(3-Aminopropyl) methacrylamide hydrochloride
[c] 2-Aminophenol
[d] Dopamine
[e] O-Aminophenol
[f] Methacrylic acid
[g] N,N-Dimethylacrylamide.

of environmentally friendly molecularly imprinted polymer nanoparticles (GreenNanoMIPs). By employing a renewable, plant-oil-based monomer, we successfully developed a sustainable method to produce green nanoMIPs. The use of this castor oil-based monomer not only supports an eco-friendly approach but also yields a biocompatible and non-immunogenic natural biomaterial. Recently Martine Esteban proposed a method to measure the greenness of MIPs with a score system [8], which in the case of GreenNanoMIPs resulted very low (Fig. S1).

Additionally, here the greener nanoMIPs were specifically addressed at targeting the cardiac troponin I (cTnI), a protein marker in the blood associated with cardiovascular events, particularly myocardial infarction (MI). Stable, monodisperse GreenNanoMIPs were produced, that demonstrated successful recognition of the cTnI protein through an epitope approach. The GreenNanoMIPs demonstrate ability to bind cTnI even in serum, suggesting high selectivity of the nanomaterials imprinted. These MIP nanoparticles align with green chemistry principles, advancing safer materials for applications in drug delivery, diagnostics, and environmental sensing.

Author contributions

The manuscript was written through contributions of all authors. All authors have given approval to the final version of the manuscript. These authors contributed equally.

Funding sources

This research was supported by Istinye University Scientific Research Projects (2022/GBAP3) and the Italian Ministry of Research and University with the PON PNRR D.M.351 funds.

Abbreviations

MIPs, molecularly imprinted polymers; SEM, scanning electron microscopy; FTIR, Fourier-transform infrared; AMR, acrylated methyl ricinoleate; cTnI, cardiac troponin I protein; MI, myocardical infarction, PBS, Phosphate-buffered saline.

Supplementary material

Synthetic space: molar equivalency % of the synthetic reagents and physical characteristics of the produced nanoparticles, physicochemical characteristics of the target peptide epitope and of selected competitors and green score for the GreenNanoMIP (PDF).

CRediT authorship contribution statement

Pinar Cakir Hatir: Writing – review & editing, Writing – original draft, Validation, Supervision, Methodology, Investigation, Funding acquisition, Conceptualization. **Alice Marinangeli:** Writing – original draft, Methodology, Investigation, Data curation. **Alessandra Maria Bossi:** Writing – review & editing, Writing – original draft, Validation, Supervision, Methodology, Investigation, Funding acquisition, Conceptualization. **Gokhan Cayli:** Writing – original draft, Project administration, Methodology.

Declaration of competing interest

The authors declare that they have no known competing financial interests or personal relationships that could have appeared to influence the work reported in this paper.

Acknowledgments

A.M.B. and A.M. acknowledge Ministry of University and Research for MUR D.M. 351 PON PNRR doctoral program. A.M.B. acknowledges the Centro Piattaforme Tecnologiche (CPT) of the University of Verona for the facilities DLS and Spectroscopy facilities. A.M.B. and P.C.H. acknowledge Verona University - Internationalisation Programme 2022. The authors also thank to Boğaziçi University's Center for Life Sciences and Technologies for conducting the SEM analyses and to Istinye University Scientific Research Projects (2022/GBAP3) for funding. The authors are grateful to Rojia Houshang for her support in conducting additional DLS measurements.

Supplementary materials

Supplementary material associated with this article can be found, in the online version, at doi:10.1016/j.talo.2025.100439.

Data availability

Data will be made available on request.

References

[1] R. Arshady, K. Mosbach, Synthesis of substrate-selective polymers by host-guest polymerization, Makromol. Chem. 182 (1981) 687–692, https://doi.org/10.1002/macp.1981.021820240.
[2] G. Wulff, A. Sarhan, Über die anwendung von enzymanalog gebauten polymeren zur racemattrennung, Angew. Chem 84 (1972) 364, https://doi.org/10.1002/ange.19720840838.

[3] B. Tse Sum Bui, K. Haupt, Molecularly imprinted polymer hydrogel nanoparticles: synthetic antibodies for cancer diagnosis and therapy, ChemBioChem 23 (2022) e202100598, https://doi.org/10.1002/cbic.202100598.
[4] A. Kumar, S. Kashyap, F. Mazahir, R. Sharma, A.K. Yadav, Unveiling the potential of molecular imprinting polymer-based composites in the discovery of advanced drug delivery carriers, Drug Discov. Today 29 (2024) 104164, https://doi.org/10.1016/j.drudis.2024.104164.
[5] Kang M.S, E. Cho, H.E. Choi, C. Amri, J.H. Lee, K.S. Kim, Molecularly imprinted polymers (MIPs): emerging biomaterials for cancer theragnostic applications, Biomater. Res. 27 (2023) 45, https://doi.org/10.1186/s40824-023-00388-5.
[6] S. Piletsky, F. Canfarotta, A. Poma, A.M. Bossi, S. Piletsky, Molecularly imprinted polymers for cell recognition, Trend. Biotechnol. 38 (2020) 368–387, https://doi.org/10.1016/j.tibtech.2019.10.002.
[7] R. Del Sole, G. Mele, E. Bloise, L. Mergola, Green aspects in molecularly imprinted polymers by biomass waste utilization, Polymers 13 (2021) 2430, https://doi.org/10.3390/polym13152430.
[8] M. Marć, W. Wojnowski, F. Pena-Pereira, M. Tobiszewski, A. Martín-Esteban, AGREEMIP: the analytical greenness assessment tool for molecularly imprinted polymers synthesis, ACS Sustain. Chem. Eng. 12 (2024) 12516–12524, https://doi.org/10.1021/acssuschemeng.4c03874.
[9] A. Martín-Esteban, Green molecularly imprinted polymers for sustainable sample preparation, J. Sep. Sci. 45 (2022) 233–245, https://doi.org/10.1002/jssc.202100581.
[10] J. Werner, A. Zgoła-Grześkowiak, T. Grześkowiak, R. Frankowski, Biopolymers-based sorbents as a future green direction for solid phase (micro)extraction techniques, TrAC - Trend. Anal. Chem. 173 (2024) 117659, https://doi.org/10.1016/j.trac.2024.117659.
[11] N.H. Godage, E. Gionfriddo, Use of natural sorbents as alternative and green extractive materials: a critical review, Anal. Chim. Acta 1125 (2020) 187–200, https://doi.org/10.1016/j.aca.2020.05.045.
[12] N. Le Goff, I. Fomba, E. Prost, F. Merlier, K. Haupt, L. Duma, A. Fayeulle, A. Falcimaigne-Cordin, Renewable plant oil-based molecularly imprinted polymers as biopesticide delivery systems, ACS Sustain. Chem. Eng. 8 (2020) 15927–15935, https://doi.org/10.1021/acssuschemeng.0c05145.
[13] P.C. Hatir, G. Cayli, Environmentally friendly synthesis and photopolymerization of acrylated methyl ricinoleate for biomedical applications, J. Appl. Polym. Sci. 136 (2019) 47969, https://doi.org/10.1002/app.47969.
[14] P.C. Hatir, Light-induced hydrogels derived from poly(ethylene glycol) and acrylated methyl ricinoleate as biomaterials, J. Appl. Polym. Sci. 139 (2022) e52754, https://doi.org/10.1002/app.52754.
[15] E. Antman, J.P. Bassand, W. Klein, M. Ohman, J.L. Lopez Sendon, L. Rydén, M. Simoons, M. Tendera, Myocardial infarction redefined—a consensus document of the Joint European Society of Cardiology/American College of Cardiology Committee for the redefinition of myocardial infarction: The Joint European Society of Cardiology/American College of Cardiology Committee, J. Am. Coll. Cardiol. 36 (2000) 959–969, https://doi.org/10.1016/s0735-1097(00)00804-4.
[16] A.M. Bossi, F. Bonini, A.P.F. Turner, S.A. Piletsky, Molecularly imprinted polymers for the recognition of proteins: the state of the art, Biosens. Bioelectron. 22 (2007) 1131–1137, https://doi.org/10.1016/j.bios.2006.06.023.
[17] A. Rachkov, N. Minoura, Towards molecularly imprinted polymers selective to peptides and proteins: the epitope approach, Biochim. Biophys. Acta Prot. Struct. Mol. Enzymol. 1544 (2001) 255–266, https://doi.org/10.1016/s0167-4838(00)00226-0.
[18] L. Pasquardini, A.M. Bossi, Molecularly imprinted polymers by epitope imprinting: a journey from molecular interactions to the available bioinformatics resources to scout for epitope templates, Anal. Bioanal. Chem 413 (2021) 6101–6115, https://doi.org/10.1007/s00216-021-03409-1.
[19] K. Kang, S. Li, L. Liu, Y. Chen, W. Zhou, J. Pei, Z. Liang, L. Zhang, Y. Zhang, Epitope imprinting technology: progress, applications, and perspectives toward artificial antibodies, Adv. Mater. 31 (2019) e1902048, https://doi.org/10.1002/adma.201902048.
[20] A. Biffis, N.B. Graham, G. Siedlaczek, S. Stalberg, G. Wulff, The synthesis, characterization, and molecular recognition properties of imprinted microgels, Macromol. Chem. Phys. 202 (2001) 163–171, https://doi.org/10.1002/1521-3935(20010101)202. :1%3C163::aid-macp163%3E3.0.co;2-m.
[21] P.Cakir Hatir, A. Cutivet, M. Resmini, B.T.S. Bui, K. Haupt, Protein-size molecularly imprinted polymer nanogels as synthetic antibodies, by localized polymerization with multi-initiators, Adv. Mater. 25 (2013) 1048–1051, https://doi.org/10.1002/adma.201203400.
[22] A.M. Bossi, A. Marinangeli, A. Quaranta, L. Pancheri, D. Maniglio, Time-resolved fluorescence spectroscopy of molecularly imprinted nanoprobes as an ultralow detection nanosensing tool for protein contaminants, Biosensors 13 (2023) 745, https://doi.org/10.3390/bios13070745.
[23] S. Choudhary, Z. Altintas, Development of a point-of-care SPR sensor for the diagnosis of acute myocardial infarction, Biosensors 13 (2023) 229, https://doi.org/10.3390/bios13020229.
[24] M.L. Yola, N. Atar, Development of cardiac troponin-I biosensor based on boron nitride quantum dots including molecularly imprinted polymer, Biosens. Bioelectron. 126 (2019) 418–424, https://doi.org/10.1016/j.bios.2018.11.016.
[25] G.K. Hasabnis, Z. Altintas, Cardiac troponin I-responsive nanocomposite materials for voltammetric monitoring of acute myocardial infarction, ACS Omega 9 (2024) 30737–30750, https://doi.org/10.1021/acsomega.4c03252.
[26] S. He, P. Zhang, J. Sun, Y. Ji, C. Huang, N. Jia, Integrating potential-resolved electrochemiluminescence with molecularly imprinting immunoassay for simultaneous detection of dual acute myocardial infarction markers, Biosens. Bioelectron. 201 (2022) 113962, https://doi.org/10.1016/j.bios.2022.113962.
[27] J. Zuo, X. Zhao, X. Ju, S. Qiu, W. Hu, T. Fan, J. Zhang, A new molecularly imprinted polymer (MIP)-based electrochemical sensor for monitoring cardiac troponin I (cTnI) in serum, Electroanalysis 28 (2016) 2044–2049, https://doi.org/10.1002/elan.201600059.
[28] Y. Ma, X.L. Shen, H.S. Wang, J. Tao, J.Z. Huang, Q. Zeng, L.S. Wang, MIPs-graphene nanoplatelets-MWCNTs modified glassy carbon electrode for the determination of cardiac troponin I, Anal. Biochem. 520 (2017) 9–15, https://doi.org/10.1016/j.ab.2016.12.018.
[29] S. Wang, J. Qin, Y. Liang, Y. Ye, Y. Guo, S. Li, Y. Liang, A magnetic SERS-imprinted sensor for the determination of cardiac troponin I based on proteolytic peptide technology, Anal. Chim. Acta 1332 (2024) 343316, https://doi.org/10.1016/j.aca.2024.343316.

Pınar Çakır Hatır is an Associate Professor and Head of the Department of Biomedical Engineering at İstinye University, Istanbul, Turkey. She received her Bachelor of Science degree in Chemistry from Boğaziçi University in 2004, followed by a Master of Science in Chemistry from the same university in 2008. In 2012, she completed her doctoral studies in Biotechnology at Sorbonne Universities, University of Technology of Compiègne, in France, where she specialized in molecularly imprinted polymers and their innovative applications in nanomedicine. Her research interests lie at the intersection of nanomedicine, smart polymers, molecular recognition, and drug delivery systems, focusing on renewable resources for biomedical applications.

Alice Marinangeli is a PhD student in Biotechnology at University of Verona, and she is passionate about the development of sensors and their application in biomedical, industrial and environmental fields. Her expertise includes the synthesis and characterization of biomimetic polymers in a nanometric format by molecular imprinting technique. Alice is dedicated to use these polymers as synthetic receptor to design optical and electrochemical sensors.

Alessandra Maria Bossi has a MSc in Biochemistry (State University of Milano, Italy) and a PhD in Polymer Chemistry (Cranfield University, UK). AM Bossi founded and currently leads the Molecular Imprinting and Analytical Sciences Group at the Dept. of Biotechnology, University of Verona. Her research is dynamic and focuses on advancing the field of molecularly imprinted polymers (MIPs), where she has been pioneering innovations in both the synthesis and application of MIPs, including MIPs made starting from biological materials. AM Bossi's has received fundings by both public and private institutions, including the Italian Ministry of University and the European Union. She is regularly invited to international conferences and is author of more than 110 papers on peer review international journals and of 7 patents.

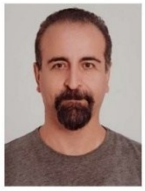

Gökhan Çaylı is a professor at Istanbul University-Cerrahpaşa, located in Istanbul, Türkiye. He obtained his Ph.D. from Boğaziçi University in 2008. His primary research focus is the synthesis of monomers and polymers derived from renewable resources as sustainable alternatives to petroleum-based materials. His expertise extends to photopolymerization, living polymerization techniques, polymer applications, and the study of interactions between nanoparticles and polymer structures.

CASTOR OIL-BASED MOLECULARLY IMPRINTED NANOPARTICLES FOR THE DETECTION OF CARDIAC TROPONIN I: TOWARDS GREEN MOLECULARLY IMPRINTED NANORECEPTORS

Pinar Cakir Hatir[*1], Alice Marinangeli[2], Alessandra Maria Bossi[2], Gokhan Cayli[3]*

[1]Department of Biomedical Engineering, Faculty of Engineering and Natural Sciences, İstinye University, Ayazağa Mah. Azerbaycan Cad. (Vadistanbul 4A Blok) 34396 Sariyer, İstanbul, Türkiye

[2]Department of Biotechnology, University of Verona, Strada Le Grazie 15, 37134 Verona, Italy

[3]Department of Engineering Sciences, Istanbul Cerrahpasa University, Avcilar Campus, 34320, Istanbul, Türkiye

**pinar.hatir@istinye.edu.tr*

Table SI1. Synthetic space: molar equivalency % of the synthetic reagents and physical characteristics of the produced nanoparticles.

Sample ID	AMR	EGMEA	MBA	Peptide	DLS (nm)	PDI
GreenNP I	45	5	-	-	>1000	>0.8
GreenNP II	25	25	-	-	>1000	>0.8
GreenNanoMIP I	45	5	50	+	80.9	0.06
Control NP I	45	5	50	-	78.2	0.09
GreenNanoMIP II	25	25	50	+	76.2	0.20
Control NP II	25	25	50	-	77.9	0.21

Table SI2. Physicochemical characteristics of the target peptide epitope and of selected competitors.

Peptide	Sequence	Molecular weight (g/mol)	Theoretical pI *	GRAVY**
NR10-FITC	FITC-NIDALSGMGR-OH	1404.52	7.00	-0.11
NR10	H-NIDALSGMGR-OH	1033.17	7.00	-0.11
NR11	H-NIDALSGMEGR-OH	1162.28	4.07	-0.42
FN11	H-FGSNVTDCSGN-OH	1100.12	3.12	-0.37

*www.novoprolab.com/tools/calc_peptide_property

**GRAVY: grand average of hydropathy. The GRAVY value is defined by the sum of hydropathy values of all amino acids divided by the peptide length. (Liu et al., 2004)

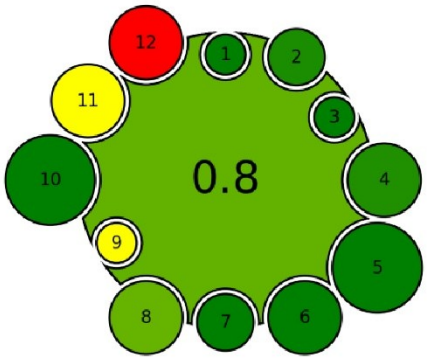

Figure SI1. Green score for the GreenNanoMIP (Marć et al., 2024)

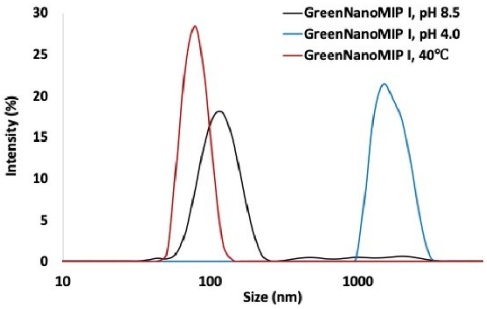

Figure SI2. Particle size distributions of GreenNanoMIP I at different conditions.

Paper IV

Highly Sensitive Biosensor for the Detection of Cardiac Troponin I in Serum via Surface Plasmon Resonance on Polymeric Optical Fiber Functionalized with Castor Oil-derived Molecularly Imprinted Nanoparticles

Summary

This work focuses on the development of a high-sensitivity optical sensor for the detection of cTnI, using castor oil-derived molecularly imprinted nanoparticles (GreenNanoMIPs), synthetized in the previous work, as synthetic recognition elements integrated into a miniaturized plastic optical fiber-based surface plasmon resonance (POF-SPR) transducer. The aim of this work was to evaluate whether these sustainable, highly stable and homogeneous nanoreceptors, originally designed for fluorescence-based sensing, could be successfully implemented into a plasmonic configuration to achieve ultrasensitive, selective, and rapid cTnI detection, thereby advancing toward point-of-care (POC) diagnostic applications. To achieve the goal of this work, the GreenNanoMIPs were covalently immobilized to the gold surface of the POF-SPR transducer through a classical EDC/NHS activation strategy, following the formation of a SAM of α-lipoic acid on the gold surface. The effectiveness of the functionalization was monitored in real time by evaluating the plasmonic spectral shifts at each modification step (bare gold surface, SAM formation, and GreenNanoMIP immobilization). A progressive red shift of the resonance wavelength, from 601.88 to 611.89 nm, confirmed the successful deposition of the nanoparticles. This result was further supported by X-ray photoelectron spectroscopy (XPS) analysis, which revealed the expected increase in the surface atomic percentages of carbon, oxygen, and nitrogen following the functionalization steps, providing independent evidence of the GreenNanoMIPs grafting onto the gold-coated POF surface.

The binding performance of the cTnI_nanoMIP-SPR-sensor was evaluated using the cTnI epitope peptide NR10 over a concentration range from 1 pM to 100 nM.

A clear concentration-dependent blue shift of the plasmonic resonance wavelength was observed, with a maximum shift of approximately 3 nm, indicating variations in the local refractive index near the gold surface upon NR10 binding to the GreenNanoMIP layer. The occurrence of a blue shift, rather than the typical red shift commonly associated with molecular adsorption on rigid plasmonic interfaces, can be attributed to the soft hydrogel nature of the GreenNanoMIP matrix, which can undergo local swelling or shrinking in response to analyte interaction. To assess the selectivity of the sensing system, the non-imprinted peptide NR11 was tested under the same conditions. In this case, no significant shift in the plasmonic resonance wavelength was observed, confirming the specific molecular recognition of the imprinted NR10 epitope by the cTnI_nanoMIP-SPR-sensor.

The sensing capability of the cTnI_nanoMIP-SPR-sensor was further evaluated using the full cTnI protein over a concentration range of 100 fM to 10 nM. Similarly, in this case, a progressive blue shift of the plasmonic resonance wavelength was observed, with a maximum shift of approximately 2 nm, confirming that the recognition mechanism for the NR10 peptide is preserved for the entire protein. To further evaluate the selectivity of the system, cytochrome c (Cyt c) and HSA were tested as non-target competitive proteins under the same experimental conditions and, in both cases, no significant resonance wavelength shifts were observed, confirming that the sensor response is exclusively associated with the specific recognition of cTnI by the GreenNanoMIPs.

The binding curve data were fitted using the Hill equation model, and the operational parameters of the sensor were calculated, yielding a LOD of 3.53×10^{-15} M, a LOQ of 1.17×10^{-14} M, and a sensitivity at low concentration of 8.49×10^{13}.

The applicability of the cTnI_nanoMIP-SPR-sensor in complex biological matrices was further assessed using model and real serum samples. The model serum was prepared by dissolving HSA at a concentration of 1 mg/mL, while real human serum was diluted 1:50 prior to analysis. To minimize nonspecific interactions arising from the complex matrix, Tween-20 (0.1% v/v) was added to both sample types before incubation. Both matrices were spiked with known concentrations of cTnI, and in all cases, the sensor provided clear spectral responses, consistent with the trends observed in buffer. Importantly, the cTnI_nanoMIP-SPR-sensor was able to

detect cTnI concentrations well below the clinical threshold (160 pM), confirming its strong potential for early-stage diagnosis of myocardial injury and its suitability for POC applications.

Overall, this study contributes to the general aim of the thesis by demonstrating an effective strategy to enhance the performance of MIP-based sensors through the use of sustainable and responsive polymeric materials. The employment of the castor-oil-derived green monomer enabled the synthesis of highly stable hydrogel-based GreenNanoMIPs, capable of retaining their recognition properties across different transduction modes (i.e. time-resolved fluorescence spectroscopy or SPR).

Published article

biosensors

MDPI

Article

Highly Sensitive Biosensor for the Detection of Cardiac Troponin I in Serum via Surface Plasmon Resonance on Polymeric Optical Fiber Functionalized with Castor Oil-Derived Molecularly Imprinted Nanoparticles

Alice Marinangeli [1,*], Pinar Cakir Hatir [2,3], Mustafa Baris Yagci [4] and Alessandra Maria Bossi [1,*]

[1] Department of Biotechnology, University of Verona, Strada Le Grazie 15, 37134 Verona, Italy
[2] Department of Biomedical Engineering, Faculty of Engineering and Natural Sciences, İstinye University, Ayazağa Mah. Azerbaycan Cad. (Vadistanbul 4A Blok) Sariyer, İstanbul 34396, Türkiye; pinar.hatir@istinye.edu.tr
[3] Nanotechnology and Advanced Materials Research Center, Istinye University, Sariyer, Istanbul 34396, Türkiye
[4] Koç University Surface Science and Technology Center (KUYTAM), Koç University, Istanbul 34450, Türkiye; byagci@ku.edu.tr
* Correspondence: alice.marinangeli@univr.it (A.M.); alessandramaria.bossi@univr.it (A.M.B.); Tel.: +39-045-8027-833 (A.M.); +39-045-8027-946 (A.M.B.)

Abstract

In this work, we report the development of a highly sensitive optical sensor for the detection of cardiac troponin I (cTnI), a key biomarker for early-stage myocardial infarction diagnosis. The sensor combines castor oil-derived biomimetic receptors, called GreenNanoMIPs and prepared via the molecular imprinting technology using as a template an epitope of cTnI (i.e., the NR10 peptide), with a portable multimode plastic optical fiber surface plasmon resonance (POF-SPR) transducer. For sensing, gold SPR chips were functionalized with GreenNanoMIPs as proven by refractive index changes and confirmed by means of XPS. Binding experiments demonstrated the cTnI_nanoMIP-SPR sensor's ability to detect both the NR10 peptide epitope and the full-length cTnI protein within minutes (t = 10 min), with high sensitivity and selectivity in buffer and serum matrices. The cTnI_nanoMIP-SPR showed an LOD of 3.53×10^{-15} M, with a linearity range of 1 pM–100 pM, outperforming previously reported sensor platforms and making it a promising tool for early-stage myocardial infarction detection.

Keywords: molecularly imprinted polymers; cardiac troponin I; myocardial infarction; biosensors; plant oil based functional monomer; castor oil monomer

Received: 6 November 2025
Revised: 15 December 2025
Accepted: 19 December 2025
Published: 23 December 2025

1. Introduction

Cardiac troponin I (cTnI) is a specific biomarker for acute myocardial infarction (AMI) and is considered the gold standard in clinical practice for diagnosing myocardial injury [1]. Elevated levels of cTnI, namely $\geq$ 0.04 ng/mL [2], are released into the bloodstream following damage to myocardial cells, i.e., after 3–12 h from the reported condition [2], making its detection essential for the early diagnosis and proper management of AMI [3]. For this reason, the demand for accurate and reliable diagnostic technologies that are able to detect low concentrations of cTnI remains a critical challenge. Immunoassays, such as enzyme-linked immunosorbent assays (ELISAs) [4], chemiluminescent immunoassays (CLIAs) [5] and radioimmunoassays (RAIs) [6], are the most widely used methods for cTnI

detection [7]. These methods provide high sensitivity and specificity due to the use of antibodies. However, they typically require a laboratory setting and specialized equipment, which may involve complex steps in preparation, and can be time-consuming and expensive. Furthermore, techniques such as RAI, which uses radioactive reagents, involve safety concerns and are subject to more stringent regulations [8]. To overcome the limitations of conventional assays, significant efforts have been focused on the development of alternative sensing platforms that are able to detect low levels of cTnI with high precision. In response to this challenge, over the last few years, sensors have emerged as promising alternatives to traditional methods, offering real-time detection and the potential for miniaturization and integration into portable devices [8]. Among these, sensors based on molecularly imprinted polymers (MIPs) have collected increasing attention due to their ability to offer selective and stable recognition of specific analytes [9–11]. MIPs are synthetic materials designed to have highly specific binding sites for a target analyte. These polymers are created through a template-assisted polymerization process, in which functional monomers and crosslinkers are polymerized in the presence of the target analyte, acting as a template [12,13]. After polymerization, the template is removed, leaving molecular cavities in the polymer that precisely match the size, shape, and functional groups of the original template. This process creates a polymer with specific recognition sites that are highly selective for the target molecule, much like antibodies, but with several key advantages. MIPs exhibit high chemical and thermal stability, a long shelf-life, and resistance to harsh environmental conditions. Unlike biological receptors, they can be produced with a simple process at a low cost and do not require cold-chain storage [14,15]. These features make MIPs particularly attractive for applications in point-of-care diagnostics, environmental monitoring, and clinical sensing platforms, where robustness, reproducibility, and scalability are essential. In this framework, advancements in MIP technology have led to improvements in the successful synthesis of polymers capable of recognizing macromolecules [16]. A particularly promising strategy has involved the use of epitope imprinting, in which short fragments of the target protein are used as a template for the imprinting process [17,18]. Peptides, which are smaller and more structurally undefined/flexible than full proteins, can serve as effective surrogates for the protein target. This strategy not only simplifies the synthesis process but also ensures that the MIP can recognize the protein in a highly specific manner by targeting key epitopes [19]. Several recent studies have demonstrated the feasibility of this method for cTnI recognition [20–23]. Building on these advances, we previously designed MIP receptors for cTnI, called GreenNanoMIPs, by adopting a peptide epitope imprinting strategy, selecting a specific fragment of the cTnI protein, the NR10 peptide, located in its C-terminal region [22]. This region was chosen due to its structural flexibility and lack of defined secondary structures, such as β-sheets, which facilitate both the imprinting process and subsequent molecular recognition [24,25]. Being located at the C-terminal region, it is accessible for recognition; it is among the targeted regions in ELISAs and was reported as an epitope for imprinting cTnI in the literature [20–22]. Moreover, the NR10 was selected because of its unique sequence (Peptide Atlas accession PAp00790335, 3601 experimental observations), which makes it highly suitable for the selective identification of human cTnI.

MIP-based sensors for cTnI detection, relying on electrochemical transduction, focused much of the innovation on improving the sensitivity of MIPs by integrating conductive nanomaterials to create more efficient and sensitive platforms. In particular, the MIP sensing layer was electrochemically polymerized, while doped with graphene and carbon nanotubes. Resulting in improved sensor sensitivity and signal amplification [26]. A notable example is Yola et al. [27], who developed an electrochemical sensor by electropolymerizing an MIP layer on a glassy carbon electrode (GCE) and enhancing the signal by doping it with boron nitride quantum dots. This approach resulted in a limit of detection (LOD) of

https://doi.org/10.3390/bios16010012

5×10^{-4} ng/mL, compatible with cTnI detection in complex biological matrices. In a similar vein, Ma et al. [28] layered graphene nanoplatelets and multi-walled carbon nanotubes on a GCE, followed by a chitosan deposition onto which a poly-methacrylic MIP layer was grown. This sandwich approach not only improved the electronic transmission rate but also enhanced the surface area, increasing the sensor's sensitivity and improving the binding kinetics for cTnI detection, resulting in an LOD of 0.027 nM (i.e., 8×10^{-4} ng/mL). Hasabnis et al. [21] demonstrated the enhancement of MIP sensor performance by a strategy based on incorporating GQDs and AuNPs into the MIP layer. This combination allowed them to achieve a LOD of 0.5 pg/mL, showcasing signal amplification and increased sensitivity. Moreover, the GQDs and AuNPs incorporated into the MIP layer also improved the affinity, reproducibility, and specificity of the sensor, making it more suitable for translation to real-world applications. While nanomaterial-assisted electrochemical MIP sensors have greatly improved the analytical performance for cTnI detection, the integration of molecular imprinting with advanced optical techniques remains relatively under-explored. One notable exception is the work by Choudhary et al. [20], who developed a point-of-care surface plasmon resonance (SPR) sensor based on the Kretschmann configuration [29] and functionalized with epitope-imprinted nanoMIPs for the real-time detection of cTnI. Their system demonstrated high reproducibility and selectivity, with an LOD of 0.52 ng/mL and a dissociation constant of 2.99×10^{-11} M, confirming the superior affinity of the imprinted receptors. However, in this configuration the LOD still remained uncompetitive compared to clinical requirements, particularly those aimed at ultra-sensitive diagnostics (i.e., the level of cTnI in the bloodstream: 0.04 ng/mL to 1.4 ng/mL within 3–12 h) [2].

Besides conventional SPR platforms, D-shaped plastic optical fiber (POF) SPR represents a highly versatile and cost-effective transducer. The D-shaped POFs provide several advantages, including a high numerical aperture, large core diameter, and remarkable mechanical flexibility, which allows the fiber to withstand tighter bend radii than glass fibers. Additionally, it has easy manipulation and low cost. Furthermore, the D-shaped POF-SPR configuration supports efficient broadband light coupling and enables remote and real-time interrogations [30]. Thanks to these advantages, SPR-POF sensors have been successfully employed for a variety of analytical and clinical applications, including the detection of proteins, metabolites, and biomarkers, using antibodies, aptamers, or MIP recognition elements. It was demonstrated that the combination of nanoMIPs that have a hydrogel nature with the D-shaped POF-SPR can lead to significant enhancements in sensor sensitivity, achieving LODs for the detection of protein analytes in the low picomolar range [31]. In particular, the analyte binding event was shown to deform the MIP nanogels, resulting in the swelling of the nanoMIPs and, hence, in blue-shifts at binding [31], in accordance with earlier reports [32]. In the present work, we developed a portable D-shaped POF-SPR functionalized with GreenNanoMIP nanogels, customized for the recognition of cTnI, with the aim of achieving the sensitivity required for in serum cardiac failure marker detection within the diagnostic levels.

2. Materials and Methods

2.1. Materials

Acrylated methyl ricinoleate (AMR) was synthesized from castor oil as described in our previous work [33]. All solvents, Ethylene glycol methyl ether acrylate (EGMEA), Lithium phenyl-2,4,6-trimethylbenzoylphosphinate (LAP), *N*,*N*′-Methylenebis(acrylamide) (MBA), Human serum albumin (HSA), cytochrome C (Cyt C), Human serum Dimethyl sulfoxide (DMSO), Phosphate-Buffered Saline (PBS), Tween20, Tris-free base Buffer, 2-(*N*-morpholino)ethanesulfonic acid (MES), *N*-(3-Dimetilaminopropyl)-*N*′-ethylcarbodiimide (EDC), and *N*-Hydroxysuccinimide (NHS), were purchased from Sigma-Aldrich (Darm-

https://doi.org/10.3390/bios16010012

stadt, Germany). Cardiac troponin I (cTnI) was purchased from GenScript. The peptides NR10 of sequence NIDALSGMGR and NR11 of sequence NIDALSGMEGR were custom-synthesized from TAG-Copenhagen.

2.2. Synthesis of GreenNanoMIPs

GreenNanoMIPs were synthesized as reported in [22]. To summarize, AMR, EGMEA, and the template-peptide solution NR10 were combined and left for 15 min to form an intermolecular complex through noncovalent interactions. The appropriate solvent mixture (90:10, DMSO: H_2O) was then added into a glass vial, maintaining a monomer concentration of 0.5% (wt/wt). MBA and the initiator (10% wt/wt relative to the total monomer weight) were introduced next. The vial was exposed to a 365 nm LED UV lamp for 2 min, after which the reaction was stopped. The solution was then treated with 2 mL of 50 mM Tris-free base and left in the dark for 30 min. The polymerization solution was transferred into dialysis membranes (12,000 Da MWCO) and dialyzed against 5 L of water, repeating this process three times. Finally, the solution was placed in a Falcon tube and freeze-dried. Non-imprinted polymer nanoparticles were produced using the same procedure but without the template-peptide.

2.3. Functionalization of SPR-Polymeric Optical Fiber (SPR-POF)

The gold surface of a D-shaped SPR-POF [30] was first plasma-cleaned and treated overnight at room temperature (RT) with α-lipoic acid at a concentration of 0.3 mM in 8% ethanolic solution, producing a self-assembled monolayer (SAM). Subsequently, the so-produced surface was activated with EDC/NHS in a two-step reaction. Firstly, 100 µL of EDC at a concentration of 20 mM in MES buffer (50 mM, pH 5.5) was added to the surface for 30 min at RT. Then, NHS at the final concentration of 20 mM in MES buffer (50 mM, pH 5.5) was mixed with GreenNanoMIPs (1 mg/mL) for 10 min at RT. Then, 100 µL of this solution was added to the surface and incubated for 2 h at room temperature. Lastly, Tris-free base was added to the surface for 10 min to block the EDC/NHS reaction [31]. At the end of the process, the SPR-POF was rinsed with MilliQ water and kept in MilliQ water ON at RT to remove all non-reacted elements. The functionalization process of the GreenNanoMIPs-SPR-POF was evaluated by monitoring the variations in the plasmonic wavelength at each step, which were computed in relation to the non-functionalized chip and considering MilliQ water as the surrounding solution.

2.4. X-Ray Photoelectron Spectroscopy (XPS)

XPS analyses of bare gold SPR-chip, α-lipoic acid-modified SPR-chip, and GreenNanoMIP-SPR-chip were carried out according to [34,35] by a Thermo Scientific K-Alpha XPS with Al K-alpha monochromatic radiation (1486.3 eV) using a 400 µm X-ray spot size. The pass energy was set to 50 eV, corresponding to an energy resolution of roughly 0.5 eV. The take-off angle was set to 90°. All measured peaks were deconvoluted and fit by using Avantage 5.9 software. C 1s peak at 284.5 eV was designated for the charge correction and peak assessment.

2.5. Portable Surface Plasmon Resonance (SPR)

Measurements were performed on a portable SPR Spectra340 (Moresense S.r.l., Milan, Italy) [36]. In particular, the SPR platform is based on a modified D-shaped SPR-POF chip (model RA1008 manufactured by Moresense S.r.l., Milano, Italy), connected to the equipment by a 3D-printed custom holder. More specifically, the experimental setup is based on a spectrometer with a VIS range of 500–730 nm and a white light source of 400–780 nm. The SPR spectra are elaborated by custom Software (Capture Spectrum Data ver.2.4.8), which mathematically analyzes the plasmonic track, identifying the minima by first and second derivatives.

https://doi.org/10.3390/bios16010012

2.6. Sensor Response to NR10 Peptide

The dose–response curves of the SPR sensor were obtained by testing the NR10 peptide concentrations ranging between 1 pM and 30 nM in PBS (10 mM, pH 7.4). The experimental measurements were carried out by placing 100 µL of the NR10 solution at different concentrations onto the SPR-POF chip. The SPR spectra were acquired every 3 min until 15 min incubation time. A washing step between each concentration was performed by gently washing the surface with PBS three times. The SPR spectra were obtained using a normalization process, which was carried out by dividing the transmitted spectra on a reference spectrum obtained in air. The absolute values of resonance wavelength variations ($|\Delta\lambda|$) at different target concentrations (c) were calculated with respect to the plasmonic spectra in the absence of the analyte as $|\Delta\lambda| = \lambda_c - \lambda_0$, where λ_c corresponds to the resonance wavelength when the NR10 concentration is c and λ_0 corresponds to the resonance wavelength of the blank (solution without the NR10). The experimental data obtained were fitted using the Hill equation model, which has been previously employed to describe binding behavior in nanoMIP-based plasmonic sensing systems [31], as reported in Equation (1):

$$\lambda = \lambda_{\_end} \frac{c^n}{(K_{app} + c^n)} \quad (1)$$

where λ is the wavelength at concentration c of the ligand; $\lambda_{\_end}$ is the value at binding saturation; n is the Hill parameter, which correlates with the number of binding sites; K_{app} is the apparent dissociation constant. The fitting was carried out by using OriginPro software (version 9.0, Origin Lab. Corp., Northampton, MA, USA).

2.7. Sensor Response to cTnI

The dose–response curves of the SPR sensor for the protein cTnI were obtained as described in the Section 2.6 paragraph. cTnI was tested at different concentrations ranging from 100 fM to 10 nM, and data were analyzed as described before.

2.8. Selectivity Test

To test the selectivity of GreenNanoMIPs grafted on SPR-POF, NR11 peptide (NIDALS-GMEGR) was chosen as a competitor. The experimental measurements were carried out by placing 100 µL of the NR11 solution at different concentrations (from 1 pM to 10 nM) onto the SPR-POF chip. Additionally, the ability of GreenNanoMIPs grafted on SPR-POF to bind non-target proteins HSA and Cyt C was tested using different concentrations of the proteins (from 1 pM to 10 nM). The measurements and analysis were carried out as described in the Section 2.6.

2.9. Measurement of cTnI in Serum

SPR-POF chips modified with GreenNanoMIPs were tested with model serum and human serum, both spiked with a fixed concentration of cTnI (100 pM). In particular, the model serum was prepared with HSA at 1 mg/mL and then spiked with 100 pM of cTnI. Human serum from a pool of healthy donors was diluted 1:50 in PB 10 mM with the addition of 0.1% Tween 20. The experimental measurements were carried out by placing 100 µL of the serum spiked with a fixed concentration of cTnI onto the SPR-POF chip. The measurements and analysis were carried out as described in the Section 2.6.

3. Results

3.1. Preparation of the cTnI-NanoMIP-SPR-Sensor and Physical Characterization

The GreenNanoMIPs for the selective recognition of cTnI were prepared by us previously, starting from a castor-oil-based monomer, and the binding abilities of these Green-

https://doi.org/10.3390/bios16010012

NanoMIPs were assessed with a time-resolved fluorescence spectroscopy, showing selectivity for the epitope template NR10 with an EC_{50} of 1.37×10^{-11} M and a stability in solution for over 1 year (details in Table S1 DLS, Figure S1 stability, Figure S6 SEM image) [22]. In the present work, we exploited the GreenNanoMIPs to devise a portable POF-SPR biosensor for the determination of cTnI. For this, the gold-coated POF surface was functionalized with the GreenNanoMIPs, as schematically illustrated in Figure 1, following the approach described by Cennamo et al. [31]. Initially, a self-assembled monolayer (SAM) was formed on the gold surfaces through the use of α-lipoic acid [37]. Subsequently, the carboxylic groups of the SAM were activated using a mixture of EDC and NHS to enable covalent coupling. The activated surface was then incubated with GreenNanoMIPs, which were immobilized through the formation of stable amidic covalent bonds. Finally, any unreacted active sites were blocked using Tris-free base buffer to prevent nonspecific adsorption [31].

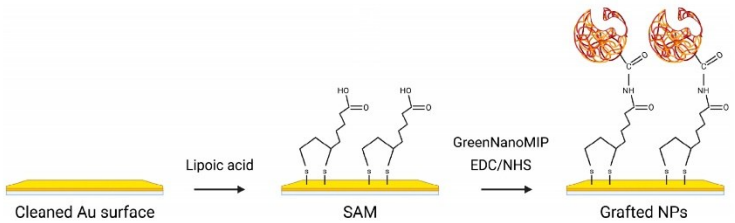

Figure 1. Schematic representation of the functionalization steps of the gold-coated POF surface with GreenNanoMIPs. The yellow surface represents the gold surface of the POF, while the red particles correspond to the GreenNanoMIPs.

As reported in Figure 2, the effectiveness of the functionalization procedure was assessed by evaluating the plasmonic spectral changes as the $|\Delta\lambda|$ computed in relation to that of the bare probe (i.e., cleaned, bare gold surface). Initially, the bare gold surface (n = 10) exhibited a plasmonic resonance at approximately 601.88 ± 1.44 nm. Following the formation of the α-lipoic acid SAM, a red-shift to 605.05 ± 1.77 nm was observed, indicating successful surface modification. Upon the grafting of GreenNanoMIPs, the resonance further shifted to 611.89 ± 1.27 nm, consistent with the increased thickness and the higher refractive index at the interface due to the presence of the polymeric layer. This functionalization procedure was repeated across multiple chips to evaluate reproducibility. As shown in Figure 2, the $|\Delta\lambda|$ observed for the formation of the α-lipoic acid SAM on the gold-coated POF was 3.17 ± 0.20 nm, and it further increased to 10.01 ± 0.20 nm after GreenNanoMIPs grafting. The standard deviations observed across multiple replicates (n = 10) were below ≤0.6%, confirming that the functionalization procedure yields consistently modified sensor surfaces with high reproducibility.

In support, X-ray photoelectron spectroscopy (XPS) analysis was carried out to independently confirm the functionalization of the gold-coated POFs with GreenNanoMIPs. XPS allowed us to inspect the surface chemical composition at each functionalization step (Table 1, details in Supplementary Information Figure S2) [34,35], verifying the presence of characteristic elemental signatures associated with the SAM and the polymeric GreenNanoMIPs layer, providing complementary evidence of successful surface modification. The chemical composition of the gold surface (C 9%; O 6%; N 0%) changed progressively with each modification step. The formation of the α-lipoic acid SAM was evidenced by an increase in carbon and oxygen contents (C 46.3%; O 25.6%, N 0%). The successful grafting of GreenNanoMIP was confirmed by the appearance of nitrogen and notable increases in both oxygen and carbon content (C 56%, O 23.5%, N 4.7%).

https://doi.org/10.3390/bios16010012

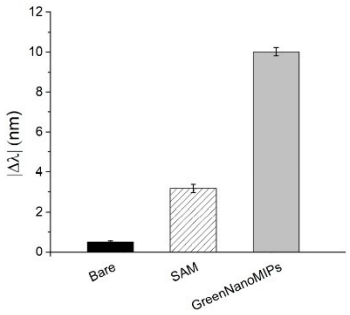

Figure 2. Absolute plasmonic resonance wavelength shifts ($|\Delta\lambda|$) of the SPR-POF after each functionalization step for the immobilization of GreenNanoMIPs: solid black bar indicates bare gold; striped bar, SAM; gray bar, GreenNanoMIPs.

Table 1. Chemical characterization determined by XPS of the different steps of chip functionalization, as shown in Figure 1. XPS data are acquired at 0° take-off angle, and the standard error does not exceed 1–2% of the reported value.

	C (%)	O (%)	N (%)
Bare	9.40	6.02	/
SAM	46.30	25.63	/
GreenNanoMIP	56.00	23.50	4.70

3.2. Kinetics of the Sensor Response

The response time of the cTnI_nanoMIP-SPR-sensor was evaluated by monitoring the evolution of the plasmonic resonance wavelength (λ) over time during the binding process. Figure 3 reports the plasmonic wavelength shift (λ) recorded for a representative NR10 concentration, plotted as a function of time (minutes). The signal gradually stabilizes, reaching equilibrium after approximately 10 min of incubation. This stabilization indicates that the binding interaction between NR10 and the GreenNanoMIP layer achieves steady-state conditions within this time frame, confirming that reliable measurements can be obtained with a rapid total assay time of 10 min.

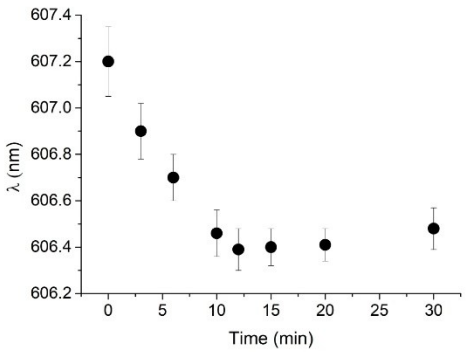

Figure 3. Kinetics of response of GreenNanoMIP-SPR-POF sensor: plasmonic resonance wavelength (λ) was plotted over time (min) for representative NR10 concentration (i.e., 100 pM).

https://doi.org/10.3390/bios16010012

3.3. Sensor Response to NR10 Peptide and Selectivity

The binding performance of the cTnI_nanoMIP-SPR sensor was evaluated for the detection of the NR10 peptide in PBS, within a concentration range from 1 pM to 100 nM. Figure 4A shows the plasmonic spectra after 10 min of incubation for each NR10 concentration, following the measurement protocol described in the Section 2. A zoomed-in view of the resonance peaks for the NR10 binding is provided in the Supplementary Information (Figure S3A). A clear concentration-dependent blue-shift in the plasmonic resonance wavelength was observed, with a maximum $|\Delta\lambda|$ of approximately 3 nm, reflecting a variation in the local refractive index near the gold surface upon the binding of NR10 to the GreenNanoMIP layer. The occurrence of a blue-shift, rather than the red-shift typically associated with molecular adsorption on rigid plasmonic interfaces, has been explained by considering the soft hydrogel nature of the GreenNanoMIP layer [31,32]. The polymeric network of the GreenNanoMIPs can absorb water and vary its degree of hydration, undergoing swelling or shrinking depending on the surrounding environment, which affects the thickness of the sensing layer, thus changing the effective refractive index [32,38,39]. Upon binding with the hydrated target analyte, soft polymer matrices undergo local deformation, hydration, and structural rearrangement, yielding to the lowering of the refractive index, hence leading to a blue-shift of the signal [31,32].

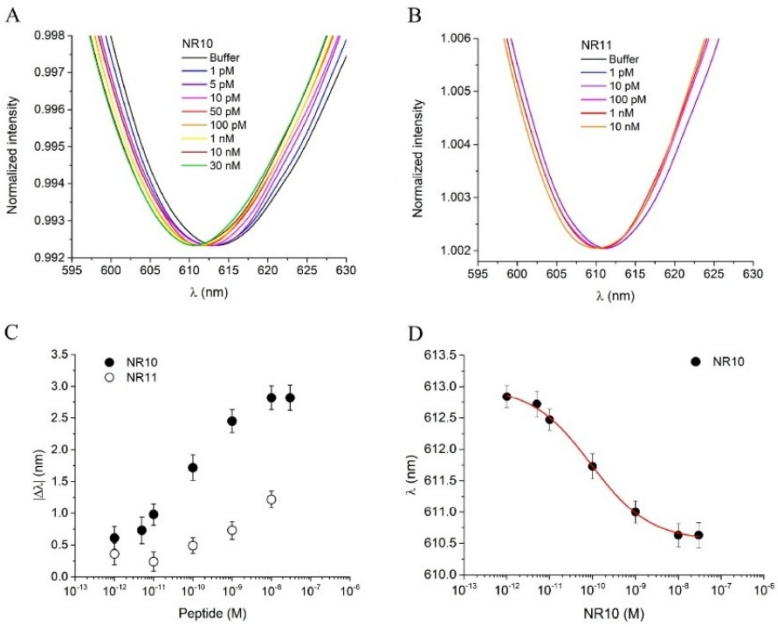

Figure 4. (**A**) Plasmonic spectra of GreenNanoMIPs-SPR-POF sensor incubated with increased concentrations of NR10 peptide (1 pM–30 nM). (**B**) Plasmonic spectra of GreenNanoMIPs-SPR-POF sensor incubated with increased concentrations of NR11 peptide (1 pM–10 nM). (**C**) Absolute plasmonic resonance wavelength shifts ($|\Delta\lambda|$) as a function of peptide concentration for the templated peptide NR10 (black dots) and the non-templated peptide NR11 (open dots). (**D**) Binding curve of NR10, showing the plasmonic resonance wavelength (λ) as a function of NR10 peptide concentration, fitted with the Hill equation model (red line).

https://doi.org/10.3390/bios16010012

To evaluate the selectivity of the cTnI_nanoMIP-SPR sensor, a structurally similar peptide, NR11, was used as a competitor, as shown in Figure 4B. A zoomed-in view of the resonance peaks for the NR11 binding is provided in the Supplementary Information (Figure S3B). NR11 differs from NR10 by a single additional glutamic acid (E) residue, resulting in comparable molecular weights (1033 Da for NR10 and 1162 Da for NR11), but with notable differences in physicochemical properties. Specifically, NR10 has an isoelectric point (pI) of 7.00, while NR11 has a lower pI of 4.07. The difference in pIs suggests that NR10 is more neutral at physiological pH (around pH 7.4), whereas NR11 is more acidic, potentially influencing its interaction with the MIP's binding sites.

Additionally, the Grand Average of Hydropathy (GRAVY) scores were −0.11 for the NR10 peptide and −0.42 for the NR11 peptide. The GRAVY score reflects the hydrophobicity or hydrophilicity of a peptide, with negative values indicating a tendency towards hydrophilicity (water solubility) and positive values indicating hydrophobicity (tendency to avoid water). The more hydrophilic nature of NR11, as indicated by its more negative GRAVY score, suggests that NR11 may have different solubility and surface interaction properties compared to NR10, further influencing the binding selectivity of the sensor. When exposed to NR11 in concentrations ranging from 1 pM to 10 nM, no significant shift in the plasmonic resonance wavelength was observed (Figure 4B), highlighting the sensor's high selectivity for the NR10 template. The dose–response curves, presented in Figure 4C, plot the absolute $|\Delta\lambda|$ as a function of analyte concentration on a semilogarithmic scale. The use of $|\Delta\lambda|$ values allows the normalization of results obtained from different sensing chips, ensuring data comparability and minimizing small baseline variations between experiments. Conversely, the fitting of the binding isotherm (Figure 4D) was performed using the absolute resonance wavelength (λ) rather than $|\Delta\lambda|$, since this approach provides direct access to the parameters $\lambda_{\_start}$ and $\lambda_{\_end}$ of the fitting equation model, which are subsequently used to calculate the main operational parameters of the sensor. In particular, the curves for the templated peptide NR10 (black dots) and the non-templated peptide NR11 (open dots) exhibit distinct binding behavior, with NR10 producing a clear response and NR11 showing negligible interaction. The statistical variability of the measurements, calculated from three replicate tests on separate chips, was 0.45%, indicating very high reproducibility. Data obtained from the NR10 binding were fitted to the Hill equation model using OriginPro software (Figure 4D), and the related fitting parameters, along with the corresponding sensor parameters, are summarized in Table 2. In particular, the cTnI_nanoMIP-SPR-sensor exhibited a $|\Delta\lambda|$ of approximately 3 nm, with half-saturation corresponding to an apparent dissociation constant (K_{app}) of 2.73×10^{-11} M. The statistical number of binding sites per particle, n, was found to be 0.49, suggesting that not all available binding sites were accessible for interaction. In terms of analytical performance, the cTnI_nanoMIP-SPR sensor exhibited a limit of detection (LOD) of 2.9×10^{-14} M, a limit of quantification (LOQ) of 9.83×10^{-14} M, and a sensitivity at low concentrations of 2.23×10^{13} M.

Table 2. Fitting parameters and sensor parameters related to GreenNanoMIPs-SPR-POF sensor's response to NR10.

Parameters	Value
$\lambda_{\_start}$ (nm)	613.45 ± 0.22
$\lambda_{\_end}$ (nm)	610.63 ± 0.18
K_{app} (M)	$2.73 \times 10^{-11} \pm 1.38 \times 10^{-11}$
n	0.49 ± 0.12

https://doi.org/10.3390/bios16010012

Table 2. *Cont.*

Parameters	Value	
R^2_{adj}	0.96589	
X^2_{red} **	0.90761	
K_{aff} (M^{-1})	3.66×10^{10}	$K_{aff} = 1/K_{app}$
Sensitivity at low concentration (nm/M)	2.23×10^{13}	$\lvert \lambda_{\_end} - \lambda_{\_start} \rvert / K_{app}$
LOQ (M)	9.83×10^{-14}	$10 \times$ St.Dev. $_{blank}$/Sensitivity $_{low\ conc}$ *
LOD (M)	2.9×10^{-14}	$3 \times$ St.Dev. $_{blank}$/Sensitivity $_{low\ conc}$ *

* St.Dev. $_{blank}$ represents the standard deviation measured when buffer is added to the sensor. ** Statistical indicator of the goodness of the fit.

3.4. Sensor Response to cTnI and Selectivity

The cTnI_nanoMIP-SPR sensor was further tested for its ability to detect the full-length cTnI in PBS, across a concentration range spanning from 100 fM to 10 nM. Figure 5A reports the plasmonic spectra obtained at different cTnI concentrations after 10 min of incubation using the same measurement protocol previously described. Zoomed-in views of the resonance peaks for cTnI, binding experiments are provided in the Supplementary Materials (Figure S4A). As observed, increasing cTnI concentrations induced a progressive blue-shift in the resonance wavelength, reaching a maximum $\lvert \Delta\lambda \rvert$ of approximately 2 nm. This shift indicates an alteration in the local refractive index at the sensor surface due to the specific interaction between the GreenNanoMIPs and the target protein, consistent with the behavior previously observed for the binding of the NR10 epitope peptide used as a template. In this case as well, the blue-shift can be attributed to the soft and hydrogel-like nature of the GreenNanoMIP layer, whose hydration-dependent swelling/shrinking and binding-induced deformation modify the optical properties of the plasmonic interface, resulting in a net shift toward shorter wavelengths.

To assess the selectivity of the cTnI_nanoMIP-SPR sensor, Cyt C and HSA were selected as non-target, competitive proteins. Both proteins were selected due to their high abundance in human plasma and their potential to interfere in complex biological matrices, especially in diagnostic applications, despite significantly differing from cTnI in terms of molecular weight, structure, and isoelectric point. Solutions of Cyt C and HSA tested over a concentration range from 1 pM to 10 pM did not induce any significant resonance wavelength shift (Figure 5B,C), indicating negligible non-specific binding and high selectivity of the cTnI_nanoMIP-SPR sensor (zoomed-in views of the shifts in Supplementary Information Figure S4B,C). As shown in the dose–response curves in Figure 5C, a clear binding response was observed exclusively for the analyte cTnI (black squares), while interfering proteins (Cyt C: red circles; HSA: blue triangles) did not produce significant signal variations. As previously described for the peptide binding experiments, the $\lvert \Delta\lambda \rvert$ values were used to construct the dose–response curves for data normalization across different chips, while the absolute resonance wavelengths (λ) were employed for Hill model fitting to extract the sensor parameters directly. Each measurement was repeated three times using independently fabricated chips, and the error bars represent the standard deviations across replicates. The experimental data for cTnI binding were fitted with the Hill equation model using OriginPro software (Figure 5E), and the corresponding extracted parameters are summarized in Table 3. The cTnI_nanoMIP-SPR sensor demonstrated exceptional sensitivity, with an LOQ of 1.17×10^{-14} M, a sensitivity at low detection of 8.49×10^{13}, and an LOD of 3.53×10^{-15} M.

https://doi.org/10.3390/bios16010012

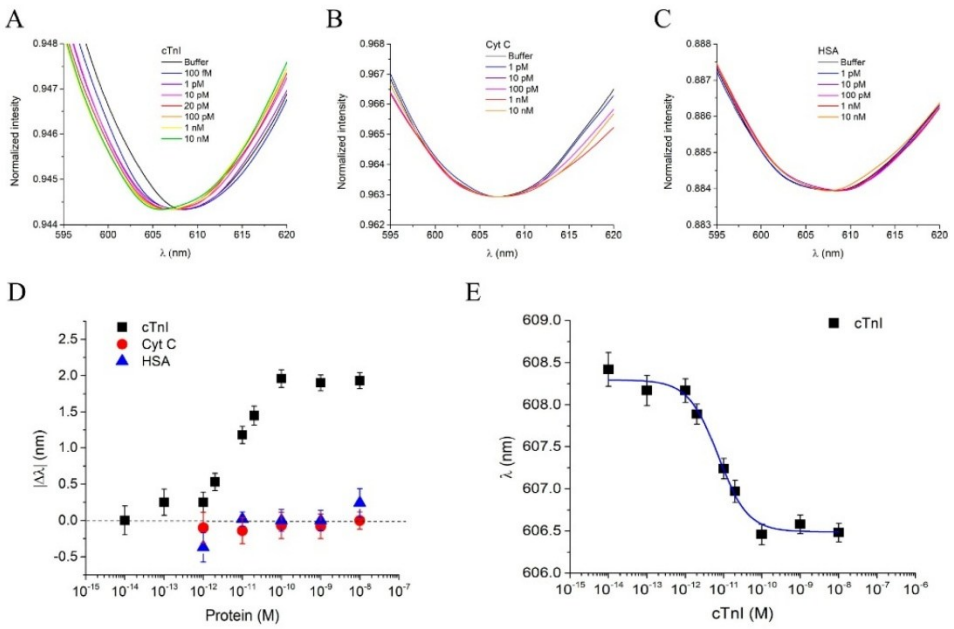

Figure 5. (**A**) Plasmonic spectra of GreenNanoMIPs-SPR-POF sensor incubated with increased concentrations of cTnI (100 fM–10 nM). (**B**) Plasmonic spectra of GreenNanoMIPs-SPR-POF sensor incubated with increased concentrations of Cyt C (1 pM–10 nM). (**C**) Plasmonic spectra of GreenNanoMIPs-SPR-POF sensor incubated with increased concentrations of HSA (1 pM–10 nM). (**D**) Plasmonic resonance wavelength shifts ($|\Delta\lambda|$) as a function of protein concentrations for cTnI (black square), Cyt C (red circles), and HSA (blue triangles). (**E**) Binding curve of NR10, showing the plasmonic resonance wavelength (λ) as a function of cTnI concentration, fitted with the Hill equation model (blue line).

Table 3. Fitting parameters and sensor parameters related to GreenNanoMIPs-SPR-POF sensor's response to cTnI.

Parameters	Value	
$\lambda_{\_start}$ (nm)	608.29 ± 0.10	
$\lambda_{\_end}$ (nm)	606.49 ± 0.05	
K_{app} (M)	$7.14 \times 10^{-12} \pm 1.45 \times 10^{-12}$	
n	1.11 ± 0.20	
R^2_{adj}	0.98266	
X^2_{red} **	0.56951	
K_{aff} (M^{-1})	1.40×10^{11}	$K_{aff} = 1/K_{app}$
Sensitivity at low concentration (nm/M)	8.49×10^{13}	$\lvert \lambda_{\_end} - \lambda_{\_start} \rvert / K_{app}$
LOQ (M)	1.17×10^{-14}	$10 \times$ St.Dev. $_{blank}$/Sensitivity $_{low\ conc}$ *
LOD (M)	3.53×10^{-15}	$3 \times$ St.Dev. $_{blank}$/Sensitivity $_{low\ conc}$ *

* St.Dev. $_{blank}$ represents the standard deviation measured when buffer is added to the sensor. ** Statistical indicators of the goodness of the fit.

https://doi.org/10.3390/bios16010012

3.5. Measurement of cTnI in Serum

To assess the performance of the cTnI_nanoMIP-SPR sensor under biological conditions, we first tested the sensor using a model serum and then a real human serum from healthy individuals (provided by a commercial source, see Materials and Methods). The model serum was created by dissolving HSA at a concentration of 1 mg/mL. This concentration was chosen because HSA is the most abundant protein in human blood, typically present at around 35–50 mg/mL, and the 1 mg/mL concentration was used to simulate the protein composition found in diluted human serum (1:50), which is among the typical conditions used for serum measurements [20]. The commercial human serum samples were diluted 1:50 to ensure consistency in protein concentration across the testing conditions. Both the model and commercial diluted human serum thus represent complex biological matrices suitable for evaluating the sensor's ability to detect cTnI in realistic conditions. The use of undiluted serum in plasmonic sensing is known to introduce substantial biofouling due to the high abundance of albumin, immunoglobulins, lipids, and other macromolecules that strongly adsorb onto the surfaces, which can interfere with the accessibility of the recognition layer and compromise the stability of the plasmonic signal. For this reason, the serum was diluted 1:50, a condition commonly adopted to mitigate matrix effects while preserving clinically relevant analyte levels. Notably, the clinical threshold associated with elevated cTnI ($\geq$0.04 ng/mL) corresponds to 0.0008 ng/mL after a 1:50 dilution, still above the LOD of the present sensor (0.000084 ng/mL). Thus, the dilution strategy reduces nonspecific adsorption without compromising the sensor's ability to detect cTnI at clinically meaningful concentrations. To further minimize non-specific interactions often caused by the complex serum matrix, Tween 20 at 0.1% v/v was added to the samples prior to incubation. This optimization effectively suppressed background signals originating from serum components, enhancing the sensor's specificity and overall detection accuracy (Figure S5). Both model and real serum samples were spiked with defined concentrations of cTnI: 100 pM for the model serum, and 50 pM and 100 pM for the human serum. As illustrated in Figure 6B, the model serum spiked with 100 pM cTnI produced a resonance wavelength shift of approximately 1.3 $\pm$ 0.1 nm (pink bar). Similarly, in the diluted human serum, the sensor yielded a shift of 1.29 $\pm$ 0.1 nm for 100 pM cTnI (dark green bar) and a distinct but lower shift of 0.7 nm for 50 pM cTnI (light green bar). Notably, the ability to detect cTnI well below the clinical threshold (160 pM) highlights the potential of the cTnI_nanoMIP-SPR sensor for early-stage diagnosis of myocardial injury. The reproducibility of the sensor was evaluated by testing multiple cTnI_nanoMIP-SPR sensors across different experimental runs. For each set of measurements, at least three separate sensor chips were used, and experiments were conducted on different days to ensure consistency over time. The response to a 100 pM cTnI solution was measured for each chip (n= 3), with the resulting resonance shift recorded as 1.25 $\pm$ 0.05 nm, as shown in Figure 6C, confirming good reproducibility of the sensor platform.

https://doi.org/10.3390/bios16010012

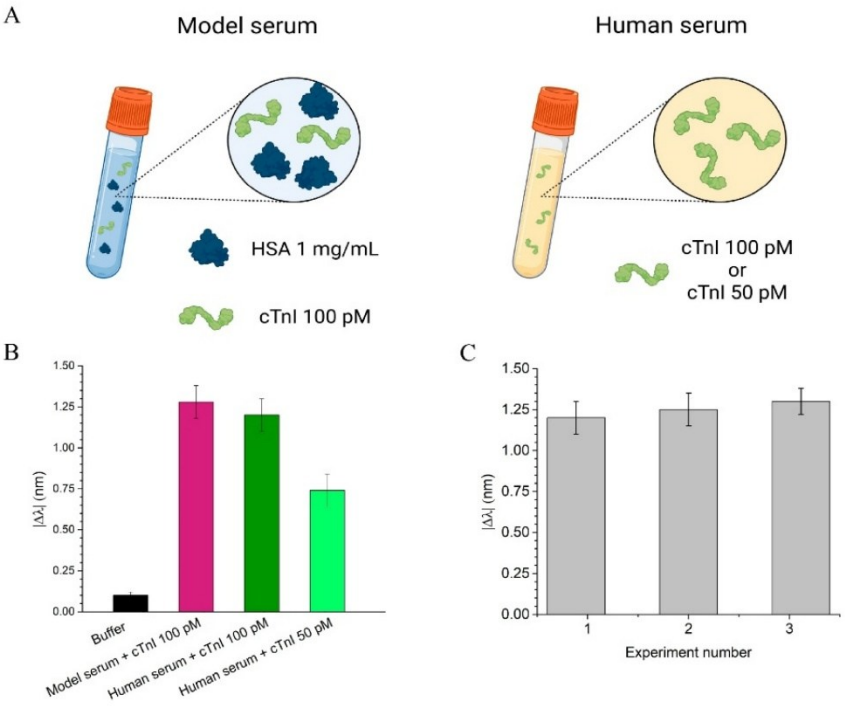

Figure 6. Evaluation of the cTnI_nanoMIP-SPR sensor performance in real samples. (**A**) Schematic representation of the tested samples: on the left, model serum consisting of HSA 1 mg/mL spiked with cTnI 100 pM; on the right, diluted human serum (1:50) spiked with cTnI at 100 pM or 50 pM. (**B**) Plasmonic resonance wavelength shifts ($|\Delta\lambda|$) in different sample matrices: model serum spiked with 100 pM of cTnI (pink bar), and human serum spiked with 100 pM (dark green bar) and 50 pM (light green bar) of cTnI. (**C**) Reproducibility test: sensor response in three independent experiments performed with human serum spiked with 100 pM cTnI.

4. Discussion

In this work, the coupling of GreenNanoMIPs with a portable D-shaped POF-SPR transducer resulted in the development of an optical sensor capable of detecting the myocardial infarction marker cTnI in serum samples, within the critical clinical range [2]. The performance of the GreenNanoMIP-SPR sensor was evaluated through a series of binding experiments, demonstrating its ability to detect both the NR10 peptide epitope and the full-length cTnI marker within minutes, with high sensitivity and selectivity. The sensor's applicability under clinically relevant conditions was further validated by testing its performance in real serum samples. The integration of biomimetic GreenNanoMIPs with a portable D-shaped POF-SPR platform led to a sensor with an LOD of 3.53×10^{-15} M. This value is significantly lower than those reported for previously developed sensor platforms, positioning it as a promising tool for the early detection of myocardial infarction. For comparison, a list of sensors for cTnI are reported in Table 4.

https://doi.org/10.3390/bios16010012

Table 4. List of SPR direct biosensors used for the detection of cTnI biomarkers reported in the literature and the current work.

Receptor Type	Detection	Range Concentration	LOD	Reference
Anti-cTnI antibody on fiber optic SPR	SPR	2500–4000 ng/mL	1 ng/mL	[40]
Monoclonal-anti-cTnI antibody on SPR	SPR	0.5–20 ng/mL	0.25 ng/mL	[41]
NanoMIPs grafted to Au on Kretschmann SPR	SPR	0.78–50 ng/mL	0.52 ng/mL	[20]
Norepinephryne MIP layer electropolymerized on Au chip for Biacore SPR	SPR	2.5–20 nM i.e., 6–48 ng/mL	460 pM i.e., 0.000011 ng/mL	[42]
GreenNanoMIPs grafted to Au on D-shaped POF-SPR	SPR	1 pM–100 nM i.e., 0.024 to 240 ng/mL	0.000084 ng/mL	This work
ELISA		0.32–200 ng/mL	0.32 ng/mL	[4]
ELISA HRP-based fluorescent		5–180 ng/mL	0.19 ng/mL	[43]
CLIA		Not indicated	0.116 pg/mL	[5]

Choudhary and Altintas et al. [20] reported an SPR-based sensor for cTnI detection, which displayed an LOD of 2.16×10^{-9} M. The SPR sensor was based on a conventional Kretschmann-configuration setup and made use of nanoMIPs with an average hydrodynamic size of 150 nm and a PDI of 0.150, prepared from a combination of acrylamides and *N*-isopropylacrylamide. The LOD achieved was remarkably similar to the results achieved for the detection of cTnI with SPR sensors equipped with monoclonal antibodies anti-cTnI [40,41]. In contrast, when the MIP was in the form of a thin layer of a few nanometers, prepared by a controlled electropolymerization of norepinephrine (NE), used as the functional monomer, and layered onto the gold chip of a Kretschmann-configuration SPR (i.e., Biacore), the sensor LOD was in the range of hundreds of pM. In SPR, binding events are detected as a change in local refractive index at the interface between the metal and the dielectric. It is expected that the ultrathin layer of poly-NE, deposited directly to the sensing interface, improves the transduction of the cTnI binding, as the specific recognition cavities on the poly-NE layer are within a distance of a few nanometers from the plasmon wave [42]. Finally, the herein reported SPR sensor based on castor oil-derived nanoMIPs was shown to exhibit a femtomolar LOD, surpassing both antibody-based SPR and nanoMIPs Kretschmann SPR approaches, while achieving an LOD similar to poly-NE MIP layers. Among the key factors contributing to this performance, there are both the herein-used multimode POF SPR setup and the characteristics of the GreenNanoMIP colloidal suspension. The multimode POF SPR setup, tested with solutions of known RI, was estimated to have a sensitivity value (S_n) of 1308×10^3 (nm/RIU) and a figure of merit (FOM) of 13.34 RIU^{-1} for pure water (n = 1.332) [44]. Concerning the GreenNanoMIP nanoparticles used as selective receptors, these display a strikingly high uniformity, as shown in Table S1. The GreenNanoMIPs exhibited a PDI equal to 0.064, which is remarkably low and indicates a very consistent particle size. It is expected that such receptors' uniformity translates into an extremely homogeneous recognition layer and into accessible binding sites, facilitating an efficient target recognition and high reproducibility of the sensor responses, as discussed earlier [45]. Additionally, the GreenNanoMIPs hydrodynamic diameter is around 80 nm, which is half the size of the cTnI nanoMIPs reported earlier in an SPR sensor [20]. As in SPR, the plasmon interrogating wave is governed by an exponential decay from the metallic surface towards the dielectric space, keeping the binding event

https://doi.org/10.3390/bios16010012

within a distance of 80 nm from the metallic surface; with respect to monitoring binding events at 150 nm from the metal surface, these can be calculated to improve the sensitivity of the measure of a factor of about 20–44 times, depending on the interrogating wavelength. At last, the GreenNanoMIPs are not only derived from a renewable source, but also exhibited an outstanding stability (up to one year in solution), supporting the solidity of the sensor's response. Beyond MIP- and antibody-based SPR platforms, Table 4 also includes representative immunoassay technologies commonly employed for cTnI quantification, such as enzyme-linked immunosorbent assays (ELISAs) [4,43] and chemiluminescent immunoassays (CLIAs) [5]. These methods typically provide dynamic ranges spanning from the low-nanogram per mL region up to hundreds of nanograms per mL, with an LOD extending from the sub-nanogram per mL level for ELISAs down to the sub-picogram per mL in the case of CLIAs. Such values reflect the sensitivity currently achievable in clinical diagnostics and define the benchmarks against which emerging biosensing approaches must be evaluated. When considered within this broader analytical landscape, the femtomolar LOD achieved by the cTnI_nanoMIP-SPR sensor falls well within, and in some cases exceeds, the sensitivity range characteristic of state-of-the-art immunoassay methodologies.

Although the present study demonstrated the feasibility of cTnI detection in diluted serum samples, the use of undiluted serum would be expected to introduce more pronounced biofouling effects due to the high content of albumin, immunoglobulins, lipids, and other macromolecules that can strongly adsorb onto plasmonic metal surfaces. Such nonspecific deposition may progressively mask the recognition layer and reduce the stability of the sensing interface during repeated measurements. While these aspects were beyond the scope of this work, future developments could integrate antifouling strategies to enhance robustness against cumulative fouling and to support measurements in more complex or minimally processed clinical samples. Overall, the present results provide the basis for an optical-sensor solution translatable into a tool for early diagnosis, offering a promising alternative in response to clinical needs.

Supplementary Materials: The following supporting information can be downloaded at https://www.mdpi.com/article/10.3390/bios16010012/s1, "Supplementary Material Marinangeli et al." contains: Table S1: Particle size and the PDI of GreenNanoMIPs; Figure S1: Particle size distributions of GreenNanoMIPs at the initial measurement and subsequently after one year. Re-printed from [22]; Figure S2: Deconvolution analysis of high-resolution XPS spectra of bare Au SPR-chip, SAM-modified SPR-chip and GreenNanoMIP functionalized SPR-chips; Figure S3: Zoomed-in view of the plasmonic spectra of GreenNanoMIPs-SPR-POF sensor incubated with increased concentrations of NR10 peptide (A) and with increased concentrations of NR11 peptide (B); Figure S4: Zoomed-in view of the plasmonic spectra of GreenNanoMIPs-SPR-POF sensor incubated with increased concentrations of cTnI (A), HSA (B) and Cyt C (C); Figure S5: Evaluation of the effect of the addition of 0.1% of Tween20 to the working buffer on the cTnI_nanoMIP-SPR-sensor performance when tested with real samples. In the absence of Tween20, human serum 1:50 (red bar) and human serum 1:50 spiked with 100 pM of cTnI (blue bar) showed similar effects on the sensor (λ = 624.16 nm and λ = 624.53 nm), demonstrating that non-specific absorption occurring at the sensor's surface was the prevailing mechanism. In contrast, when Tween20 was added to the buffer, the matrix effect on the sensor observed for diluted human serum (red bar) accounted for a λ = 614.55 nm, indicating a reduced matrix effect. More importantly, when human serum 1:50 spiked with 100 pM of cTnI (blue bar) was placed on the sensor, the expected blue-shift (λ = 612.84 nm) that correlated with the cTnI spiked concentration was observed; Figure S6: SEM image of GreenNanoMIPs.

Author Contributions: Conceptualization, A.M.B. and A.M.; methodology, A.M.B. and A.M.; validation, A.M., P.C.H., M.B.Y. and A.M.B.; formal analysis, A.M., P.C.H., M.B.Y. and A.M.B.; investigation, A.M. and P.C.H.; resources, A.M.B.; data curation, A.M., P.C.H. and A.M.B.; writing—original draft preparation, A.M., P.C.H., M.B.Y. and A.M.B.; writing—review and editing, A.M., P.C.H., M.B.Y. and

https://doi.org/10.3390/bios16010012

A.M.B.; supervision, A.M.B. and P.C.H.; project administration, A.M.B.; funding acquisition, A.M.B. All authors have read and agreed to the published version of the manuscript.

Funding: This research was funded by the Ministry of University and Research for MUR D.M. 351 PON PNRR.

Institutional Review Board Statement: Not applicable.

Informed Consent Statement: Not applicable.

Data Availability Statement: Data are available upon request.

Acknowledgments: A.M.B. and A.M. acknowledge the Ministry of University and Research for MUR D.M. 351 PON PNRR doctoral program. A.M.B. and P.C.H. acknowledge Verona University—Internationalisation Programme 2022. We kindly acknowledge Gokhan Cayli for contributing in the synthesis of the monomer AMR which was used to synthesise the GreenNanoMIP, according to [22].

Conflicts of Interest: The authors declare no conflicts of interest.

Abbreviations

The following abbreviations are used in this manuscript:

MIPs	Molecularly imprinted polymers
cTnI	Cardiac troponin I
POF	Plastic optical fiber
SPR	Surface plasmon resonance

References

1. Ge, W.H.; Lin, Y.; Li, S.; Zong, X.; Ge, Z.C. Identification of Biomarkers for Early Diagnosis of Acute Myocardial Infarction. *J. Cell Biochem.* **2018**, *119*, 650–658. [CrossRef] [PubMed]
2. Mahajan, V.S.; Jarolim, P. How to interpret elevated cardiac troponin levels. *Circulation* **2011**, *124*, 2350–2354. [CrossRef]
3. Chen, Y.; Tao, Y.; Zhang, L.; Xu, W.; Zhou, X. Diagnostic and prognostic value of biomarkers in acute myocardial infarction. *Postgrad. Med. J.* **2019**, *95*, 210–216. [CrossRef]
4. Hsieh, Y.F.; Lin, K.J. Rapid-Test Kit for Cardiac Troponin I: A Reliable Enzyme-Linked-Immuno-Substrate-Assay-Based Biosensor for Daily-Use Naked-Eye Detection and Pharmacokinetic Studies for Myocardial Infarction in Cardiovascular Disease. *ACS Pharmacol. Transl. Sci.* **2024**, *7*, 2369–2378. [CrossRef]
5. Zhao, H.; Lin, Q.; Huang, L.; Zhai, Y.; Liu, Y.; Deng, Y.; Su, E.; He, N. Ultrasensitive chemiluminescence immunoassay with enhanced precision for the detection of cTnI amplified by acridinium ester-loaded microspheres and internally calibrated by magnetic fluorescent nanoparticles. *Nanoscale* **2021**, *13*, 3275–3284. [CrossRef] [PubMed]
6. Westgard, S. A-003 Beckman Coulter DxI 9000 Immunoassay Analyzer's High Sensitivity Troponin I achieves> 90% six sigma performance when assessed against clia 2024 performance goals. *Clin. Chem.* **2024**, *70*, hvae106.003. [CrossRef]
7. Campu, A.; Muresan, I.; Craciun, A.M.; Cainap, S.; Astilean, S.; Focsan, M. Cardiac Troponin Biosensor Designs: Current Developments and Remaining Challenges. *Int. J. Mol. Sci.* **2022**, *23*, 7728. [CrossRef]
8. Ebrahimi, S.; Alivirdiloo, V.; Hajiabbasi, M.; Masoumi, S.; Mohammadi, M.; Hosseini, S.; Gargari, S.O.; Mobed, A. Cardiac Troponin I Biosensors: Innovations in Real-Time Diagnosis of Cardiovascular Diseases. *Anal. Sci. Adv.* **2025**, *6*, e70009. [CrossRef]
9. Leibl, N.; Haupt, K.; Gonzato, C.; Duma, L. Molecularly Imprinted Polymers for Chemical Sensing: A Tutorial Review. *Chemosensors* **2021**, *9*, 123. [CrossRef]
10. Wackerlig, J.; Lieberzeit, P.A. Molecularly imprinted polymer nanoparticles in chemical sensing–Synthesis, characterisation and application. *Sens. Actuators B Chem.* **2015**, *207*, 144–157. [CrossRef]
11. Asif, I.M.; Di Giulio, T.; Gagliani, F.; Malitesta, C.; Mazzotta, E. Advances in the Direct Nanoscale Integration of Molecularly Imprinted Polymers (MIPs) with Transducers for the Development of High-Performance Nanosensors. *Biosensors* **2025**, *15*, 509. [CrossRef] [PubMed]
12. Wulff, G.; Sarhan, A.; Zabrocki, K. Enzyme-analogue built polymers and their use for the resolution of racemates. *Tetrahedron Lett.* **1973**, *14*, 4329–4332. [CrossRef]
13. Arshady, R.; Mosbach, K. Synthesis of substrate-selective polymers by host-guest polymerization. *Macromol. Chem. Phys.* **1981**, *182*, 687–692. [CrossRef]

https://doi.org/10.3390/bios16010012

14. Vlatakis, G.; Andersson, L.I.; Müller, R.; Mosbach, K. Drug assay using antibody mimics made by molecular imprinting. *Nature* **1993**, *361*, 645–647. [CrossRef]
15. Kadhem, A.J.; Gentile, G.J.; Fidalgo de Cortalezzi, M.M. Molecularly Imprinted Polymers (MIPs) in Sensors for Environmental and Biomedical Applications: A Review. *Molecules* **2021**, *26*, 6233. [CrossRef]
16. Bossi, A.; Bonini, F.; Turner, A.P.; Piletsky, S.A. Molecularly imprinted polymers for the recognition of proteins: The state of the art. *Biosens. Bioelectron.* **2007**, *22*, 1131–1137. [CrossRef]
17. Rachkov, A.; Minoura, N.; Shimizu, T. Peptide separation using molecularly imprinted polymer prepared by epitope approach. *Anal. Sci.* **2022**, *17*, 609–612. [CrossRef]
18. Pasquardini, L.; Bossi, A.M. Molecularly imprinted polymers by epitope imprinting: A journey from molecular interactions to the available bioinformatics resources to scout for epitope templates. *Anal. Bioanal. Chem.* **2021**, *413*, 6101–6115. [CrossRef]
19. Altintas, Z.; Takiden, A.; Utesch, T.; Mroginski, M.A.; Schmid, B.; Scheller, F.W.; Süssmuth, R.D. Integrated approaches toward high-affinity artificial protein binders obtained via computationally simulated epitopes for protein recognition. *Adv. Funct. Mater.* **2019**, *29*, 1807332. [CrossRef]
20. Choudhary, S.; Altintas, Z. Development of a Point-of-Care SPR Sensor for the Diagnosis of Acute Myocardial Infarction. *Biosensors* **2023**, *13*, 229. [CrossRef] [PubMed]
21. Hasabnis, G.K.; Altintas, Z. Cardiac Troponin I-Responsive Nanocomposite Materials for Voltammetric Monitoring of Acute Myocardial Infarction. *ACS Omega* **2024**, *9*, 30737–30750. [CrossRef] [PubMed]
22. Hatir, P.C.; Marinangeli, A.; Bossi, A.M.; Cayli, G. Castor oil-based molecularly imprinted nanoparticles for the detection of cardiac troponin I: Towards green molecularly imprinted nanoreceptors. *Talanta Open* **2025**, *11*, 100439. [CrossRef]
23. Saczek, J.; Jamieson, O.; McClements, J.; Dann, A.; Johnson, R.E.; Stokes, A.D.; Crapnell, R.D.; Banks, C.E.; Canfarotta, F.; Spyridopoulos, I.; et al. Troponin I biomarker sensing from clinical patient samples using molecularly imprinted polymer nanoparticles for advancing healthcare approaches in cardiovascular disease. *Biosens. Bioelectron.* **2025**, *282*, 117467. [CrossRef]
24. Mier, A.; Maffucci, I.; Merlier, F.; Prost, E.; Montagna, V.; Ruiz-Esparza, G.U.; Bonventre, J.V.; Dhal, P.K.; Tse Sum Bui, B.; Sakhaii, P.; et al. Molecularly Imprinted Polymer Nanogels for Protein Recognition: Direct Proof of Specific Binding Sites by Solution STD and WaterLOGSY NMR Spectroscopies. *Angew. Chem. Int. Ed. Engl.* **2021**, *60*, 20849–20857. [CrossRef]
25. Zeng, Z.; Hoshino, Y.; Rodriguez, A.; Yoo, H.; Shea, K.J. Synthetic polymer nanoparticles with antibody-like affinity for a hydrophilic peptide. *ACS Nano* **2010**, *4*, 199–204. [CrossRef]
26. Lahcen, A.A.; Amine, A. Recent advances in electrochemical sensors based on molecularly imprinted polymers and nanomaterials. *Electroanalysis* **2019**, *31*, 188–201. [CrossRef]
27. Yola, M.L.; Atar, N. Development of cardiac troponin-I biosensor based on boron nitride quantum dots including molecularly imprinted polymer. *Biosens. Bioelectron.* **2019**, *126*, 418–424. [CrossRef]
28. Ma, Y.; Shen, X.L.; Wang, H.S.; Tao, J.; Huang, J.Z.; Zeng, Q.; Wang, L.S. MIPs-graphene nanoplatelets-MWCNTs modified glassy carbon electrode for the determination of cardiac troponin I. *Anal. Biochem.* **2017**, *520*, 9–15. [CrossRef] [PubMed]
29. Kretschmann, E.; Raether, H. Radiative decay of non radiative surface plasmons excited by light. *Z. Naturforsch. A* **1968**, *23*, 2135–2136. [CrossRef]
30. Cennamo, N.; Massarotti, D.; Conte, L.; Zeni, L. Low cost sensors based on SPR in a plastic optical fiber for biosensor implementation. *Sensors* **2011**, *11*, 11752–11760. [CrossRef] [PubMed]
31. Cennamo, N.; Maniglio, D.; Tatti, R.; Zeni, L.; Bossi, A.M. Deformable molecularly imprinted nanogels permit sensitivity-gain in plasmonic sensing. *Biosens. Bioelectron.* **2020**, *156*, 112126. [CrossRef]
32. Matsui, J.; Akamatsu, K.; Nishiguchi, S.; Miyoshi, D.; Nawafune, H.; Tamaki, K.; Sugimoto, N. Composite of Au nanoparticles and molecularly imprinted polymer as a sensing material. *Anal. Chem.* **2004**, *76*, 1310–1315. [CrossRef]
33. Cakir Hatir, P.; Cayli, G. Environmentally friendly synthesis and photopolymerization of acrylated methyl ricinoleate for biomedical applications. *J. Appl. Polym. Sci.* **2019**, *136*, 47969. [CrossRef]
34. Wen, X.; Linton, R.W.; Formaggio, F.; Toniolo, C.; Samulski, E.T. Self-assembled monolayers of hexapeptides on gold: Surface characterization and orientation distribution analysis. *J. Phys. Chem. A.* **2004**, *108*, 9673–9681. [CrossRef]
35. Ray, S.; Shard, A.G. Quantitative analysis of adsorbed proteins by X-ray photoelectron spectroscopy. *Anal. Chem.* **2011**, *83*, 8659–8666. [CrossRef]
36. Pasquardini, L.; Cennamo, N.; Arcadio, F.; Perri, C.; Chiodi, A.; D'agostino, G.; Zeni, L. Immuno-SPR biosensor for the detection of Brucella abortus. *Sci. Rep.* **2023**, *13*, 22832. [CrossRef]
37. Pasquardini, L.; Cennamo, N.; Malleo, G.; Vanzetti, L.; Zeni, L.; Bonamini, D.; Salvia, R.; Bassi, C.; Bossi, A.M. A Surface Plasmon Resonance Plastic Optical Fiber Biosensor for the Detection of Pancreatic Amylase in Surgically-Placed Drain Effluent. *Sensors* **2021**, *21*, 3443. [CrossRef] [PubMed]
38. Annunziata, M.; Arcadio, F.; Borriello, A.; Bencivenga, D.; Piccirillo, A.; Stampone, E.; Zeni, L.; Cennamo, N.; Della Ragione, F.; Guida, L. A novel plasmonic optical-fiber-based point-of-care test for periodontal MIP-1α detection. *iScience* **2023**, *26*, 108539. [CrossRef]

https://doi.org/10.3390/bios16010012

39. Cennamo, N.; Bencivenga, D.; Annunziata, M.; Arcadio, F.; Stampone, E.; Piccirillo, A.; Della Ragione, F.; Zeni, L.; Guida, L.; Borriello, A. Plasmon resonance biosensor for interleukin-1β point-of-care determination: A tool for early periodontitis diagnosis. *iScience* **2023**, *27*, 108741. [CrossRef] [PubMed]
40. Masson, J.F.; Obando, L.; Beaudoin, S.; Booksh, K. Sensitive and real-time fiber-optic-based surface plasmon resonance sensors for myoglobin and cardiac troponin I. *Talanta* **2004**, *62*, 865–870. [CrossRef] [PubMed]
41. Wei, J.; Mu, Y.; Song, D.; Fang, X.; Liu, X.; Bu, L.; Zhang, H.; Zhang, G.; Ding, J.; Wang, W.; et al. A novel sandwich immunosensing method for measuring cardiac troponin I in sera. *Anal. Biochem.* **2003**, *321*, 209–216. [CrossRef]
42. Baldoneschi, V.; Palladino, P.; Banchini, M.; Minunni, M.; Scarano, S. Norepinephrine as new functional monomer for molecular imprinting: An applicative study for the optical sensing of cardiac biomarkers. *Biosens. Bioelectron.* **2020**, *157*, 112161. [CrossRef] [PubMed]
43. Liu, J.; Ruan, G.; Ma, W.; Sun, Y.; Yu, H.; Xu, Z.; Yu, C.; Li, H.; Zhang, C.W.; Li, L. Horseradish peroxidase-triggered direct in situ fluorescent immunoassay platform for sensing cardiac troponin I and SARS-CoV-2 nucleocapsid protein in serum. *Biosens. Bioelectron.* **2022**, *198*, 113823. [CrossRef] [PubMed]
44. Špačková, B.; Wrobel, P.; Bocková, M.; Homola, J. Optical biosensors based on plasmonic nanostructures: A review. *Proc. IEEE* **2016**, *104*, 2380–2408. [CrossRef]
45. Marinangeli, A.; Chianella, I.; Radicchi, E.; Maniglio, D.; Bossi, A.M. Molecularly Imprinted Polymers Electrochemical Sensing: The Effect of Inhomogeneous Binding Sites on the Measurements. A Comparison between Imprinted Polyaniline versus nanoMIP-Doped Polyaniline Electrodes for the EIS Detection of 17β-Estradiol. *ACS Sens.* **2024**, *9*, 4963–4973. [CrossRef]

https://doi.org/10.3390/bios16010012

biosensors

MDPI

Supplementary Materials

Highly Sensitive Biosensor for the Detection of Cardiac Troponin I in Serum via Surface Plasmon Resonance on Polymeric Optical Fiber Functionalized with Castor Oil-Derived Molecularly Imprinted Nanoparticles

Alice Marinangeli [1,*], Pinar Cakir Hatir [2,3], Mustafa Baris Yagci [4] and Alessandra Maria Bossi [1,*]

[1] Department of Biotechnology, University of Verona, Strada Le Grazie 15, 37134 Verona, Italy
[2] Department of Biomedical Engineering, Faculty of Engineering and Natural Sciences, İstinye University, Ayazağa Mah. Azerbaycan Cad. (Vadistanbul 4A Blok) Sariyer, İstanbul 34396, Türkiye; pinar.hatir@istinye.edu.tr
[3] Nanotechnology and Advanced Materials Research Center, Istinye University, Sariyer, Istanbul 34396, Türkiye
[4] Koç University Surface Science and Technology Center (KUYTAM), Istanbul 34450, Türkiye; byagci@ku.edu.tr
* Correspondence: alice.marinangeli@univr.it (A.M.); alessandramaria.bossi@univr.it (A.M.B.); Tel.: +39-045-8027-833 (A.M.); Tel.: +39-045-8027-946 (A.M.B.)

1. Hydrodynamic size and polydispersity index (PI) of GreenNanoMIPs

Table S1. Particle size and the PDI of GreenNanoMIPs.

Sample	Particle size (nm)	PDI
GreenNanoMIPs	80.9	0.064

2. Stability of GreenNanoMIP over time

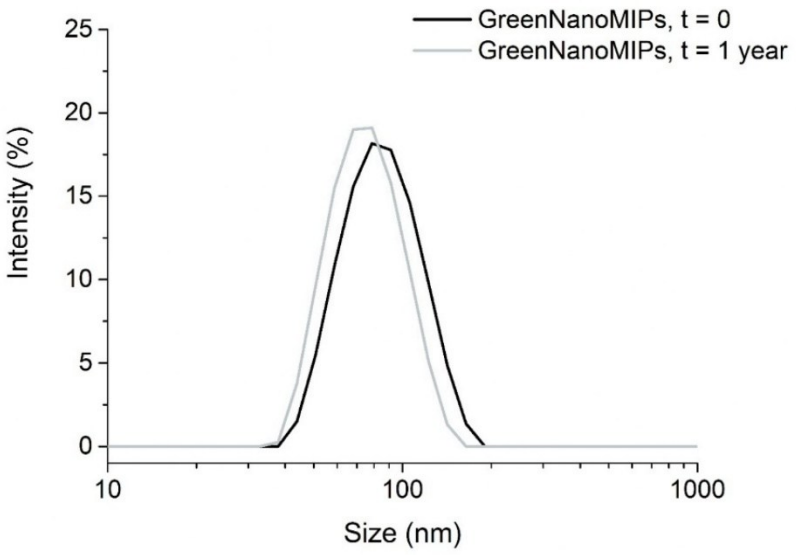

Figure S1. Particle size distributions of GreenNanoMIPs at the initial measurement and subsequently after one year. Re-printed from [22].

3. X-Ray Photoelectron Spectroscopy

https://doi.org/10.3390/bios16010012

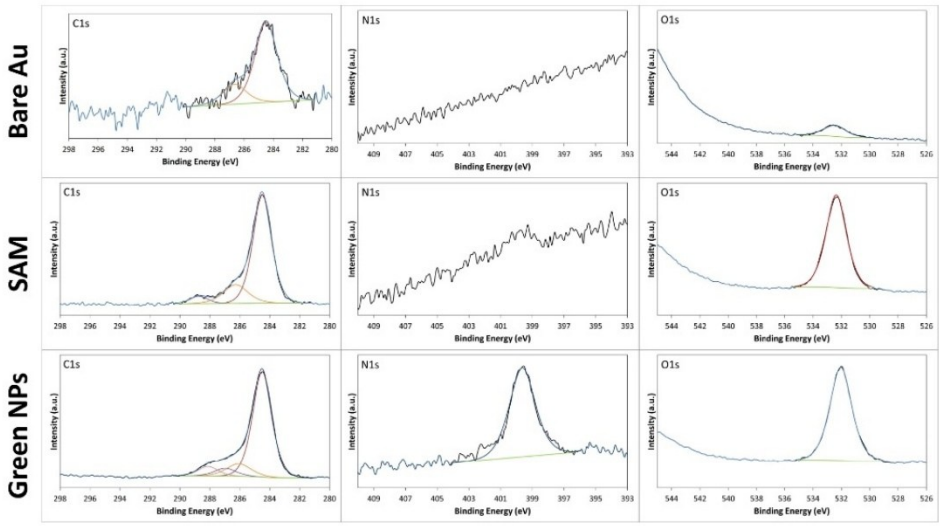

Figure S2. Deconvolution analysis of high-resolution XPS spectra of bare Au SPR-chip, SAM-modified SPR-chip and GreenNanoMIP functionalized SPR-chips.

4. Zoomed-in view of the plasmonic spectra of GreenNanoMIPs-SPR-POF for the binding of NR10 and NR11 peptide

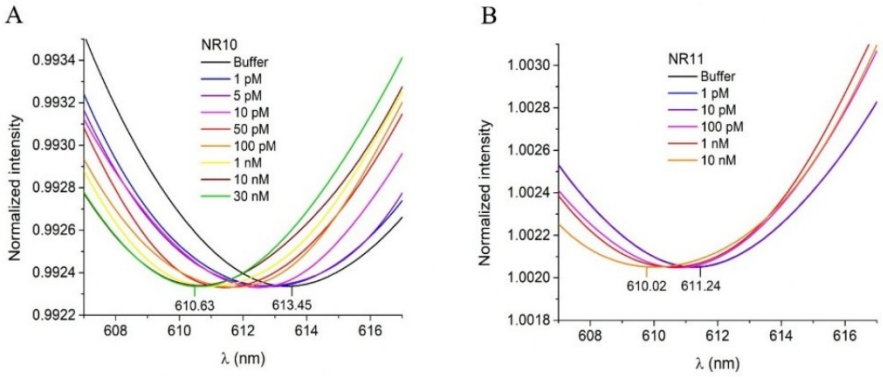

Figure S3. Zoomed-in view of the plasmonic spectra of GreenNanoMIPs-SPR-POF sensor incubated with increased concentrations of NR10 peptide (A) and with increased concentrations of NR11 peptide (B).

5. Zoomed-in view of the plasmonic spectra of GreenNanoMIPs-SPR-POF for the binding of cTnI, HSA and Cyt C

https://doi.org/10.3390/bios16010012

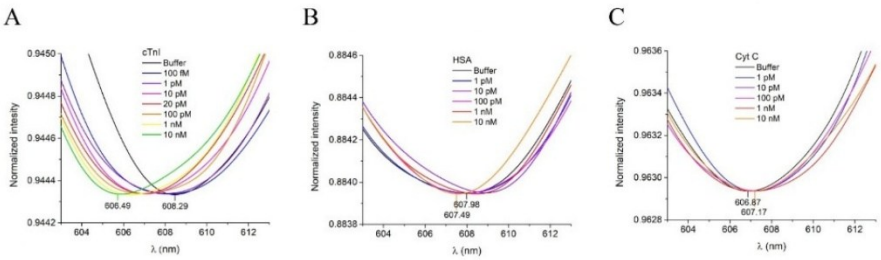

Figure S4. Zoomed-in view of the plasmonic spectra of GreenNanoMIPs-SPR-POF sensor incubated with increased concentrations of cTnI (A), HSA (B) and Cyt C (C).

6. Measurement of cTnI in serum with and without Tween20

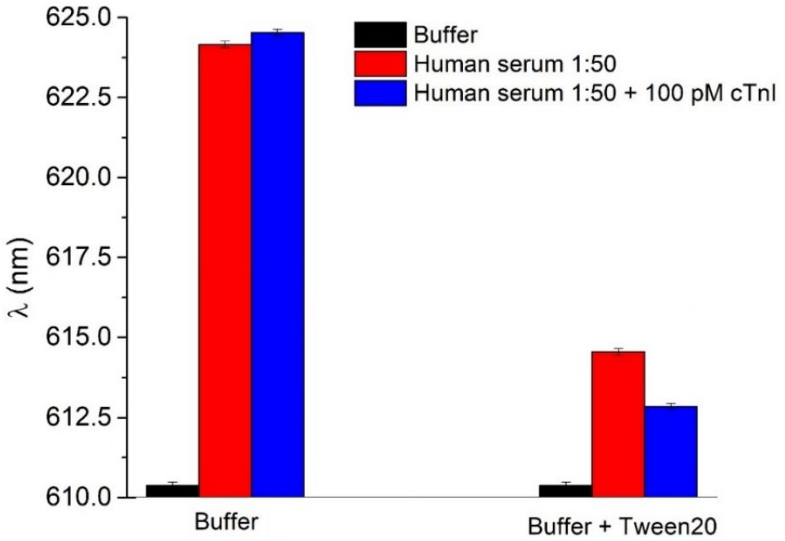

Figure S5. Evaluation of the effect of the addition of 0.1% of Tween20 to the working buffer on the cTnI_nanoMIP-SPR-sensor performance when tested with real samples. In the absence of Tween20, human serum 1:50 (red bar) and human serum 1:50 spiked with 100 pM of cTnI (blue bar) showed similar effects on the sensor (λ= 624.16 nm and λ= 624.53 nm), demonstrating that non-specific absorption occurring at the sensor's surface was the prevailing mechanism. In contrast, when Tween20 was added to the buffer, the matrix effect on the sensor observed for diluted human serum (red bar) accounted for a λ = 614.55 nm, indicating a reduced matrix effect. More importantly, when human serum 1:50 spiked with 100 pM of cTnI (blue bar) was placed on the sensor, the expected blue-shift (λ= 612.84 nm) that correlated with the cTnI spiked concentration was observed.

7. SEM imaging of GreenNanoMIPs

SEM images were collected with a JCM-5000 NeoScope QUATTRO S. Prior to SEM analysis, the GreenNanoMIPs were resuspended in distilled water to a final concentration

https://doi.org/10.3390/bios16010012

of 1 mg/mL. A small volume of the sample was drop-casted onto a clean surface, air-dried and subsequently examined under SEM. Figure S6 shows the GreenNanoMIPs at different magnifications. The size of the GreenNanoMIPs matches with DLS data.

It is worth noting that the air-drying process of GreenNanoMIPs yields aggregation artefacts.

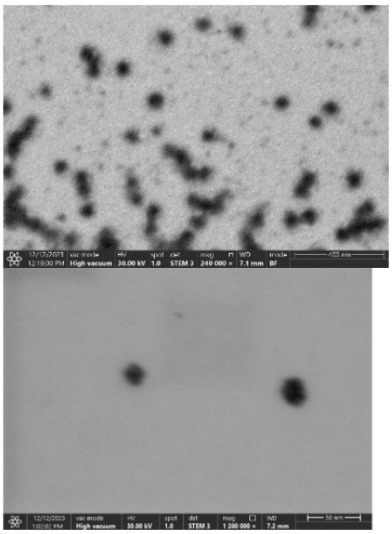

Figure S6. SEM image of GreenNanoMIPs.

https://doi.org/10.3390/bios16010012

Conclusions

The research presented in this PhD thesis demonstrates the versatility, robustness and high potential of MIPs as synthetic receptors for the development of advanced sensing systems, showing how a rational design of their structure, obtained through a careful control of size and chemical composition, combined with high sensitivity transduction strategies, can substantially enhance the performance of analytical recognition of the sensor platforms.

A major outcome of this work is the demonstration that controlling the morphology and homogeneity of the recognition sites is crucial for achieving high-performance sensing. The use of nanostructured MIPs, particularly spherical nanoMIPs, has proven effective in increasing the accessibility of binding sites and enhancing mass transfer, ultimately enabling the detection of analytes at ultra-low concentrations.

A complementary outcome of this thesis is the demonstration that the homogeneity of the imprinted binding sites plays a decisive role in determining the quality of the sensing response. By comparing a conventional electropolymerized MIP layer, characterized by an intrinsically heterogeneous distribution of recognition sites, with architectures incorporating pre-synthesized homogeneous nanoMIPs within the conductive layer, it became evident that uniformity in site structure directly influences both sensitivity and reproducibility. Sensors based on homogeneous nanoMIPs exhibited more defined binding behaviour, improved signal-to-noise ratios and lower detection limits, confirming that minimizing site heterogeneity is essential for achieving robust and analytically reliable MIP-based sensors.

Another significant contribution of this thesis is the advancement of optical transduction methods applied to MIP-based sensors. By incorporating fluorescent probes into the polymer matrix and optimizing their interaction with the template molecule, it was possible to tailor the photophysical behaviour of the resulting nanoMIPs and achieve enhanced signal responsiveness. The introduction of time-resolved fluorescence spectroscopy as a detection method further expands the potential of MIP-based sensors, demonstrating that fluorescence lifetime

measurements, which are still barely explored in MIP-based sensor field, offer a powerful and highly sensitive readout for monitoring binding events.

The thesis also contributes to the growing interest in innovative materials for imprinting by demonstrating that eco-friendly monomers derived from renewable resources can be successfully employed in MIP synthesis. The GreenNanoMIPs developed exhibited excellent recognition properties and stability, confirming that environmentally friendly approaches can be pursued without compromising analytical performance. Their successful implementation in both fluorescence- and plasmonic-based sensors further highlights their versatility and applicability across different platforms.

Overall, the results of this thesis confirm the strong potential of MIPs as reliable synthetic receptors for sensing applications, and illustrate how different approaches can contribute to the development of more sensitive, selective and robust MIP-based platforms. The present work is foreground to the translations of MIP-sensors into real-world applications, including for determining analytes in complex matrices. From this work, it emerges that the next research challenges to face encompasses ensuring the MIP's recognition homogeneity beyond the current result of the thesis, including testing synthetic strategies based on solid phase approaches; inspecting matrix effects, so to optimize the sensing response; actuating chemical strategies to fine-manipulating the placement of fluorescent tags, particularly by taking advantages of high-wavelength emissions and longer lifetimes inorganic fluorescent dyes, such as lanthanide-based dyes, as a resource for high photostability, long emission lifetimes, sharp emission spectra, and excellent sensitivity in a variety of different samples, including biologicals.